Funcionalización superficial de aleaciones de titanio mediante anodizado para aplicaciones biomédicas

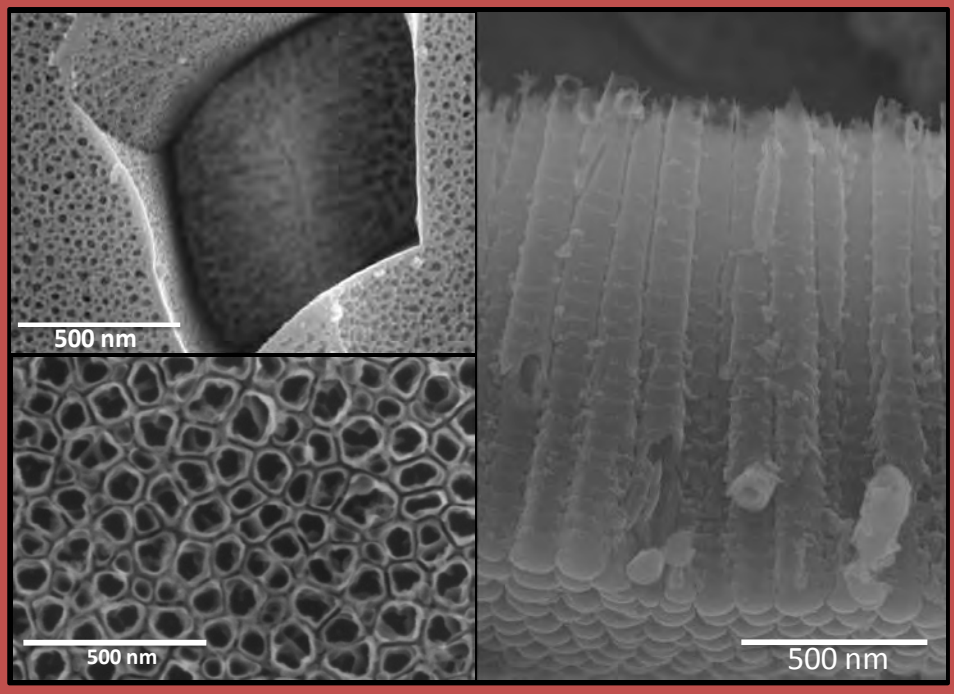

Juan Manuel Hernández López

TESIS DOCTORAL 2015

Funcionalización superficial de aleaciones de titanio mediante anodizado para aplicaciones biomédicas

TESIS DOCTORAL

JUAN MANUEL HERNÁNDEZ LÓPEZ

MADRID, JUNIO DE 2015

Memoria presentada para optar al título de Doctor en Electroquímica por la Universidad Autónoma de Madrid a través del programa de Doctorado en Electroquímica. Ciencia y Tecnología.

Bajo la dirección de la doctora:

María Ángeles Arenas Vara

Científica Titular
Dpto. de Ingeniería de Superficies, Corrosión y Durabilidad
Centro Nacional de Investigaciones Metalúrgicas (CENIM-CSIC)

Índice

Agradecimientos

Este trabajo ha sido realizado gracias a la financiación proporcionada por el Proyecto SMOTI MAT2009-13751, el Proyecto FUNCOAT CSD 2008-0023 del programa CONSOLIDER-INGENIO 2010 del Ministerio de Economía y Competitividad y al Programa JAE-Predoc del CSIC, patrocinado en parte por el Fondo Social Europeo.

Llegado a este momento me gustaría agradecer a todas las personas que han aportado tanto en lo académico como en lo personal.

En primer lugar me gustaría agradecer a dos personas que me han apoyado, guiado y enseñado durante todos estos años y representan un ejemplo de constancia, honestidad y sapiencia a seguir: María Ángeles Arenas -Geles- y Ana Conde, gracias a ambas.

A mi directora de tesis -Geles- por su ayuda, su tiempo y la dedicación que tuvo para dirigirme en este proceso formativo.

A la gente que he conocido durante mi estancia en el grupo COPROMAT, con los cuales he compartido momentos agradables y pláticas amenas durante el café: Alfonso Vázquez, Juan Damborenea, Iñaki García, Cristina Muñoz, Meritxell Ruiz, Elena Gracia, Juan Ahuir, Mar Bayod, Miguel Marín y José Gómez.

Finalmente, a DULCE YAAHID FLORES RENTERIA la persona que siempre me ha apoyado y animado a seguir adelante, que es un pilar en mi vida y el motor que me impulsa a esforzarme día a día, GRACIAS.

Resumen

Los grandes avances tecnológicos del siglo XX permitieron impulsar el desarrollo de nuevos materiales y dispositivos en diversos campos de la tecnología. Entre ellos destaca la medicina, siendo las áreas de medicina cardiovascular, reconstructiva y ortopédica donde el desarrollo para stents, válvulas cardiacas, implantes dentales, espinales, prótesis osteoarticulares totales y/o parciales, ha supuesto un gran avance de enorme repercusión económica y social.

A este éxito han contribuido en gran medida los materiales metálicos. Sin embargo, su uso no está todavía exento de inconvenientes. Uno de los principales problemas asociados a los implantes metálicos son las infecciones post-operatorias que pueden llegar a provocar el rechazo del implante. Una forma de prevenir estas infecciones es modificar la superficie del implante para dotarla con propiedades antibacterianas. Diferentes técnicas de modificación superficial como: tratamientos térmicos, recubrimientos sol-gel, tratamientos con laser, pulverización catódica, implantación iónica, anodizado, etc., han sido usadas con el fin de dotar a los distintos biomateriales y en especial a los implantes de titanio, de propiedades que permitan prevenir o eliminar el riesgo de infecciones. De entre dichas técnicas, el anodizado es un proceso que permite crecer capas de óxido de nanoestructura, espesor y composición controladas a partir de la optimización de las condiciones de crecimiento. En el presente trabajo de investigación se han crecido capas anódicas sobre dos aleaciones de titanio, Ti6Al4V y Ti13Nb13Zr, a partir de diferentes electrolitos acuosos, con el objetivo de diseñar nuevas nanoestructuras de óxido de titanio con morfología y composición química controlada que inhiban la adherencia bacteriana.

El trabajo realizado en esta tesis engloba desde la definición de las condiciones de crecimiento y su optimización -composición y pH del baño de anodizado, voltaje/corriente aplicados, tiempos de crecimiento,

temperatura-, hasta la caracterización morfológica, estequiométrica, microestructural de las capas crecidas y su estabilidad química en una solución fisiológica simulada (PBS) que permita entender cuál será su respuesta en el interior del cuerpo humano. Para ello, se han empleado una gran variedad de técnicas, entre las que destacan, las de caracterización superficial: microscopía electrónica de barrido (SEM) y transmisión (TEM), espectroscopía de energía dispersiva de rayos X (EDS), espectrometría de retrodispersión Rutherford (RBS), espectroscopía fotoelectrónica de rayos X (XPS), espectrometría Raman, difracción de rayos X (XDR), perfilometría confocal y determinación de la energía superficial. Así como, técnicas más específicas para el estudio de la estabilidad química de las capas como: las técnicas electroquímicas de estado estacionario y no estacionario (DC y AC).

Se han logrado crecer capas anódicas dopadas con flúor en un rango de espesores que van desde el nivel nanométrico (decenas) hasta el micrómetro (~2 μm), con contenidos de flúor que varían entre el 4 y el 12 % at. y con diferentes morfologías, compacta (barrera), nanoporosa y nanotubular, a partir de baños acuosos a 20 °C y en tiempos comprendidos entre los 5 y los 90 minutos.

El análisis de las capas crecidas muestra que se trata, principalmente, de un óxido amorfo cuya composición depende tanto de la aleación, como de la composición del baño de anodizado. Las capas anódicas generadas en Ti6Al4V, tienen una composición molecular media que es una mezcla de TiO_x, con $x<2$, Al_2O_3, V_2O_5 y TiF_4. Mientras que en la aleación Ti13Nb13Zr la capa está principalmente compuesta por un óxido complejo $(TiNbZrO)_x$ con $x<1$ y fluoruros de los elementos presentes en la aleación, NbF_5, ZrF_4 TiF_4.

La caracterización electroquímica de las capas anódicas revela que las superficies modificadas presentan en general una mejora en su comportamiento frente a la corrosión que depende íntimamente de la nanoestructura de las capas. Además, un resultado especialmente

interesante es el derivado de una interpretación cuidadosa y exhaustiva de los espectros de impedancia que permite correlacionar la respuesta del sistema con la nanoestructura de las capas, haciendo que la impedancia sea una herramienta muy potente para caracterizar las capas de óxido de titanio crecidas por el proceso de anodizado.

Finalmente, la caracterización biológica de los distintos óxidos crecidos se realizó en colaboración con los investigadores pertenecientes a los grupos de Reumatología y Metabolismo Óseo, y Microbiología del Instituto de Investigación Sanitaria (IIS)-Fundación Jiménez Díaz dirigidos por los doctores Pedro Esbrit y Jaime Esteban, respectivamente.

Los resultados obtenidos sobre las capas anódicas crecidas en la aleación Ti6Al4V muestran que el contenido de flúor en las capas anódicas es el responsable de la disminución, hasta en un 50 %, de la adherencia de *Staphylococcus aureus y Staphylococcus epidermidis,* procedentes tanto de cepas de colección como de cepas clínicas extraídas de pacientes que habían desarrollado infección. Además, la presencia del flúor no altera la respuesta celular ni la mineralización en comparación con la aleación Ti6Al4V sin anodizar. Muy al contrario, en algunos casos la presencia de este elemento en nanoestructuras concretas mejora la función osteogénica.

Lista de publicaciones

La presente Tesis doctoral se basa en las publicaciones que ha dado lugar este trabajo de investigación, las cuales se enumeran a continuación:

3.1: E. Matykina, J.M. Hernandez-López, A. Conde, C. Domingo, J.J. de Damborenea, M.A. Arenas, Morphologies of nanostructured TiO_2 doped with F on Ti–6Al–4V alloy, ***Electrochimica Acta***, 56 (2011) 2221-2229.

3.2: J.M. Hernández-López, A. Conde J.J. de Damborenea, M.A. Arenas, TiO_2 nanotubes with tunable morphologies, ***RSC Advances***, 4 (2014) 62576-62585.

3.3: J.M. Hernández-López, A. Conde, J.J. de Damborenea, M.A. Arenas, The influence of intertubular spacing of TiO_2 anodic layers on electrochemical response, (Manuscrito en preparación).

3.4a: M.A. Arenas, C. Pérez-Jorge, A. Conde, E. Matykina, J. M. Hernández-López, R. Pérez-Tanoira, J.J. de Damborenea, E. Gómez-Barrena, J. Esteba, Doped TiO_2 anodic layers of enhanced antibacterial properties, ***Colloids and Surfaces B: Biointerfaces***, 105 (2013) 106-112.

3.4b: D. Lozano, J.M. Hernández-López, P. Esbrit, M.A. Arenas, E. Gómez-Barrena , J. de Damborenea, J. Esteban, C. Pérez-Jorge, R. Pérez-Tanoira, A. Conde, Influence of the nanostructure of F-doped TiO_2 films on osteoblast growth and function, ***J Biomed Mater Res Part A***, 103A (2015): 1985-1990

3.5: J.M. Hernández-López, A. Conde, J.J. de Damborenea, M.A. Arenas, Correlation of the nanostructure of the anodic layers fabricated on Ti13Nb13Zr with the electrochemical impedance response, ***Corrosion Science***, 94 (2015) 61-69.

Capítulo 1

Introducción

TITANIO

El titanio (Ti) está presente alrededor de la corteza terrestre en un 0,6%, por lo que es el cuarto metal estructural más abundante después del aluminio, hierro y magnesio. Posee una estructura hexagonal compacta (hcp) a temperatura ambiente y presión atmosférica llamada fase α, mientras que a la misma presión pero a temperaturas elevadas se transforma a la fase β de estructura cúbica centrada en el cuerpo (bcc), figura 1a, siendo la temperatura de transformación de 882±2 °C para el Ti puro. Esta transformación alotrópica permite obtener aleaciones con microestructura tipo α, β o α+β, dependiendo de los elementos presentes en la aleación que estabilizarán una u otra fase. Las aleaciones de titanio se dividen en tres grandes grupos dependiendo de sus elementos de aleación, figura 1.1b, [1-4]:

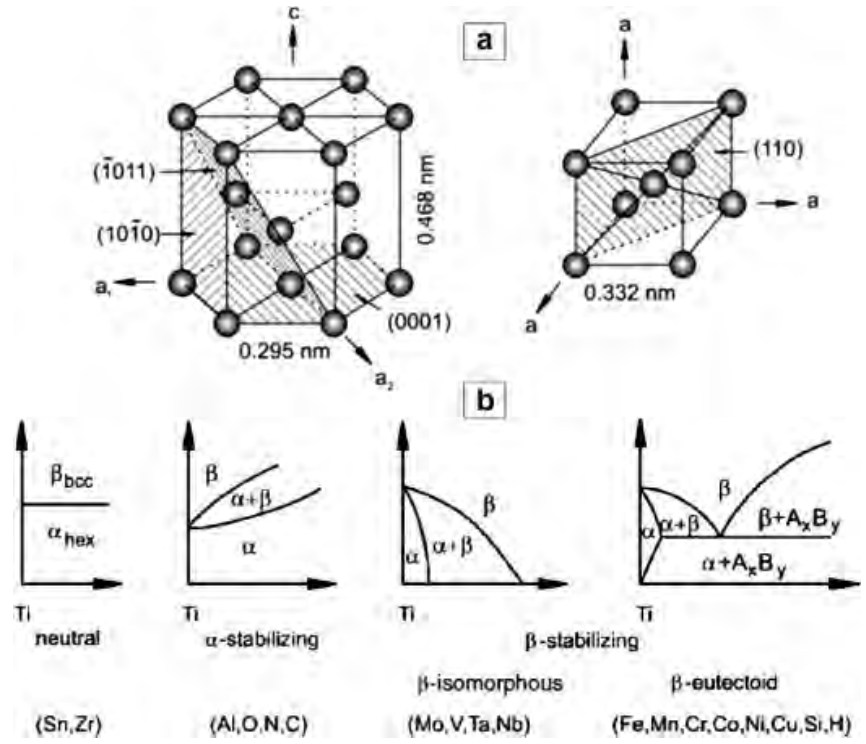

Figura 1.1. Estructuras cristalinas, hcp y bcc (a) y efecto de los elementos aleantes presentes en la matriz de titanio en la microestructura de la aleación (b)[4].

Alfa (α)

Los elementos que son capaces de estabilizar la fase alfa aumentando la temperatura en la cual esta fase se transforma en beta, se conocen como elementos alfa estabilizadores. El aluminio (Al), carbono (C), oxígeno (O) y nitrógeno(N) son los elementos más representativos de este grupo. Estos elementos tienen diferentes propiedades: el Al presenta un carácter sustitucional, mientras que el O, N y C poseen un carácter intersticial que aumenta la resistencia mecánica del titanio. El aluminio es el elemento α-estabilizador más usado en la mayoría de las aleaciones comerciales debido a su baja densidad. Sin embargo, la cantidad de este elemento que puede añadirse a la aleación es limitada, ya que a partir de un 8% en peso de Al aumenta la fragilidad de estas aleaciones por la formación de compuestos intermetálicos.

Beta (β)

Entre los elementos beta estabilizadores se encuentran el vanadio (V), molibdeno (Mo), niobio (Nb), talio (Tl) y cromo (Cr), por mencionar algunos. Estos elementos como su nombre indica, estabilizan la fase beta a temperatura ambiente y proporcionan características específicas, como por ejemplo, una mayor tenacidad a la fractura en comparación con las aleaciones tipo α, haciendo que las aleaciones beta se puedan emplear en procesos de estampación en frío. Además, es posible aumentar su resistencia mecánica mediante tratamientos térmicos. El principal inconveniente de estas aleaciones es que pueden presentar segregación de intermetálicos por la alta concentración de beta estabilizadores, fragilizando la aleación en ciertas condiciones de trabajo. No obstante, este problema puede minimizarse mediante la aplicación de un tratamiento térmico adecuado que homogenice la composición química durante el proceso de solidificación de la aleación.

Alfa + beta (α+β)

Estas aleaciones contienen una concentración suficiente de elementos beta estabilizadores para provocar que la fase beta persista hasta temperatura ambiente. En general son más duras que las aleaciones alfa y pueden someterse a tratamientos térmicos de envejecimiento para obtener mayor resistencia mecánica.

Actualmente, estas aleaciones son las que presentan una mayor demanda comercial, especialmente la aleación Ti-6Al-4V, denominada también Ti grado 5 según la norma ASTM B367, representando más del 50% del uso total de las aleaciones de titanio. Esta aleación se emplea fundamentalmente como material estructural debido a sus excelentes propiedades mecánicas y su alta resistencia a la corrosión [3, 5].

Por lo tanto, como norma general, tanto los elementos estabilizadores de ambas fases como los elementos llamados neutros (que no modifican en gran medida las temperaturas de transición) elevan la resistencia mecánica del titanio puro, mejorando sus prestaciones y permitiendo así su uso en distintas aplicaciones industriales.

La popularidad del titanio y sus aleaciones en distintos campos de la Ciencia y Tecnología, se refleja en el gran número de artículos científicos publicados sobre estos materiales en las diferentes áreas del conocimiento, tal y como se recoge en SCOPUS, una de las bases especializadas en búsquedas bibliográficas de carácter científico, figura 1.2.

Los temas relacionados con la salud engloban diferentes aplicaciones biomédicas como prótesis temporales y/o permanentes, y las publicaciones relativas al titanio y sus aleaciones se sitúan en la quita posición en el ranking de publicaciones realizadas en esta área de investigación. Ello se debe, entre otras cosas, a su alta resistencia a la corrosión, su buena biocompatibilidad, su baja densidad y el valor del módulo de elasticidad, más cercano al del hueso en comparación con otros materiales metálicos (aceros inoxidables, aleaciones de Co-Cr) empleados también en estas aplicaciones, figura 1.3 [6].

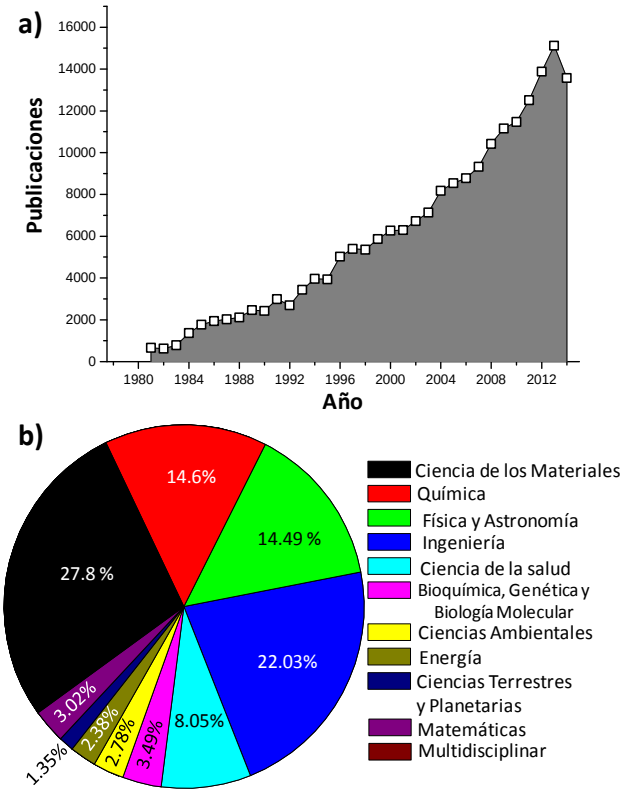

Figura 1.2. Número de artículos publicados a lo largo de los últimos 30 años en temas relacionados con el titanio y sus aleaciones (a) y principales áreas en las cuales se realiza la investigación (b) (Datos obtenidos de SCOPUS).

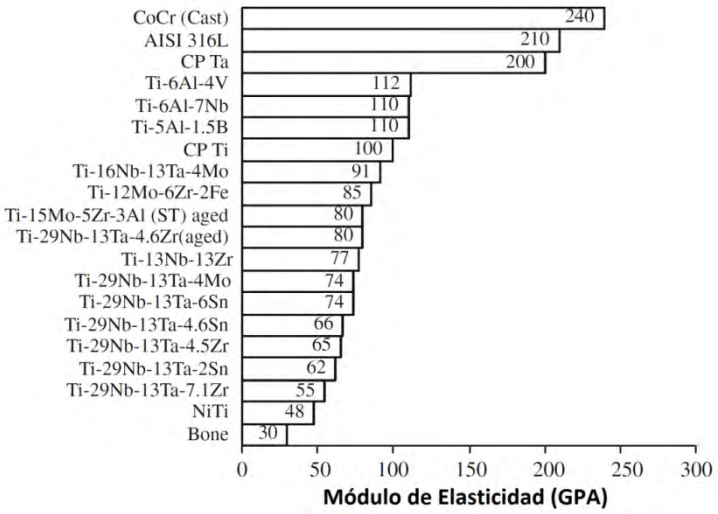

Figura 1.3. Módulo de elasticidad de aleaciones biomédicas[6].

En este sentido, es importante además destacar que el uso del titanio y sus aleaciones tiene una gran importancia en el desarrollo social ya que existen numerosos dispositivos de implantación en los cuales se utilizan estas aleaciones metálicas, con el fin de sustituir o fijar diferentes partes del cuerpo, figura 1.4.

Figura 1.4. Esquema de la utilización de prótesis de titanio en distintas partes del cuerpo humano [7]

BIOMATERIALES

Un biomaterial se define como un material no biológico que se utiliza en un dispositivo médico destinado a interactuar con sistemas biológicos, ya sea para reemplazar extremidades, tejidos o/y órganos, o bien para aumentar su funcionalidad [8, 9]. Dentro de la definición de biomateriales están incluidos materiales de diferente naturaleza química, como: materiales compuestos, polímeros, cerámicos y metálicos [6].

Las principales características que deben cumplir los biomateriales metálicos es que sean **biofuncionales**, es decir, que el material cumpla con las funciones para las cuales fue diseñado exhibiendo buenas propiedades físicas y mecánicas, que sean **biocompatibles**, definiéndose ésta como la ausencia de reacciones fisicoquímicas nocivas entre el material implantado y su entorno, que presenten una **alta resistencia a la corrosión** y al **desgaste**, por lo que los materiales implantados no deben liberar iones o partículas metálicas al interaccionar con los fluidos corporales y que favorezcan la **oseointegración**, siendo esta característica necesaria para que la superficie del implante se integre con el hueso adyacente [6, 9, 10].

Sin embargo, esto no siempre es posible ya que entre los principales inconvenientes de los biomateriales metálicos se encuentran los problemas causados por la corrosión y el desgaste debido a que están en contacto directo con ambientes fisiológicos agresivos y sometidos a cargas mecánicas. La formación de productos de corrosión influye en el deterioro de la superficie metálica y disminuye la capacidad protectora del material, dando lugar a reacciones negativas entre el implante y su entorno biológico, creando de forma progresiva irritación y/o inflamación que pueden desencadenar el rechazo de la prótesis [6, 11-13].

En este sentido, el titanio y sus aleaciones (Ti cp., Ti6Al4V, Ti3Al, TiN, TiAl, TiC, Ti13Nb13Zr, etc.) muestran mayor viabilidad que los demás materiales metálicos empleados como biomateriales, debido a su buena resistencia a la fatiga, relativamente bajo módulo elástico, baja densidad, excelente resistencia a la corrosión y biocompatibilidad, siendo estas dos últimas propiedades asociadas a la presencia en la superficie de un óxido nativo (TiO_2) denso y protector que se forma de manera natural en aire o agua a temperatura ambiente y que presenta un espesor de 2-10 nanómetros [9, 12, 14]. No obstante, el TiO_2 posee una bioactividad limitada que hace que se necesiten tiempos muy largos para que se produzca su unión con el hueso yuxtapuesto lo que puede traducirse en una deficiente oseointegración que puede conducir al fallo del implante. Este hecho ha

originado que el crecimiento de películas de TiO_2 de manera controlada sea uno de los campos de investigación que mayor atención ha recibido en los últimos años [11].

INFECCIONES PROTÉSICAS

Además de los problemas asociados al material, la innegable presencia de microorganismos durante el procedimiento de implantación puede desencadenar un problema de infección en la zona circundante a la intervención debido a la adherencia de bacterias sobre el dispositivo implantado que posteriormente pueden dar lugar a la formación de estructuras conocidas como biopelículas. Estas biopelículas pueden interferir en la función prevista causando una hospitalización prolongada, complejos procedimientos de revisión, el rechazo del implante que conlleva la remoción del mismo o la eliminación completa de la zona infecta y en el peor de los casos la muerte, sin mencionar las cargas sociales que ésto representa [9, 10, 15-17]. Además, el esperado aumento en el uso de implantes, figura 1.5 a, por el incremento de la expectativa de vida puede agravar dicho problema. De hecho, en los Estados Unidos de América [18-22], las infecciones de artroplastia total de cadera o artroplastia total de rodilla se producen con una incidencia del 1.5-2.5% para intervenciones primarias encontrándose en las revisiones las tasas de infección más altas (2-20%), figuras 1.5 b y c. El coste del tratamiento de una artroplastia infectada es entorno a $50000 dólares por paciente, y representa alrededor de $250 millones de dólares por año. Además, entre el 1-2.7% de los casos que sufren infección, desencadenan la muerte del paciente.

En España, se estima que el número de artroplastias de cadera y rodilla anuales es de aproximadamente 70000 [22-26], de los cuales el 0.5-2.5% desarrollan una infección protésica, lo que supone unos 350-1750 pacientes cada año. Este número posiblemente aumentará ya que se prevé un mayor uso de implantes de este tipo.

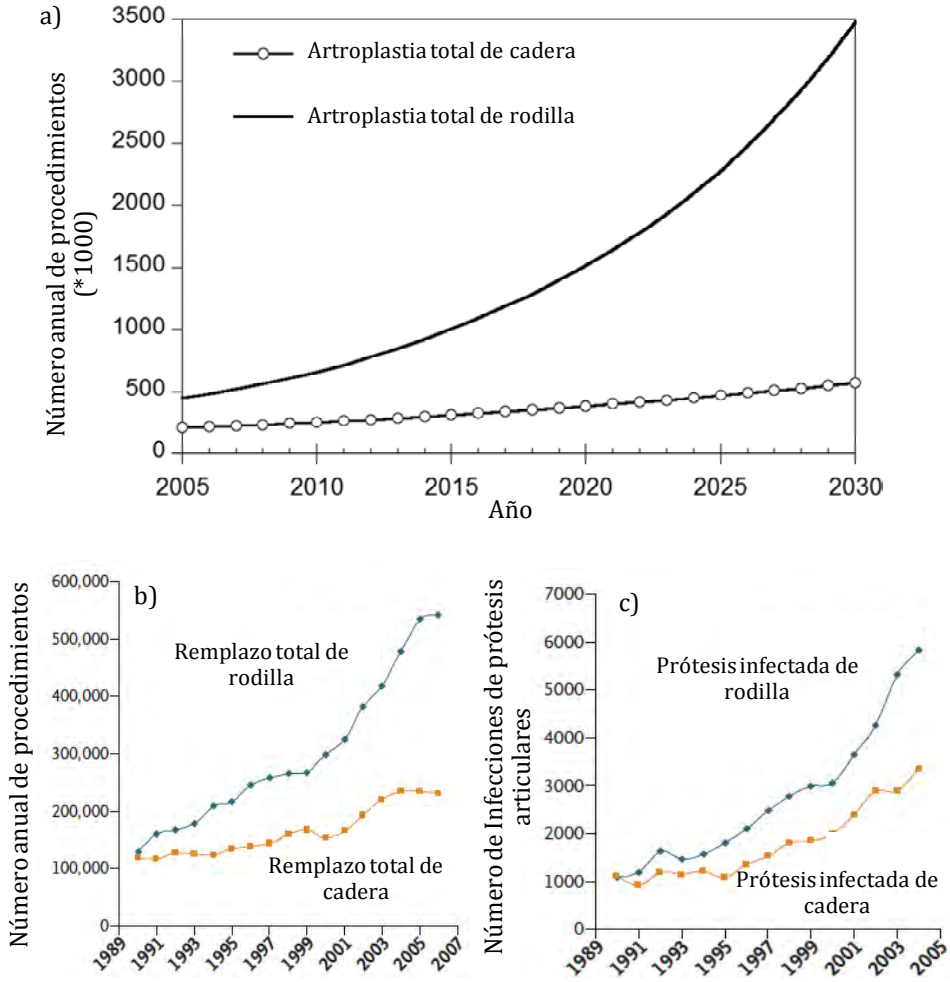

Figura 1.5. Número y estimación de artroplastias primarias total de cadera y de rodilla en los Estados Unidos de América desde 2005 hasta 2030 (a) [18]. Número de remplazos producidos en artroplastias totales realizadas desde 1990 hasta 2006 (b) y el número de infecciones primarias asociadas a éstos, para el mismo período de tiempo [20].

Existen varios factores de riesgo para que se produzcan infecciones protésicas, entre los que destaca: una cirugía previa en el sitio de la prótesis, artritis reumatoide, estados inmunodeprimidos, diabetes, mal estado nutricional, obesidad, edad avanzada, el virus de la inmunodeficiencia humana (VIH) y enfermedades autoinmunes [21, 27, 28]. Los microorganismos que causan la infección podrían provenir de una

o más fuentes, entre las que principalmente se encuentran los propios microorganismos que viven sobre la piel y aquellos que pueden ser transportados por el aire desde un foco de infección distante [21, 29]. Los microorganismos *Staphylococcus aureus* y *Staphylococcus epidermidis* son los microorganismos a los cuales se les asocian el 65% de las infecciones de prótesis articulares [15, 21, 30, 31].

Gristina y col. [16] propusieron que el destino final de un implante podía ser conceptualizado como una carrera por la superficie en la que existe una competención entre las células del tejido y las bacterias por colonizar su superficie. Si las células ganan la carrera, habrá menos superficie disponible para la colonización bacteriana y el éxito del implante aumentará.

Una vez que la bacteria alcanza la superficie del implante, la adhesión bacteriana desempeña un papel fundamental en el desarrollo de las infecciones asociadas a los implantes. El proceso de adhesión bacteriana, sobre la superficie de los implantes se puede dividir en dos fases que dependen del tiempo (figura 1.6):

- La fase I involucra asociaciones reversibles con la superficie del implante y ocurre durante las primeras 2 horas después de la implantación. Estas asociaciones se dan a través de fuerzas de Van der Waals, interacciones electrostáticas, puentes de hidrógeno, uniones dipolo-dipolo, interacciones hidrofóbicas.
- La Fase II se inicia entre 2-3 horas después de haberse implantado el biomaterial. La adhesión de las bacterias al sustrato metálico se vuelve más fuerte como resultado de uniones covalentes o iónicas entre las bacterias y el biomaterial. A partir de este momento, el crecimiento de las bacterias en comunidades bacterianas se lleva a cabo hasta formar una biopelícula o biofilm en aproximadamente 24 horas. Esta biopelícula protege a las bacterias adheridas de las defensas del huésped y de los antibióticos administrados por vía sistémica,

permitiendo liberar bacterias en estado planctónico de la estructura de la biopelícula para comenzar el ciclo de nuevo en otra parte del implante [16, 17, 21, 29, 32-36].

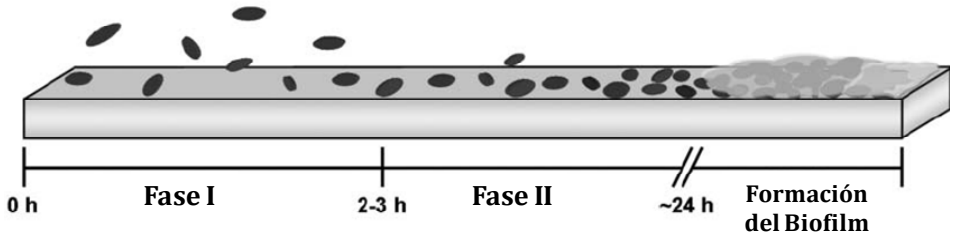

Figura 1.6. Representación de la adhesión bacteriana a la superficie de un biomaterial [34].

Por tanto, una de las estrategias para impedir o reducir el proceso de adhesión inicial de las bacterias sobre la superficie de los biomateriales para evitar así la formación de la biopelícula y el proceso infeccioso, consiste en modificar la superficie de los biomateriales.

Entre los procesos que permiten la funcionalización de la superficie destacan los tratamientos químicos que utilizan ácidos, bases fuertes y peróxido de hidrógeno que modifican la superficie debido a las reacciones químicas que se producen en la interfase metal/solución, la implantación de iones, el anodizado, etc., todos ellos procesos que no modifican las dimensiones de la pieza inicial [8, 11, 37-39].

Esta última técnica, el anodizado, es una de las técnicas más versátiles y económicas para la funcionalizar las superficies de titanio [8, 37, 38, 40-43] y es el proceso empleado en el presente trabajo de investigación. El proceso de anodizado permite la generación de nanoestructuras de óxido de titanio que combinan el diseño de una morfología definida (apartado 3.2), por ejemplo nanotubos de óxido de titanio en forma de botella, con una composición química controlada (apartados 3.1-3.2 y 3.5), que consigue dotar a la superficie de una funcionalidad distinta a la del material másico. En este trabajo se han conseguido crecer capas anódicas con propiedades antibacterianas, que además, han mostrado que favorecen la proliferación

celular y la mineralización, tal y como se recoge en el apartado 3.4 de la presente tesis doctoral.

ANODIZADO

El anodizado consiste en el crecimiento mediante un proceso electroquímico de películas de óxido de espesor controlado y con mejores propiedades protectoras que los óxidos formados de manera natural sobre el metal. El Al[44], Ti[37], Nb[45], Ta[46], Zr[47], Zn[48], Mg[49] y sus aleaciones pueden anodizarse mediante la elección de las condiciones adecuadas de anodizado, siendo posiblemente el anodizado de aluminio uno de los procesos más implantados en la industria desde inicios del siglo XIX [44, 50]. Estos metales pueden anodizarse porque sus óxidos son termodinámicamente estables, presentando valores de potencial de reducción muy negativos, tal y como se recoge en la Tabla 1.1 [51].

Para realizar el proceso de anodizado generalmente se emplea una celda electroquímica de dos electrodos, en la que el ánodo es el material en el cual se desea crecer la capa de óxido y el cátodo es una placa o varilla de un material químicamente inerte en el baño de anodizado. Ambos electrodos se conectan a un circuito eléctrico externo para establecer una diferencia de voltaje o corriente entre ellos, figura 1.7. Los materiales más empleados como cátodos son el grafito, el acero inoxidable, y el platino. La elección del material del cátodo influye en mayor o menor medida en la velocidad de crecimiento de las capas anódicas u originar cambios en la morfología del óxido (espesor de la capa de óxido, diámetro de los poros o nanotubos, etc.) debido a que puede variar la velocidad de algunas reacciones, afectando directamente en la sobretensión producida entre el cátodo y el ánodo [38].

Reacción	Potencial (V)
$Au^{3+} + 3e^- \leftrightarrow Au$	1.42
$Cu^{2+} + 2e^- \leftrightarrow Cu$	0.34
$2H^+ + 2e^- \leftrightarrow H2$	0.00
$Ni^{2+} + 2e^- \leftrightarrow Ni$	-0.23
$Fe^{2+} + 2e^- \leftrightarrow Fe$	-0.44
$Cr^{3+} + 3e^- \leftrightarrow Cr$	-0.71
$Zn^{2+} + 2e^- \leftrightarrow Zn$	-0.76
$Ta^{5+} + 5e^- \leftrightarrow Ta$	-0.81
$Nb^{3+} + 3e^- \leftrightarrow Nb$	-1.10
$Zr^{4+} + 4e^- \leftrightarrow Zr$	-1.54
$Ti^{2+} + 2e^- \leftrightarrow Ti$	-1.63
$Al^{3+} + 3e^- \leftrightarrow Al$	-1.66
$Mg^{2+} + 2e^- \leftrightarrow Mg$	-2.38

Tabla 1.1. Potenciales Estándar de reducción.

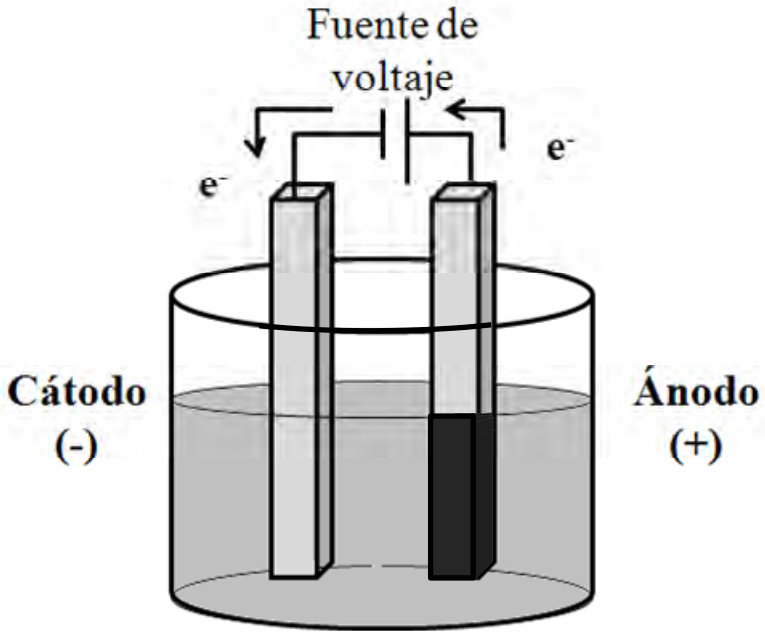

Figura 1.7. Esquema de una celda electroquímica de dos electrodos empleada en los procesos de anodizado.

ANODIZADO DE TITANIO

En el caso del titanio y sus aleaciones, no es hasta 1999 cuando Zwilling y col. [52, 53] publicaron por primera vez el crecimiento de capas porosas de óxido de titanio crecidas por anodizado en electrolitos que contenían iones fluoruro. Estos autores encontraron que el óxido crecido no era completamente homogéneo (poros ordenados) debido a las fluctuaciones de corriente, y atribuían el pequeño espesor de las capas que obtenían al establecimiento de un equilibrio entre el crecimiento del óxido y su disolución química en el electrolito empleado. A partir de este primer trabajo se ha producido la publicación de un extenso número de artículos científicos entre los que destacan los trabajos de Schmuki y col.[54-63] y Grimes y col.[38, 64-71], relativos al crecimiento de nanoestructuras auto-ordenadas de manera relativamente rápida y sencilla en titanio y en aleaciones binarias de titanio [37, 72, 73].

Las morfología, composición y espesor de las capas anódicas pueden modificarse en función de los diferentes parámetros del proceso de anodizado como son: la naturaleza del electrolito empleado (orgánico o acuoso) y su composición, el pH, la temperatura del baño, el tiempo de tratamiento, el voltaje aplicado, etc [38, 72, 74-77]. Dependiendo de las condiciones de crecimiento se pueden obtener dos morfologías distintas, figura 1.8:

- Capa compacta, conocida como capa barrera (capa libre de poros), figura 1.8a.
- Capa dúplex, formada por una capa porosa/tubular en la parte externa de la película y una capa barrera generada en la intercara óxido/metal. En la presente tesis denominaremos a estas capas como capas nanoporosas (figura 1.8b) o nanotubulares (figura 1.8c) dependiendo de si se han formado o no espacios inter-tubulares entre los poros.

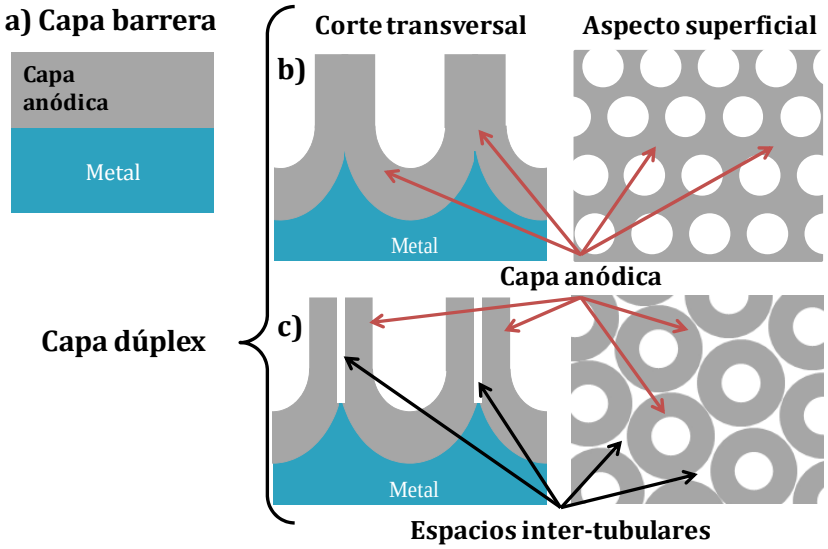

Figura 1.8. Esquema del tipo de morfologías obtenidas mediante anodizado, capa barrera (compacta) (a); capas dúplex con estructura nanoporosa (b) o nanotubular (c).

Regonini y col. [72] explican de manera detallada el efecto de cada uno los parámetros del proceso de anodizado en el crecimiento y morfología de las capas anódicas. En la figura 1.9 se presenta de manera esquemática el efecto de cada variable del proceso en las propiedades de las capas dúplex de TiO_2 (longitud, diámetro del poro/nanotubo y acabado superficial)[77].

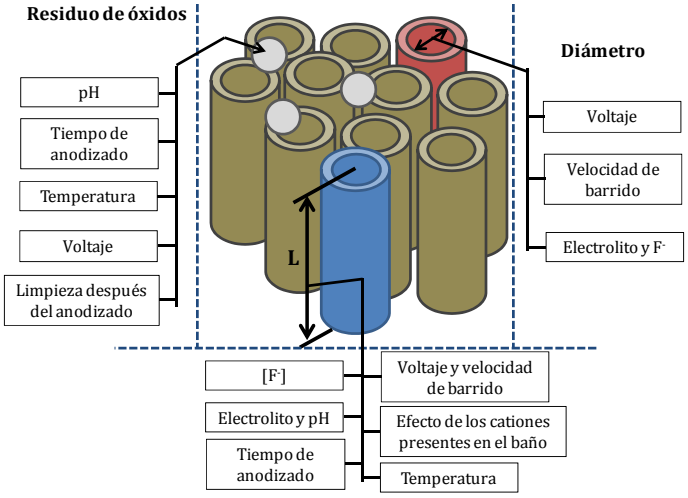

Figura 1.9. Esquema de la influencia de los parámetros de anodizado en el crecimiento de estructuras dúplex de TiO_2 [77].

No obstante, entre los diferentes parámetros del proceso de anodizado, la composición del baño y el voltaje aplicado influyen de manera determinante en el mecanismo de crecimiento y en las características de la capa anódica. A continuación se detalla el efecto de estos dos parámetros en la morfología y espesor de las capas anódicas:

1) Composición del baño de anodizado.

A diferencia de lo que sucede en aluminio, en el titanio y sus aleaciones se generan capas barrera en electrolitos ácidos (sulfúrico, fosfórico y bórico) debido a la gran estabilidad del óxido de titanio crecido en estos medios. Por tanto, para generar capas nanoporosas/nanotubulares sobre titanio es necesario emplear electrolitos que contengan iones fluoruros y/o cloruros, debido a que la solubilidad del óxido de titanio en estos casos es mayor. En este sentido, existen muchos trabajos publicados en la bibliografía [37, 38, 63, 72, 75, 76, 78-83] en los que se señala que el pH, la concentración de fluoruros, el contenido de agua (en el caso de baños orgánicos) y la temperatura del electrolito afectarán directamente a las características morfológicas de los nanotubos generados.

Grimes y col. [38] propusieron una clasificación de capas nanoporosas/nanotubulares crecidas en titanio y sus aleaciones en cuatro generaciones según el electrolito empleado para fabricarlas.

La primera generación de nanotubos de óxido de titanio es aquella en la cual el crecimiento de las capas nanoporosas o nanotubulares de TiO_2 se crecen en soluciones acuosas ácidas con HF. Se caracteriza por la elevada disolución química del TiO_2 y por alcanzar espesores máximos de unos cientos de nanómetros, entre 100-500 nm [70, 84-86].

Para la segunda generación de capas nanotubulares de óxido de titanio se utiliza en vez de ácido fluorhídrico, sales de fluoruro [87-89]. Se logran obtener capas de espesor de hasta varios micrómetros. Ello es debido al control de la acidificación auto-inducida en el fondo del poro lo que genera

un gradiente de pH en el interior del nanotubo que permite el crecimiento de nanotubos con una longitud de hasta ~ 6μm.

La tercera generación, a diferencia de las dos primeras en las cuales la naturaleza del electrolito era acuosa, emplea electrolitos de naturaleza orgánica con sales de fluoruro (0.1 - 0.5 wt%) y pequeñas cantidades de agua (0.1 - 5 wt%). Se obtienen capas nanotubulares de espesores comprendidos entre los nanómetros hasta 1 mm [54, 71, 90-93]. La obtención de espesores tan grandes se debe fundamentalmente a la disminución del contenido de agua en el electrolito, lo que resulta en una disminución en la velocidad de disolución química de la capa de óxido. En este caso, el mecanismo que controla el crecimiento de la capa anódica es el de flujo asistido por el campo eléctrico[78, 94-96], del cual se hablará más adelante.

Y por último, la cuarta generación de nanotubos de TiO_2, cuya definición es la más controvertida. Grimes y col. [38] la definen como aquella en la que la fabricación de nanotubos de óxido de titanio se realiza en electrolitos acuosos libres de fluoruros, como ácido oxálico, fórmico, sulfúrico o perclórico [97-99]. Las principales características de estas capas es la formación de nanoestructuras no homogéneas sobre la superficie y espesores de capa que van desde los nanómetros hasta los micrómetros. Sin embargo, Schmuki [72, 100-102] utiliza el término cuarta generación para referirse más específicamente a las capas anódicas crecidas sobre titanio puro y aleaciones binarias de titanio en estos electrolitos orgánicos con pequeñas cantidades de agua, pero que poseen estructuras auto organizadas y de geometrías avanzadas, como nanotubos tipo bambú, nanotubos de doble pared, sistemas multicapa de nanotubos, nanotubos con diámetro variable, etc.

2) El voltaje aplicado.

La importancia del voltaje aplicado en el proceso de anodizado además de ser determinante en la generación de nanoestructuras avanzadas

pertenecientes a la cuarta generación de nanotubos según la descripción propuesta por Schmuki, radica en que éste determina la fuerza del campo eléctrico a través de la capa de óxido y tiene un efecto directo sobre las reacciones de oxidación y disolución asistida por el campo que se producen durante la formación de las estructuras nanotubulares.

En las capas barrera, el voltaje aplicado -V-, está relacionado con el factor de crecimiento -*fg*- y con su espesor -*d*-, de acuerdo a la ecuación 1.1:

$$f_g = {}^{d}/_{V} \qquad (1.1)$$

Por tanto, un aumento del voltaje aplicado origina un aumento en el espesor de la capa barrera. En el caso del titanio, el factor de crecimiento de las capas barrera varía entre 1.3 a 3.3 nm/V dependiendo del medio de crecimiento [74, 103].

El potencial aplicado para crecer capas nanoporosas/nanotubulares generalmente oscila entre 5-30 V y de 10-60 V en electrolitos acuosos y orgánicos, respectivamente [37, 72]. El diámetro de los nanotubos, tanto en la boca como en su parte inferior, está también directamente relacionado por la magnitud del potencial aplicado.

Por otra parte, en la bibliografía se indica que en las capas anódicas crecidas sobre aluminio, titanio y aleaciones binarias de titanio existe una relación lineal 1:2 entre la velocidad de crecimiento de la capa barrera y la velocidad de crecimiento del diámetro de los nanotubos/nanoporos [59, 60, 104-106], figura 1.10. Yasuda y col. [59] propusieron que la formación del nanotubo se produce inicialmente de forma hemisférica, Fig. 1.10b, pudiéndose estimar el diámetro inicial de los nanotubos/nanoporos crecidos sobre Ti y TiZr en una solución acuosa con NH_4F mediante la ecuación 1.2:

$$d_{nanotubo} = 2r = 2f_g V \qquad (1.2)$$

donde r es el radio del nanoporo/nanotubo.

Esta relación varía dependiendo de la composición química de la aleación, su microestructura, la naturaleza del electrolito (orgánico o acuoso), etc.

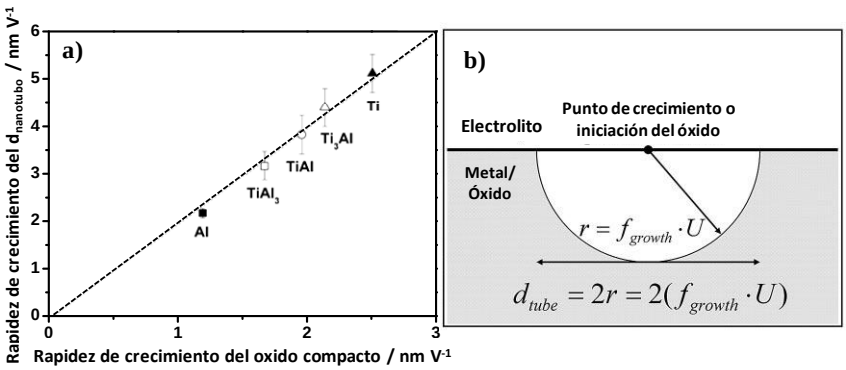

Figura 1.10. Correlación entre los datos de la bibliografía para las velocidades de crecimiento de las capas barrera (*fg*) y la distancia interior del poro (d_{int}), (a), modelo propuesto por Yasuda y col. (b) [59, 106]

MECANISMO DE CRECIMIENTO DE LA CAPA ANÓDICA

En este apartado se describe el mecanismo de crecimiento de las capas de óxido de titanio atendiendo a su morfología. En primer lugar, se explica el proceso de fabricación de capas barrera crecidas en un medio de anodizado en el cual la solubilidad del óxido de titanio es baja y en segundo lugar, el crecimiento de capas dúplex en las cuales la disolución química de la capa anódica durante su crecimiento desempeña un papel importante [37, 38, 56, 72].

CAPAS BARRERA

En medios de anodizado donde la solubilidad del óxido de titanio es baja, en la superficie del ánodo de titanio (Ti) se produce la reacción de oxidación dando lugar a la formación de iones Ti^{4+} (reacción 1.1). Estos iones reaccionan con los OH^- provenientes de la reducción del H_2O en el cátodo (reacción 1.7) y con los O^{2-} de la desprotonación del OH^- (reacción 1.2), debidas ambas reacciones al campo eléctrico impuesto. Por tanto, sobre la superficie del ánodo se forma un óxido de titanio de acuerdo a la

reacción 1.3, un óxido hidratado de titanio (reacción 1.4) que puede convertirse en óxido de titanio (reacción 1.5) y el desprendimiento de oxígeno debido a la oxidación del medio (reacción 1.6) [37, 38, 107-109].

$$Ti \rightarrow Ti^{4+} + 4e^{-} \quad [1.1]$$

$$OH^{-} \rightarrow O^{2-} + H^{+} \quad [1.2]$$

$$Ti^{4+} + 2O^{2-} \rightarrow TiO_2 \quad [1.3]$$

$$Ti^{4+} + 4OH^{-} \rightarrow Ti(OH)_4 \quad [1.4]$$

$$Ti(OH)_4 \rightarrow TiO_2 + 2H_2O \quad [1.5]$$

$$2H_2O \rightarrow 4H^{+} + 4e^{-} + O_2 \quad [1.6]$$

Mientras que en el cátodo se produce la evolución de hidrógeno, reacción 1.7, proveniente de la reducción del H_2O, y reacción 1.8:

$$2H_2O + 2e^{-} \rightarrow 2OH^{-} + H_2 \quad [1.7]$$

$$2H^{+} + 2e^{-} \rightarrow H_2 \quad [1.8]$$

La combinación de estas reacciones da como resultado la reacción global del proceso de anodizado:

$$2Ti + 6H_2O \rightarrow 2TiO_2 + 6H_2 + O_2 \quad [1.9]$$

En la figura 1.11 se presenta de manera esquemática el proceso de crecimiento de las capas anódicas de óxido de titanio y las reacciones que intervienen en el proceso.

El mecanismo que controla del proceso de anodizado en este tipo de medios es el denominado régimen de campo alto o "High-field regime" en inglés [72, 108, 110], figura 1.12. Según este mecanismo, la corriente/voltaje aplicada durante el anodizado crea un campo eléctrico a través del óxido que activa dos mecanismos de conducción: la migración iónica de iones O^{2-} hacia la intercara óxido/metal e iones Ti^{4+} hacia la interfase óxido/electrolito-; y la conducción electrónica.

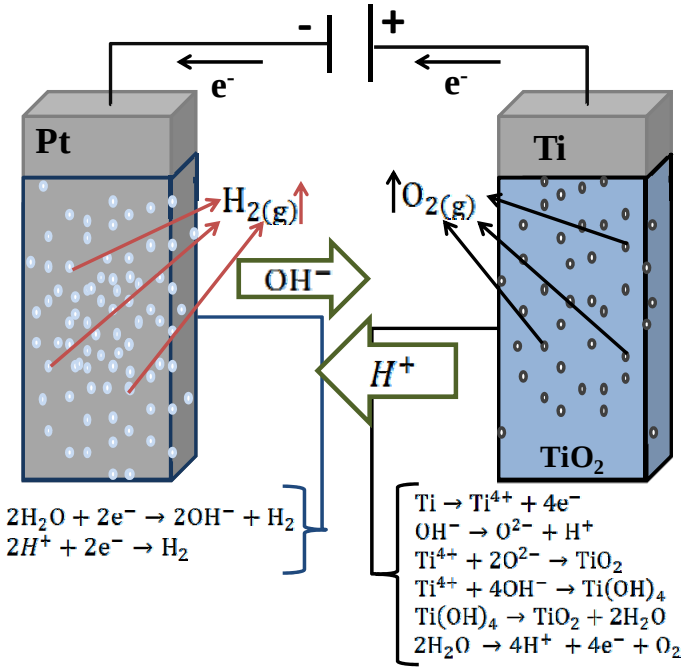

Figura 1.11. Esquema simplificado de las reacciones que ocurren sobre el cátodo y el ánodo de la celda electroquímica durante el proceso de anodizado.

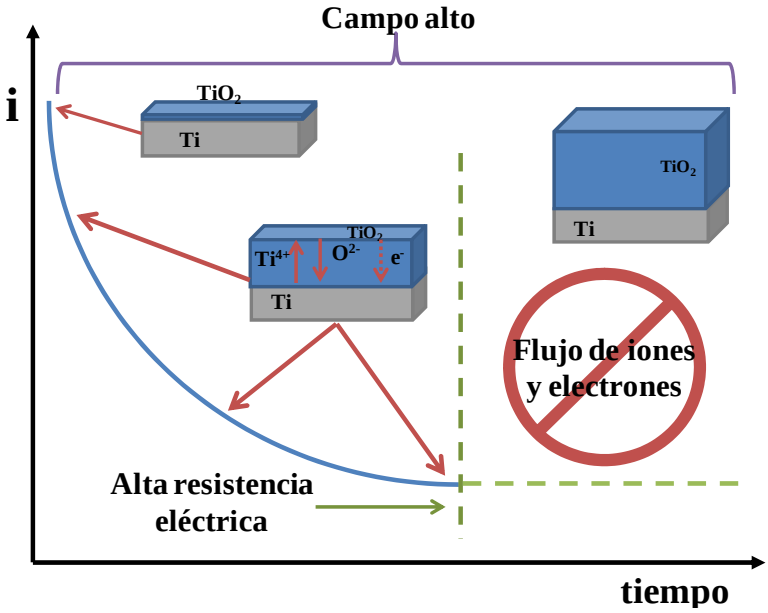

Figura 1.12. Curva de intensidad-tiempo que se recoge durante la formación de las capas barrera de TiO_2 crecidas a voltaje constante en un medio donde la solubilidad del óxido es muy baja.

Por tanto, el mecanismo de migración iónica cooperativa es el responsable del crecimiento de la capa. Cada uno de estos iones contribuye de manera distinta a su crecimiento, mientras que el Ti^{4+} con número de transporte es ~0.4, es el responsable del 40% de la capa anódica, el O^{2-} lo es del 60% restante en virtud de su número de tranporte,~0.6. De manera que el crecimiento de la capa sucede no sólo en la intercara metal/óxido sino también en la intercara óxido/electrolito. Dicho proceso sucede hasta que la película de óxido alcanza un espesor crítico que ralentiza el proceso de oxidación y finalmente cesa, cuando el aumento de la resistencia eléctrica de la capa impide el flujo de iones y electrones [37, 103, 111].

La conducción electrónica es responsable de la evolución de oxígeno en la interfase óxido/electrolito y se observa en el ánodo durante el proceso de anodizado. Esta conducción electrónica en el titanio es comparativamente más alta que en el aluminio, debido a la naturaleza semiconductora del óxido de titanio, en comparación con la naturaleza aislante del óxido de aluminio.

Los primeros estudios sobre la conductividad iónica dentro las películas de óxido se realizaron en aluminio encontrando que la densidad de corriente -*i*-, recogida durante el crecimiento de la capa de óxido, depende exponencialmente de la fuerza del campo eléctrico -*F*- según la ec. 1.3[80, 110, 112, 113]:

$$i = \alpha \cdot e^{(\beta \cdot F)} \qquad (1.3)$$

donde α y β son constantes experimentales que dependen de la temperatura. Ello implica que los procesos que ocurren en las intercaras (metal/óxido y óxido/electrolito) no determinan la velocidad de migración de los iones dentro de la capa anódica y que el óxido que crece es homogéneo; por lo tanto, la fuerza del campo a lo largo de la capa de óxido es constante. La fuerza del campo eléctrico a través de la película de óxido puede ser estimada a partir del espesor del óxido (*d*) y de la caída de potencial (ΔE) según la ec. 1.4: [110, 114]:

$$F = {\Delta E}/{d} \qquad (1.4)$$

Una vez aplicada una diferencia de potencial entre el ánodo y el cátodo, la densidad de corriente disminuye exponencialmente debido al aumento del espesor de la capa de óxido y por lo tanto, a una disminución de la fuerza del campo eléctrico, ec. 1.5:

$$i = \alpha * e^{(\beta * {\Delta E}/{d})} \qquad (1.5)$$

Así, el crecimiento de la capa anódica está controlado por la fuerza del campo eléctrico en soluciones donde la disolución del óxido es muy baja [103, 110, 111, 115].

La eficiencia del proceso de anodizado durante el crecimiento de las capas barrera puede disminuir debido a distintos procesos, entre los que se encuentran [103, 108, 110, 111, 116]:

- Formación de sub-óxidos con distinta estructura y composición química a lo largo de la capa anódica.
- Incorporación de aniones distintos al oxígeno desde el electrolito durante el crecimiento del óxido, ya que esta incorporación puede influir en la movilidad de los iones, la conductividad, las propiedades dieléctricas, la velocidad de crecimiento y la estabilidad química del óxido.
- Formación de burbujas de oxígeno gas que quedan ocluidas en el óxido, modificando localmente la conductividad eléctrica. Los iones oxígeno que migran hacia el interior de la capa anódica pueden perder sus electrones y convertirse en oxígeno molecular produciendo burbujas.
- Ruptura de la capa anódica (Breakdown) debido a la formación local de altas densidades de corriente en heterogeneidades presentes en la interfase óxido/electrolito.
- Disolución de la capa de óxido: Disolución química de la capa debido a cambios locales de pH en la superficie del óxido y disolución de la capa por efecto del campo eléctrico que depende de la actividad de

los iones metálicos en la superficie del óxido (eyección de iones Ti^{4+} al electrolito).

- Reacciones de transferencia de electrones. Evolución de oxígeno e hidrógeno en la superficie del ánodo y del cátodo, respectivamente.

CAPAS DE ESTRUCTURA DÚPLEX

Cuando el óxido de titanio presenta una alta solubilidad en el medio de anodizado, como sucede en el caso de baños con iones fluoruros, el electrolito afecta en gran medida al proceso de anodizado y por consiguiente, a las características de las capas anódicas crecidas.

En medios con fluoruros, además de las reacciones químicas que se producen durante la formación de las capas barrera (reacciones 1.1-1.8), la presencia de estos iones en el baño produce la disolución química del $Ti(OH)_4$ y TiO_2 que se están formando o reaccionan con los iones Ti^{4+} que migran en la capa anódica hacia la interfase óxido/electrolito (debido al efecto del campo eléctrico), dando lugar a la formación del compuesto soluble TiF_6^{2-}, reacciones 1.10-1.12, respectivamente.

$$Ti(OH)_4 + 6F^- \rightarrow TiF_6^{2-} + 4OH^- \qquad [1.10]$$

$$TiO_2 + 6F^- + 4H^+ \rightarrow TiF_6^{2-} + 2H_2O \qquad [1.11]$$

$$Ti^{4+} + 6F^- \rightarrow TiF_6^{2-} \qquad [1.12]$$

Además, y debido a la mayor velocidad de migración iónica de los iones F^- respecto al O^{2-} por su menor radio iónico, se produce otra reacción en la intercara metal/óxido, que conduce a la formación del compuesto, reacción 1.13:

$$Ti^{4+} + F^- \rightarrow TiF_4 \qquad [1.13]$$

Dependiendo de la concentración de fluoruros en el electrolito, se obtienen capas anódicas con distinta morfología. Para contenidos de fluoruros en el baño de anodizado muy bajos, ≤ 0.05 wt.% HF, el mecanismo de formación de la capa es el descrito para el crecimiento de una capa barrera de TiO_2. Es decir, el crecimiento del óxido está gobernado por el régimen de campo

alto, figura 1.12, pero las capas presentan una morfología no uniforme. Por el contrario, si la concentración de fluoruros en el medio es alta, ≥ 4 wt.% HF, la capa de óxido no se formará ya que los iones Ti^{4+} reaccionan con los fluoruros del baño formando $[TiF_6]^{2-}$, según las reacciones 1.10-1.12. Mientras que a concentraciones intermedias de fluoruros en el electrolito, la formación del óxido y disolución de $[TiF_6]^{2-}$ tiene lugar simultáneamente dando origen a la formación de un óxido con estructura nanoporosa o nanotubular [37, 41, 72, 80, 86] dependiendo de las condiciones de anodizado. Generalmente, a tiempo largos de anodizado, la formación de las estructuras nanotubulares es consecuencia de la disolución del TiF_4 el cual presenta una mayor solubilidad que el óxido de titanio en el medio de anodizado.

El modelo clásico que explica las etapas del crecimiento de las estructuras nanoporosas/nanotubulares de TiO_2 [37, 38, 53, 70, 72, 77, 79] se muestra, de manera esquemática, en la figura 1.13, junto con la evolución de la densidad de corriente recogida durante un proceso de anodizado a voltaje constante. Dicho modelo asume la formación inicial de una capa barrera de TiO_2 sobre la superficie del titanio de acuerdo al "régimen de campo alto". Esta etapa se manifiesta en la gráfica de densidad de corriente frente al tiempo por una caída abrupta de la misma, fase I. A continuación, se observa un aumento de la corriente, fase II, relacionado con la disminución de la resistencia de la capa anódica por la generación de defectos superficiales (*pits*) provocados por la disolución localizada del óxido lo que da lugar a la formación de los poros. Estos poros crecen fundamentalmente por efecto de la disolución asistida por el campo eléctrico (field-assisted disolution) y por la acidificación local debida a la oxidación e hidrólisis del titanio (disolución química) en el fondo del poro, generando un gradiente de pH entre el fondo y la boca de los mismos. A medida que éstos se vuelven más grandes, la disolución preferencial en la base de poro por efecto del campo eléctrico (field-assisted disolution) es más fuerte y ejerce el control sobre el crecimiento de la capa anódica, en comparación con su

efecto sobre la pared del poro/tubo donde la disolución química tiene mayor influencia. Finalmente, la corriente alcanza un valor constante, fase III, momento a partir del cual se alcanza un estado de equilibrio entre la formación del óxido en la intercara metal/óxido y la velocidad de disolución química en la interfase óxido/electrolito.

En este sentido, es importante destacar que la principal diferencia entre las capas barrera y las capas nanoporosas/nanotubulares reside en que mientras el crecimiento de las capas barrera ocurre tanto en la intercara metal/óxido como en la interfase óxido/electrolito, en el caso de las capas nanotubulares el crecimiento sucede exclusivamente en la intercara metal/óxido [72, 80, 110].

Por otro lado, la morfología de las capas nanoestructuradas depende en gran medida del proceso de disolución química que, en medios acuosos con fluoruros, es muy elevado y en algunas ocasiones, es el proceso principal que gobierna la etapa III - crecimiento de los poros/tubos- [72, 87].

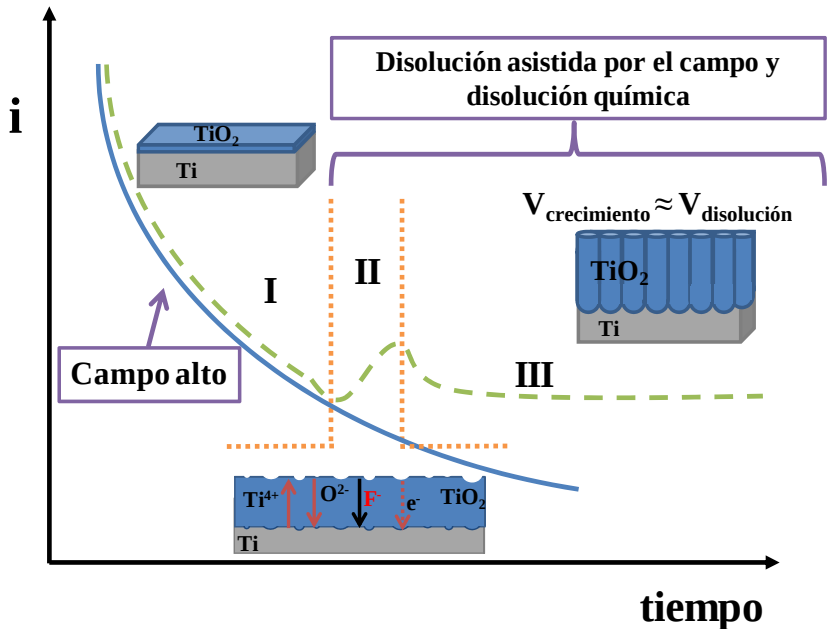

Figura 1.13. Curva densidad de corriente–tiempo que se recoge durante el crecimiento de una capa de TiO_2 a voltaje constante en un medio con fluoruros.

Así, el crecimiento de estructuras dúplex consiste en un proceso competitivo entre la formación de la capa anódica (reacción 1.9) y su disolución tanto por efecto del campo eléctrico que debilita las uniones entre el titanio y el oxígeno (disolución asistida por el campo) [72, 77, 79, 117, 118] como por la presencia de iones fluoruro en el medio de anodizado (disolución química).

No obstante, aunque la disolución asistida por el campo es el mecanismo que clásicamente se ha usado para describir el crecimiento de capas nanoporosas/nanotubulares, Skeldon y col. [119, 120] propusieron un nuevo mecanismo conocido como "flujo plástico asistido por el campo" (flow model o field-assisted plastic flow) para explicar el crecimiento de las capas anódicas porosas en aluminio. Estos autores demostraron que el desarrollo de los poros en la capa anódica se debe al desplazamiento del óxido de la capa barrera hacia las paredes de los poros. Esto fenómeno es posible gracias a que durante el crecimiento de la capa anódica, las propiedades mecánicas del óxido, y más concretamente su plasticidad, cambian por efecto del campo eléctrico (electrostricción), resultando en un aumento del espesor de la capa anódica a valores superiores a los esperados teóricamente [37, 72, 120, 121]. La figura 1.14 esquematiza ambos mecanismos de crecimiento, la "disolución asistida por el campo eléctrico" y el "flujo plástico asistido por el campo". Para ello, estos autores depositaron por sputtering una aleación en forma de sándwich, Al/Al-30%W/Al, y la anodizaron en ácido fosfórico. El seguimiento de la posición de la capa de W durante las diferentes etapas del proceso de anodizado les permitió determinar la influencia de cada uno de los mecanismos. Si el mecanismo que controlaba el crecimiento de los poros era la disolución asistida por el campo, la capa de tungsteno se movería hacia la intercara óxido/electrolito a través de las paredes de los poros de forma uniforme conforme creciera la capa porosa, localizándose únicamente en las paredes de los poros (fig 1.14a). Por el contrario, si es el mecanismo controlante era el de flujo asistido por el campo, la capa de tungsteno se localizaría tanto en

la capa barrera como en las paredes de los poros (fig. 1.14b). Los estudios realizados mediante TEM permitieron confirmar que la morfología de la capa crecida en fosfórico es principalmente debida al flujo de óxido hacia las paredes de los poros desde la región de la capa barrera bajo los mismos. Posteriormente, estos mismos autores [95, 96] realizaron estudios similares en titanio empleando electrolitos orgánicos con sales de NH_4F, concluyendo que durante la generación de las capas nanotubulares en estos medios pueden estar activos tanto el mecanismo de disolución asistida por el campo eléctrico en los primeros instantes de formación de la capa anódica, y posteriormente domina el mecanismo de flujo plástico asistido por el campo eléctrico durante el crecimiento de las estructuras nanotubulares.

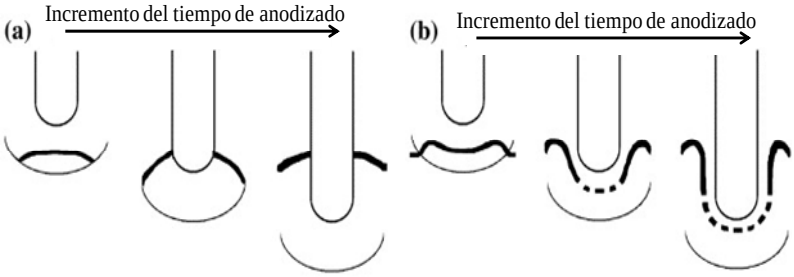

Figura 1.14. Esquema del mecanismo que controla el crecimiento de una capa anódica y posición del marcador de W empleado. a) Mecanismo de disolución asistida por el campo; (b) Modelo de flujo plástico asistido por el campo [121].

El estudio del mecanismo de crecimiento de las capas anódicas es uno de los objetivos fundamentales de la presente tesis doctoral y se aborda principalmente en los apartados 3.1, 3.2 y 3.5 para explicar las características morfológicas que presentan las capas anódicas crecidas tanto en Ti6Al4V como en la aleación Ti13Nb13Zr.

Referencias

[1] G. Lütjering, J.C. Williams, Titanium, in, Springer, 2007, pp. 442.
[2] C. Leyens, M. Peters, in: Titanium and Titanium Alloys: Fundamentals and Applications, Wiley-VCH Verlag GmbH & Co. KGaA, 2005, pp. 532.
[3] A. Handbook, Properties and Selection: Nonferrous Alloys and Special-Purpose Materials, ASM INTERNATIONAL.
[4] D. Banerjee, J.C. Williams, Perspectives on Titanium Science and Technology, Acta Materialia, 61 (2013) 844-879.
[5] ASTM International: ASTM B367-93. Standard Specification for Titanium and Titanium Alloy Castings, in, 1993.
[6] M. Geetha, A.K. Singh, R. Asokamani, A.K. Gogia, Ti based biomaterials, the ultimate choice for orthopaedic implants – A review, Progress in Materials Science, 54 (2009) 397-425.
[7] A.W. Tan, B. Pingguan-Murphy, R. Ahmad, S.A. Akbar, Review of titania nanotubes: Fabrication and cellular response, Ceramics International, 38 (2012) 4421-4435.
[8] X. Liu, P.K. Chu, C. Ding, Surface nano-functionalization of biomaterials, Materials Science and Engineering: R: Reports, 70 (2010) 275-302.
[9] D.R. Buddy, S.H. Allan, J.S. Frederick, E.L. Jack, Biomaterials science: An Introduction to Materials in Medicine, Academic Press, 2004.
[10] I.N. Ana Morato, Concha Toribio, El Futuro de los Biomateriales: Tendencias tecnológicas a medio y largo plazo, in, Madrid, 2004.
[11] D.V. Shtansky, N.A. Gloushankova, A.N. Sheveiko, M.A. Kharitonova, T.G. Moizhess, E.A. Levashov, F. Rossi, Design, characterization and testing of Ti-based multicomponent coatings for load-bearing medical applications, Biomaterials, 26 (2005) 2909-2924.
[12] M. Niinomi, Mechanical biocompatibilities of titanium alloys for biomedical applications, Journal of the Mechanical Behavior of Biomedical Materials, 1 (2008) 30-42.
[13] J.R. Birch, T.D. Burleigh, Oxides Formed on Titanium by Polishing, Etching, Anodizing, or Thermal Oxidizing, Corrosion, 56 (2000) 1233-1241.
[14] E. Eisenbarth, D. Velten, M. Müller, R. Thull, J. Breme, Biocompatibility of β-stabilizing elements of titanium alloys, Biomaterials, 25 (2004) 5705-5713.
[15] H.J. Busscher, H.C. van der Mei, G. Subbiahdoss, P.C. Jutte, J.J.A.M. van den Dungen, S.A.J. Zaat, M.J. Schultz, D.W. Grainger, Biomaterial-Associated Infection: Locating the Finish Line in the Race for the Surface, Science Translational Medicine, 4 (2012) 153rv110.
[16] A.G. Gristina, P. Naylor, Q. Myrvik, Infections from biomaterials and implants: a race for the surface, Medical Progress through Technology, 14 (1988) 205-224.

[17] L. Zhao, P.K. Chu, Y. Zhang, Z. Wu, Antibacterial coatings on titanium implants, Journal of biomedical materials research. Part B, Applied biomaterials, 91 (2009) 470-480.
[18] S. Kurtz, K. Ong, E. Lau, F. Mowat, M. Halpern, Projections of primary and revision hip and knee arthroplasty in the United States from 2005 to 2030, The Journal of Bone & Joint Surgery, 89 (2007) 780-785.
[19] S.M. Kurtz, E. Lau, J. Schmier, K.L. Ong, K. Zhao, J. Parvizi, Infection Burden for Hip and Knee Arthroplasty in the United States, The Journal of Arthroplasty, 23 (2008) 984-991.
[20] J.L. Del Pozo, R. Patel, Infection Associated with Prosthetic Joints, New England Journal of Medicine, 361 (2009) 787-794.
[21] S. Esposito, S. Leone, Prosthetic joint infections: microbiology, diagnosis, management and prevention, International Journal of Antimicrobial Agents, 32 (2008) 287-293.
[22] A.E. González-Vélez, C. Díaz-Agero Pérez, A. Robustillo-Rodela, V. Monge-Jodrá, Incidencia y factores asociados a la infección de localización quirúrgica tras artroplastia de cadera, Revista Española de Cirugía Ortopédica y Traumatología, 59 (2011) 270-276.
[23] E. Gómez-Barrena, N.G. Padilla-Eguiluz, E. García-Rey, J. Cordero-Ampuero, E. García-Cimbrelo, Factors influencing regional variability in the rate of total knee arthroplasty, The Knee, 21 (2014) 236-241.
[24] M.P.-J. Peremarch, Estudio de adherencia bacteriana y formación de biopelículas en materiales de Ti-6Al-4V anodizado, in: Departamento de Microbiología I, Universidad Complutense de Madrid, Madrid, 2013, pp. 100.
[25] La hospitalización de las personas mayores en el Sistema Nacional de Salud CMBD, in: E. comentadas (Ed.), Ministerio de Sanidad, Servicios Sociales e Igualdad, Madrid, 2010, pp. 38.
[26] Unidad de Evaluación de Tecnologías Sanitarias, Estándares de uso adecuado de tecnologías sanitarias. Artroplastia total de cadera, in, Consejería de Sanidad de la Comunidad de Madrid, Madrid, Spain, 2010, pp. 86.
[27] E.F. Berbari, A.D. Hanssen, M.C. Duffy, J.M. Steckelberg, D.M. Ilstrup, W.S. Harmsen, D.R. Osmon, Risk Factors for Prosthetic Joint Infection: Case-Control Study, Clinical Infectious Diseases, 27 (1998) 1247-1254.
[28] P. Hoekman, P. Van de Perre, J. Nelissen, B. Kwisanga, J. Bogaerts, F. Kanyangabo, Kigali, Increased frequency of infection after open reduction of fractures in patients who are seropositive for human immunodeficiency virus, Journal of Bone and Joint Surgery - Series A, 73 (1991) 675-679.
[29] P. Maathuisa, S. Bulstraa, H. van der Meib, J. van Horna, H. Busscherb, Biomaterial-associated surgery and infection a review of literature, Detection, prevention and direct post-operative intervention in orthopaedic implant infection, (2007) 17.

[30] C.P.-J. Peremarch, R.P. Tanoira, M.A. Arenas, E. Matykina, A. Conde, J.J. De Damborenea, E.G. Barrena, J. Esteban, Bacterial adherence to anodized titanium alloy, Journal of Physics: Conference Series, 252 (2010) 012011.
[31] P. Fernández-Viladrich, J. García-Lechuz, M.R. Jaume, Guía de recomendaciones para el diagnóstico y tratamiento de las infecciones asociadas a biomateriales, in, Guías Clínicas SEIMC 2006.
[32] J. Esteban, D. Molina-Manso, I. Spiliopoulou, J. Cordero-Ampuero, R. Fernández-Roblas, A. Foka, E. Gómez-Barrena, Biofilm development by clinical isolates of Staphylococcus spp. from retrieved orthopedic prostheses, Acta Orthopaedica, 81 (2010) 674-679.
[33] R. Bürgers, T. Gerlach, S. Hahnel, F. Schwarz, G. Handel, M. Gosau, In vivo and in vitro biofilm formation on two different titanium implant surfaces, Clinical Oral Implants Research, 21 (2010) 156-164.
[34] E.M. Hetrick, M.H. Schoenfisch, Reducing implant-related infections: active release strategies, Chemical Society Reviews, 35 (2006) 780-789.
[35] M. Quirynen, M. De Soete, D. Van Steenberghe, Infectious risks for oral implants: a review of the literature, Clinical Oral Implants Research, 13 (2002) 1-19.
[36] W. Teughels, N. Van Assche, I. Sliepen, M. Quirynen, Effect of material characteristics and/or surface topography on biofilm development, Clinical Oral Implants Research, 17 (2006) 68-81.
[37] P. Roy, S. Berger, P. Schmuki, TiO_2 nanotubes: synthesis and applications, Angewandte Chemie, 50 (2011) 2904-2939.
[38] C. A.Grimes, G. K.Mor, TiO_2 Nanotube Arrays: Synthesis, Properties, and Applications, in, Springer, 2009, pp. 358.
[39] T. Goto, Surface coating technology for biomaterials—morphology and nano-structure control, International Congress Series, 1284 (2005) 248-256.
[40] K. Das, S. Bose, A. Bandyopadhyay, TiO_2 nanotubes on Ti: Influence of nanoscale morphology on bone cell–materials interaction, Journal of Biomedical Materials Research Part A, 90A (2009) 225-237.
[41] S. Minagar, C.C. Berndt, J. Wang, E. Ivanova, C. Wen, A review of the application of anodization for the fabrication of nanotubes on metal implant surfaces, Acta biomaterialia, 8 (2012) 2875-2888.
[42] K. Vasilev, Z. Poh, K. Kant, J. Chan, A. Michelmore, D. Losic, Tailoring the surface functionalities of titania nanotube arrays, Biomaterials, 31 (2010) 532-540.
[43] C. Yao, E.B. Slamovich, T.J. Webster, Enhanced osteoblast functions on anodized titanium with nanotube-like structures, Journal of Biomedical Materials Research Part A, 85A (2008) 157-166.
[44] J.W. Diggle, T.C. Downie, C.W. Goulding, Anodic oxide films on aluminum, Chemical Reviews, 69 (1969) 365-405.

[45] R.L. Karlinsey, Preparation of self-organized niobium oxide microstructures via potentiostatic anodization, Electrochemistry Communications, 7 (2005) 1190-1194.
[46] I.V. Sieber, P. Schmuki, Porous Tantalum Oxide Prepared by Electrochemical Anodic Oxidation, Journal of The Electrochemical Society, 152 (2005) C639-C644.
[47] W.-J. Lee, W.H. Smyrl, Zirconium Oxide Nanotubes Synthesized via Direct Electrochemical Anodization, Electrochemical and Solid-State Letters, 8 (2005) B7-B9.
[48] C.Y. Kuan, J.M. Chou, I.C. Leu, M.H. Hon, Formation and field emission property of single-crystalline Zn microtip arrays by anodization, Electrochemistry Communications, 9 (2007) 2093-2097.
[49] Y. Mizutani, S.J. Kim, R. Ichino, M. Okido, Anodizing of Mg alloys in alkaline solutions, Surface and Coatings Technology, 169–170 (2003) 143-146.
[50] C. Lu, Z. Chen, Anodic Aluminum Oxide-Based Nanostructures and Devices, in: H.S. Nalwa (Ed.) Encyclopedia of Nanoscience and Nanotechnology, American Scientific Publishers, 2011, pp. 235-259.
[51] V. Christian, M. Jacques, M.P. Schmidt, Corrosion of Aluminium, Elsevier, 2004.
[52] V. Zwilling, M. Aucouturier, E. Darque-Ceretti, Anodic oxidation of titanium and TA6V alloy in chromic media. An electrochemical approach, Electrochimica Acta, 45 (1999) 921-929.
[53] V. Zwilling, E. Darque-Ceretti, A. Boutry-Forveille, D. David, M.Y. Perrin, M. Aucouturier, Structure and physicochemistry of anodic oxide films on titanium and TA6V alloy, Surface and Interface Analysis, 27 (1999) 629-637.
[54] J.M. Macak, H. Tsuchiya, L. Taveira, S. Aldabergerova, P. Schmuki, Smooth Anodic TiO_2 Nanotubes, Angewandte Chemie International Edition, 44 (2005) 7463-7465.
[55] X. Feng, J.M. Macak, P. Schmuki, Robust Self-Organization of Oxide Nanotubes over a Wide pH Range, Chemistry of Materials, 19 (2007) 1534-1536.
[56] J.M. Macák, H. Tsuchiya, P. Schmuki, High-Aspect-Ratio TiO_2 Nanotubes by Anodization of Titanium, Angewandte Chemie International Edition, 44 (2005) 2100-2102.
[57] J.M. Macak, H. Tsuchiya, L. Taveira, A. Ghicov, P. Schmuki, Self-organized nanotubular oxide layers on Ti-6Al-7Nb and Ti-6Al-4V formed by anodization in NH_4F solutions, Journal of biomedical materials research. Part A, 75 (2005) 928-933.
[58] H. Tsuchiya, J.M. Macak, L. Müller, J. Kunze, F. Müller, P. Greil, S. Virtanen, P. Schmuki, Hydroxyapatite growth on anodic TiO_2 nanotubes, Journal of Biomedical Materials Research Part A, 77A (2006) 534-541.

[59] K. Yasuda, J.M. Macak, S. Berger, A. Ghicov, P. Schmuki, Mechanistic Aspects of the Self-Organization Process for Oxide Nanotube Formation on Valve Metals, Journal of The Electrochemical Society, 154 (2007) C472-C478.
[60] K. Yasuda, P. Schmuki, Control of morphology and composition of self-organized zirconium titanate nanotubes formed in $(NH_4)_2SO_4/NH_4F$ electrolytes, Electrochimica Acta, 52 (2007) 4053-4061.
[61] J.M. Macak, S. Albu, D.H. Kim, I. Paramasivam, S. Aldabergerova, P. Schmuki, Multilayer TiO_2–Nanotube Formation by Two-Step Anodization, Electrochemical and Solid-State Letters, 10 (2007) K28-K31.
[62] P. Schmuki, H. Tsuchiya, L. Taveira, K. Sirotna, J.M. Macak, Anodization of Ti: Formation of Self-Organized Titanium Oxide Nanotube-Layers in: P.M.a.V. Maurice (Ed.) Passivation of Metals and Semiconductors, and Properties of Thin Oxide Layers, Elsevier 2006, pp. 179-186.
[63] F. Thébault, B. Vuillemin, R. Oltra, J. Kunze, A. Seyeux, P. Schmuki, Modeling of Growth and Dissolution of Nanotubular Titania in Fluoride-Containing Electrolytes, Electrochemical and Solid-State Letters, 12 (2009) C5-C9.
[64] K.G. Ong, O.K. Varghese, G.K. Mor, C.A. Grimes, Numerical Simulation of Light Propagation Through Highly-Ordered Titania Nanotube Arrays: Dimension Optimization for Improved Photoabsorption, Journal of Nanoscience and Nanotechnology, 5 (2005) 1801-1808.
[65] K. Shankar, J. Bandara, M. Paulose, H. Wietasch, O.K. Varghese, G.K. Mor, T.J. LaTempa, M. Thelakkat, C.A. Grimes, Highly Efficient Solar Cells using TiO_2 Nanotube Arrays Sensitized with a Donor-Antenna Dye, Nano Letters, 8 (2008) 1654-1659.
[66] K. Shankar, G.K. Mor, H.E. Prakasam, O.K. Varghese, C.A. Grimes, Self-Assembled Hybrid Polymer–TiO_2 Nanotube Array Heterojunction Solar Cells, Langmuir, 23 (2007) 12445-12449.
[67] O.K. Varghese, M. Paulose, C.A. Grimes, Long vertically aligned titania nanotubes on transparent conducting oxide for highly efficient solar cells, Nat Nano, 4 (2009) 592-597.
[68] O.K. Varghese, M. Paulose, K. Shankar, G.K. Mor, C.A. Grimes, Water-Photolysis Properties of Micron-Length Highly-Ordered Titania Nanotube-Arrays, Journal of Nanoscience and Nanotechnology, 5 (2005) 1158-1165.
[69] C.A. Grimes, Synthesis and application of highly ordered arrays of TiO_2 nanotubes, Journal of Materials Chemistry, 17 (2007) 1451-1457.
[70] G.K. Mor, O.K. Varghese, M. Paulose, N. Mukherjee, C.A. Grimes, Fabrication of tapered, conical-shaped titania nanotubes, Journal of Materials Research, 18 (2003) 2588-2593.
[71] M. Paulose, K. Shankar, S. Yoriya, H.E. Prakasam, O.K. Varghese, G.K. Mor, T.A. Latempa, A. Fitzgerald, C.A. Grimes, Anodic growth of highly

ordered TiO_2 nanotube arrays to 134 μm in length, Journal of Physical Chemistry B, 110 (2006) 16179-16184.
[72] D. Regonini, C.R. Bowen, A. Jaroenworaluck, R. Stevens, A review of growth mechanism, structure and crystallinity of anodized TiO_2 nanotubes, Materials Science and Engineering: R: Reports, 74 (2013) 377-406.
[73] J.M. Macak, H. Tsuchiya, A. Ghicov, K. Yasuda, R. Hahn, S. Bauer, P. Schmuki, TiO_2 nanotubes: Self-organized electrochemical formation, properties and applications, Current Opinion in Solid State and Materials Science, 11 (2007) 3-18.
[74] A. Ghicov, P. Schmuki, Self-ordering electrochemistry: a review on growth and functionality of TiO_2nanotubes and other self-aligned MOx structures, Chemical Communications, (2009) 2791-2808.
[75] J. Wang, Z. Lin, Anodic Formation of Ordered TiO_2 Nanotube Arrays: Effects of Electrolyte Temperature and Anodization Potential, The Journal of Physical Chemistry C, 113 (2009) 4026-4030.
[76] C.L. Chok, B.L. NG, F.K. Yam, The effects of fluoride-based electrolyte concentrations on the morphology of self-organized titania nanotubes, Optoelectronics and advanced materials – rapid communications, 4 (2010) 148-150.
[77] G. Liu, K. Wang, N. Hoivik, H. Jakobsen, Progress on free-standing and flow-through TiO_2 nanotube membranes, Solar Energy Materials and Solar Cells, 98 (2012) 24-38.
[78] S.P. Albu, P. Schmuki, Influence of anodization parameters on the expansion factor of TiO_2 nanotubes, Electrochimica Acta, 91 (2013) 90-95.
[79] A. Cipriano, C. Cipriano, H. Miller, Liu, Anodic Growth and Biomedical Applications of TiO_2 Nanotubes, Journal of Biomedical Nanotechnology, 10 (2014) 2977-3003.
[80] D. Kowalski, D. Kim, P. Schmuki, TiO_2 nanotubes, nanochannels and mesosponge: Self-organized formation and applications, Nano Today, 8 (2013) 235-264.
[81] A. Valota, D.J. LeClere, P. Skeldon, M. Curioni, T. Hashimoto, S. Berger, J. Kunze, P. Schmuki, G.E. Thompson, Influence of water content on nanotubular anodic titania formed in fluoride/glycerol electrolytes, Electrochimica Acta, 54 (2009) 4321-4327.
[82] A. Valota, D.J. LeClere, T. Hashimoto, P. Skeldon, G.E. Thompson, S. Berger, J. Kunze, P. Schmuki, The efficiency of nanotube formation on titanium anodized under voltage and current control in fluoride/glycerol electrolyte, Nanotechnology, 19 (2008) 355701.
[83] S. Yoriya, N. Bao, C.A. Grimes, Titania nanoporous/tubular structures via electrochemical anodization of titanium: effect of electrolyte conductivity and anodization voltage on structural order and porosity, Journal of Materials Chemistry, 21 (2011) 13909-13912.

[84] D. Gong, C.A. Grimes, O.K. Varghese, W. Hu, R.S. Singh, Z. Chen, E.C. Dickey, Titanium oxide nanotube arrays prepared by anodic oxidation, Journal of Materials Research, 16 (2001) 3331-3334.
[85] O.K. Varghese, D. Gong, M. Paulose, C.A. Grimes, E.C. Dickey, Crystallization and high-temperature structural stability of titanium oxide nanotube arrays, Journal of Materials Research, 18 (2003) 156-165.
[86] R. Beranek, H. Hildebrand, P. Schmuki, Self-organized porous titanium oxide prepared in H_2SO_4/HF electrolytes, Electrochemical and Solid-State Letters, 6 (2003) B12-B14.
[87] J.M. Macák, H. Tsuchiya, P. Schmuki, High-aspect-ratio TiO_2 nanotubes by anodization of titanium, Angewandte Chemie - International Edition, 44 (2005) 2100-2102.
[88] Q. Cai, M. Paulose, O.K. Varghese, C.A. Grimes, The effect of electrolyte composition on the fabrication of self-organized titanium oxide nanotube arrays by anodic oxidation, Journal of Materials Research, 20 (2005) 230-236.
[89] J.M. Macak, K. Sirotna, P. Schmuki, Self-organized porous titanium oxide prepared in Na_2SO_4/NaF electrolytes, Electrochimica Acta, 50 (2005) 3679-3684.
[90] C. Ruan, M. Paulose, O.K. Varghese, G.K. Mor, C.A. Grimes, Fabrication of highly ordered TiO_2 nanotube arrays using an organic electrolyte, Journal of Physical Chemistry B, 109 (2005) 15754-15759.
[91] S. Yoriya, H.E. Prakasam, O.K. Varghese, K. Shankar, M. Paulose, G.K. Mor, T.J. Latempa, C.A. Grimes, Initial studies on the hydrogen gas sensing properties of highly-ordered high aspect ratio TiO_2 nanotube-arrays 20 μm to 222 μm in length, Sensor Letters, 4 (2006) 334-339.
[92] H.E. Prakasam, K. Shankar, M. Paulose, O.K. Varghese, C.A. Grimes, A new benchmark for TiO_2 nanotube array growth by anodization, Journal of Physical Chemistry C, 111 (2007) 7235-7241.
[93] M. Paulose, H.E. Prakasam, O.K. Varghese, L. Peng, K.C. Popat, G.K. Mor, T.A. Desai, C.A. Grimes, TiO_2 Nanotube Arrays of 1000 μm Length by Anodization of Titanium Foil: Phenol Red Diffusion, The Journal of Physical Chemistry C, 111 (2007) 14992-14997.
[94] D.-J. Yang, H.-G. Kim, S.-J. Cho, W.-Y. Choi, Thickness-conversion ratio from titanium to TiO_2 nanotube fabricated by anodization method, Materials Letters, 62 (2008) 775-779.
[95] S. Berger, J. Kunze, P. Schmuki, D. LeClere, A.T. Valota, P. Skeldon, G.E. Thompson, A lithographic approach to determine volume expansion factors during anodization: Using the example of initiation and growth of TiO_2-nanotubes, Electrochimica Acta, 54 (2009) 5942-5948.
[96] D.J. LeClere, A. Velota, P. Skeldon, G.E. Thompson, S. Berger, J. Kunze, P. Schmuki, H. Habazaki, S. Nagata, Tracer investigation of pore formation in

anodic titania, Journal of the Electrochemical Society, 155 (2008) C487-C494.
[97] C. Richter, E. Panaitescu, R. Willey, L. Menon, Titania nanotubes prepared by anodization in fluorine-free acids, Journal of Materials Research, 22 (2007) 1624-1631.
[98] C. Richter, Z. Wu, E. Panaitescu, R.J. Willey, L. Menon, Ultra-High-Aspect-Ratio Titania Nanotubes, Advanced Materials, 19 (2007) 946-948.
[99] K. Nakayama, T. Kubo, A. Tsubokura, Y. Nishikitani, H. Masuda, Anodic Formation of High-Aspect-Ratio Titania Nanotubes, Meeting Abstracts, MA2005-02 (2006) 819.
[100] J.M. Macak, S.P. Albu, P. Schmuki, Towards ideal hexagonal self-ordering of TiO_2 nanotubes, Physica Status Solidi - Rapid Research Letetrs, 1 (2007) 181-183.
[101] S.P. Albu, A. Ghicov, J.M. Macak, P. Schmuki, 250 μm long anodic TiO_2 nanotubes with hexagonal self-ordering, Physica Status Solidi - Rapid Research Letetrs, 1 (2007) R65-R67.
[102] Y. Shin, S. Lee, Self-Organized Regular Arrays of Anodic TiO_2 Nanotubes, Nano Letters, 8 (2008) 3171-3173.
[103] J.W. Schultze, M.M. Lohrengel, Stability, reactivity and breakdown of passive films. Problems of recent and future research, Electrochimica Acta, 45 (2000) 2499-2513.
[104] S. Bauer, S. Kleber, P. Schmuki, TiO_2 nanotubes: Tailoring the geometry in H_3PO_4/HF electrolytes, Electrochemistry Communications, 8 (2006) 1321-1325.
[105] W. Lee, R. Ji, U. Gosele, K. Nielsch, Fast fabrication of long-range ordered porous alumina membranes by hard anodization, Nat Mater, 5 (2006) 741-747.
[106] S. Berger, H. Tsuchiya, P. Schmuki, Transition from Nanopores to Nanotubes: Self-Ordered Anodic Oxide Structures on Titanium−Aluminides, Chemistry of Materials, 20 (2008) 3245-3247.
[107] J.P. O'Sullivan, G.C. Wood, The Morphology and Mechanism of Formation of Porous Anodic Films on Aluminium, 1970.
[108] A. Mazzarolo, M. Curioni, A. Vicenzo, P. Skeldon, G.E. Thompson, Anodic growth of titanium oxide: Electrochemical behaviour and morphological evolution, Electrochimica Acta, 75 (2012) 288-295.
[109] Z. Jing-zhong, B. Yang, Z. Kun, L. Ye, K. Lu, Preparation of separated and open end TiO2 nanotubes, Ceramics International.
[110] M.M. Lohrengel, Thin anodic oxide layers on aluminium and other valve metals: high field regime, Materials Science and Engineering: R: Reports, 11 (1993) 243-294.
[111] J.W. Schultze, M.M. Lohrengel, D. Ross, Nucleation and growth of anodic oxide films, Electrochimica Acta, 28 (1983) 973-984.

[112] G.T. Burstein, R.J. Cinderey, Evolution of the corrosion potential of repassivating aluminium surfaces, Corrosion Science, 33 (1992) 475-492.
[113] J.O.M. Bockris, R.E. White, B.E. Conway, Modern Aspects of Electrochemistry No. 20, Springer US, 1989.
[114] W. Lee, K. Schwirn, M. Steinhart, E. Pippel, R. Scholz, U. Gosele, Structural engineering of nanoporous anodic aluminium oxide by pulse anodization of aluminium, Nat Nano, 3 (2008) 234-239.
[115] D. Landolt, Corrosion and Surface Chemistry of Metals, EPFL Press, 2007.
[116] B.J. Hwang, J.R. Hwang, Kinetic model of anodic oxidation of titanium in sulphuric acid, J Appl Electrochem, 23 (1993) 1056-1062.
[117] T. Hepel, M. Hepel, R.A. Osteryoung, Thermodynamic and Photoelectrochemical Behavior of the n-TiO_2 Electrode in Fluoride-Containing Solutions, Journal of The Electrochemical Society, 129 (1982) 2132-2141.
[118] W. Wilhelmsen, A.P. Grande, The influence of hydrofluoric acid and fluoride ion on the corrosion and passive behaviour of titanium, Electrochimica Acta, 32 (1987) 1469-1474.
[119] P. Skeldon, G.E. Thompson, S.J. Garcia-Vergara, L. Iglesias-Rubianes, C.E. Blanco-Pinzon, A Tracer Study of Porous Anodic Alumina, Electrochemical and Solid-State Letters, 9 (2006) B47-B51.
[120] S.J. Garcia-Vergara, P. Skeldon, G.E. Thompson, H. Habazaki, A flow model of porous anodic film growth on aluminium, Electrochimica Acta, 52 (2006) 681-687.
[121] S.J. Garcia-Vergara, P. Skeldon, G.E. Thompson, H. Habazaki, Formation of porous anodic alumina in alkaline borate electrolyte, Thin Solid Films, 515 (2007) 5418-5423.

Capítulo 2

Objetivos

OBJETIVO GENERAL

El objetivo principal de la presente tesis es la funcionalización de aleaciones de titanio, Ti6Al4V y Ti13Nb13Zr, para reducir las infecciones protésicas.

Para la consecución de dicho objetivo se ha empleado la técnica de anodizado. Esta técnica permite modificar la morfología y la composición de la superficie de manera controlada para funcionalizar aleaciones de titanio.

OBJETIVOS ESPECÍFICOS

- Diseño, crecimiento y caracterización de capas anódicas sobre la aleación Ti6Al4V en electrolitos acuosos con iones fluoruro incorporados mediante la adición de HF en el medio, y optimización de las condiciones de crecimiento para la obtención de estructuras nanotubulares (apartado 3.1).

- Diseño de un nuevo proceso de anodizado para la obtención de estructuras nanotubulares de diámetro variable a lo largo de la capa (nanotubos en forma de botella) y espesores mayores al micrómetro, empleando como medio de anodizado electrolitos tampón con NH_4F, (apartado 3.2).

- Estudio de la estabilidad química in vitro de las capas anódicas crecidas sobre Ti6Al4V tanto en baños que contienen HF como NH_4F, correlacionando la respuesta electroquímica con la morfología final de la capa(apartado 3.3).

- Caracterización de las propiedades antibacterianas (apartado 3.4a) y de la respuesta osteogénica de las capas crecidas sobre Ti6Al4V (apartado 3.4b).

- Optimización del proceso de anodizado descrito en el apartado 3.1 para su aplicación en la aleación Ti13Nb13Zr y caracterización electroquímica de las capas en una solución fisiológica simulada, PBS (apartado 3.5).

Capítulo 3

Presentación de las publicaciones y contribución original del doctorando

Presentación de las publicaciones y contribución original del doctorando

Esta tesis se basa en seis artículos de investigación, cinco de los cuales ya se encuentran publicados en distintas revistas especializadas. Aunque cada trabajo es el resultado de una estrecha colaboración entre coautores, a continuación describo, a grandes rasgos, mi contribución en cada uno de los trabajos presentados.

En el apartado 3.1, que recoge el crecimiento y caracterización morfológica y composicional de las primeras capas anódicas crecidas en la aleación Ti6Al4V empleando un electrolito acuoso mezcla de H_2SO_4/HF, a dos voltajes de crecimiento distintos, 20 y 60 V, he contribuido en la determinación de las condiciones de crecimiento en las cuales era posible la obtención de estructuras nanotubulares y en la síntesis, caracterización, análisis y la discusión de los resultados.

En el apartado 3.2, se presenta el crecimiento y caracterización de capas anódicas crecidas sobre la aleación Ti6Al4V mediante la aplicación de un escalón de potencial en una solución tampón con el fin de obtener estructuras con diferente diámetro a lo largo de la capa nanotubular y con espesores superiores al micrómetro. Esta publicación es la continuación del trabajo realizado en nuestro grupo de investigación con nombre *"Growth of TiO_2-based nanotubes on Ti-6Al-4V alloy"*, que explora la generación de capas anódicas crecidas en la misma solución tampón pero a un potencial constante. En este trabajo he contribuido en la realización de los diferentes procesos de anodizado, su caracterización, análisis y en la discusión de los resultados.

En el apartado 3.3 se estudia la correlación entre morfología y respuesta electroquímica en una solución tampón fosfato salino (PBS) a 37 °C de capas anódicas con tres morfologías de capa bien definidas: estructuras nanoporosas, duales (capa porosa en la interfase óxido/electrolito y capa

nanotubular en la parte más interna de la capa anódica) y nanotubulares. He contribuido en la realización de los diferentes procesos anodizados, su caracterización electroquímica, simulación de los espectros de impedancia electroquímica, análisis y discusión de los resultados.

El apartado 3.4 a y b representan el esfuerzo y la colaboración con dos grupos del Instituto de Investigación Sanitaria-Fundación Jiménez Díaz. En el apartado 3.4a se identifica la relación entre morfología de la capa y contenido de flúor para determinar cuál de ellas controla la respuesta antibacteriana observada en trabajos previos. Mientras que el apartado 3.4b analiza el crecimiento y mineralización de células osteoblásticas en diferentes nanoestructuras de óxido de titanio. En ambos trabajos he contribuido en la preparación de todas las muestras empleadas en los ensayos biológicos y en la discusión de los resultados.

En el apartado 3.5, se realizó el crecimiento de diferentes nanoestructuras sobre la aleación Ti13Nb13Zr, que además de no contener aleantes que pudieran ser perjudiciales para el cuerpo humano, como lo es el aluminio en el caso de la aleación Ti6Al4V, presenta un modulo de Young con valores más cercanos a los del hueso en comparación con la aleación Ti6Al4V. En este caso se obtienen capas de mayor espesor a las crecidas en la aleación Ti6Al4V empleando las mismas condiciones de anodizado. He contribuido generando las diferentes capas anódicas, realizando su caracterización morfológica, composicional y electroquímica y participando en el análisis y la discusión de los resultados.

3.1 Morphologies of nanostructured TiO_2 doped with F on Ti–6Al–4V alloy

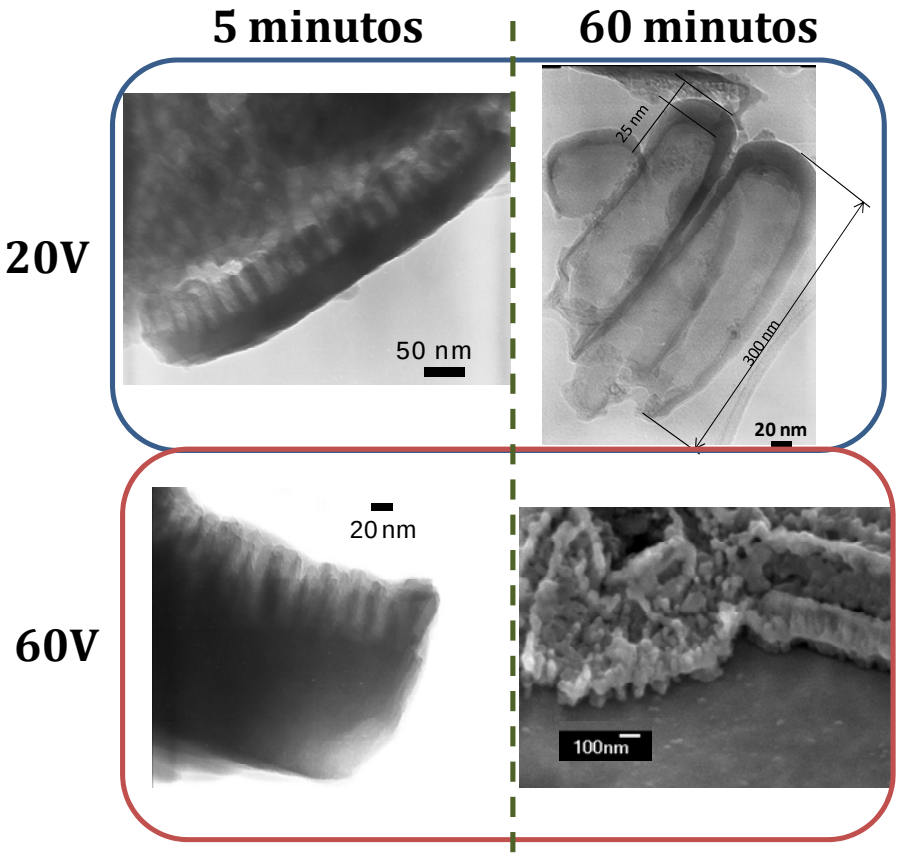

Morphologies of nanostructured TiO_2 doped with F on Ti–6Al–4V alloy

El titanio y sus aleaciones es uno de los materiales más empleados en la industria y en especial en el área biomédica debido a su biocompatibilidad, atribuida a la formación de una capa nativa de TiO_2 sobre su superficie. Entre los distintos procesos de modificación superficial empleados con el fin de mejorar las propiedades de este óxido superficial destaca la oxidación anódica (anodizado), que permite el crecimiento de capas de TiO_2 de distintas morfologías y espesores, así como la incorporación de elementos del electrolito dentro de la capa de óxido que se forma.

En este apartado se estudia el desarrollo, crecimiento y optimización de nanotubos de óxido de titanio dopados con flúor sobre la aleación Ti-6Al-4V en baños de ácido sulfúrico/fluorhídrico. El contenido de flúor en las películas es de especial interés, ya que la presencia de este elemento ha sido relacionado con propiedades antibacterianas. El efecto del tiempo de anodización, el voltaje, la composición y la microestructura de la película se estudiaron mediante microscopía electrónica de barrido y transmisión, espectroscopía de retrodispersión de Rutherford (RBS) y espectroscopía Raman.

Se obtienen películas de óxido de titanio con contenidos de flúor del 4-6 at.% y del 6-13 at.% para capas crecidas a 20 y 60V, respectivamente. Los espesores de las capas crecidas a 20 V son de 110 nm para 5 minutos de anodizado y de 230 nm para 60 minutos. En el caso de las capas anódicas crecidas a 60 V presentaron espesores superiores a los obtenidos para 20V y cercanos a los 500nm para 60 minutos de anodizado. Por tanto, el crecimiento de capas anodizas dopadas con flúor sobre la aleación de Ti6Al4V depende tanto del voltaje como del tiempo de anodizado empleado, influyendo dichos parámetros en la morfología, el espesor y en la eficiencia del proceso de anodizado. Así mismo, el empleo de las distintas técnicas de caracterización, nos permitió determinar que las capas crecidas están formadas por una matriz de óxido de titanio amorfo con nanocristales de rutilo, además de V_2O_5 y Al_2O_3.

Este apartado reproduce íntegramente el texto del siguiente manuscrito:

E. Matykina, J.M. Hernandez-López, A. Conde, C. Domingo, J.J. de Damborenea, M.A. Arenas, Morphologies of nanostructured TiO_2 doped with F on Ti–6Al–4V alloy, ***Electrochimica Acta***, Volume 56, Issue 5, 2011, Pages 2221-2229, ISSN 0013-4686, doi: 10.1016/j.electacta.2010.11.069

que se encuentra en la sección de **compendio de publicaciones** bajo el formato de la revista en la que fue publicado.

Morphologies of nanostructured TiO_2 doped with F on Ti–6Al–4V alloy

E. Matykina[a], J.M. Hernandez-López[a], A. Conde[a], C. Domingo[b], J.J. de Damborenea[a], M.A. Arenas[a,]

[a] Departamento de Corrosión y Protección, Centro Nacional de Investigaciones Metalúrgicas (CENIM-CSIC), Avda. Gregorio del Amo 8, 28040 Madrid, Spain.

[b] Instituto de Estructura de la Materia, CSIC, Serrano 123, 28006 Madrid, Spain.

Abstract

The formation of nanotubes in sulphuric/hydrofluoric acid electrolyte at controlled voltage is investigated on Ti–6Al–4V alloy used for load-bearing prosthetic applications. The effects of anodizing time and voltage on film morphology, composition and microstructure are studied by scanning and transmission electron microscopy, Rutherford backscattering spectroscopy (RBS), and Raman spectroscopy. Fluorine content in the films was of a particular interest for enhancement of antibacterial properties of the surface. The efficiencies of film formation are determined as about 40% and 80% for anodizing at 20 V and 60 V respectively for shorter anodizing time and as about 1 and 5% for longer anodizing time. For 5 min of anodizing, higher voltage conditions results in a thicker barrier layer. At extended anodizing time a further disruption of the nanotubular morphology and formation of approximately 1.5 μm-thick nanoporous film is promoted. The films grown at 20 V contain from 4 at.% to 6 at.% of fluorine. RBS detects about 13 at.% of fluorine incorporated in the film formed at 60 V for 60 min, possibly associated with a greater film thickness. The oxide film material consists of amorphous titania matrix doped with V_2O_5 and Al_2O_3.

Keywords: Ti–6Al–4V alloy; Nanotubes; Anodizing; Fluorine

1. Introduction

Titanium and its alloys are widely used as biomaterials for dental implant and orthopaedic prosthesis applications due to their high strength-to-weight ratio, corrosion resistance and bio-inertness [1,2]. However, the thin, air-formed oxides present on the metal surfaces do not promote a direct chemical bond with bone tissue, thus surface modifications, altering topography and chemical composition of these materials, are required to enhance direct structural and functional anchoring of the prosthesis to the living bone (osseointegration). The most common surface treatments of commercially available implants and prosthesis encompass pickling [3], sandblasting [4], plasma spraying [5,6], anodizing [7], micro-arc oxidation [8,9].

For decades, until recently, cell interactions and bone response were studied on implant surfaces with micrometer-scale topography. Latest researches have shown that nanoscale topography as well as the order of the nanofeatures organisation is a critical factor promoting early cell responses to the implant surface [10-15]. Hence the fabrication of highly ordered TiO_2 nanotube films for biomedical applications is attracting much attention.

The advantages of the method are easy control of the nanotube diameter and thickness by use of adequate electrolyte and anodizing regime parameters, such as voltage and time [16]. Typically TiO_2 nanotubes as-formed on pure titanium are amorphous, however their crystal structure can be influenced by alloying elements [17,18] or radically modified by post-annealing [19,23].

Although the majority of TiO_2 nanotube research has been done on c.p. titanium and regularities and mechanisms of film formation have been well enough elucidated [24-31], the formation of TiO_2 nanotubes on titanium alloys has been also reported [18,23,32-42]. High strength titanium alloys are used for load-bearing prosthetic applications [43-46], where the reduction of the probability of infection during surgery and healing process is one of the primary goals. Ion incorporation (e.g. silver, fluorine) into

titanium surface has been shown as effective method of providing antibacterial properties [47]. Additionally, fluoride ions are known to induce formation of fluorapatite in the surrounding bone and thus improve the bone anchorage to titanium implant [48-51].

In this connection TiO_2 nanotubes are of particular interest, as majority of the electrolytes used for anodizing are fluoride-based, hence the nanotubes always contain a certain amount of incorporated fluorine. Fluorine content in the nanotubes may vary depending on the electrolyte and anodizing conditions [26] and [28].

The present work investigates the development of self-organised TiO_2 nanotubes with sufficient fluorine content on Ti–6Al–4V alloy and aims for optimisation of the nanotube layer thickness, morphology and composition.

2. Experimental

A 18 mm Ø rod of Ti–6Al–4V alloy ELI grade according to the standard ASTM F136-02 supplied by SURGIVAL was cut into 2 mm thick disk specimens, ground through successive grades of SiC paper to 1200 grade, degreased with a detergent and rinsed in tap water followed by deionised water. The specimens were then chemically polished in a mixture of HF (48 wt.%):HNO_3 (70 wt.%):H_2O with volume ratio 1:4:5 for 5 min at room temperature under continuous agitation at 400 rpm, rinsed in distilled water and dried in cold air. The working area was 2.54 cm^2.

Nanotubes were formed in a two-electrode cell by anodizing the specimens at constant voltage controlled at 20 V and 60 V in the electrolyte containing 1 M H_2SO_4 and 0.15 wt.% HF for 5 and 60 min at temperature controlled at 20°C according to the patent described elsewhere [52]. Platinum mesh was used as a cathode. Voltage–time and current–time responses of anodizing were acquired at 0.1 Hz sampling rate using a zero-ohm ammeter.

The plan view morphology of nanotubular oxide films was examined by field emission gun scanning electron microscopy (FEG–SEM) utilizing JSM6500F JEOL instrument equipped with EDX facilities, operated at 15 keV for EDX analysis and 7 keV for secondary electron imaging. Each of

the area and local EDX analysis results are quoted as an average of 3 measurements.

Electron-transparent sections, nominally 40 nm thick, were prepared by ultramicrotomy and observed by a JEOL JEM 2010 TEM, instrument operated at 200 keV. Other sections were also prepared by scratching the surface of anodized specimens with a scalpel and collecting them on a TEM grid.

The presence of fluorine in the oxide films was first assessed semiquantitatively by EDX. The stoichiometric composition of the oxide films was further determined by Rutherford backscattering spectrometry (RBS), using 3.045 MeV (resonant energy for $^{16}O(a, a_0)^{16}O$ reaction) He^+ ions produced by the van de Graff accelerator of the Centro de Micro-Analisis de Materiales (CMAM), Madrid. The incident ion beam was normal to the specimen surface with 10 μC dose scattered ions detected at 170°. Data were interpreted using the SIMNRA program.

Raman spectra were obtained with a Renishaw Raman System RM2000 equipped with a Leica microscope (using magnification 50×), an electrically refrigerated CCD camera and an Ar^+ laser at 514.5 nm with exit power of 3 mW as excitation source, The spectra were taken with a spectral resolution of 4 cm^{-1} and acquisition times of 100 s. Raman spectra of the films annealed at 400 °C for 2 h were also measured.

3. Results and discussion

3.1. Current response during anodizing

In all experiments current transients showed good reproducibility. Typical current density–time responses for anodizing of Ti–6Al–4V alloy in mixed sulphuric/hydrofluoric acid electrolyte at constant voltage (Fig. 1) comprised three stages: (i) an initial surge to ~27.3 mA cm^{-2} and ~104 mA cm^{-2} for anodizing at 20 V and 60 V, respectively, followed by a rapid decay to a minimum of ~0.5 mA cm^{-2} and ~0.6 mA cm^{-2} respectively, (ii) a plateau at the minimum current density for a period of ~500 s and

~950 s, respectively, and (iii) further progressive increase to ~1.7 mA cm^{-2} and ~1.8 mA cm^{-2} until anodizing ends after 3600 s.

Stage (i) is typically ascribed to growth of barrier layer, hence the associated resistance increase and current decay. The charge densities passed during stage (i) in the present work were ~0.046 and ~0.119 C cm^{-2} for 20 V and 60 V, respectively, (Table 1) that is equivalent to the growth of 25 and 64 nm of barrier amorphous layer at 100% efficiency. Notably, no stabilisation of current density has occurred at the stage (iii), unlike observed by Macak et al. [30] for nanotube formation on pure titanium in H_2SO_4/HF electrolyte and on Ti–6Al–4V in $(NH_4)_2SO_4/NH_4F$ electrolyte [32]. Typically, such stabilisation of current density following an increase from some minimum is associated with self-organisation of the nanotubes and their steady state growth, where electrochemical oxidation (barrier film growth) and chemical dissolution are balanced.

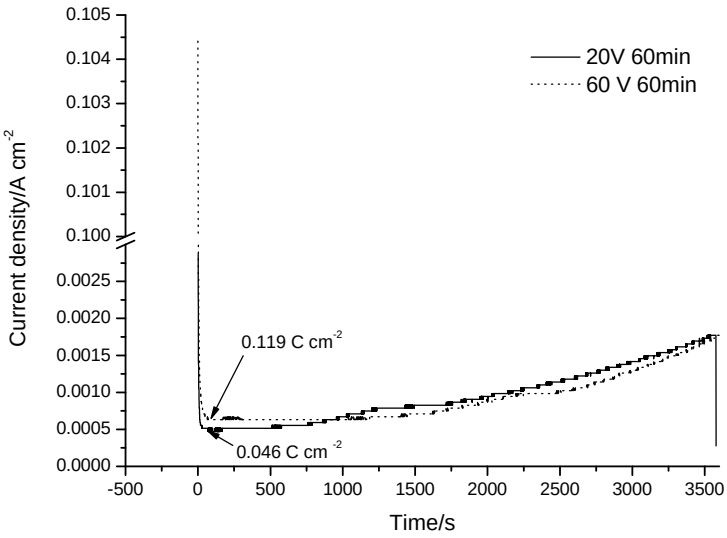

Fig. 1. Current density–time responses for anodizing of Ti–6Al–4V in sulphuric/hydrofluoric acid electrolyte at 20 and 60 V for 60 min at 20°C.

The charge densities passed following 5 min of anodizing at 20 V and at 60 V (Table 1) were sufficient to oxidize 43 nm and 70 nm of pure titanium, presuming that oxidation occurs with 100% efficiency. With the same assumption, the expected thicknesses of compact amorphous titanium oxide are 85 and 138 nm, respectively.

Film	Charge, A s cm^{-2}	Oxidized titanium, nm	Expected oxide thickness, [b] nm	Barrier thickness, [c] nm	Total thickness, [c] nm
20 V 5 min	0.156	43	85	~45	~110
20 V 60 min	3.45	949	1876	~25	~230
60 V 5 min	0.254	70	138	~140	~200
60 V 60 min	3.38	930	1838	~75	~500

[a] Calculated for pure titanium assuming 100% current efficiency
[b] Calculated for compact amorphous film assuming 100% current efficiency.
[c] Measured using TEM

Table 1. Parameters of the porous films formed on Ti-6Al-4V in sulphuric/hydrofluoric acid electrolyte.

3.2. Film morphology and compositions

3.2.1. Nanotubes formed at 20 V

Before anodizing the chemically polished substrate was examined by FEG–SEM and its general composition as well as the local compositions of α- and β-phase were analysed by EDX. Fig. 2 shows typical morphology of Ti–6Al–4V alloy with dispersed 2–3 μm long β-phase particles of irregular shapes (point A). Local composition analysis of the particles disclosed that they are enriched in vanadium and deficient in aluminium compared with the composition of the α-phase (point B) (Table 2). Further, β-phase particles contained about 1.3 at.% of iron, which was absent in the α-phase. About 1 at.% of fluorine was found in the α-phase, that apparently originated from etching solution.

Five minutes of anodizing at 20 V resulted in oxidation of the α-phase with formation of randomly arranged nanotubes of about 20 nm in diameter (Fig. 3(a) and (b)). The area EDX analysis of the porous film formed on α-phase detected about 4.2 at.% of fluorine and traces of sulphur (Table 2). No nanotubular film was formed on β-phase grains, which appeared recessed, compared with the surrounding α-matrix and revealed a nanoscale irregular surface topography.

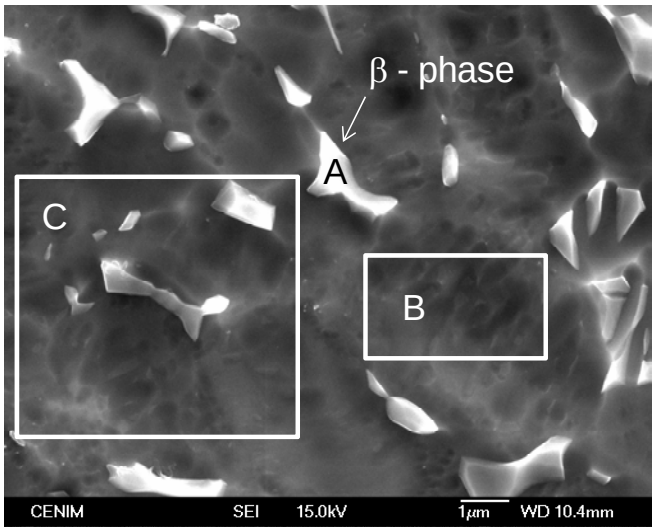

Fig. 2. Secondary electron micrograph of Ti–6Al–4V chemically polished in HNO_3/HF mixture.

Following anodizing at 20 V for 60 min the oxide film exhibits a clear self-organised morphology with the nanotube diameter increased to ~100 nm and approximately 30 nm inter-spacing. The nanotubular oxide contains about 4 at.% of fluorine (area A, Fig. 3(c)) and less than 0.1 at.% of sulphur; the fluorine content in the film appeared to decrease with anodizing time from 0.08 to 0.06 of F/Ti ratio.

Film	Area / Point	Ti	O	F	Al	V	S	Fe	Al/Ti	V/Ti	F/Ti
*	A	77.35	-	-	6.9	14.43	-	1.32	0.09	0.19	-
	B	85.97	-	1.04	10.95	2.04	-	-	0.13	0.02	-
	C	86.17	-	-	10.15	3.67	-	-	0.12	0.04	-
20 V 5 min	A	55.58	31.66	4.23	6.5	1.98	0.05	-	0.12	0.04	0.08
20V 60 min	A	63.35	23.01	3.97	8.27	1.36	0.05	-	0.13	0.02	0.06
	B	80.4	-	0.47	7.62	10.43	0.03	1.04	0.09	0.13	0.01
60V 5 min	A	38.90	50.92	3.96	4.37	1.61	0.25	-	0.11	0.04	0.10
60V 60 min	A	43.17	44.83	5.0	5.24	1.74	0.02	-	0.12	0.04	0.12

*Before anodizing

Table 2. Results of area EDX analysis at.% of Ti–6Al–4V anodized in sulphuric/hydrofluoric acid electrolyte.

The Al/Ti and V/Ti ratios remained unchanged (0.13 and 0.02, respectively) compared with chemically polished substrate. The dissolution of the β-phase becomes obvious (Fig. 3(c) and (d)) which is in agreement with [32] and occurs due to high solubility of vanadium oxides, β-phase being rich in vanadium. However, whether the dissolution of the β-phase is partial or complete could not be confirmed by the utilised characterisation methodology. The local EDX analysis of the β-phase (point B, Fig. 3d) revealed no oxygen presence; traces of fluorine (<0.5 at.%) and sulphur (<0.05 at.%). The dissolution of the β-phase during anodizing led to its depletion in vanadium: V/Ti ratio decreased from 0.19 to 0.13 compared with local β-phase composition of the chemically polished substrate; the Al/Ti ratio remained unaffected at 0.09 (Table 2).

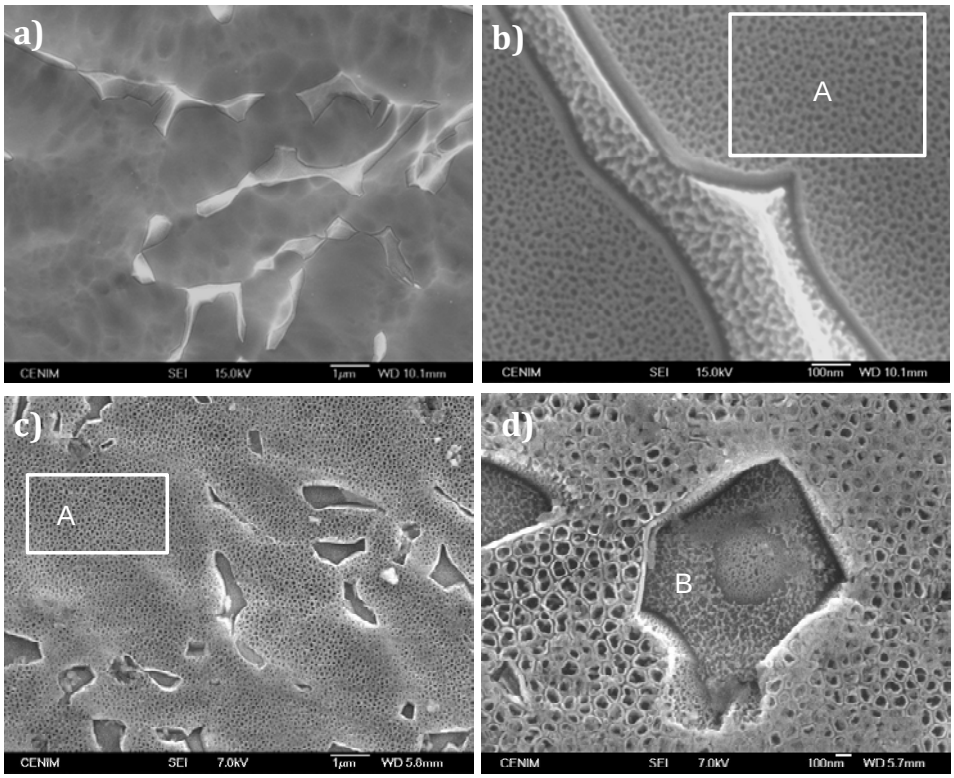

Fig. 3. Plan-view secondary electron micrographs of anodic oxide films formed on Ti–6Al–4V in sulphuric/hydrofluoric acid electrolyte at 20 V for 5 min (a and b) and 60 min (c and d) at 20 °C.

In some areas of the surface a deposit is visible on the surface of the nanotubular film (Fig. 3d), which has been identified previously as titanium (IV) oxyhydroxide $TiO(OH)_2$, or $Ti(OH)_4$[30] and [53]. It may be associated with relatively high current density that leads to local concentration of hydrated species at the mouth of the pore exceeding the precipitation threshold. Precipitation of $TiO(OH)_2$ and/or $Ti(OH)_4$ typically occur on pure titanium as a result of hydrolysis of TiO_2 at the pore initiation stage when current densities are sufficiently high; further, chemical dissolution of TiF_4 also proceeds with formation of $Ti(OH)_4$. The precipitate then re-dissolves with increased anodizing times and following current decay. In the present case however a continuous current increase was observed, thus the conditions for re-dissolution of hydrolysed species have never been reached. The precipitate of hydrolysis products can be discerned in transmission electron micrographs (Fig. 4(b) and (d)) as substance with grainy appearance, often blocking the mouth of the nanotubes (Fig. 4(c-inset)).

The transmission electron micrograph of a scraped material in Fig. 4(a) shows a detached nanotubular oxide film formed for 5 min, comprising a ~45 nm-thick barrier layer and a ~55 nm-thick porous part that reveals a well-defined tubular microstructure with both internal tube diameter and tube wall thickness being about 20–25 nm. The nanotubes formed by anodizing for 60 min disclose variability in circumferential shape (Fig. 4(b)), length and diameter (Fig. 4(c) and (d)). The average length of the nanotubes appears to be ~230 nm, the maximum length being ~300 nm. The variability in nanotube internal diameter (100–200 nm) apparent in Fig. 4(b) may however arise from a different angle of cross-sectional view, as the nanotubes are not of perfect cylindrical shape. All micrographs of the nanotubes formed for 60 min disclosed a reproducible 25 nm-thick barrier layer that corresponds to the charge passed at the stage (i) of current response. The nanotube wall thickness was reduced from ~13 nm at the bottom to ~6 nm at the mouth of the nanotube. The thinning of the nanotube walls towards the outer part of the film is a well known fact for nanotube formation on pure titanium, related to continuous dissolution of

TiO_2 and TiF_4 along the entire nanotube length [28], and a new material being formed at the metal/film interface.

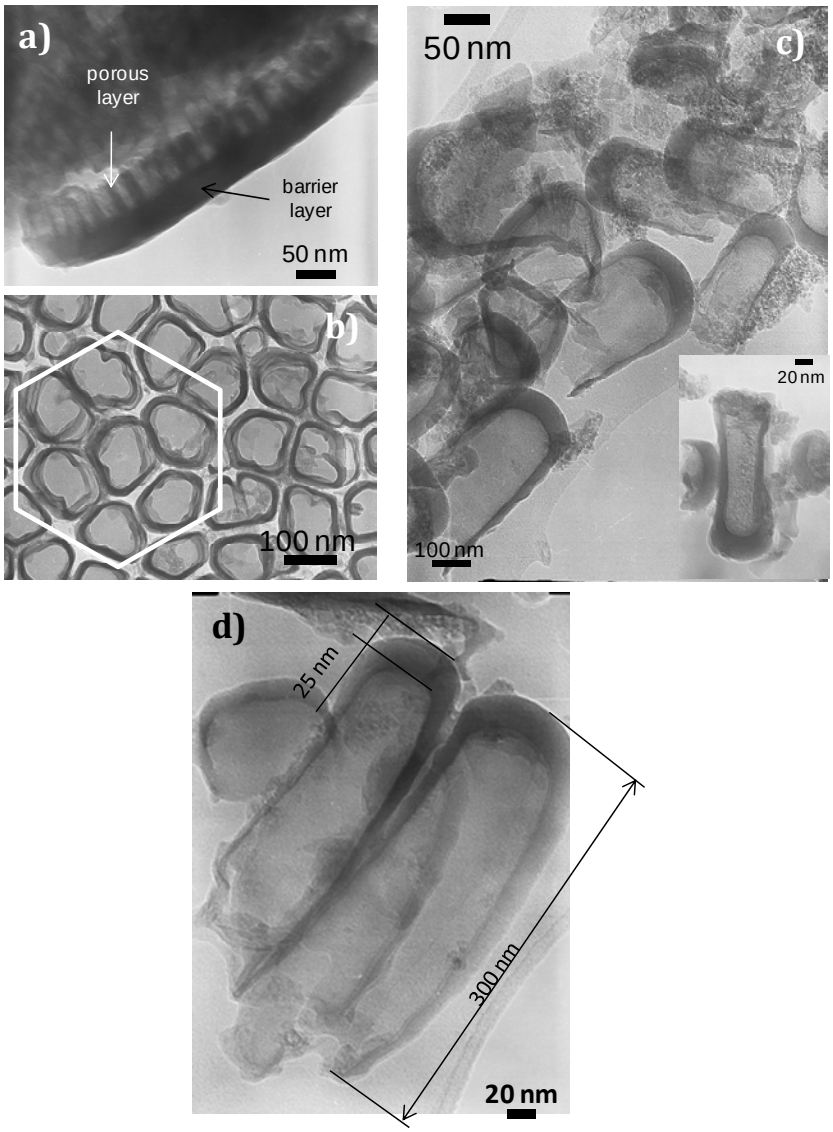

Fig. 4. Transmission electron micrographs of anodic oxide films formed on Ti-6Al-4V in sulphuric/hydrofluoric acid electrolyte at 20 V for 5 min (a) and 60 min (b-d) at 20 °C.

Using the nanotube geometry and assuming that nanotubes are cylinders sealed at one end (with 25 nm-thick bottom, 112 nm average external diameter and 9 nm-thick average wall) and arranged in hexagonal arrays

(Fig. 4(b)), the volume porosity of the film formed for 60 min is estimated as 83.4%.

3.2.2. Nanotubes formed at 60 V

The morphology of the porous film formed at 60 V for 5 min (Fig. 5(a) and (b)) was largely similar to the one formed at 20 V for 5 min and disclosed analogous dissolution of the β-phase. The general area composition of the film (area A, Fig. 5(a)) disclosed F/Ti ratio of 0.1, slightly higher than in the films formed at 20 V (Table 2). TEM micrographs of the ultramicrotomed sections of the film disclosed a ~180 nm-thick film with a well developed ~140 nm-thick barrier layer and initiating nanotubes with ~15 nm of internal diameter (Fig. 6(a–c)). The anodizing for extended time resulted in disruption of order and tubular morphology and formation of a sponge-like nanoporous material, with a nanopore size varying from ~15 nm to ~100 nm (Fig. 5(c) and (d)). Relatively deep cavities appear to form in the places of β-phase, the mouth of the cavities seem to narrow due to the overflow of the surrounding oxide film. The 30° tilted view of the fractured film disclosed a variation of the film thickness in the range of 0.4–0.85 μm. The general composition of the film indicates the highest F/Ti ratio of 0.12 of all four coatings. No continuous barrier layer could be discerned at the given resolution. TEM micrographs of the scraped film indicate that the inner part of the film possibly retains nanotubular morphology, with the variation of the thickness of the barrier layer in the range of 50–125 nm (Fig. 6(f) and (g)).

The formation ratio of the barrier layer for short anodizing times was found as 2.25 and 2.33 nm V^{-1} for 20 and 60 V films respectively. At the extended anodizing times both ratios decreased to 1.25 nm V^{-1} (assuming the average thickness of the barrier layer of the film formed at 60 V as 75 nm). This drastic drop in the formation ratio is associated with the chemical dissolution process which strongly affects the structure and composition of the anodic layers. Previously the formation ratio of the nanotubes on pure titanium in non-aqueous electrolyte at 20 V for 2000 s was estimated at 1.35 nm V^{-1}[23], whereas a formation ratio of a typical

barrier titania film grown at constant current in aqueous electrolyte is about 2.2 nm V^{-1}[54].

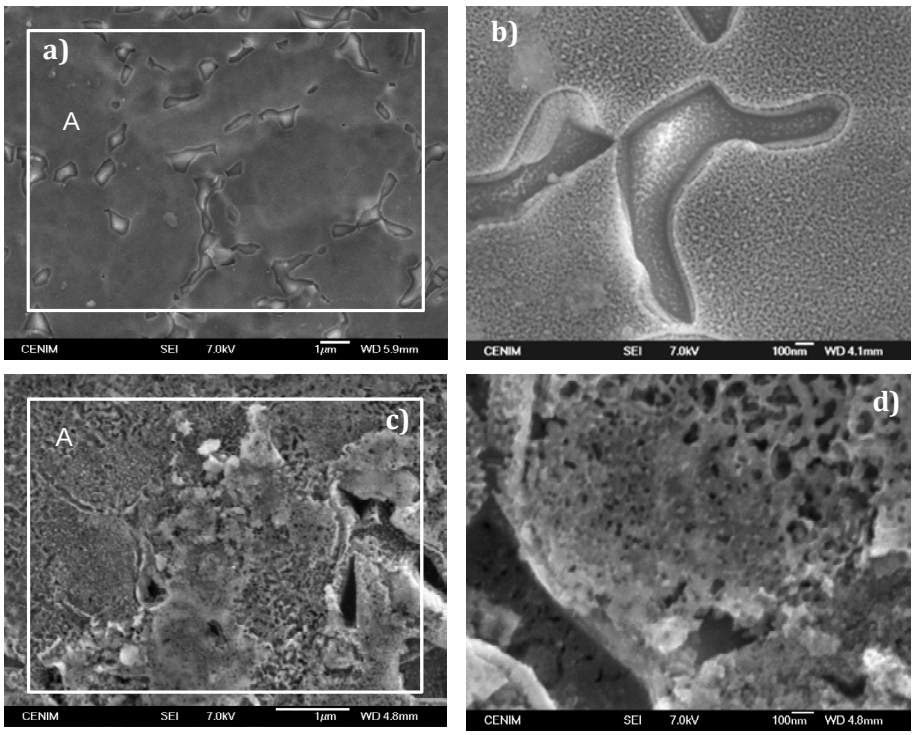

Fig. 5. Plan-view secondary electron micrographs of anodic oxide films formed on Ti-6Al-4V in sulphuric/hydrofluoric acid electrolyte at 60 V for 5 min (a, b) and 60 min (c, d) at 20 °C.

The ratio of the real thickness of the film to the expected thickness of titanium oxidized with 100% current efficiency was 2.56 and 2.86 for films formed for 5 min at 20 V and 60 V, respectively. The value of 2.54 was reported for titanium anodized at constant voltage in glycerol electrolyte [26], whereas calculations for compact amorphous formed with 100% efficiency produce a ratio of 1.95. Evidently, measured thickness of the films formed for short times exceeds the expected thickness of the oxide by approximately 30% (Table 1). This length expansion may occur as a result of (i) incorporation of fluoride, aluminium and vanadium species into the oxide and (ii) flow of the growing oxide up the walls due to the plasticity of the film material under the electric field and the film growth stresses as demonstrated previously on pure titanium by Berger and LeClere [27,55].

Originally a flow dependent formation has been developed for porous alumina [56-60].

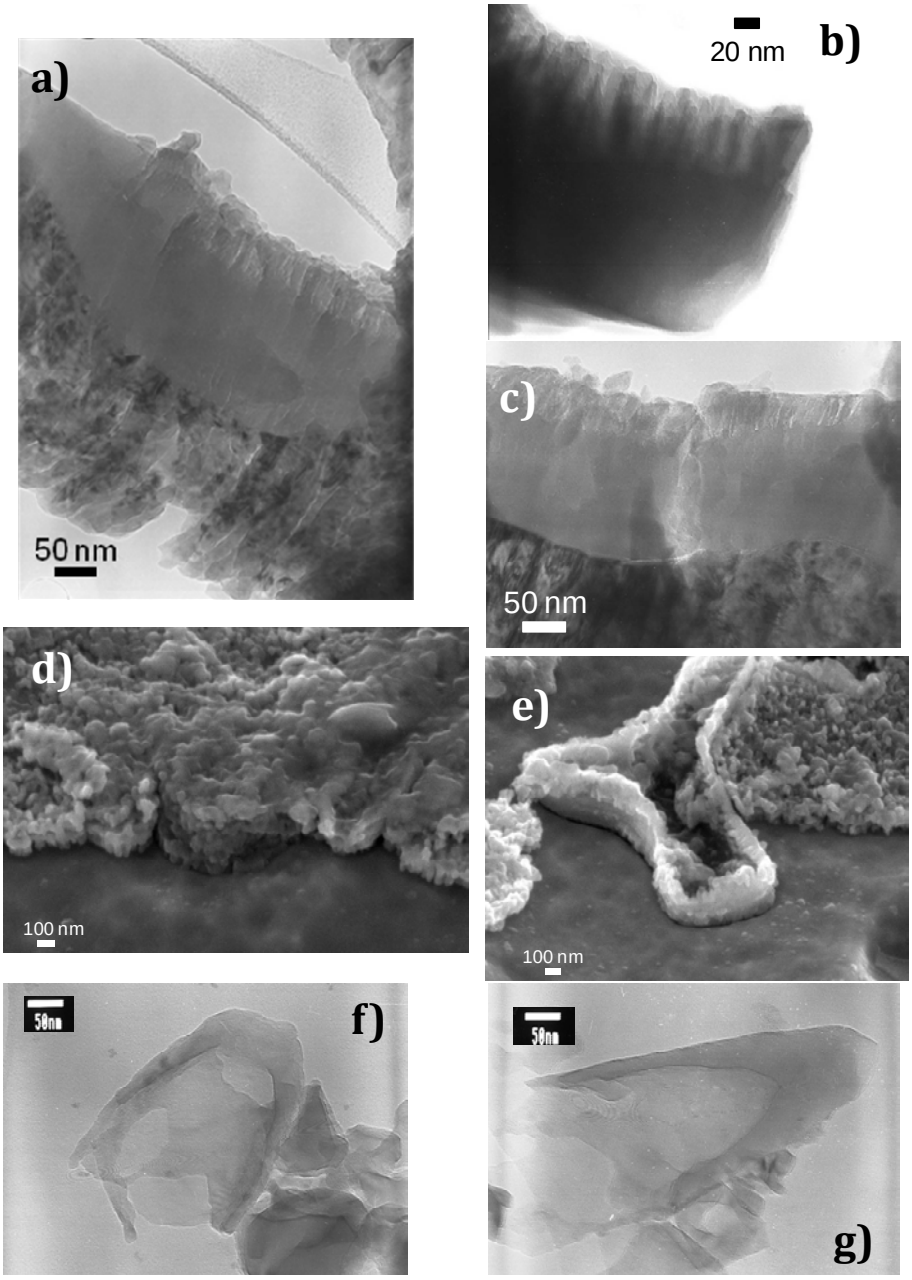

Fig. 6. Transmission electron micrographs (a-c, g, f) and secondary electron micrographs (d, e) of anodic oxide films formed on Ti-6Al-4V in sulphuric/hydrofluoric acid electrolyte at 60 V for 5 min (a-c) and 60 min (d-f) at 20 °C.

3.3. Film microstructure

Raman spectra of the films formed both at 20 and 60 V are presented in Fig. 7 (Ib–Ie). The broad bands centered at 454 and 617 cm^{-1} correspond to amorphous TiO_2[61]. The third very broad band centered at 850–890 cm^{-1} should arise from V–O–R (R = Ti, Al) bonds, as it has been shown that both, V_2O_5–TiO_2 doped [62] and V_2O_5–Al_2O_3 doped compounds [63] exhibit Raman bands around 860 cm^{-1}. The Raman intensity of the 20 V films is much weaker than for 60 V, possibly associated with lower thickness of the films formed at low voltage. The amorphous character of the TiO_2 nanotubes deduced from Raman data agrees with TEM observations, where, at the employed resolution, no nanocrystals were disclosed in any of the examined films.

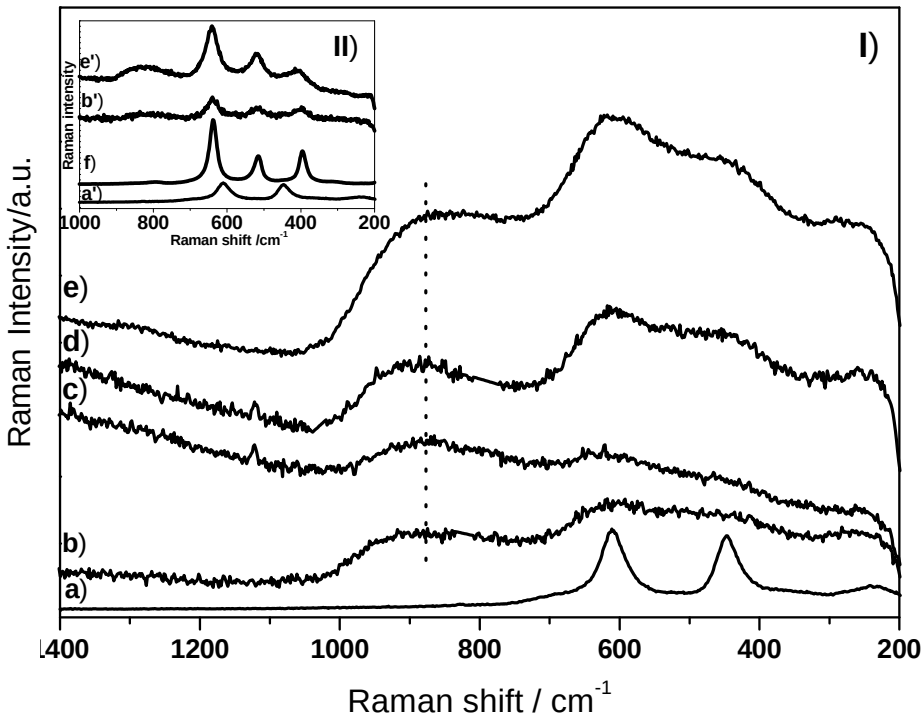

Fig. 7. I) Raman spectra of anodic oxide films formed on Ti-6Al-4V in sulphuric/hydrofluoric acid electrolyte at 20ºC, at controlled voltage and time: b) 20 V 5 min; c) 20V 60 min; d) 60V 5 min; e) 60 V 60 min. Spectrum e) here presented is divided by 3. Raman spectrum of rutile (a) is included for comparison. II) b'), e´): Raman spectra of films Ib) and Ie), respectively, annealed at 400ºC during 120 minutes. Raman spectra of pure rutile (a´) and anatase (f) TiO2 phases are also shown for comparison.

This result is in apparent contradiction with other results previously reported on titanium anodized in a mixture of sulphuric/hydrofluoric acid electrolyte [64]. There, higher voltages result in formation of mixed anatase–rutile structure with anatase/rutile ratio increasing with voltage. No such effect is observed in our case.

Raman spectra of the films annealed at 400 °C for 2 h (Fig. 7(IIb′) and (IIe′)), show narrower bands at 397, 514 and 638 cm^{-1} corresponding to anatase, as well as a band centered at 830 cm^{-1} which indicates the presence of V–O–Ti bonds.

3.4. Efficiencies of film formation

In addition to semi-quantitative EDX the oxide films were examined by RBS in order to determine the composition of the film and efficiency of the nanotube formation. RBS spectra for the different samples are shown in (Fig. 8(a)). The fittings of the spectra for all the specimens except the one obtained at 60 V for 60 min were performed as a monolayer of the oxide with uniformly distributed species. The thickness of the film formed at 60 V for 60 min exceeded the depth detection limit for RBS; the accuracy of fitting was further affected by the increased roughness of the film, compared to other specimens, and therefore the simulation of the spectrum was performed as a multilayered fitting, with the yield of the outermost layer quoted. The effects of the roughness of the metal/film and film/air interfaces, non-uniformity of the film thickness and film porosity are reflected in the sloping edges of the spectra corresponding to titanium yield from the metal/film interface. Vanadium manifested itself as a small slope of the edge of the spectra at ~800 channel. The presence of aluminium was indicated by a small step in the overall spectrum yield. Fluorine did not yield a prominent peak due to its relatively low content and the fact that RBS is less sensitive to the light elements than to the heavy elements because the scattering cross-section is proportional to the square of atomic number of the detected species. However due to a large yield from oxygen at its resonant scattering energy it was possible to simulate

the total composition with reasonable accuracy, as fitting of the oxygen peak was very sensitive to the presence of fluorine in the total balance.

The compositions of the films and current efficiencies are given in Table 3. The nanotubes formed at 20 V contained ~6 at.% and ~4 at.% of fluorine after 5 and 60 min of anodizing respectively, which is in agreement with the values determined by XPS for nanotubes formed on Ti–6Al–4V alloys in mildly acidic electrolyte in [32]. The decrease in the fluorine content apparently occurs due to intensive dissolution of TiF_4 in the walls of the nanotubes. First studies performed to evaluate the adhesion of bacteria revealed a decrease of adherence either for collections or clinical strains of two species of bacteria *Staphylococcus epidermis* and *Staphylococcus aureus*. This decrease occurs for any of the F contents obtained under these anodizing conditions [65].

On the other hand, the nanotubes formed at 60 V revealed an increases of fluorine from ~6 at.% to ~13 at.% with anodizing time. Notably, fluorine content in the film formed at 60 V for 5 min was similar to that of the film formed at 20 V for 5 min, despite almost twice lower thickness of the latter. Since the length of the nanoporous part of the film is approximately the same in both cases, it is possible that fluorine is mostly incorporated into the porous part of the film, as thickness of the barrier layer for the 60 V is nearly 3 times of that for the 20 V. However barrier and porous parts of the films could not be discriminated by RBS, and the spectra were best fitted in a single-layer simulation. Similarly, the increase of fluorine with time for anodizing at 60 V can be explained by a greater thickness of the nanoporous film. The average stoichiometric composition estimated from the RBS fitting is gathered in Table 3.

The real density of the 20 V 60 min film material composed of $Ti_2O_3 0.11Al_2O_3$ (molar mass 137.55 g M^{-1}) with the film thicknesses derived from RBS (225×10^{15} atoms cm^{-2}) and TEM (~300 nm) was determined as 0.571 g cm^{-3}. Assuming a calculated material density for a non-porous oxide with composition $Ti_2O_3 0.11Al_2O_3$ as 4.28 g cm^{-3} the

volume porosity of the film was found as 86.6%, which is in good agreement with the one calculated previously from film geometry.

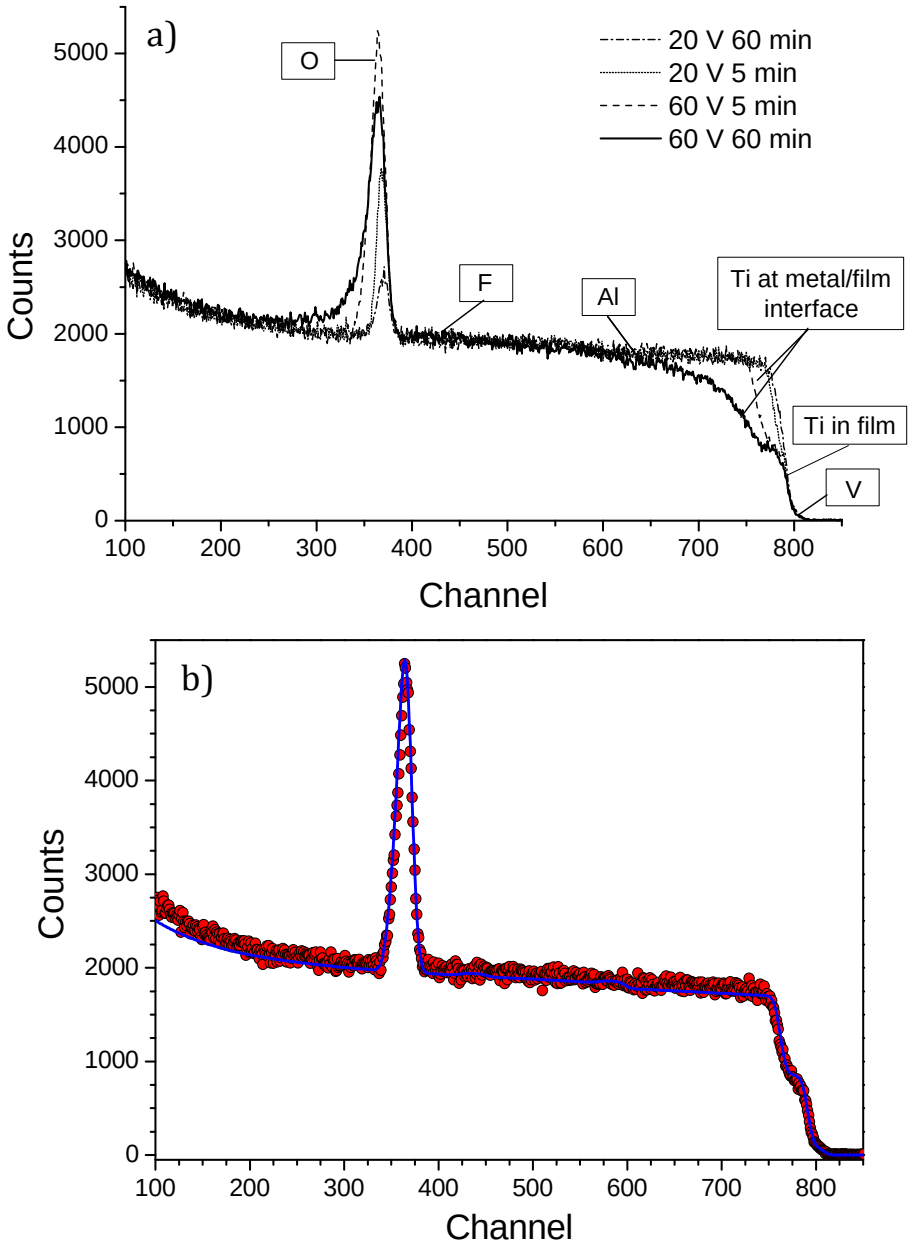

Fig. 8. Rutherford backscattering analysis spectra for anodic oxide films formed on Ti-6Al-4V in sulphuric/hydrofluoric acid electrolyte (a) and fitting of the spectra for the film formed at 60 V for 5 min (b): dotted line–original data, solid line - simulation.

Film	Ti	O	F	Al	V	Average molecular composition	Efficiency %
20V 5 min	96.56	193.80	21.6	21.60	6.25	$TiO_{1.6}{\cdot}0.06TiF_4{\cdot}0.12Al_2O_3{\cdot}0.033V_2O_5$	39.7
20V 60 min	68.32	128.24	9.42	14.49	4.53	$TiO_{1.44}{\cdot}0.036TiF_4{\cdot}0.11Al_2O_3{\cdot}0.034V_2O_5$	1.3
60V 5 min	316.00	596.90	62.78	63.84	24.30	$TiO_{1.47}{\cdot}0.05TiF_4{\cdot}0.105Al_2O_3{\cdot}0.035V_2O_5$	79.8
60V 60 min	280.06	510.12	130.03	60.00	20.00	$TiO_{1.5}{\cdot}0.13TiF_4{\cdot}0.12Al_2O_3{\cdot}0.04V_2O_5$	5.3

Table 3. Composition of the porous films (atoms cm-2×1015) formed on Ti-6Al-4V in sulphuric acid/hydrofluoric acid electrolyte, determined using RBS.

The real density of the 20 V 60 min film material composed of $Ti_2O_30.11Al_2O_3$ (molar mass 137.55 g M^{-1}) with the film thicknesses derived from RBS (225×10^{15} atoms cm^{-2}) and TEM (~300 nm) was determined as 0.571 g cm^{-3}. Assuming a calculated material density for a non-porous oxide with composition $Ti_2O_30.11Al_2O_3$ as 4.28 g cm^{-3} the volume porosity of the film was found as 86.6%, which is in good agreement with the one calculated previously from film geometry.

The efficiencies were derived using ratio of titanium ions determined by RBS in each film and titanium ions due in the film if all the charge passed during film formation was spent on oxidation of titanium (Table 1). Calculations were made using the electrochemical equivalent and density of pure titanium. The efficiency of the film formation both at 20 V and 60 V dropped remarkably with extended anodizing times from original ~40% and ~80%, respectively to ~1% and ~5%, respectively. Typically about 48–50% efficiency is reported for nanotubes formed in glycerol [26] and H_2SO_4/HF electrolytes [30] at 20 V and 20 °C for 40–60 min of anodizing.

Conventional formation of anodic titania proceeds with outward migration of Ti^{4+} and inward migration of O^{2-} ions through the film thickness with the transport numbers of ~0.4 and 0.6 respectively [66]. The growth of TiO_2 nanotubes is a result of competing electrochemical oxidation of titanium

$$Ti+2H_2O \rightarrow TiO_2+4H^++4e^- \quad (1)$$

and chemical dissolution of the anodic film material.

$$TiO_2+6HF\rightarrow[TiF_6]^{2-}+2H^+ + 2H_2O \quad (2)$$

Thus the film develops at the titanium/film interface due to the inward migration of O^{2-} ions. Oxygen evolution may be one of the factors determining the efficiency loss. Although no visible oxygen evolution has been observed in the present work at any conditions, and Raman Spectroscopy did not detected the presence of nanocrystalline rutile in the present films, oxygen evolution, associated with nanocrystallisation of the film, may take place [67]. The reduced efficiency is largely attributed to chemical dissolution of the film, dissolution of TiF_4, according to reaction

$$TiF_4 + 4H_2O = Ti(OH)_4 + 4HF \quad (3)$$

field-assisted ejection of outwardly migrating Ti^{4+}, field-assisted dissolution of the film, dissolution due to increased acidification of the bottom of the pore and physical loss due to detachment of the film at high current densities [68].

4. Conclusions

(1) Anodizing of Ti-6Al-4V alloy in sulphuric/hydrofluoric acid electrolyte at controlled voltage proceeds with formation of nanotubes on α-phase and recession of β-phase due to partial or complete dissolution.

(2) Anodizing for 5 min at 20 V and 60 V results in formation of 40-50 nm-long nanotubes of 15-20 nm in diameter. Self-organised nanotubes of 100 nm in diameter and about 230 nm-long with about 86% volume porosity are formed following anodizing at 20 V for 60 min. Disruption of self-ordering and of tubular morphology occurs with the voltage increase, while thickness of the film formed at 60 V achieves in the average 1 μm after 60 min of anodizing.

(3) Twice higher efficiency of film formation is achieved at 60 V anodizing compared with 20 V anodizing for shorter anodising times (5 min). The efficiency of film formation decreases with time from about 40% and 80% to about 1 and 5% for anodizing at 20 V and 60 V respectively.

(4) Fluorine content decreases with anodizing time from ~6 at.% to ~4 at.% in the nanotubes formed at 20 V and increases from ~6 at.% to ~13 at.% in the nanotubes formed at 60 V, the latter associated with a greater film thickness.

(5) The microstructure of the nanotubes determined by Raman spectroscopy comprises an amorphous matrix with nanocrystalline inclusions of rutile and vanadium and aluminium oxides. According to the relative peak intensity the amount of the nanocrystalline material increases at higher anodizing voltage and time.

Acknowledgement

The authors thank Spanish Ministry of Science and Innovation for support of this work (SMOTI MAT2009-13751, FUNCOAT Consolider-Ingenio 2010 CSD2008-00023).

References

[1] D.M. Brunette, P. Tengvall, M. Textor, P. Thomsen, Titanium in Medicine, Springer, 2001.
[2] H.L. Freese, M.G. Volas, J.R. Wood, M. Textor, Titanium and its Alloys in Biomed- ical Engineering. Encyclopedia of Materials: Science and Technology, Elsevier Ltd., Oxford, 2001, p. 9374.
[3] M. Browne, P.J. Gregson, Biomaterials 15 (1994) 894.
[4] T. Albrektsson, A. Wennerberg, Int. J. Prosthodont. 17 (2004) 536.
[5] C. Sittig, M. Textor, N.D. Spencer, M. Wieland, P.H. Vallotton, J. Mater. Sci. Mater. Med. 10 (1999) 35.
[6] M. Taborelli, M. Jobin, P. Francois, P. Vaudaux, M. Tonetti, S. Szmukler-moncler, J.P. Simpson, P. Descouts, Clin. Oral Implant. Res. 8 (1997) 208.
[7] J.A. Disegi, Anodizing treatments for titanium implants, in: Proceedings of the Sixteenth Southern Biomedical Engineering Conference, Biloxi, MS, USA, 1997, 4–6 April.
[8] Y. Tanaka, J. Mater. Sci. 40 (2005) 3081.
[9] Y.-T. Sul, C.B. Johansson, Y. Jeong, A. Wennerberg, T. Albrektsson, Clin. Oral Implant. Res. 13 (2002) 252.
[10] M.M. Stevens, J.H. George, Science 310 (2005) 1135.
[11] J. Park, S. Bauer, K. Von Der Mark, P. Schmuki, Nano Lett. 7 (2007) 1686.
[12] F. Barrère, T.A. Mahmood, K. de Groot, C.A. van Blitterswijk, Mater. Sci. Eng. R: Report 59 (2008) 38.
[13] G. Mendonca, D.B.S. Mendonca, F.J.L. Aragao, L.F. Cooper, Biomaterials 29 (2008) 3822.

[14] K. Das, S. Bose, A. Bandyopadhyay, J. Biomed. Mater. Res. A 90A (2009) 225.
[15] J. Park, S. Bauer, K.A. Schlegel, F.W. Neukam, K.v.d. Mark, P. Schmuki, Small 5 (2009) 666.
[16] J.M. Macak, H. Tsuchiya, A. Ghicov, K. Yasuda, R. Hahn, S. Bauer, P. Schmuki, Curr. Opin. Solid State Mater. Sci. 11 (2007) 3.
[17] S.B. Aldabergenova, A. Ghicov, S. Albu, J.M. Macak, P. Schmuki, Non-Cryst. Solids 354 (2008) 2190.
[18] X.J. Feng, J.M. Macak, S.P. Albu, P. Schmuki, Acta Biomater. 4 (2008) 318.
[19] A. Ghicov, H. Tsuchiya, J.M. Macak, P. Schmuki, Phys. Stat. Sol. (A) 203 (4) (2006) R28.
[20] J.M. Macak, S. Aldabergerova, A. Ghicov, P. Schmuki, Phys. Stat. Sol. (A) 203 (10) (2006) R67.
[21] B. Luo, H. Yang, S. Liu, W. Fu, P. Sun, M. Yuan, Y. Zhang, Z. Liu, Mater. Lett. 62 (2008) 4512.
[22] S.-J. Cho, K.-S. Mun, D.-J. Yang, H.-P. Hun-Park, Y.-J. Park, J.-O. Kim, W.-Y. Choi, Ceram. Process Res. 9 (2008) 449.
[23] S. Sreekantan, Z. Lockman, R. Hazan, M. Tasbihi, L.K. Tong, A.R. Mohamed, J. Alloy Compd. 485 (2009) 478.
[24] J.M. Macak, K. Sirotna, P. Schmuki, Electrochim. Acta 50 (2005) 3679.
[25] A. Ghicov, H. Tsuchiya, J.M. Macak, P. Schmuki, Electrochem. Commun. 7 (2005) 505.
[26] A. Valota, D.J. LeClere, T. Hashimoto, P. Skeldon, G.E. Thompson, S. Berger, J. Kunze, P. Schmuki, Nanotechnology 19 (2008) 355701.
[27] S. Berger, J. Kunze, P. Schmuki, D. LeClere, A.T. Valota, P. Skeldon, G.E. Thompson, Electrochim. Acta 54 (2009) 5942.
[28] A. Valota, D.J. LeClere, P. Skeldon, M. Curioni, T. Hashimoto, S. Berger, J. Kunze, P. Schmuki, G.E. Thompson, Electrochim. Acta 54 (2009) 4321.
[29] H. Tsuchiya, J.M. Macak, A. Ghicov, A.S. RÃder, L. Taveira, P. Schmuki, Corros. Sci. 49 (2007) 203.
[30] J.M. Macak, H. Tsuchiya, S. Berger, S. Bauer, S. Fujimoto, P. Schmuki, Chem. Phys. Lett. 428 (2006) 421.
[31] S. Bauer, S. Kleber, P. Schmuki, Electrochem. Commun. 8 (2006) 132.
[32] J.M. Macak, H. Tsuchiya, L. Taveira, A. Ghicov, P. Schmuki, J. Biomed. Mater. Res. Part A 75 (2005) 928.
[33] A. Ghicov, S. Aldabergenova, H. Tsuchiya, P. Schmuki, Angew. Chem. Int. Ed. 45 (2006) 6993.
[34] H. Tsuchiya, S. Berger, J.M. Macak, A. Ghicov, P. Schmuki, Electrochem. Commun. 9 (2007) 2397.
[35] K. Yasuda, P. Schmuki, Electrochim. Acta 52 (2007) 4053.
[36] K. Yasuda, P. Schmuki, Adv. Mater. 19 (2007) 1757.

[37] K. Yasuda, J.M. Macak, S. Berger, A. Ghicov, P. Schmuki, J. Electrochem. Soc. 154 (2007) C472.
[38] A. Ghicov, M. Yamamoto, P. Schmuki, Angew. Chem. Int. Ed. 47 (2008) 7934.
[39] S. Berger, H. Tsuchiya, P. Schmuki, Chem. Mater. 20 (2008) 3245.
[40] Y -C. Nah, A. Ghicov, D. Kim, S. Berger, P. Schmuki, J. Am. Chem. Soc. 130 (2008) 16154.
[41] V.S. Saji, H.C. Choe, W.A. Brantley, Acta Biomater. 5 (2009) 2303–2310.
[42] H. Tsuchiya, T. Akaki, J. Nakata, D. Terada, N. Tsuji, Y. Koizumi, Y. Minamino, P. Schmuki, S. Fujimoto, Corros. Sci. 51 (2009) 1528.
[43] B.C. Carr, T. Goswami, Mater. Des. 30 (2009) 398.
[44] M. Long, H.J. Rack, J. Biomater. 19 (1998) 1621.
[45] D.O. Meredith, M.O. Riehle, A.S.G. Curtis, R.G. Richards, J. Mater. Sci. Mater. Med. 18 (2007) 405.
[46] M. Geetha, A.K. Singh, R. Asokamani, A.K. Gogia, Prog. Mater. Sci. 54 (2009) 397.
[47] M. Yoshinari, Y. Oda, T. Kato, K. Okuda, Biomaterials 22 (2001) 2043.
[48] J.E. Ellingsen, J. Mater. Sci. Mater. Med. 6 (1995) 749.
[49] J. Guo, R.J. Padilla, W. Ambrose, I.J. De Kok, L.F. Cooper, Biomaterials 28 (2007) 5418.
[50] Z.M. Isa, G.B. Schneider, R. Zaharias, D. Seabold, C.M. Stanford, Int. J. Oral Maxillofac. Implant. 21 (2006) 203.
[51] L.F. Cooper, Y. Zhou, J. Takebe, J. Guo, A. Abron, A. Holmeın, J.E. Ellingsen, Biomaterials 27 (2006) 926.
[52] M.A. Arenas, A. Conde, J. de Damborenea, E. Matykina, J.M. Esteban Moreno, E. Gomez Barrena, C. Perez-Jorge- Permarch, R. Perez Tanoira, Patent. Application number: P201030720, Spain, (14-05-2010).
[53] L.V. Taveira, J.M. Macak, H. Tsuchiya, L.F.P. Dick, P. Schmuki, J. Electrochem. Soc. 152 (2005) B405.
[54] H. Habazaki, K. Shimizu, S. Nagata, P. Skeldon, G.E. Thompson, G.C. Wood, J.Electrochem. Soc. 149 (2002) B70.
[55] D.J. LeClere, A. Velota, P. Skeldon, G.E. Thompson, S. Berger, J. Kunze, P. Schmuki, H. Habazaki, S. Nagata, J. Electrochem. Soc. 155 (2008) C487.
[56] S.J. Garcia-Vergara, L. Iglesias-Rubianes, C.E. Blanco-Pinzon, P. Skeldon, G.E. Thompson, P. Campestrini, Proc. R. Soc. A 462 (2006) 2345.
[57] S.J. Garcia-Vergara, P. Skeldon, G.E. Thompson, H. Habakaki, Appl. Surf. Sci. 254 (2007) 1534.
[58] S.J. Garcia-Vergara, P. Skeldon, G.E. Thompson, H. Habazaki, Corros. Sci. 49 (2007) 3772.
[59] S.J. Garcia-Vergara, P. Skeldon, G.E. Thompson, T. Hashimoto, H. Habazaki, J. Electrochem. Soc. 154 (2007) C540.
[60] S.J. Garcia-Vergara, P. Skeldon, G.E. Thompson, H. Habazaki, Electrochim. Acta 52 (2006) 681.

[61] A.G. Gaynor, R.J. Gonzalez, R.M. Davis, R.J. Zallen, J. Mater. Res. 12 (7) (1997) 1755.
[62] G.N. Kryukova, G.A. Zenkovets, G. Mestl, R. Schlögl, React. Kinet. Catal. L 80 (2003) 161.
[63] K. Scheurell, G. Scholz, E. Kemnitz, J. Solid State Chem. 180 (2007) 749–758.
[64] M. Bestetti, S. Franz, M. Cuzzolin, P. Arosio, P.L. Cavallotti, Thin Solid Films 515 (2007) 5253.
[65] C. Pérez-Jorge Peremarch, R. Pérez Tanoira, M.A. Arenas, E. Matykina, A. Conde, J.J. de Damborenea, E. Gómez Barrena, J. Esteban, J. Phys.: Conf. Ser. (2010) Pending of publication.
[66] H. Habazaki, K. Fushimi, K. Shimizu, P. Skeldon, G.E. Thompson, Electrochem. Commun. 9 (2007) 1222.
[67] H. Habazaki, M. Uozumi, H. Konno, K. Shimizu, S. Nagata, K. Takayama, Y. Oda, P. Skeldon, G.E. Thompson, J. Electrochem. Soc. 152 (2005) B263.
[68] L.V. Taveira, J.M. Macak, K. Sirotna, L.F.P. Dick, P. Schmuki, J. Electrochem. Soc. 153 (2006) B137

3.2 TiO_2 nanotubes with tunable morphologies

Electrolyte		time (min) t_1	time (min) t_2	Voltage (V) V_1	Voltage (V) V_2	Nomenclature
1M $NH_4H_2PO_4$	0.15M NH_4F	30	60	10	20	10-20V
	0.3M NH_4F			10	20	10-20V
				20	30	20-30V
				20	40	20-40V
	0.45M NH_4F			10	20	10-20V

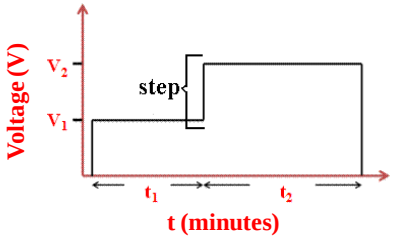

DUPLEX NANOSTRUCTURE

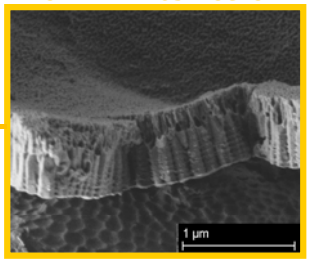

BOTTLE SHAPED NANOTUBES

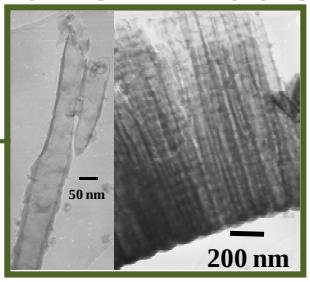

NON HOMOGENEOUS NANOLAYER

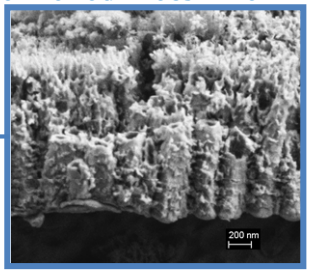

TiO_2 nanotubes with tunable morphologies

La estructura, morfología y composición de capas nanotubulares de óxido de titanio crecidos mediante anodizado en electrolitos acuosos, como se discutió en el apartado anterior, depende fundamentalmente del voltaje, tiempo y la composición del baño empleada. En este apartado se estudia como la variación de estos parámetros permite la generación de capas de TiO_2 sobre la aleación Ti6Al4V con morfologías y espesores diseñados a medida. El objetivo es la obtención de estructuras con diámetro de poro variable (en forma de botella) y espesor en el rango micrométrico. Estas nanoestructuras podrían ser de especial interés para ser empleadas como sistemas de administración de fármacos en prótesis ortopédicas. En este trabajo se ha estudiado la influencia del voltaje aplicado y la composición del baño de anodizado (empleando una solución tampón con distintas concentraciones de sales de fluoruro) en las características de la capa anódica. La morfología y estequiometría de las distintas capas anódicas crecidas se ha caracterizado mediante las curvas de densidad de corriente/tiempo recogidas durante el proceso de anodizado, microscopía electrónica de barrido y transmisión y espectroscopía de retrodispersión de Rutherford (RBS).

Los resultados obtenidos indicaron que un aumento gradual en la concentración de fluoruros en el baño de anodizado, de 0.15 M, 0.3M a 0.45M NH_4F, para un escalón de voltaje aplicado de 10-20 V, permite la obtención de capas nanotubulares de diferentes morfologías, pasando desde una estructura bimodal compuesta por nanotubos y nanoporos, hasta una estructura única nanotubular de diámetro variable. Mientras que para una misma concentración de fluoruros, 0.3 M NH_4F, y diferentes valores de potencial en el escalón aplicado, se observó que es posible la obtención de estructuras con diámetro de poro variable por efecto del voltaje y que conforme aumenta el voltaje aplicado, la homogeneidad de las capas anódicas disminuye. Además, se explica el mecanismo de crecimiento de las capas anódicas, de ambos casos estudiados.

Este apartado reproduce íntegramente el texto del siguiente manuscrito:

J.M. Hernández-López, A. Conde, J.J. de Damborenea, M.A. Arenas, TiO_2 nanotubes with tunable morphologies, ***RCS Advances***, Volume 4, Issue 107, 2014, Pages 62576-62585, ISSN 2046-2069, doi: 10.1039/c4ra11457d.

que se encuentra en la sección de **compendio de publicaciones** bajo el formato de la revista en la que fue publicado

TiO_2 nanotubes with tunable morphologies

J.M. Hernández-López[a], A. Conde[a], J.J. de Damborenea[a], M.A. Arenas[a]

[a] Departamento de Corrosión y Protección, Centro Nacional de Investigaciones Metalúrgicas (CENIM-CSIC), Avda. Gregorio del Amo 8, 28040 Madrid, Spain.

Abstract

Titanium anodic oxide layers with bottle shaped nanotubular structure have been grown in an electrolyte containing NH_4F, applying voltage steps. The grown layers were analyzed using scanning and transmission electron microscopy (SEM and TEM), and Rutherford backscattering spectroscopy (RBS). The results show that for a concentration of 0.15 M of NH_4F in the anodizing bath, and a step of 10 to 20 V produces an oxide with a double morphology comprised of nanotubes at the oxide/metal interface and nanopores at the oxide/electrolyte interface of the anodic layer. Higher concentration of F^- in the bath, 0.3 and 0.45 M NH_4F, enhanced the chemical dissolution of the anodic layer resulting in nanotubular structures along the oxide layer. Therefore, the bottle shaped nanotubular structures that show a well defined morphology are obtained in a bath containing a concentration of 0.3 M NH_4F and applying a voltage step of 10-20 V.

Keywords: Anodizing, Ti6Al4V alloy, Bottle shaped nanotubes, Titanium dioxide, Step voltage

1. Introduction

In recent years, the growth and/or deposition of titanium thin films and titanium oxide layers have received considerable attention in a variety of fields of endeavour such as: tissue engineering, drug delivery systems, orthopaedic implants, gas sensors, lithium ion batteries, solar cells, photovoltaic devices and have therefore encouraged its study and development[1-7]. Different techniques such as laser, sputtering, sol-gel, thermal oxidation, electrophoresis and electroplating have been used to obtain TiO_2 layers. Nevertheless, these techniques are limited when it

comes to controlling the thickness of TiO_2 and/or when dealing with the lack of uniformity in the grown layer [8, 9].

By contrast, the anodizing process allows to fabricate uniform TiO_2 layers with a controlled thickness and a variety of nanostructures that differs from barrier to porous layers, depending on the composition of the electrolyte used and the growth conditions (temperature, stirring, voltage and/or current applied) [10, 11]. Zwilling et al in 1999 [12] obtained self-organized TiO_2 nanoporous structures using diluted hydrofluoric acid solutions. Subsequent works showed that in these HF containing solutions, the thickness of TiO_2 anodic layer was limited to 500-600 nm. The chemical dissolution resulting from the high acidity of the bath and the presence of fluorides [13], is responsible for this limitation in thickness. This drawback is overcome by the use of buffer solutions containing NaF or NH_4F (where the chemical dissolution is decreased), along with pH control of the anodizing bath, leading to TiO_2 layers up to 2 μm thick[14, 15]. It was precisely this increase in the thickness of the nanostructured TiO_2 layers which made it possible to expand the niche of applications of TiO_2 layers in those uses in which the nanostructure and thickness are critical, such as TiO_2 fuel cells, which have improved their efficiency and service life by increasing the surface area [16, 17].

However, in addition to thickness, it is also possible to modify the diameter of the nanotubes by varying the applied voltage. Mor et al. [5], fabricated porous TiO_2 layers with conical structures on titanium applying voltage ramps in an HF solution. The conical nanotubular layers had variable inner diameters throughout but the thickness of the oxide layer was limited to 200 nm. Similar nanostructures were obtained in organic electrolytes by applying ramps with ascending and descending voltages, leading to thicker anodic oxide layers and, therefore, greater surface areas of interest in the photocatalytic applications [18-22]. Liu et. al. [23] fabricated TiO_2 nantotubes with periodically changing morphology by using periodic pulses consisting of high and low voltages. However, the main drawbacks are either the instability of the organic baths, or the longer times required to achieve the desired thicknesses. In addition, most of the works are focused on pure

titanium or titanium binary alloys and few papers are devoted to fabricate tailored nanotubes in the micrometer range on technologically relevant substrates such as Ti6Al4V alloy.

The objective of the present work is the growth of thick anodic layers in the micrometer range, with bottle shaped nanotubular structures in Ti6Al4V alloy in short times, less than two hours, and in aqueous anodizing baths that could be of interest for drug delivery control systems in orthopaedic prostheses. The work correlates the influence of the anodizing process parameters: the concentration of fluoride in the bath and the application of increasing voltage steps on the fabricated nanostructures.

2. Experimental Procedure

Ti–6Al–4V alloy specimens of ELI grade according to the standard ASTM F136-02 supplied by SURGIVAL were ground using successive grades of SiC paper to 1200 grade, degreased with a detergent and rinsed in tap water followed by deionised water.

The specimens were then chemically polished in a mixture of HF(40 wt%):HNO_3(70 wt.%):H_2O with a volume ratio of 1:4:5 for 5 min, at room temperature under continuous agitation at 400 rpm, rinsed in distilled water and dried in cold air. The working area was 2.54 cm^2. Electrolytes containing 1 M $NH_4H_2PO_4$ and 0.15, 0.3 and 0.45 M NH_4F were prepared. Bottle shaped nanotubes were formed in a two-electrode cell. The specimens were anodized at stepped voltage with the first Voltage (V_1) applied for 30 min followed by a second voltage step (V_2) applied for 60 min, as seen in Figure 1. The temperature was controlled at 20^oC. Platinum mesh was used as a cathode. The voltages were applied using LAB/SM 1300 DC power supply (ET Power Systems Ltd). Current-time responses of anodizing were acquired at 0.1 Hz sampling rate using a zero-ohm ammeter connected in series with the electrochemical cell.

The plan-view morphology of the nanotubular oxide films was examined by field emission gun scanning electron microscopy (FEG-SEM) utilizing JSM6500F Philips instrument equipped with EDX facilities and a ZEISS

Ultra 55 scanning electron microscope. Electron-transparent sections were prepared by scratching the surface of the anodized specimens with a scalpel and collecting the pieces of the oxide on a TEM grid. TEM grids were observed using a JEOL JEM 2010 instrument operated at 200 keV.

The stoichiometric composition of the oxide films was further determined by Rutherford Backscattering spectroscopy (RBS), using the following Non-Rutherford Elastic Backscattering Cross Sections: He^+ ions with the energy of 3.045 MeV (resonant energy for $^{16}O(\alpha,\alpha_0)^{16}O$ reaction), 3.777 MeV (resonant energy for $^{19}F(\alpha,\alpha_0)^{19}F$ reaction) and 5.725 MeV (resonant energy for $^{27}Al(\alpha,\alpha_0)^{27}Al$ reaction) were produced by the van de Graff accelerator located at the Centro de Micro-Análisis de Materiales (CMAM), Madrid. The incident ion beam was normal to the surface of the specimen with 10μC dose scattered ions detected by a mobile detector at 165°. Data were interpreted using the SIMNRA program.

Electrolyte		time (min)		Voltage (V)		Nomenclature
		t_1	t_2	V_1	V_2	
$1M\ NH_4H_2PO_4$	$0.15M\ NH_4F$	30	60	10	20	10-20V
	$0.3M\ NH_4F$			10	20	10-20V
				20	30	20-30V
				20	40	20-40V
	$0.45M\ NH_4F$			10	20	10-20V

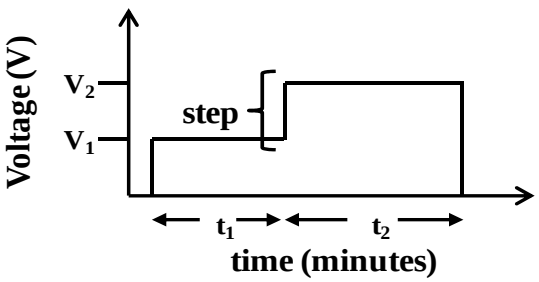

Figure 1. Fabrication conditions of nanotubes grown on Ti6Al4V.

3. Results and discussion

3.1. Current density versus time response

In the following sections, the current transients recorded during anodizing process were evaluated to determine the influence of the composition of the anodizing bath and voltage steps applied, i.e. electric field, on the anodic layers grown.

3.1.1. Influence of the composition of the anodizing bath

The current density versus time curves collected during the anodizing of Ti and its alloys, show significant growth aspects of the anodic oxide layer and its morphology [8, 18, 21, 24]. Figure 2 shows the evolution of the current density versus time during the anodizing of the Ti6Al4V alloy in a 1 M $NH_4H_2PO_4$ bath with different concentrations of NH_4F applying voltage steps. In this figure, it is observed that the current-time transient, recorded for the different concentrations of NH_4F used, is similar to that described by other authors for the anodizing of Ti and its alloys in aqueous media [5, 8]. Three different stages are distinguished: the growth of the high resistance oxide barrier layer -stage I-; pores nucleation -stage II-; and the steady state (growth of nanotubes)-stage III-.

In this electrolyte, the pore initiation stage can be attributed to both the field-assisted ejection of Ti^{4+} ions into the electrolyte and the chemical dissolution of the oxide due to the presence of fluoride ions readily forming cavities within the oxide.

The three stages plotted in the current density versus time response are observed for each applied step voltage, V_1 = 10 V for 30 minutes and V_2 = 20 V for 60 minutes, Figures 2b and 2c. The steady state current density recorded on stage III corresponding to the first applied voltage, V_1 = 10V, is 0.2 mA/cm^2 for the bath containing 0.15 M NH_4F and increases to 1.5 mA/cm^2 for 0.45 M NH_4F, Figure 2b. The steady current density recorded for the second voltage step, V_2 = 20V, increases approximately 0.2 mA/cm^2 compared to the values showed for the first voltage step for all the NH_4F concentrations studied, Figure 2c.

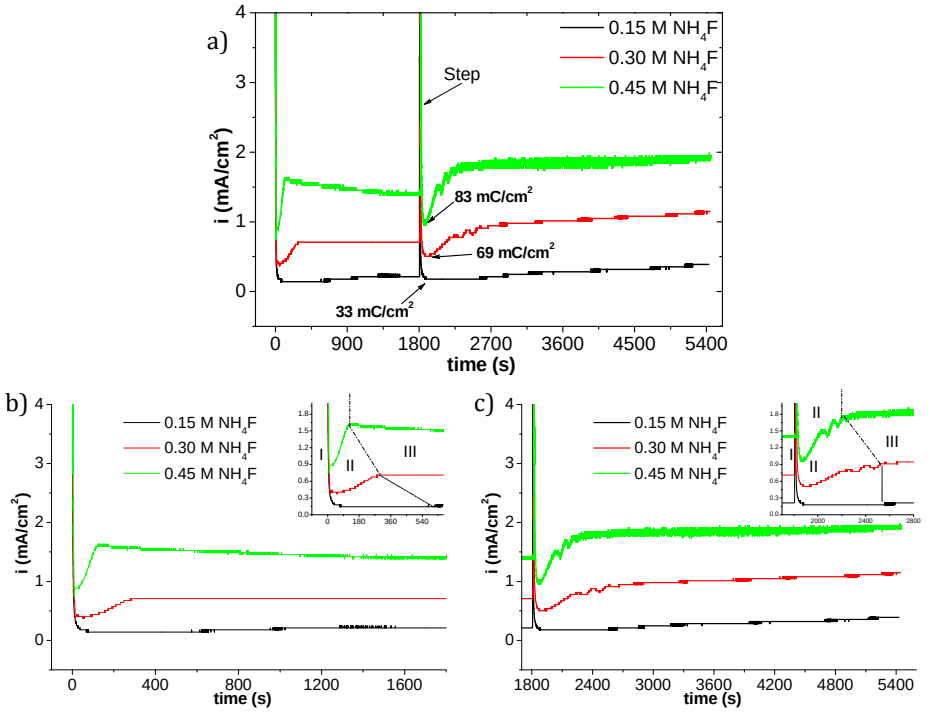

Figure 2. Current density–time responses of anodizing of Ti6Al4V at 10 V for 30 minutes followed by second voltage step at 20 V for 60 minutes (a), i vs.t response related to V_1=10 V for 30 minutes (b) and V_2= 20 V for 60minutes (c).

The increase in steady current density depending on the fluoride concentration in the bath indicates a greater chemical dissolution of the anodic layers with the fluoride content in the electrolyte.

The value of the final voltage (V_2) determines the features of the anodic oxide layer grown on the oxide/metal interface [18-21, 25]. Therefore, the charge density related to the thickness of the barrier layer is calculated by integrating the stage I from the current density vs. time response corresponding to the second voltage step. These values vary between 33-83 mC/cm² depending on the fluoride concentration in the bath, Table 1. Assuming that all the charge are only employed to form a dense layer of amorphous TiO_2 [21], the thickness of barrier layer varies from 18 to 45 nm, Table 1.

Similarly, by calculating the total charge density used in the anodizing process, it can be seen that the total charge density increases with the

fluoride content in the bath, from 1.393 to 9.322 mC/cm^2 (Table 1). Assuming an efficiency of 100% for the titanium anodizing process, the thickness of the anodic layer would be 758 nm for a concentration of 0.15 M NH_4F, 2615 nm for 0.3 M NH_4F , and 5071 nm for 0.45 M NH_4F, Table 1. However, as expected, the thickness values of the TiO_2 layers measured by SEM differ significantly from the theoretical values calculated, Table 1, as it will be discussed later. This difference is increased with the fluoride content in the bath due to the higher chemical dissolution of the anodic layer which occurs in presence of fluorides since the dissolution rate of the oxide layer increases considerably with the F^- content [26].

[X] M NH_4F	Step (30-60min)	Barrier Film Charge mC/cm^2	Expected Barrier oxide thickness, nm[a]	Charge C/cm^2	Expected oxide thickness, nm[a]	NT inner diameter mouth [b]/ bottom[c], nm	Barrier layer thickness, nm[c]	Total thickness, nm[b]
0.15	**10 - 20V**	33	18	1.393	758	~15 / 53	41	~661
0.3		69	38	4.807	2615	~47 / 69	39	~1355
0.45		83	45	9.322	5071	~63 / 65	40	~1585

[a] Calculate for compact amorphous film assuming 100% current efficiency
[b] Measured by SEM.
[c] Measured by TEM.

Table 1. Parameters of nanotubes formed in 1M $NH_4H_2PO_4$/[X] M NH_4F.

3.1.2. Influence of the Electric Field

To study the influence of the electric field on the nanostructure of the anodic layers, the magnitude of the voltage steps was varied for a specific concentration of fluorides, 0.3 M NH_4F.

Figure 3 shows the anodizing curves obtained for 0.3 M NH_4F solution using different voltage steps. The evolution of the i vs. t curves is similar to those described in Figure 2. Thus, after applying a voltage step of 10 V, an abrupt decrease in the current density related to the formation of the oxide barrier layer is observed, followed by the nucleation of the pores which does not exceed 300 seconds. Finally, the current density is maintained

constant indicating that the steady state, in which the growth of the nanotubes takes place, has been reached (Figure 3).

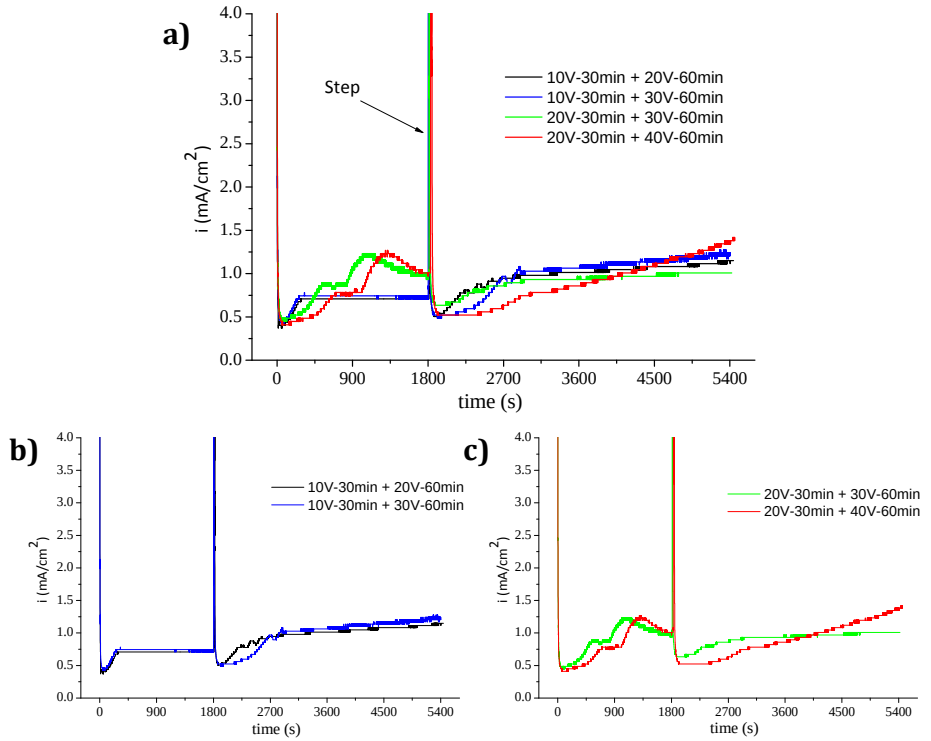

Figure 3. Current density-time responses of anodizing of Ti6Al4V in 1 M $NH_4FH_2PO_4$/0.3 M NH_4F at different voltage steps (a), with V_1=10V (b), with V_1=20 V (c).

Upon applying the second voltage step, either 20 or 30 V, the current density at the steady state depicts higher oscillations than during the first voltage step of 10V. This is due to the increase of the field-assisted dissolution of the anodic layer at voltages higher than 10 V, unbalancing the formation and dissolution of the anodic oxide layer. The current density evolution at the steady state for a given $\Delta V=V_2-V_1$, indicates that the current density depends primarily on the applied ΔV rather than on the absolute values of each step, V_1 and V_2, see figures 3b and 3c. Nevertheless, in the last 30 minutes of the 20-40V treatment, the current density increases continuously, without actually reaching any steady state, thus revealing a greater field-assisted dissolution of the anodic layer at high voltages.

The results suggest that the main process occurring at stage III- (constant nanotubular layer thickness over time) is field-assisted dissolution instead of "flow assisted" due to the significant level of dissolution of the oxide layer in this aqueous media.

3.2. Film morphology

In this section, the film morphology of the anodic layers fabricated using different anodizing conditions were characterized using scanning electron microscopy and transmission electron microscopy.

The morphology of the nanotubular layers fabricated in Ti6Al4V alloy by applying 10-20 V voltage steps in baths containing different NH_4F concentrations is shown in Figure 4. In all cases the formation of nanotubes preferentially grown in the α phase, enriched in aluminium, along with the dissolution of the oxides in β phase is observed. Such morphology has been widely described for F^- containing aqueous electrolytes. The absence of porous structures in the β phase relates to the high solubility of vanadium oxides formed on this phase[5, 8, 12, 15, 27, 28].

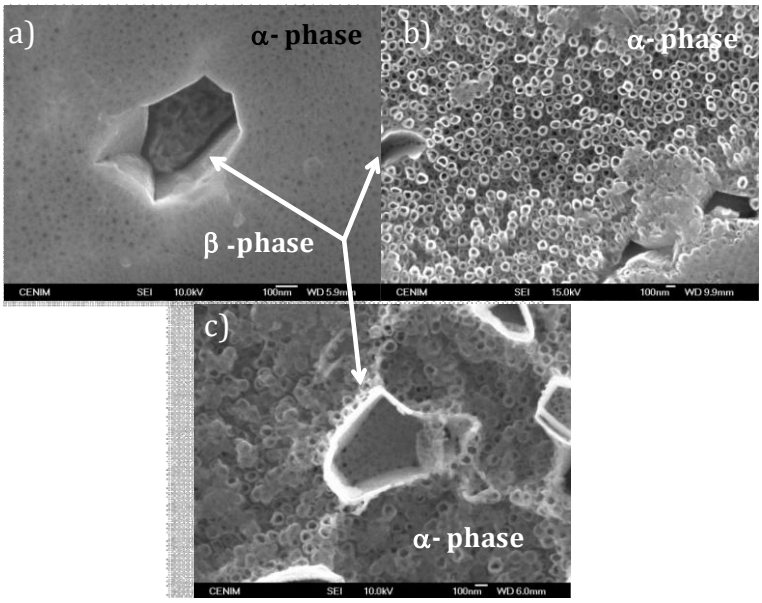

Figure 4. Scanning electron micrographs. Morphology of the anodic layers grown at V_1=10V for 30 minutes and V_2=20V for 60 minutes on Ti6Al4V using (a) 0.15 M, (b) 0.3 M and (c) 0.45 M NH_4F.

The micrographs gathered in Figure 4 show the influence of the NH_4F concentration in the nanotube inner diameter in the mouth, which varies from 15-63 nm for 0.15 M and 0.45 M NH_4F, respectively, Table 1. This increase in the inner diameter of the nanotube is a result of the chemical dissolution of the nanotube walls due to the presence of fluorides in the electrolyte [27, 29], according to the following reaction:

$$TiO_2 + 6F^- + 4H^+ \rightarrow TiF_6{}^{2-} + 2H_2O \quad (1)$$

This reaction may be further enhanced by the weakness of the bond between adjacent Ti and O due to the electric field (field-assisted dissolution).

Additionally in Figure 4b and 4c it can be observed that in some areas the mouths of nanotubes appear to be plugged by a white oxide. This oxide is the result of the solubilization of the titanium and precipitation in form of hydrated species ($TiO(OH)_2$ or $Ti(OH)_4$) [24, 28, 30, 31].

The thickness of the grown layers measured by SEM varies from 661 nm for the anodic layer fabricated in the bath with the lowest concentration of fluoride, up to 1585 nm approximately, for the layer obtained in a bath with the highest concentration, 0.45 M NH_4F, Table 1.

Figures 5a-f show the cross section of the anodic layers. Nanotubular structure can be distinguished in α phase, while cavities caused by the preferential dissolution of the oxide formed in β phase are observed. It is important to highlight that the lowest concentration of fluoride, 0.15 M NH_4F, promotes a layer with double nanoporous-nanotubular structure, Figure 5a-b. This complex morphology comprises an outer nanoporous part (~180 nm thick) and inner nanotubular part. In the literature this bi-layered structure has been reported on pure titanium [32] but also Ti6Al4V [27]. The explanation about the mechanism for the transition from nanoporous to nanotubular structure is unclear. According to Crawford et al.[32], the nanotubes grow deeper into the alloy due to the competition of oxide growth and chemical dissolution at the bottom of the nanotube. As nanotubes continue to grow, the nanoporous layer is subjected to chemical dissolution, resulting in thinning and eventual disappearance.

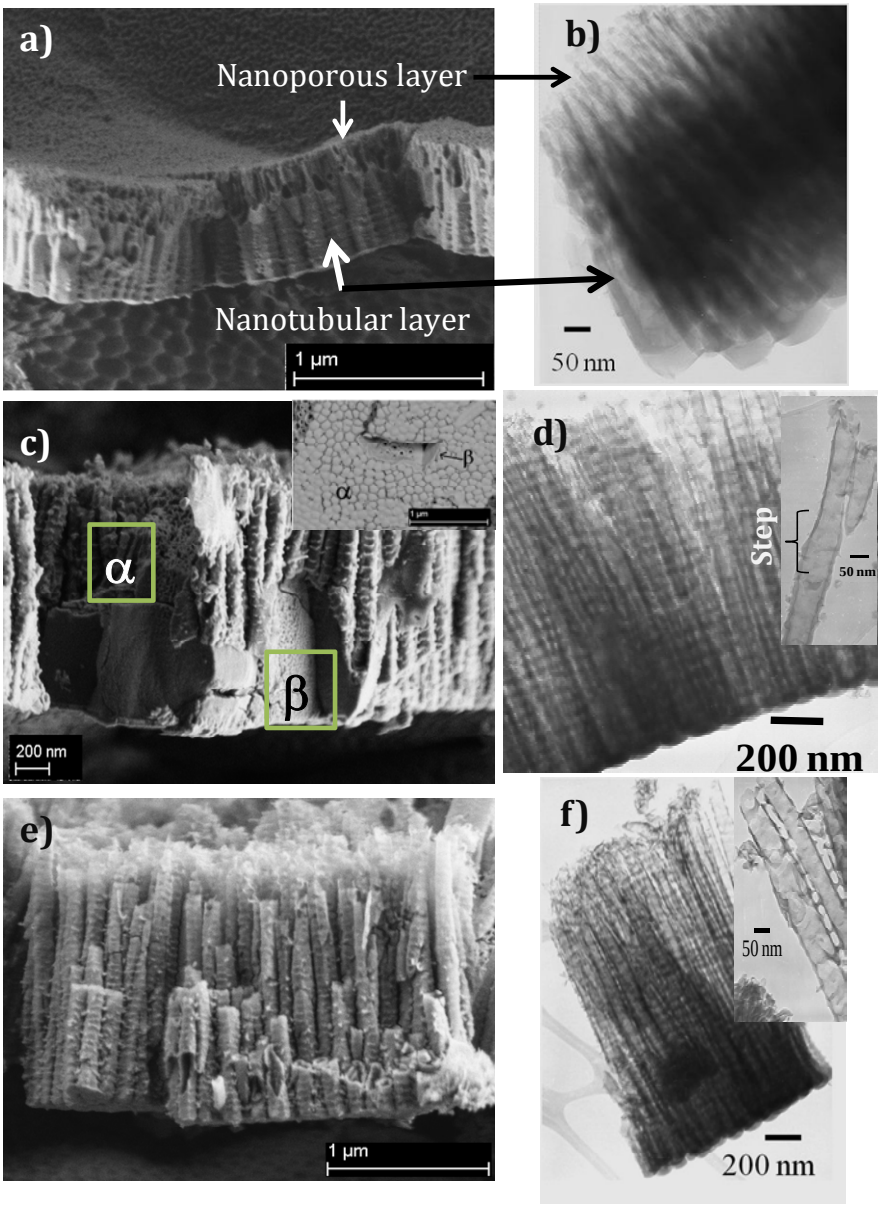

Figure 5. Cross sections of anodic layers fabricated at 10-20V in 1M $NH_4H_2PO_4$ with (a,b) 0.15 M, (c, d) 0.3 M and (e, f) 0.45 M of NH_4F.

Conversely, the layers grown in baths with 0.3 M and 0.45 M NH_4F have just a nanotubular structure throughout the thickness, Figure 5 c-f. The nanoporous layer disappears at higher concentration of fluorides in the bath, 0.3 and 0.45 M, since the nanoporous layer is subjected to a most

intense chemical dissolution due to the higher fluorides presence in the bath. The thickness of the barrier layer at the bottom of the nanotubes is about 40 nm, Table 1, suggesting an oxide growth rate of 2 nm/V within 60 min of anodizing.

The images of the cross-section of the anodic layers obtained by TEM clearly show the change in the nanotube inner diameter from the bottom to the mouth with the applied voltage step, Figure 5 d and f. Table 1, shows the inner diameters of the mouth and of the bottom of the nanotubes grown applying the stepped voltage, 10-20 V for the three anodizing baths. It can be seen that the best defined bottle shaped nanotubular structures are obtained for the bath containing 0.3 M NH_4F. The design of bottle-shaped nanotubes with thicknesses greater than micrometer, is specially interesting for controlled drug delivery systems in orthopaedic prostheses [33]. In addition, by applying different voltage steps, in a bath containing 0.3 M NH_4F promotes changes in the nanotubular structures with regard to those previously described, Figure 6 a-h. The anodizing process performed at 10-30 V, Figure 6c-d, shows poorly defined pores throughout the surface area, while the layers grown at 20-30 V Figure 6 e, show better defined nanotubular structures, similar to those obtained at 10 -20 V, Figure 6 a. In the 20-40 V treatment, Figure 6g, the formation of the nanotubes is not homogeneous over the entire surface, showing that the film looses integrity and collapses. Values of the inner diameter in the mouth and in the bottom of the nanotubes are included in Table 2.

Nanotubes inner diameter depends primarily on the applied voltage since the voltage determines the electric field strength across the oxide, thus affecting the migration of ions and ultimately the nanotube inner diameter. The upper diameter (mouth diameter) is related to the value of the first applied voltage during the growth of the anodic layers. Layers which are grown with an initial voltage of 20 V (20-30 V and 20-40 V) have a larger pore diameter, in the range of 63-67 nm, compared to layers grown with an initial voltage of 10 V (10-20 V and 10 -30 V) with diameters comprises between 39-47 nm, Table 2. Nanotubes bottom diameter depends on the second applied voltage. Values vary from 69 nm for 20 V to 90 nm for 40 V.

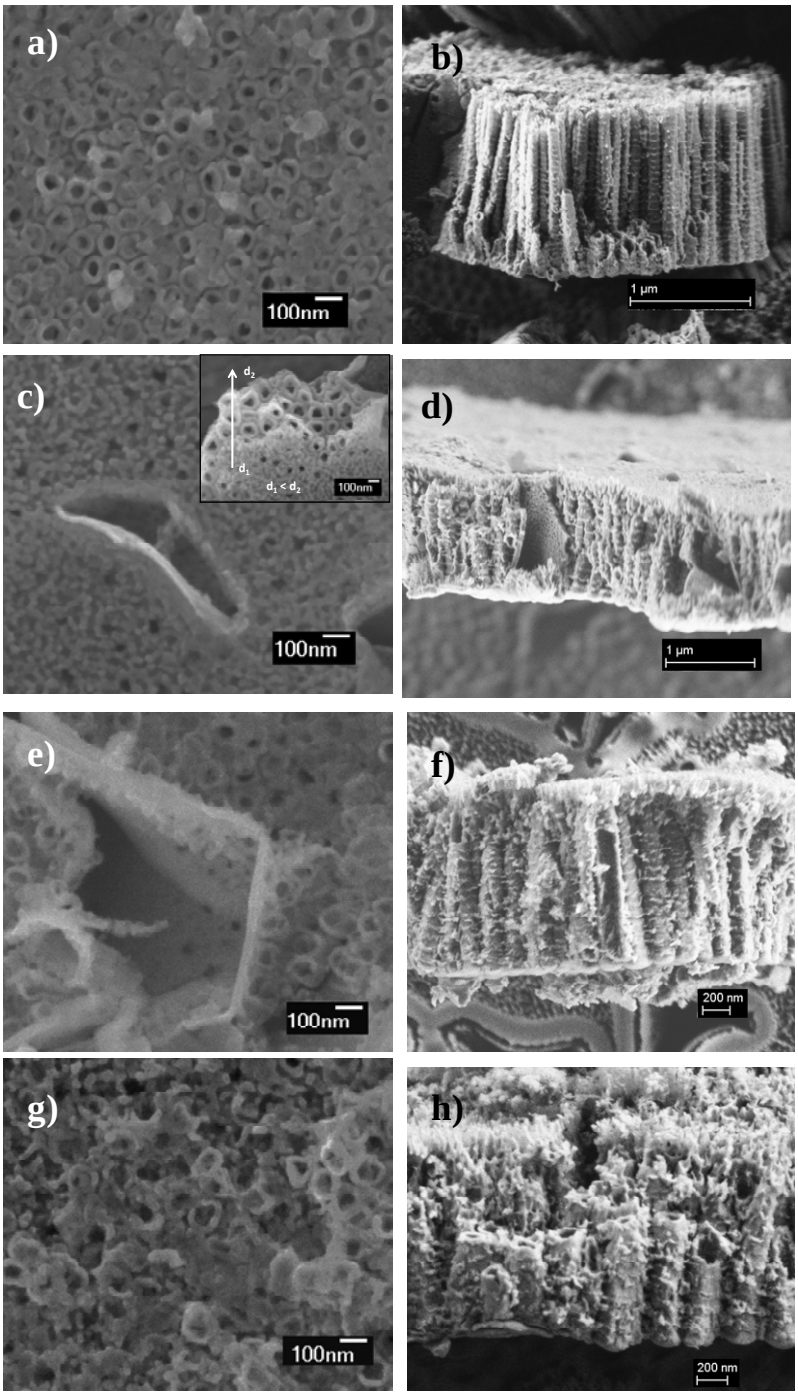

Figure 6. Scanning electron micrographs. Morphology of the anodic layers grown in 1 M $NH_4H_2PO_4$+0.3 M NH_4F at: (a, b) 10-20 V, (c, d) 10-30 V, (e, f) 20-30 V, (g, h) 20-40 V.

Electrolyte	Step V_1 30min	Step V_2 60min	Charge C/cm²	Expected oxide thickness[a] nm	NT inner diameter mouth/bottom nm	Total thickness, nm[b]	Name
1M $NH_4H_2PO_4$ + 0.3M NH_4F	10V	20V	4.807	2615	~ 47 / 69	~1355	10-20V
	10V	30V	4.946	2690	~ 39 / 57*	~1383	10-30V
	20V	30V	4.999	2720	~ 67 / 90	~1450	20-30V
	20V	40V	5.207	2839	~ 63 / 90*	~1187	20-40V

[a] Calculate for compact amorphous film assuming 100% current efficiency.
[b] Measured by SEM.
* Measured at half of the oxide.

Table 2. Parameters of nanotubes formed at different voltage steps.

Assuming an efficiency of 100% for the titanium anodizing process, the thickness of the anodic layer fabricated using the different voltage steps applied ranges between 2600 and 2800 nm, Table 2. The thickness of the anodic layers measured by SEM are about 1400 nm for all anodic layers except for the layer grown at 20-40 V, which showed a smaller thickness, 1187 nm, Table 2. This difference can be attributed to the stronger electric field at 40 V compared to that obtained at lower applied voltages. This implies that there is a higher dissolution rate for the oxide being formed. This is clearly revealed in the anodizing curves, by the increasing current density recorded at stage III pointing out that a steady state is not reached, Figure 3.

For the oxide layers fabricated, either in the solutions containing different fluoride concentrations, or varying the voltage steps, Figure 5 and 6, the formation of ribs on the wall of the nanotubes is observed. Ribs have been widely described in the literature in aqueous electrolytes and organic electrolytes with a water content higher than 5% [18, 34-36]. Its formation occurs in a non-continuous way and is due to several factors such as the aggressiveness of the anodizing bath; mechanical stress generated during the growth of nanotubular oxide; the expansion factor; and the electric field generated by applying high voltage.

The inward migration of O^{2-} ions during anodization fills the volume of metal consumed, but the outward migrating Ti^{4+} ions do not contribute to growth at the metal/oxide interface but pass directly into the solution. Fluoride ions migrate inward at twice the rate of oxygen ions across the layer and form a fluoride-rich layer at the metal–oxide interface. This fluoride-rich layer is more soluble in the anodizing electrolyte than the relatively pure TiO_2 forming the majority of the layer thickness. The dissolution of the fluoride rich layer placed between the nanotubes walls (TiF_4), according to reactions 2 and 3, increases the inter-space distance between the nanotubes. Therefore, the electrolyte accesses throughout the inter-space, and promotes the growth of a new barrier layer between the walls of adjacent nanotubes to form the ribs, in accordance with reaction 4 [27, 35, 37]:

$$TiF_4 + 2H_2O \rightarrow H^+ + [TiF_4(OH)H_2O]^- \quad (2)$$

$$[TiF_4(OH)H_2O]^- + HF \rightarrow [TiF_5 \cdot H_2O]^- \quad (3)$$

$$Ti + 2H_2O \rightarrow TiO_2 + 4H^+ + 4e^- \quad (4)$$

Figure 6h shows that the greater amplitude of the voltage step, i.e. 20-40 V, favours the formation of ribs along the nanotube to a greater extent than the other conditions studied. Moreover, in this case it appears that the inter-space distance is greater than at lower voltages thus indicating greater field-assisted dissolution of the nanotube walls at the highest applied voltages.

3.3. Efficiency of film formation and composition

In order to determine the composition of the anodic layers and estimate the efficiency of the anodizing process, the oxide layers were analysed by means of Rutherford Backscattering Spectroscopy (RBS).

Figure 7a presents the RBS spectra corresponding to the anodic layers grown at voltage steps 10-20 V in electrolytes with different NH_4F concentrations. All the spectra show a well-defined peak in channel 475 associated with oxygen, with the same number of counts, but with different width. The most significant difference among the spectra collected in

Figure 7a, is depicted in the slope plotted between channels 850 and 950 and is related to the presence of titanium in the anodic layer. As the concentration of fluoride in the electrolyte increases, the formation of a more pronounced step is observed. This step is related to the different thickness of the anodic layers, while the slope can be attributed to: differences in the roughness of the metal/oxide and oxide/surface interfaces; porosity of the grown layer; and heterogeneity of the oxide formed

RBS spectra show a similar trend in the thickness of the anodic layers in relation to that measured by SEM. The layer fabricated in 0.15 M NH_4F has the lowest thickness, while those grown in 0.3 M y 0.45 M NH_4F are thicker and similar between them.

In order to determine the composition and thickness of the oxides grown, the simulation of RBS spectra was conducted using the SIMRA software, Figures 7b and 8b. In order to simulate these complex oxide layers, the fitting of the spectra was performed assuming various layers of varying composition and thicknesses. The results show good agreement between the fitted and experimental data, for all cases.

The composition of the anodic layers in 10^{15} atoms·cm^{-2} and at.% is gathered in Table 3. It can be observed that the chemical composition for the layers fabricated in solutions containing different NH_4F concentrations are similar among them, showing 33 to 34 at.% for oxygen, 47 to 51 at.% for titanium, 4 to 7 at.% for aluminium, 3 at.% for vanadium and fluorine contents about 9-10 at.%, Table 3.

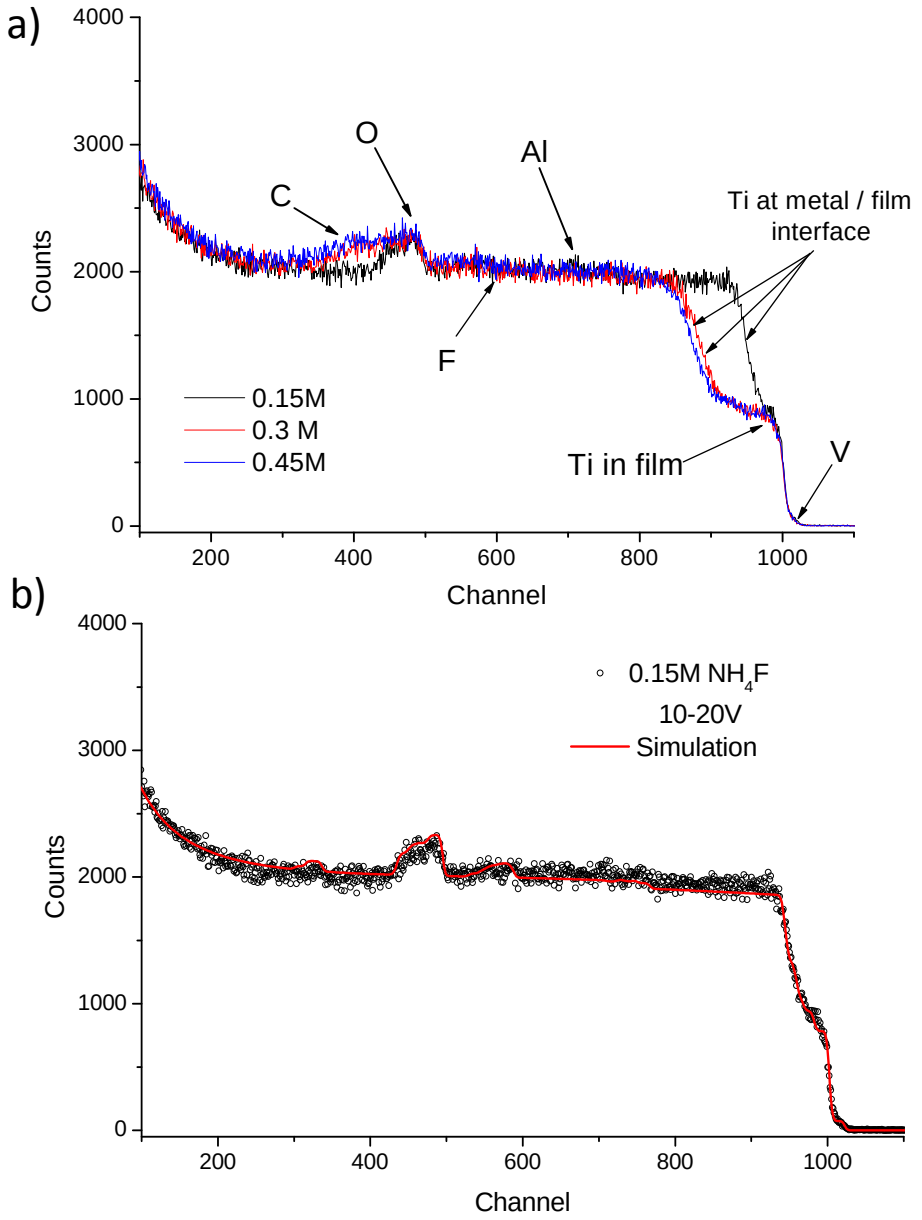

Figure 7. Rutherford backscattering analysis spectra for anodic oxide films formed on Ti-6Al-4V in 1 M $NH_4FH_2PO_4$ + [x] M NH_4F electrolyte at 10V for 30 min and 20V for 60 min, acquired at 3.777 MeV (a) and fitting of the spectra for the film formed in 0.15 M NH_4F (b) circles- original data, solid line- simulation.

Film [M] NH_4F	Ti	O	F	Al	V	Average molecular composition	Efficiency (%)
	(x 10^{15}at·cm^{-2}/at.%)						
0.15	743 /33	1142 /51	221 /10	92 /4	60 /3	$TiO_{1.24}$ 0.080TiF_4 0.067Al_2O_3 0.044V_2O_5	34.24
0.30	1760 /34	2389 /47	485 /9	346 /7	145 /3	$TiO_{0.92}$ 0.074TiF_4 0.106Al_2O_3 0.044V_2O_5	23.53
0.45	1802 /33	2594 /47	536 /10	383 /7	156 /3	$TiO_{0.98}$ 0.080TiF_4 0.115Al_2O_3 0.047V_2O_5	12.42

Table 3. Composition of the nanotubular films (x 10^{15} atoms cm^{-2}), and at.% of each element, formed on Ti-6Al-4V in 1M $NH_4H_2PO_4$ electrolyte containing different NH_4F concentrations, applying a voltage step of 10V for 30 minutes and 20V for 60 minutes.

The composition of the layers was determined assuming the stoichiometric formation of V_2O_5, Al_2O_3 and TiF_4. The average molecular composition of the nanotubes formed on Ti–6Al–4V alloys can be expressed as $TiO_{1.24}$·0.080TiF_4·0.067Al_2O_3·0.044V_2O_5 for the layer grown in 0.15 M NH_4F while for the layers grown at 0.3 and 0.45 M NH_4F, the titanium oxide is composed of $TiO_{0.92}$ and $TiO_{0.98}$, respectively, Table 3. Similar contents of TiF_4, Al_2O_3 and V_2O_5 are found for layers fabricated with 0.3 M and 0.45 M NH_4F.

RBS spectra for layers grown in an electrolyte with 0.3 M of NH_4F and different voltage steps, Figure 8a, are similar to those obtained for the anodic layers grown with different concentrations of NH_4F. A well-defined oxygen peak of similar width is observed in all growth conditions. There are no great differences in thickness between the layers. The anodic oxide layer fabricated at 20-30 V is slightly thicker, while the layer grown at 20-40 V, has the lowest thickness. These results are in agreement with those measured in the SEM images as is summarised in Table 2.

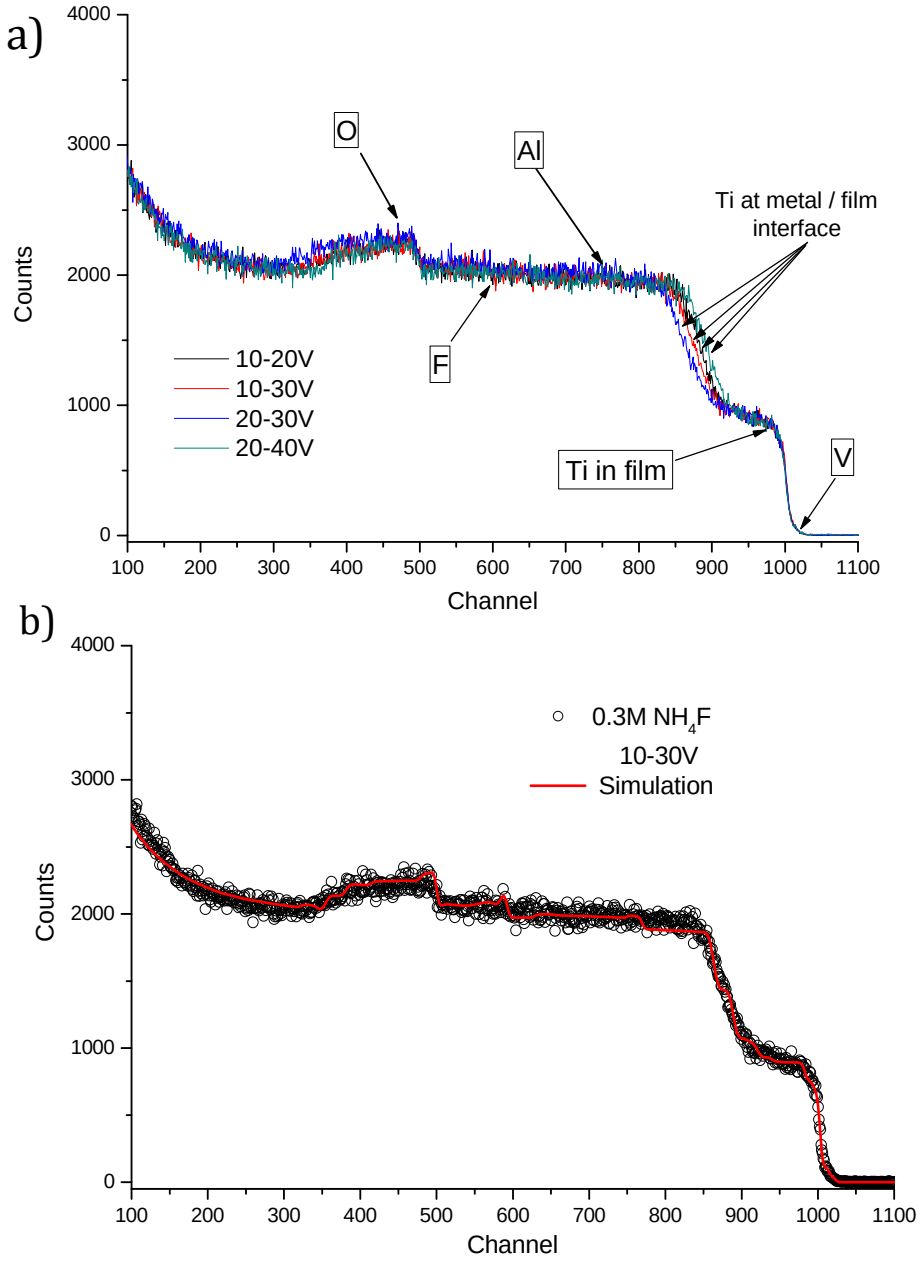

Figure 8. Rutherford backscattering analysis spectra for anodic oxide films formed on Ti-6Al-4V in 1M $NH_4FH_2PO_4$ + 0.3 M NH_4F electrolyte at different voltage steps, acquired at 3.777 MeV (a), fitting of the spectra for the film formed at 10-30V, (b): circles- original data, solid line- simulation.

The composition of the titanium oxide layers is similar in all cases, showing 33 to 36 at.% for oxygen, 45 to 47 at.% for titanium, 7 at.% for aluminium, 2 to 3 at.% for vanadium and fluorine contents about 9-12 at.%, Table 4. The layer grown at 20-30 V presents a slightly higher Ti/O ratio, showing an average molecular composition expressed as $TiO_{0.98}{\cdot}0.094TiF_4{\cdot}0.111Al_2O_3{\cdot}0.045V_2O_5$, while the oxide grown at 20-40 V, revealing a lower ratio of Ti/O, is composed of $TiO_{0.87}{\cdot}0.073TiF_4{\cdot}0.098Al_2O_3{\cdot}0.039V_2O_5$, Table 4.

Film	Ti	O	F	Al	V	Average molecular composition	Efficiency (%)
	(x 10^{15}at·cm^{-2}/at.%)						
10-20V	1760 /34	2389 /47	485 /9	346/ 7	145/ 3	$TiO_{0.92}$ $0.074TiF_4$ $0.106Al_2O_3$ $0.044V_2O_5$	23.53
10-30V	1842 /34	2429 /45	630 /12	372/ 7	132/ 2	$TiO_{0.93}$ $0.093TiF_4$ $0.109Al_2O_3$ $0.037V_2O_5$	25.73
20-30V	1938 /33	2724 /46	668 /11	387/ 7	158/ 3	$TiO_{0.98}$ $0.094TiF_4$ $0.111Al_2O_3$ $0.045V_2O_5$	24.72
20-40V	1674 /36	2121 /45	447 /10	303/ 7	124/ 3	$TiO_{0.87}$ $0.073TiF_4$ $0.098Al_2O_3$ $0.039V_2O_5$	22.13

Table 4. Composition of the nanotubular films (x 10^{15} atoms cm^{-2}), and at.% of each element, formed on Ti-6Al-4V in 1M $NH_4H_2PO_4$+0.3M NH_4F, at different voltage steps.

The efficiency of the anodizing process has been estimated using the expression that relates the concentration of titanium obtained from RBS spectra (concentration of Titanium in 10^{15} atoms·cm^{-2}, second column in Tables 3 and 4) and the calculated from the charge recorded during the anodizing (Tables 1 and 2), assuming that all the charge is consumed to oxidize titanium (100% efficiency):

$$Efficiency = \frac{Ti\ atoms \cdot cm^{-2}(RBS)}{Ti\ atoms \cdot cm^{-2}(current - time\ curves)} x100 \quad (5)$$

where the Ti atoms·cm^{-2} are estimated as follows:

$$Ti\ atoms \cdot cm^{-2}(current - time\ curves) = Charge\ recorded\ x\ 1{,}5597 \cdot 10^{18}\frac{at}{C} \quad (6)$$

$$1{,}5597 \cdot 10^{18}\frac{at}{C} = 275\frac{nm}{C}x\frac{\rho x N_A}{W_M}$$

being 275 nm·cm^2/C the titanium consumed by charge unit, ρ the titanium density, N_A the Avogadro´s Number and W_M the titanium molecular weight.

The results reveal an efficiency about 34.2% for the bath containing 0.15 M NH_4F, and 12.4% for the bath with 0.45 M NH_4F, Table 3. The efficiency decreases with the fluoride concentration in the bath despite the influence of the F^- content on the charge, as can be seen in the increasing current density response described in the curves in figure 2. This means that not all the collected charge is used to grow the titanium oxide, but that part of it is due to either the dissolution of both the nanotubes formed in the α phase and the oxidation of the β phase, or to the oxygen evolution at the anode. The higher the fluoride concentration in the anodizing electrolyte, the lower the process efficiency. This response has been also described for TiO_2 anodic layers fabricated in similar electrolytes at constant voltages[27, 28].

The efficiency of the anodizing process performed in the present work, applying voltage steps, Table 4, is 22% to 25%. It appears that efficiency of the anodizing process is not influenced by the voltages or by the ΔV applied. The results suggest that the growth efficiency depends mainly on the chemical dissolution of the oxide due to the fluoride presence in the electrolyte more than the field-assisted dissolution of the oxide and field-assisted ejection of Ti ions into the electrolyte.

4. Conclusions

In this paper it has been demonstrated that it is possible to design TiO_2 oxide layers with bottle-shaped nanostructures by controlling the anodizing electrolyte and the applied voltage steps.

For the anodic layer fabricated applying voltage steps of 10-20 V, the F^- concentration mainly influenced the inner nanotubes diameter, which also

depends on the value of the voltage applied. Electrolytes with low fluoride concentration, 0.15 M NH_4F, lead to anodic layers with double morphology, nanoporous on the oxide/solution interface and nanotubular on the metal/oxide interface. Conversely, at higher fluoride concentrations, 0.3 M and 0.45 M NH_4F, only a nanotubular oxide layer with variable inner diameter along the layer is fabricated. Therefore, the growth of bottle-shaped nanotubular oxide layers is achieved only when apply a voltage steps using the adequate fluoride concentration in the electrolyte. The best bottle-shaped morphology is obtained in the anodizing bath containing 0.3 M NH_4F with a inner diameter about 47 nm at the mouth and about 69 nm at the bottom. This anodic layer is homogeneous and thicker than one micrometer.

Other voltage steps, 10-30 V, 20-30 V or 20-40 V, applied in the same anodizing bath-0.3 M NH_4F- lead to oxide layers thicker than the micrometer but their nanostructures are not well defined.

Ribs on the wall of the nanotubes are observed for the oxide layers fabricated, either in the solutions containing different fluoride concentrations, or varying the voltage steps. Nevertheless, the formation of ribs are favoured for the greater amplitude of the voltage step, i.e. 20-40 V, than the other conditions studied. Additionally, the inter-space distance is also greater at 40 V than at lower voltages thus indicating greater field-assisted dissolution of the nanotube walls at the highest applied voltages.

The efficiency of the anodizing process decreases with the fluorides concentration in the bath, from 34.2% for 0.15 M NH4F, 22 % for 0.3 M NH4F to 12.4% for 0.45 M NH4F, and is practically constant for the different voltages applied, about 22-25 %. It appears that efficiency of the anodizing process depends mainly on the chemical dissolution of the oxide due to the fluoride concentration in the electrolyte more than the field-assisted dissolution of the oxide and field-assisted ejection of Ti ions into the electrolyte.

Acknowledgements

The authors acknowledge to the Spanish Ministry of Science and Innovation -under Consolider-Ingenio 2010 CSD 2008-0023 FUNCOAT Project and to the Spanish Ministry of Economy and Competitiveness- under MUNSUTI Project -MAT2013-48224-C2-1-R-. Mr. J. M.Hernández-López wishes to thank to CSIC for his PhD grant JAE-predoc.

References

1. S. Minagar, C. C. Berndt, J. Wang, E. Ivanova and C. Wen, Acta Biomater, 2012, 8, 2875-2888.
2. M. Geetha, A. K. Singh, R. Asokamani and A. K. Gogia, Progress in Materials Science, 2009, 54, 397-425.
3. B. M. Holzapfel, J. C. Reichert, J. T. Schantz, U. Gbureck, L. Rackwitz, U. Noth, F. Jakob, M. Rudert, J. Groll and D. W. Hutmacher, Adv Drug Deliv Rev, 2012.
4. L. Zhao, P. K. Chu, Y. Zhang and Z. Wu, J Biomed Mater Res B Appl Biomater, 2009, 91, 470-480.
5. G. K. Mor, O. K. Varghese, M. Paulose, K. Shankar and C. A. Grimes, Sol. Energy Mater.Sol. Cells, 2006, 90, 2011-2075.
6. E. Gultepe, D. Nagesha, S. Sridhar and M. Amiji, Adv Drug Delivery Reviews, 2010, 62, 305-315.
7. O. R. Brian and G. Michael, Nat., 1991, 353, 737-740.
8. P. Roy, S. Berger and P. Schmuki, Angew Chem Int Ed Engl, 2011, 50, 2904-2939.
9. T. Goto, Intl. Congress Series, 2005, 1284, 248-256.
10. Y.-T. Sul, C. B. Johansson, Y. Jeong and T. Albrektsson, Medical Engineering & Phy., 2001, 23, 329-346.
11. G. Liu, K. Wang, N. Hoivik and H. Jakobsen, Sol. Energy Mater.Sol. Cells, 2012, 98, 24-38.
12. V. Zwilling, E. Darque-Ceretti, A. Boutry-Forveille, D. David, M. Y. Perrin and M. Aucouturier, Surface and Interface Analysis, 1999, 27, 629-637.
13. C. A.Grimes and G. K.Mor, Springer, 2009, p. 358.
14. A. Ghicov, H. Tsuchiya, J. M. Macak and P. Schmuki, Electrochemistry Communications, 2005, 7, 505-509.
15. J. M. Macak, H. Tsuchiya, L. Taveira, A. Ghicov and P. Schmuki, J Biomed Mater Res A, 2005, 75, 928-933.
16. Y. Li, H. Yu, W. Song, G. Li, B. Yi and Z. Shao, Intl. Journal of Hydrogen Energy, 2011, 36, 14374-14380.
17. J. Lin, J. Chen and X. Chen, Nano. Research Lett., 2011, 6, 1-5.
18. D. Guan, P. J. Hymel and Y. Wang, Electrochim. Acta, 2012, 83, 420-429.
19. X. Wang, S. Zhang and L. Sun, Thin Solid Films, 2011, 519, 4694-4698.

20. X. Wang, R. Chen, J. Zheng, P. Nie, H. Xie and X. Zhao, J. of Wuhan University of Technology-Mater. Sci. Ed., 2012, 27, 866-870.
21. D. Guan and Y. Wang, Nanoscale, 2012, 4, 2968-2977.
22. D. Wang, Y. Liu, B. Yu, F. Zhou and W. Liu, Chem. Mater., 2009, 21, 1198-1206.
23. Y. Liu, D. Wang, L. Cao, S. Chen, Electrochemistry Communications, 2012, 23, 68–71
24. L. V. Taveira, J. M. Macák, H. Tsuchiya, L. F. P. Dick and P. Schmuki, J. of The Electrochem. Soc., 2005, 152, B405.
25. J. M. Macak, S. Albu, D. H. Kim, I. Paramasivam, S. Aldabergerova and P. Schmuki, Electrochem. and Solid-State Letters, 2007, 10, K28-K31.
26. J. M. Macak, H. Hildebrand, U. Marten-Jahns and P. Schmuki, J. of Electroanalytical Chemistry, 2008, 621, 254-266.
27. E. Matykina, A. Conde, J. de Damborenea, D. M. y. Marero and M. A. Arenas, Electrochim. Acta, 2011, 56, 9209-9218.
28. E. Matykina, J. M. Hernandez-López, A. Conde, C. Domingo, J. J. de Damborenea and M. A. Arenas, Electrochim. Acta, 2011, 56, 2221-2229.
29. K. Yasuda and P. Schmuki, Electrochim. Acta, 2007, 52, 4053-4061.
30. J. M. Macak, H. Tsuchiya, A. Ghicov, K. Yasuda, R. Hahn, S. Bauer and P. Schmuki, Current Opinion in Solid State and Materials Science, 2007, 11, 3-18.
31.K. Yasuda, J. M. Macak, S. Berger, A. Ghicov and P. Schmuki, J. of The Electrochem. Soc., 2007, 154, C472-C478.
32. G.A. Crawford, N. Chawla, Acta Mater., 2009, 57, 854-867.
33. J.M. Hernández López , M.A. Arenas, A. L. Doadrio, A. Conde, C. Pérez-Jorge, J.J. de Damborenea, M. Vallet-Regi, E. Gómez-Barrena and J. Esteban. Proceedings of the 22nd Annual Meeting of the European Orthophaedic Research Sociaty, Nantes, France, 2014.
34. Y. A. Buslaev and V. A. Shcherbakov, J Struct Chem, 1966, 7, 332-336.
35. A. Valota, D. J. LeClere, P. Skeldon, M. Curioni, T. Hashimoto, S. Berger, J. Kunze, P. Schmuki and G. E. Thompson, Electrochim. Acta, 2009, 54, 4321-4327.
36. J. M. Macak, H. Tsuchiya, L. Taveira, S. Aldabergerova and P. Schmuki, Angewandte Chemie International Edition, 2005, 44, 7463-7465.
37. C. Lin, S. Chen and L. Cao, Mat. Sci. in Semiconductor Process., 2013, 16.

3.3 CARACTERIZACIÓN ELECTROQUÍMICA:

The influence of intertubular spacing of TiO_2 anodic layers on electrochemical response

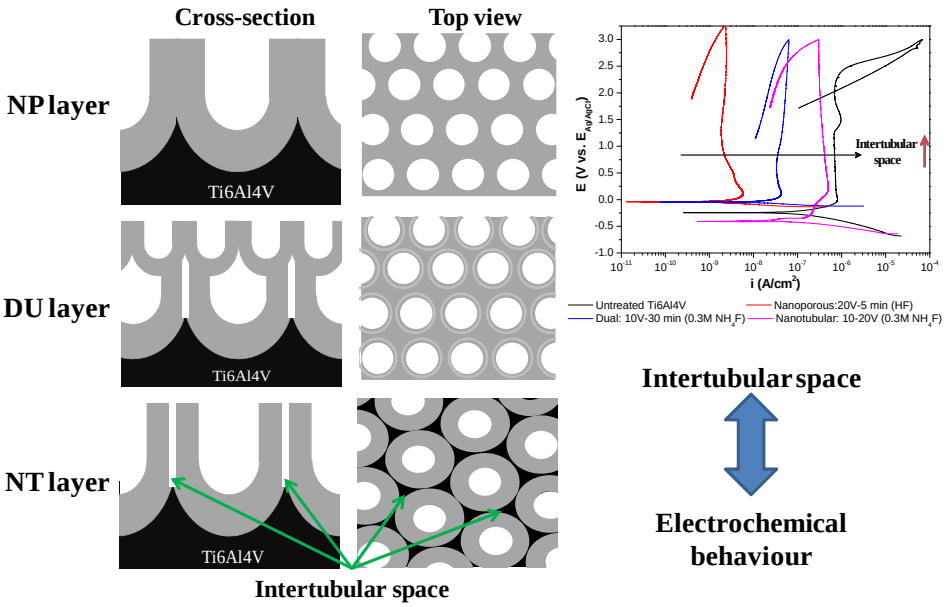

(Manuscrito en Preparación)

CARACTERIZACIÓN ELECTROQUÍMICA:

The influence of intertubular spacing of TiO_2 anodic layers on electrochemical response

El estudio de los procesos de corrosión que ocurren sobre la superficie de los implantes metálicos es fundamental, ya que puede afectar a la biocompatibilidad y a la integridad mecánica del dispositivo protésico. En este sentido, el titanio y sus aleaciones presentan una buena resistencia frente a la corrosión en la mayoría de los medios acuosos. Dicho comportamiento es debido a la formación de una película de TiO_2 de manera natural sobre su superficie metálica.

La generación de capas anódicas con características distintas a las del óxido nativo, como: espesor, morfología y composición química pueden modificar el comportamiento electroquímico del titanio y sus aleaciones.

El objetivo de este apartado es el estudio del comportamiento electroquímico de las capas de óxido de titanio con tres morfologías bien definidas: nanoporosas, dual (tubular en la parte más cercana a la intercara metal/óxido y una nanoporosa en la interfase óxido/electrolito) y nanotubulares, obtenidas mediante diferentes procesos de anodizado. Poniendo especial énfasis en relacionar la morfología de las capas anódicas con su respuesta electroquímica en una solución fisiológica simulada -PBS-, usando microscopia electrónica de barrido (SEM) para la caracterización morfológica y curvas de polarización potenciodinámicas y espectroscopía de impedancia electroquímica (EIS) para la caracterización electroquímica.

Los resultados mostraron que las capas anódicas con morfología nanoporosa crecidas a 20 V durante 5 minutos en un medio de H_2SO_4/HF presentan la mayor resistencia a la corrosión debido a que estas estructuras presentan capas barrera de mayor espesor en comparación a las capas anódicas con morfología dual o nanotubular.

Los espectros de impedancia revelaron que las capas con morfología nanoporosa y dual presentan el mismo mecanismo electroquímico, el cual está gobernado por la respuesta de la capa barrera de los nanoporos o nanotubos.

Por el contrario, las capas con morfología nanotubular muestran un comportamiento totalmente distinto a las capas nanoporosas o con morfología dual. En este caso, los espectros de impedancia muestran una evolución con el tiempo de inmersión. A tiempos cortos de inmersión, la constante de tiempo en frecuencias medias-altas está asociada al óxido nativo que cubre la superficie del sustrato expuesto a través de los espacios intertubulares. A tiempos ≥24h, las capas nanotubulares muestran una evolución distinta dependiendo del valor del espaciado intertubular. Para espaciados ≤ 15 nm, los espectros de impedancia, revelan tanto la respuesta asociada a la capa barrera de estas estructuras como la respuesta del óxido nativo que cubre el sustrato expuesto a través de los espacios intertubulares, mientras que para espaciados superiores (~ 30 nm), en los espectros únicamente se observa la señal asociada al sustrato.

The influence of intertubular spacing of TiO_2 anodic layers on electrochemical response

J.M. Hernández-López, A. Conde, J.J. de Damborenea, M.A. Arenas

[1]National Centre for Metallurgical Research (CENIM-CSIC), Avda. Gregorio del Amo 8, 28040, Madrid Spain.

Abstract

Anodic layers with varying morphological features, namely nanoporous-NP-; dual (nanopores and nanotubes in the same layer) -DU- and nanotubular -NT- morphology, were grown on Ti6Al4V alloy in H_2SO_4/HF and $NH_4H_2PO_4$ electrolytes at different applied voltages and times. The electrochemical characterization of the anodic layers was carried out using potentiodynamic polarization curves and electrochemical impedance spectroscopy.The polarization curves showed a decrease in passive current density depending on the morphology as follow: NP>DU>NT≥ Untreated Ti6Al4V alloy. Additionally, EIS measurements for NP and DU specimens revealed impedance spectra controlled by the response of the barrier layer. Conversely, the response of the nanotubular layers depends on the sizes of the intertubular space and the immersion time. At shorter immersion times, the impedance spectra of all nanotubular layers only reveal the response of the substrate exposed to the electrolyte through the intertubular space at short immersion times. However, at longer immersion times, ≥24h, the impedance spectra of the nanotubular layers vary with the size of the intertubular spaces. Intertubular spaces ≤15 nm show two contributions in the EIS spectra corresponding to the response of the barrier layer (hf) as well as the response of the native oxide covering the substrate (mf), while for the NT layers with intertubular spaces of ~30 nm, the EIS spectra only show the response of the substrate covered by the native oxide of the substrate at the bottom of the intertubular spaces.

Keywords: Nanotubes, nanoporous, anodic films, corrosion, polarization curves, EIS.

1. Introduction

The anodizing process has been used in recent times to grow TiO_2 oxide layers with different morphologies, such as barrier layers, nanoporous, dual and nanotubular structures, to functionalize the surface of the titanium and its alloys for different technological applications. The specific morphology of the anodic layers is determined by the growth conditions and depends on the composition of the bath, the temperature, the anodizing time, and current/potential applied [1-4].

The determination of the electrochemical behaviour of the anodic layers is critical for many applications such as biomaterials, where the protective properties of the layers control the cation elution and, therefore, the viability of the prosthetic device. In this regard, the broad research on anodic layers grown on titanium, and its alloys, has focused on identifying the electrochemical processes that occur which are influenced by the applied voltage or the electrolyte features during their growth [5-8], or on the electrochemical behaviour of native layers grown on titanium and their alloys [6, 9-13]. However, the influence of the morphological features of the anodic oxides on the electrochemical response and protective properties in biological solutions has been little studied [14-17].

Saji et al.[17] sstudied the corrosion characteristics of the anodic layers grown on Ti-35Nb-5Ta-7Zr alloy in Ringer's solution at 37 ºC and concluded that the nanotubular layer showed lower corrosion resistance in comparison to nanoporous layer and bare alloy due to the distinctly separated oxide/bare alloy interface shown by the nanotubes layers. Similarly, later on, the authors [16] studied the electrochemical response of anodic layers grown on Ti13Nb13Zr in PBS solution at 37 °C and demonstrated that the corrosion resistance of anodic layers with nanoporous morphology is higher than that obtained for the nanotubular

layer due to the small pore sizes and the absence of interpores spaces. However the relationship between the electrochemical response and the intertubular spaces has been not studied.

The polarization curves and electrochemical impedance spectroscopy (EIS) are the most used techniques to investigate a broad range of experimental systems, as well as to identify the processes associated with reaction kinetics on the surface morphology [18-21]. However, one of the difficulties of the EIS technique is the determination of the physical information of the system from the constant phase element (CPE). For instance, to estimate the capacitance, some authors have proposed two ways to estimate it, assuming two different time constant distributions on the surface of the material. The first one, associated with the distribution along the electrode surface (2-D) and the second one assuming a normal distribution to the electrode surface (3-D) [22-26].

Hirschorn et al.[27] estimated the thickness of the human skin and Nb2O5 anodic layers by determining the effective capacitance from the constant-phase element parameters, demonstrating the relevance of using the correct formula that corresponds to a given type of distribution (2-D or 3-D).

The aim of this work is to determine the electrochemical behaviour of oxide layers with different morphologies obtained by anodizing: nanoporous (NT), dual (DU), and nanotubular (NT) structures grown on Ti6Al4V alloy and which have been characterized from morphological and compositional view point in previous works [28-30]. The anodic layers were characterized by SEM, potentiodynamic polarization curves and electrochemical impedance spectroscopy in a phosphate buffer saline solution (PBS). In addition, the values of the thickness of the oxide, mainly the thickness of the barrier layer, obtained from the simulations of the impedance diagrams and the estimation of the effective capacitances are compared with those measured by TEM.

2. Experimental procedure

Specimens of 18mm ∅ of Ti6Al4V ELI alloy were ground through successive grades of SiC paper up to 1200 grade, degreased with detergent and rinsed with tap water followed by deionised water. The specimens were then chemically polished in a mixture of HF(40 wt.%):HNO_3(70 wt.%):H_2O with a volume ratio of 1:4:5 for 5 minutes, at room temperature under continuous stirring at 400 rpm, rinsed in distilled water and dried in cold air.

Anodic layers were formed in a two-electrode cell by anodizing. Three solutions which contained 1M H_2SO_4/0.15 wt.% HF, 1M $NH_4H_2PO_4$/0.15M NH_4F and 1M $NH_4H_2PO_4$/0.3M NH_4F were used in order to obtain different morphologies: nanoporous, dual, and nanotubular, layers. The experimental conditions used are summarized in Table 1. To simplify the sample nomenclature throughout the paper, the voltage, the time and origin of fluorides, for example, 20V-5min (HF) or 10V-30 min (0.15M NH_4F) are included in the sample designation. For all cases, temperature was kept constant at 20 ^oC, and platinum mesh was used as cathode. The plan views of the anodic films were examined by field emission gun scanning electron microscopy (FEG-SEM) using a JSM6500F Philips instrument, at 7 keV for secondary electron imaging.

Electrolyte		**Morphology**		
		Nanoporous (NP)	**Dual (DU)**	**Nanotubular (NT)**
1M H_2SO_4 + 0.15wt.%HF		20V-5 min	---	20V-60 min
1M $NH_4H_2PO_4$	**0.15 M NH_4F**	10V-30 min	20V-60 min	---
	0.3 M NH_4F	---	10V-30 min	20V-60 min
		---	---	10V-30 min+ 20V-60 min (10-20V)

Table 1. Conditions of fabrication of the anodic films grown on Ti6Al4V.

The electrochemical measurements were carried out by triplicate in a conventional three-electrode cell. Before starting the electrochemical tests, the samples remained in the solution for 1 hour to stabilize the open circuit potential (OCP). The working electrode was the untreated Ti6Al4V ELI alloy and the different anodic layers grown; an Ag/AgCl electrode (saturated KCl) was used as reference electrode, and the counter electrode was a platinum wire. The electrolyte used was a phosphate buffered saline solution (PBS) containing 150 mM NaCl, 9.99 mM KH_2PO_4, and 9.02 mM $Na_2H_2PO_4$, with a pH range between 7.2-7.4. All the tests were carried out at 37 ± 2 °C. Corrosion behaviour was evaluated by potentiodynamic polarization curves and electrochemical spectroscopy impedance using a Gamry Reference 600 potentiostat. The potentiodynamic curves were conducted at a scan rate of 0.16 mV/s. The potential scan was started in the anodic direction from a potential value of −0.3 V vs. OCP to 3 V with respect to the Ag/AgCl electrode. The reverse scan was started when the current density reached a cut-off value of 0.25 mA/cm^2.

EIS measurements were performed applying a sinusoidal signal of 10 mV of amplitude in a frequency range from 100 kHz to 10 mHz, and recording 10 points per decade. Measurements were carried out periodically during 4 weeks of immersion. The experimental data were analyzed using graphical methods and the ZVIEW software.

3. Results and discussion.

In order to understand the relationship between the morphology of the anodic layers and their electrochemical response, anodic layers with three different morphologies were fabricated: nanoporous layers, NP, (fig. 1a and b), which show pores in the oxide surface and a barrier layer at the bottom of the film; dual layers, DU, (fig. 1c and d), characterized by having a bimodal morphology -nanopores in the outer part and nanotubes in the inner part of the layer- associated with a high initiation nucleation density of nanoporous at the initial times of anodization [31]; and nanotubular

layers, NT, (fig. 1e and f), characterized by the growth of nanotubes with well-defined walls and the emergence of inter-space distances between nanotubes due to the increase of dissolution of the anodic layer. The intertubular spacing varies from ~15 nm for anodic layers grown in NH4F electrolyte up to 30 nm for layers grown at 20V-60min (HF) [28-30].

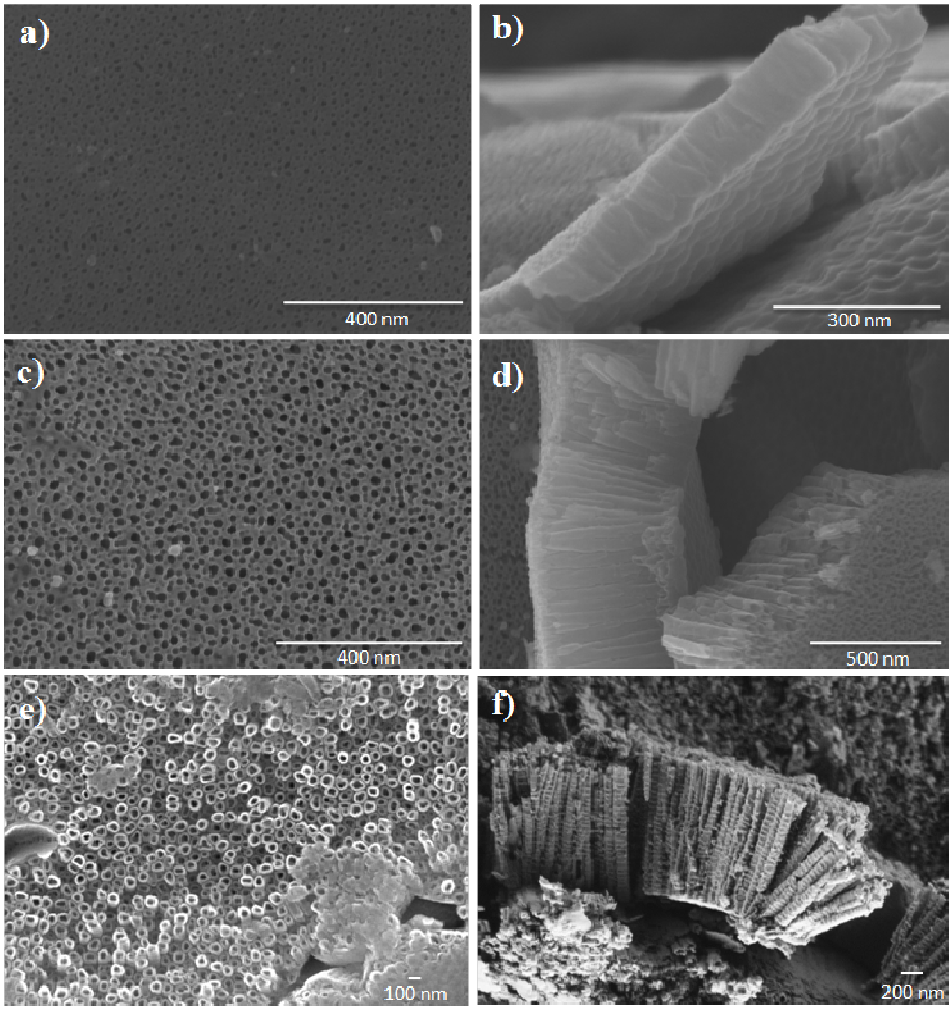

Figure 1. Scanning electron micrographs of the anodic layers grown on Ti6Al4V which showing the different morphologies. Nanoporous morphology grown at 10V-30 min (0.15M NH_4F) (a, b) duplex morphology grown at 10V-30 min (0.3M NH_4F) (c, d) and nanotubular morphology grown at 10-20V (0.3M NH_4F) (e, f).

It is important to highlight that a barrier layer placed at the bottom of the nanotube also exists for the specimens DUAL and NT.

Literature widely reports the growth of these morphologies, at varying voltage/current conditions, for different anodizing times and electrolytes. The mechanism responsible for the growth of the anodic layer with the morphologies described is rather complex but it can be roughly described as the balance among the field-assisted oxidation reaction of the titanium, the field-assisted dissolution, and the chemical dissolution of the anodic layers[1-4, 7, 28, 31, 32]

3.1 Potentiodynamic Polarization Curves

Figure 2 displays the potentiodynamic curves in PBS solution at 37 ºC of the anodic layers (NP, DU, NT). The untreated Ti6Al4V alloy and the anodic layers showed the typical passive behaviour characterized by a vertical anodic branch [33-35]. The corrosion potential (E_{corr}) was ~-250 mV vs. Ag/AgCl for the untreated Ti6Al4V alloy and ~-50 mV vs. Ag/AgCl, and ~14 mV vs. Ag/AgCl for the NP layers grown at 20V-5 min (HF), and 10V-30 min (0.15M NH_4F), respectively, fig. 2a. The passive current density (i_{pass}) of the NP film grown at 20V-5 min (HF) was ~1.90E−9 A/cm^2, while the layers fabricated at 10V-30 min (0.15M NH_4F) showed higher ipass, 1.64E−8 A/cm^2, but still about two and one order of magnitude lower than the untreated Ti6Al4V alloy, 6.91E-7 A/cm^2.

The corrosion potential of the DU layers is on the same order as the untreated Ti6Al4V alloy. The potentiodynamic curves of the anodic layers grown at 20V-60 min (0.15M NH_4F) and 10V-30 min (0.3M NH_4F) showed features similar to the NP layers but with values of ipass of ~1.06E-7 and ~4.00E-8 A/cm^2, respectively, Fig. 2b.

Similarly, the NT layers exhibit a similar corrosion potential to the untreated Ti6Al4V alloy, about -237 mV vs. Ag/AgCl for 20V-60 min (0.3M NH_4F) and -413 mV vs. Ag/AgCl for 10-20V (0.3M NH_4F). Conversely, the potentiodynamic curves of the NT layers exhibit some differences, Fig. 2c. The passive current density for the anodic layers grown at 20V-60 min (HF), 20V-60 min (0.3M NH_4F) and 10-20V (0.3M NH_4F) is ~1.13E-7,

~2.76E-7 and ~3.95E-7 A/cm^2, respectively. In all cases, the passive current density is less than one order of magnitude lower than the untreated Ti6Al4V.

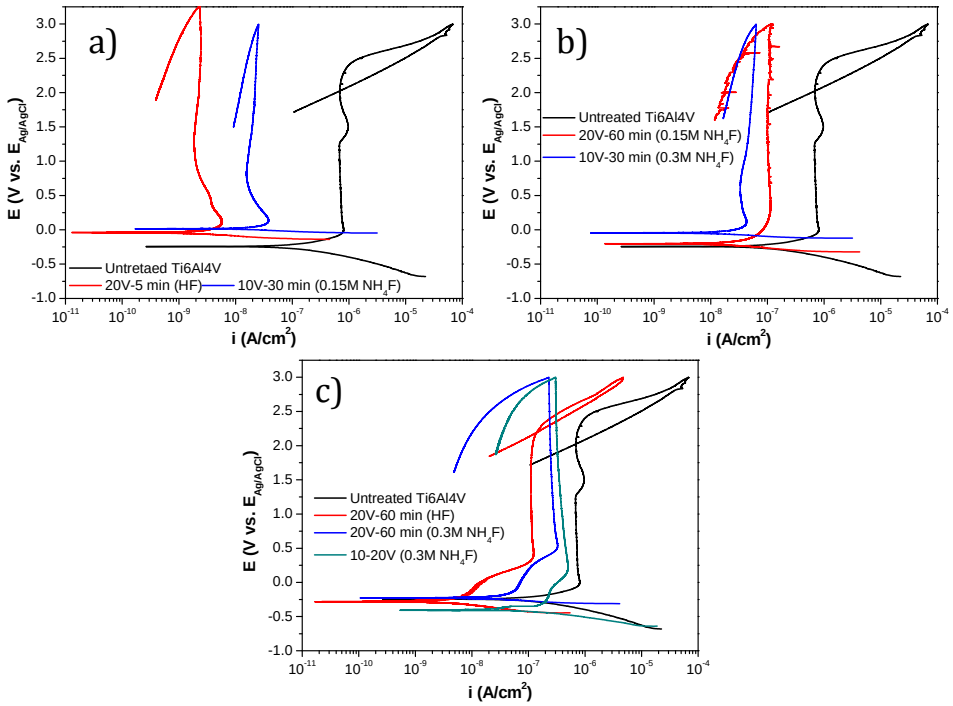

Figure 2. Potentiodynamic curves of the anodic oxide grown with different morphologies: NP (a), DU (b) and NT (c).

Furthermore, all the NT layers -20V-60 min (HF), 20V-60min (0.3M NH_4F) and 10-20V (0.3M NH_4F)- showed in the anodic branch an active-passive transition stage above the corrosion potential of about 100 mV length. This transition stage was not observed for the anodic layers with NP or DU morphology. This response can be explained as a result of the growth and coarsening of the oxide layer onto the titanium alloy surface [7, 10, 36] placed at the bottom of the inter-spacing, in accordance with the following reaction:

$$Ti + H_2O \leftrightarrow TiO_2 + 2H^+ + 4e^- \quad (1)$$

Additionally, the nanotubular layer grown at 20V-60 min (HF), in addition to showing the i_{pass} and E_{corr} values closest to the untreated Ti6Al4V alloy, showed a breakdown potential at ~2.28V vs. Ag/AgCl followed by a current increase which is associated with the pitting development [11, 37, 38]. This value is similar to that described by the untreated Ti6Al4V alloy. This behaviour is not observed in layers with NP or DU morphology or even the NT layers grown in electrolytes containing NH_4F. It appears that just in the NT layers with specific morphological features, the electrolyte that penetrates through the inter-space promotes pitting. This response is observed just for the NT layer with an inter-tubular space of ~30 nm, the greatest of the evaluated layers.

Previous works in the literature did not consider the influence of the morphology of the anodic layers on the corrosion kinetics or the electrochemical response, rather they related the lower i_{pass} and the more active E_{corr} values with modifications of the active surface area due to structural inhomogeneities of the anodic films, resulting from oxygen evolution and changes in the electrical characteristics occurring during the anodizing process[7, 15, 39, 40].

3.2 Electrochemical Spectroscopy Impedance

In addition to the analysis of the anodic layers performed by means of potentiodynamic curves, which showed the influence of the morphology of the anodic layer on corrosion kinetics and chemical stability, the corrosion mechanism was also evaluated, at longer immersion times, by electrochemical impedance spectroscopy, EIS. Figures 3 to 6 showed the EIS spectra of the untreated Ti6Al4V alloy and the anodic layers with NP, DU and NT morphologies at different immersion times 0, 24, 168 and 672 hours.

The EIS spectra of the untreated Ti6Al4V alloy showed the typical behaviour of a metal covered by a thin oxide passive film with one time-constant for all immersion times (fig. 3). The response is characterized by a

phase angle of about ~85° indicating a nearly pure-capacitive behaviour related to the high stability of the native titanium oxide in the PBS electrolyte [41-43].

The anodic layers showed a more complex behaviour. The EIS spectra of the NP anodic layers (fig. 4), DU (fig. 5) and NT morphology grown at 20V-60 min (HF) (fig. 6a), revealed a similar response along the test (up to 672 h). Two time-constants are clearly observed, the first one at the frequency range of 10^5 to ~10^0 Hz is related to the response of the barrier layer at the bottom of the anodic structures, and the second time-constant described at ~10^0 to 10^{-2} Hz is associated with a diffusion process.

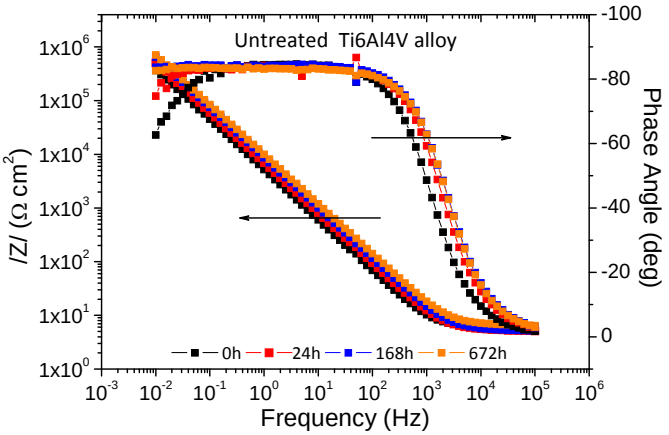

Figure 3. EIS-spectra of Ti6Al4V alloy without treatment.

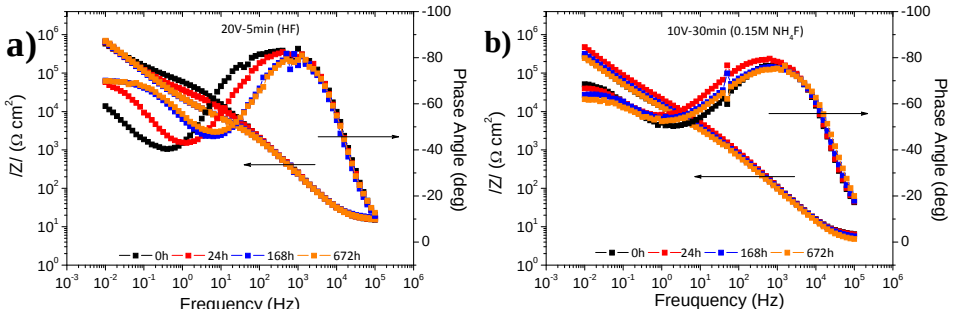

Figure 4. EIS-spectra of anodic layers with NP morphology grown in 1M H_2SO_4/0.15 wt.% HF (a) and 1M $NH_4H_2PO_4$+0.15M NH_4F (b).

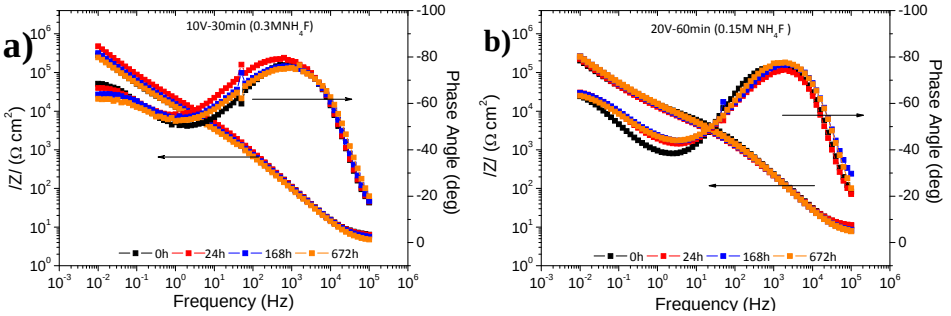

Figure 5. EIS-spectra of anodic layers with DU morphology grown in 1M $NH_4H_2PO_4$+0.3M NH_4F (a), and 1M $NH_4H_2PO_4$+0.15M NH_4F (b).

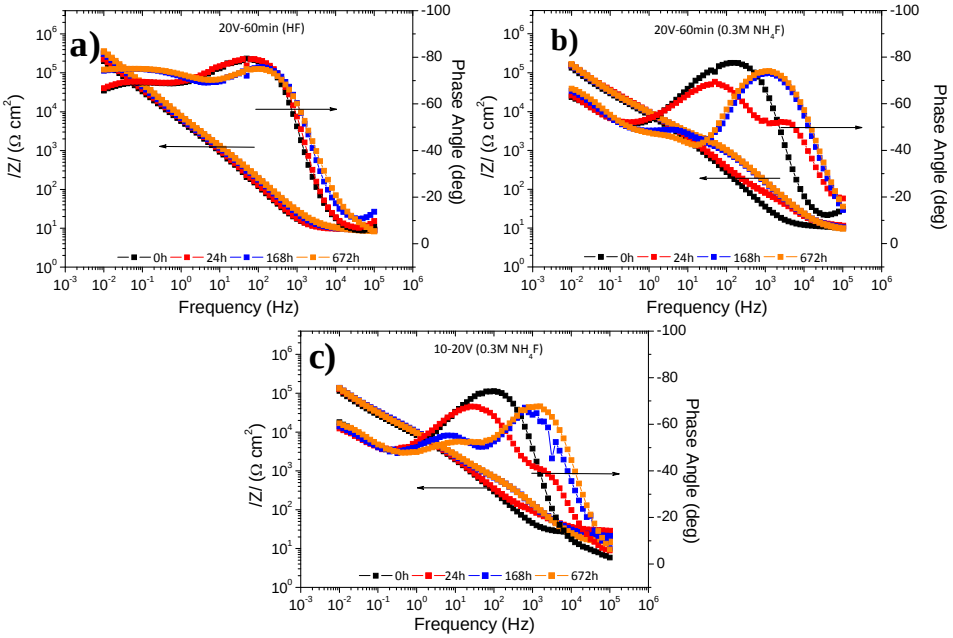

Figure 6. EIS-spectra of anodic layers with NT morphology grown in 1M H_2SO_4/0.15 wt.% HF (a) and 1M $NH_4H_2PO_4$+0.3M NH_4F at voltage constant (b) and with step voltage (c).

Although at 0h of immersion, the NT anodic layers grown at 20V-60min (0.3M NH_4F) and 10-20V (0.3M NH_4F) showed a similar response to the layers with NP and DU morphologies, after 24 h of immersion a new time-constant is clearly revealed at higher frequencies, 10^5-10^3 Hz, Fig. 6b and 6c. From 168h to the end of the test (672h), the EIS spectra practically

remain constant, showing three time-constants located at frequency ranges of 10^{5}-10^{2} Hz, 10^{2}- $5{\cdot}10^{-1}$ Hz and $5{\cdot}10^{-1}$-10^{-2} Hz.

For these NT layers, the impedance response recorded at short immersion times (<24h) is related to the response of the Ti6Al4V alloy placed at the bottom of the intertubular space. The two time-constants placed at medium and low frequencies correspond to the native oxide layer placed at the bottom of the inter-tubular space and a diffusion process, respectively. For longer immersion times to 24h, a third time-constant appears at high frequency range, corresponding to the response of the barrier layer, while those placed at medium and low frequencies are related to the response of the native oxide layer of the substrate, and to the diffusion process, respectively.

The meaning of the time constants observed in the EIS spectra of the anodic films grown on Ti6Al4V is still controversial. A common explanation of the two time constants recorded in most of the EIS spectra of anodic layers are classically associated with the response of the outer porous layer at high frequencies and the barrier layer at the bottom of the anodic structure at low-medium frequency. While the third time constant described at low frequencies is related to a diffusion process [7, 8, 12, 13, 41-44].

However, more recently some authors have shown some discrepancy with this interpretation that relates the time constant placed at high frequencies to the outer porous layer [6, 7, 14]. They consider the values corresponding to the high frequencies parameters to be in better agreement with the features of the barrier layer than the porous ones.

In the present work, various electrical equivalent circuits are proposed to explain the behaviour of the untreated Ti6Al4V alloy and the different anodic layers. Table 2 summarises the different equivalent circuits used.

For the untreated Ti6Al4V alloy, two equivalent circuits are proposed to explain the responses obtained at varying immersion times. From 0-24h,

the electrochemical impedance response was modelled by a Randles equivalent circuit, using a constant phase element to model the slight deviations from the ideal response. For longer immersion times, from 24 to 672h, the equivalent circuit comprises a resistor, Re -electrolyte resistance- in series with a CPE.

<table>
<tr><th></th><th colspan="2">time (h)</th></tr>
<tr><th>Morphology</th><th>0-24</th><th>> 24-672</th></tr>
<tr><td>Untreated Ti6Al4V alloy</td><td> 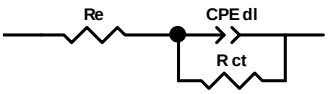
</td><td> 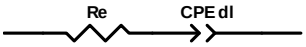
</td></tr>
<tr><th></th><th colspan="2">0-672</th></tr>
<tr><td>Nanoporous and Dual</td><td colspan="2"> 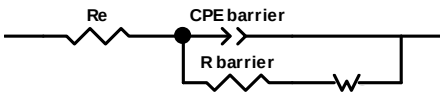
</td></tr>
<tr><th></th><th><24</th><th>≥ 24-672</th></tr>
<tr><td>Nanotubular</td><td> 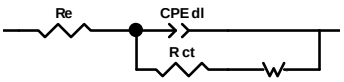
</td><td> 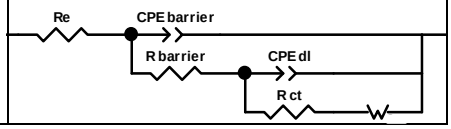
</td></tr>
</table>

Table 2. Equivalent circuits used to fit the impedance data.

It is important to remark that the use of CPE is frequently employed to fit impedance data arising from a broad range of experimental systems. Where the CPE impedance is expressed in terms of model parameters α and Q, as:

$$Z_{CPE} = {}^{1}/_{(j\omega)^{\alpha}Q} \quad (2)$$

where Z_{CPE} denotes the impedance of the CPE, *j* the imaginary unit, ω the angular frequency, Q the CPE-magnitude and α the CPE-power ($0 \leq \alpha \leq 1$).

The CPE in the untreated Ti6Al4V alloy was associated with the double layer of the substrate covered by a native oxide film -Q_{dl}- with values of 33.90 $\mu Ss^{\alpha}/cm^2$ for 0h and 18.14 $\mu Ss^{\alpha}/cm^2$ at 672h, while the charge transfer resistance -R_{ct}-, varies from 0.93 to 3.61 $M\Omega cm^2$ for 0h and 24h,

respectively. Table 3 shows the values of the electrical parameters obtained for the untreated Ti6Al4V alloy in the fittings using the described circuits for each immersion time.

Untreated Ti6Al4V alloy					
	Parameters\time (h)	0	24	168	672
	R_e (Ω cm²)	5.92	5.24	5.29	6.59
	CPE_{dl} (μSs$^{\alpha}$/cm²)	33.90	25.66	20.59	18.14
	α	0.94	0.94	0.94	0.93
	R_{ct} (MΩ cm²)	0.93	3.61	-	-
	Chi-sqr (10^{-3})	1.25	1.43	1.00	0.45
2-D distribution	**C_{eff} (μF/cm²)**	19.93	13.85	-	-
	$d_{2\text{-}D}$ (nm)	1.38	1.98	-	-
2-D distribution (Blocking electrode)	**C_{eff} (μF/cm²)**	-	-	11.11	8.89
	$d_{B\text{-}e}$ (nm)	-	-	2.47	3.09

Tabla 3. Calculated parameters of the equivalent circuits for the untreated Ti6Al4V alloy.

For the analysis of the EIS-spectra of the anodic layers, Orazem et al. [45] proposed the use of some graphic representation to extract the experimental values of the CPE parameters (Q and α) recorded at high frequencies after short immersion times, 0h. From the logarithmic plot of the absolute value of the imaginary part of the impedance versus frequency, the CPE exponent -α- can be estimated from the slope at high frequency range. Figure 7a shows the α values estimated for the specimens NP 10V-30 min (0.15M NH_4F) -0.95-; DU, 20V-60 min (0.15M NH_4F), -0.90-; and NT 20V-60 min (0.3M NH_4F), -0.91-.

Subsequently, the CPE magnitude -Q- is obtained from the following equation:

$$Q = \sin\left(\frac{\alpha\pi}{2}\right)\frac{-1}{Z_j(2\pi f)^{\alpha}} \quad (3)$$

The logarithmic plot of Q versus frequency for each estimated α value, fig 7b, allows the estimation of the Q parameter from the plateau described at high-frequency. The Q values obtained for the NP, DU and NT specimens are 1.70, 1.98 and 10.6 μSsᵅ/cm², respectively.

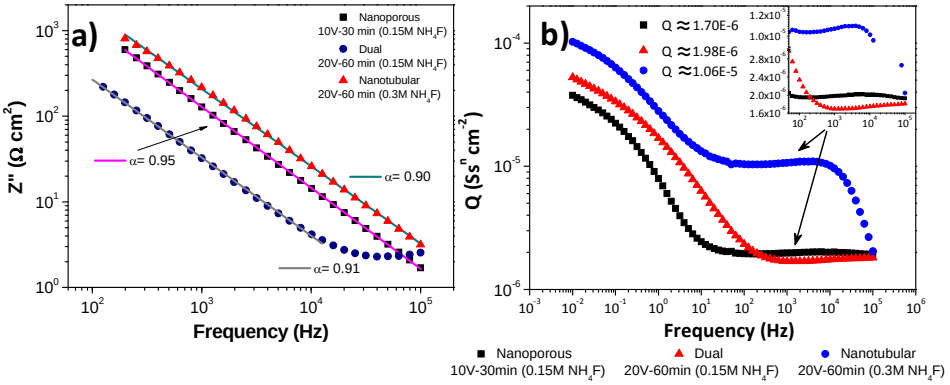

Figure 7. Determination of CPE parameters of the anodic layers with different morphologies by graphical methods, α determination (a) and Q determination (b), at 0 h of immersion.

These experimental values were then used for the first fitting of the experimental data of the spectra using the Zview software.

To simulate the two time-constant responses observed in the impedance spectra of the NP and DU morphology, a CPE in parallel with a resistance (R) were used. Both components were associated with the response of the barrier layer, which is connected in series with a diffusive component (W) associated with the diffusion process in the layer.

The values corresponding to the $CPE_{barrier}$ of the NP layer 20V-5 min (HF) and 10V-30 min (0.15M NH_4F) were 1.09 and 2.61 μSsᵅ/cm². The $R_{barrier}$ values for 20V-5 min (HF) are in the range of 37.5 kΩcm² at 0 h and 5.35 kΩcm² after 672h, while for the specimen 10V-30 min (0.15M NH_4F) the values were 21.18 kΩcm² at 0h and 1.81 kΩcm² at 672h, Table 4.

NANOPOROUS MORPHOLOGY									
		20V-5 min (HF)				10V-30 min (0.15M NH_4F)			
time(h)/ Parameters		0	24	168	672	0	24	168	672
R_e (Ω cm²)		14.78	15.52	16.90	15.50	6.12	6.09	5.11	4.20
$CPE_{barrier}$ (μSs$^{\alpha}$/cm²)		1.13	1.09	1.12	1.14	1.88	2.08	2.49	2.61
α		0.94	0.94	0.94	0.94	0.95	0.94	0.93	0.93
$R_{barrier}$ (kΩ cm²)		37.80	14.53	6.04	5.35	21.18	4.15	2.13	1.81
W	CPE_w (μSs$^{\alpha}$/cm²)	9.82	14.54	16.29	15.07	18.04	21.88	28.20	29.45
	α	0.46	0.48	0.64	0.64	0.50	0.55	0.55	0.53
	C_w (μF/cm²)	57.50	35.14	44.69	42.80	71.20	80.17	130.35	160.90
Chi-sqr (10^{-3})		0.76	1.00	1.48	1.17	0.21	0.70	0.59	0.44
2-D distribution	C_{eff} μF/cm²	0.56	0.57	0.58	0.58	1.05	1.07	1.08	1.14
	$d_{2\text{-}D}$, nm	49.28	48.13	47.07	47.39	26.10	25.62	25.33	24.03
3-D distribution	C_{eff} μF/cm²	0.94	0.85	1.26	1.27	1.60	1.57	1.69	1.77
	$d_{3\text{-}D}$, nm	31.62	34.27	23.20	22.93	18.29	18.58	17.28	16.49

Tabla 4. Parameter values of the equivalent circuits for the anodic layers with NP morphology.

The anodic layers with DU morphology, 20V-60 min and 10-30 min, showed values in the same order of magnitude of the NP layers, with $CPE_{barrier}$ values about 2.19 to 4.76 μSs$^{\alpha}$/cm² respectively but, with a constant value of $R_{barrier}$ a ~2.88 kΩcm² for the layer grown at 20V-60 min (HF). Conversely, for the layer grown at 10V-30 min (0.15M NH_4F) the $R_{barrier}$ decreased from 7.95 to 3.43 kΩcm² from 0 to 672 hours of immersion, Table 5.

Finally, the NT anodic layers grown at 20V-60 min (0.3MNH_4F) and 10-20V (0.3M NH_4F) showed two different responses depending on the immersion time. At short immersion times, the spectrum is similar to NP and DU layers and therefore, it can be simulated with the same equivalent circuit. However, the meaning of each element of the equivalent circuit is different. On the other hand, at longer immersion times, to simulate the third time-

constant a CPE and R in parallel must be added to the equivalent circuit previously used to simulate the NP and DU layers.

DUAL MORPHOLOGY									
		20V-60 min (0.15M NH_4F)				10V-30 min (0.3M NH_4F)			
time (h)/ Parameters		0	24	168	672	0	24	168	672
R_e (Ω cm^2)		8.66	9.24	6.75	8.66	6.52	5.81	5.05	4.15
$CPE_{barrier}$ ($\mu Ss^{\alpha}/cm^2$)		2.61	2.70	2.19	2.61	2.71	3.25	4.27	4.76
α		0.87	0.87	0.89	0.87	0.92	0.91	0.88	0.88
$R_{barrier}$ (kΩ cm^2)		3.05	2.64	2.81	3.05	7.95	7.44	4.45	3.43
W	CPE_w ($\mu Ss^{\alpha}/cm^2$)	42.44	40.62	33.22	26.65	23.46	15.47	21.08	24.96
	α	0.44	0.49	0.50	0.51	0.53	0.55	0.56	0.55
	C_w ($\mu F/cm^2$)	253.86	177.59	134.82	104.42	70.76	59.48	103.32	152.23
Chi-sqr (10^{-3})		0.83	0.66	0.82	0.41	0.59	0.51	0.66	0.65
2-D distribution	C_{eff} $\mu F/cm^2$	0.50	0.56	0.55	0.56	1.10	1.07	1.04	1.07
	$d_{2\text{-}D}$, nm	55.20	49.43	50.33	48.61	24.84	25.60	26.48	25.67
3-D distribution	C_{eff} $\mu F/cm^2$	1.24	1.29	1.16	1.09	1.98	2.22	2.53	2.70
	$d_{3\text{-}D}$, nm	23.66	22.63	25.17	26.83	14.76	13.13	11.54	10.82

Tabla 5. Values of the equivalent circuits parameters for the anodic layers with DU morphology.

Conversely, the NT layers grown at 20V-60 min (HF) did not show this third time-constant and the response is simulated by the same equivalent circuit as the NP and DU layers.

The NT layer fabricated at 20V-60 min (HF) presents values of CPE around to ~18.9 $\mu Ss^{\alpha}/cm^2$ throughout the whole test, Table 6. These values of the CPE are higher than those exhibited by the nanoporous or duplex layers, $CPE_{barrier}$, but ranged on the same order of magnitude as the untreated sample CPE_{dl}. The time constant, therefore, appears related to the response of the exposed substrate, placed at the bottom of the intertubular space, which is covered by a native oxide, thus corresponding to CPE_{dl}, R_{ct}.

NANOTUBULAR MORPHOLOGY													
		20V-60 min (HF)				20V-60 min (0.3M NH_4F)				10-20V (0.3M NH_4F)			
time (h)/ Parameters		0	24	168	672	0	24	168	672	0	24	168	672
R_e (Ω cm^2)		9.61	9.36	9.13	8.86	10.58	10.88	9.82	8.48	24.71	27.91	20.31	14.64
$CPE_{barrier}$ $\mu Ss^{\alpha}/cm^2$		-	-	-	-	-	2.77	2.57	2.63	-	5.64	3.97	2.41
α		-	-	-	-	-	0.9	0.90	0.89	-	0.85	0.86	0.91
$R_{barrier}$ (kΩ cm^2)		-	-	-	-	-	0.99	1.89	1.57	-	0.15	1.32	0.80
CPE_{dl} $\mu Ss^{\alpha}/cm^2$		20.97	18.64	17.12	18.87	9.71	5.14	11.83	12.72	9.30	6.77	9.59	22.03
α		0.93	0.93	0.90	0.87	0.92	0.96	0.85	0.81	0.92	0.87	0.85	0.65
R_{ct} (kΩ cm^2)		4.94	5.84	3.59	6.37	3.77	3.38	8.45	11.04	3.60	8.14	9.49	23.16
W	CPE_w $\mu Ss^{\alpha}/cm$	24.18	20.95	15.50	9.66	44.64	35.67	39.10	27.03	47.95	37.66	36.97	29.11
	α	0.68	0.69	0.78	0.79	0.50	0.48	0.54	0.6	0.46	0.49	0.51	0.59
	C_w $\mu F/cm^2$	-	-	-	-	240.41	186.45	180.15	120.32	282.82	313.93	292.50	153.52
Chi-sqr (10^{-3})		1.52	1.87	2.99	1.04	2.84	0.46	0.08	0.1	0.88	0.08	0.91	0.05
2-D distribution	C_{eff} $\mu F/cm^2$	11.17	10.01	6.35	5.13	4.30	0.86	0.76	0.72	4.29	1.10	0.88	0.89
	$d_{2\text{-}D}$ nm	2.46	2.74	4.33	5.35	6.38	31.94	36.21	38.39	6.40	25	31.34	30.99
3-D distribution	C_{eff} $\mu F/cm^2$	17.73	15.89	12.49	13.74	7.24	3.31	1.39	1.50	6.80	1.54	1.71	1.31
	$d_{3\text{-}D}$ nm	1.65	1.84	2.34	2.13	4.03	8.29	21	18.27	4.30	18.91	17.05	22.30

Table 6. Values of the equivalent circuits parameters for the anodic layers with NT morphology.

Similarly, at short immersion times (<24h), the other two nanotubular layers grown in 0.3M NH_4F show a time constant described at high-medium frequencies which is associated with the exposed substrate via the intertubular spacing. Thus, the CPE_{dl} of the nanotubular anodic layers grown at 20V-60 min (0.3M NH_4F) and 10-20V (0.3M NH_4F), is ~9.5 $\mu Ss^{\alpha}/cm^2$. After 24 hours immersion, the CPE_{dl} decreases to 5.14 and 6.77

$\mu Ss^{\alpha}/cm^2$ and then increases again to 12.72 and 22.03 $\mu Ss^{\alpha}/cm^2$ at 672h, respectively. The CPE related to the time constant described at high frequencies remains steady from 24h to 672h: ~2.65 $\mu Ss^{\alpha}/cm^2$ for 20V-60 min (0.3M NH_4F); and ~4 $\mu Ss^{\alpha}/cm^2$ for 10-20V (0.3M NH_4F), Table 6. These values are similar to those found for the $CPE_{barrier}$ of the nanoporous and dual layers, Table 4 and 5. Moreover, the corresponding $R_{barrier}$ values of these anodic layers are ~1 $k\Omega cm^2$ in both growth conditions, which are similar to that reported in the literature for the nanotubular layers grown in HF-containing electrolytes on the Ti13Nb13Zr alloy [16].

The results suggest that in the NT layers, the intertubular space determines the response and evolution of the system with immersion time. For intertubular spaces lower than 20 nm, a third time constant related to the barrier layer is resolved at higher frequencies, while for the NT layers with a greater intertubular space, the impedance response is mainly due to the substrate placed at the bottom of these intertubular spaces.

In the former case, the thickening of the native oxide occurred during the immersion in the PBS solution and allows distinguishing both the native oxide layer of the exposed substrate through the intertubular spacing as well as the barrier layer at medium and high frequency range, respectively.

It is noteworthy that in all simulated spectra for NP, DU and NT, the α of the CPE used to simulate the time constant at low frequencies, is about 0.5, confirming that this time constant is related to diffusive processes.

3.2.1 Determination of Capacitance from CPE

The analysis of the electrical elements of each equivalent circuit is very important to extract the information from the physical system analyzed. However, obtaining the relevant information is not always easy and must be done carefully, when an accurate characterization of the system is required, such as in anodic oxide layers.

The determination of the capacitance from the CPE values obtained from simulations is vital, because from the C it is possible to estimate the value of the thickness, d, of a layer according to:

$$d = {\varepsilon\varepsilon_0}/{C} \quad (7)$$

where ε is the dielectric constant and ε_0 is the vacuum permittivity 8.85E-14 F/cm.

In the present work, the ε is the dielectric constant of the TiO_2 amorphous and a value of 33 [46] was used to estimate the thickness of the barrier layer of the different anodic layers, and was compared with the thickness reported for the barrier layers measured by TEM in previous works [28-30].

Recently, however, more literature has shown that the capacitance might be more difficult to obtain when there is a surface or axial distribution of the capacitances as result of the presence of heterogeneities such as grain boundaries or other variations [6, 21, 23-25, 27]. In this case, literature defines the concept of effective capacitance, C_{eff}, to refer the resulting capacitance of a surface, having either a surface distribution -2D- or an axial/ normal distribution - 3D - of time-constants [27].

The estimations of such C_{eff} depend on the time-constant distribution. For a 2-D distribution, the effective capacitance has a more complex expression dependent on the electrolyte and polarization resistances [6, 27] by the following expression:

$$C_{eff} = Q^{1/\alpha}\left(\frac{1}{R_e} + \frac{1}{R_t}\right)^{(\alpha-1)/\alpha} \quad (4)$$

where CPE is defined according to equation (2), Q is the magnitude of the CPE, α is exponent of the CPE, R_e is the electrolyte resistance, and R_t is the charge-transfer resistance. This expression is equivalent to that defined by Brug et al. [47] for a surface distribution with a different definition of the Z_{CPE} parameters, $Z_{CPE} = Q/(jw)^{1-\alpha}$.

In the case that R_t becomes infinitely large (blocking electrode), the eq. 4 can be expressed as [27]:

$$C_{eff} = Q^{1/\alpha} * R_e^{(1-\alpha)/\alpha} \quad (5)$$

Conversely for a 3-D distribution, thus an axial distribution through the surface layer, the effective capacitance associated with CPE can be expressed as [27]:

$$C_{eff} = Q^{1/\alpha} * R_f^{(1-\alpha)/\alpha} \quad (6)$$

where R_f is the film resistance. This equation is equivalent to that proposed by Hsu and Mansfeld [48] in terms of w_{max}, eq. 7:

$$C_{eff} = Q w_{max}^{(\alpha-1)} \quad (7)$$

Therefore, the C_{eff} obtained from the CPE values corresponding to the high frequency time constant applying the different expressions for 2-D or 3-D distribution are shown in Tables 3 to 6.

For the untreated alloy, Table 3, the C_{eff} was only calculated assuming a 2-D distribution using (eq. 4 and eq.5), depending on the immersion times, since at longer immersion times than 24h, the untreated Ti6Al4V alloy shows a capacitive behaviour; thus, a blocking electrode. The C_{eff}, values are about 19.93 μF/cm² at 0h which decreases to 8 μF/cm² at 672h. These values are typical for an electrochemical double layer of a metal. The thickness of the native TiO_2 layer grown on the untreated Ti6Al4V alloy, varies from 1.38 nm at 0h to 3.09 nm at 672h, which is in agreement with the values reported in literature for the native oxide [49-51].

Assuming a 2-D distribution, during the entire immersion time, the average thicknesses estimated for the nanoporous layers, are ~48 nm for the layer fabricated at 20V-5min (HF) and ~25 nm for the layer grown at 10V-30 min (0.15M NH_4F). Conversely, assuming a 3-D distribution, these specimens exhibit smaller average thicknesses on the order of ~28 and ~18 nm, respectively, Table 4.

The thickness of the layer grown at 20V-5 min (HF) calculated with a 2-D distribution is closer to the value measured by TEM (40 nm) [30], suggesting that the surface distribution is more suitable for nanoporous morphology.

Similarly, the anodic layer with dual morphology shows that the thickness of the barrier layer calculated, from the C_{eff}, is greater when the expression for 2-D distribution is used, Table 5. The anodic layer grown at 10V-30 min (0.3M NH_4F) has an average barrier layer thickness ~25 nm and ~12 nm assuming 2-D or 3-D distributions, respectively. Similarly, the anodic film grown at 20V-60 min (0.3M NH_4F) shows a thickness of about ~51 nm for a 2-D distribution, while the thickness is about ~25 nm when the expression for 3-D distribution is used. As in the NP morphology, 2D distribution supplies a more accurate value for the barrier layers of DU morphology specimens, since the average thickness estimated is in agreement with the values measured by TEM, ~45 nm.

Finally, the NT layer fabricated at 20V-60 min (HF) showed similar thickness values to those calculated for the untreated Ti6Al4V alloy, using either the 2-D or 3-D expressions. The average thickness values vary from ~2.46 nm at 0h to ~5.35 nm at 672h for 2-D distribution, while for a 3-D distribution they vary from ~1.65 nm at 24h to ~2.13nm at 672h.

For the other two NT layers grown at 20V-60 min (0.3M NH_4F) and 10-20V (0.3M NH_4F) the thicknesses increase with time. For the anodic layer grown at 20V-60 min (0.3M NH_4F), assuming 2-D distribution, the thickness varies from 6.38 nm at 0h, 31.94 nm at 24 h, to 38.39 nm at 672h, while a 3-D distribution exhibits the same increasing trend but at lower values, from 4.03 nm at 0h to 18.27 nm at 672h. This evolution confirms that only the time constant clearly defined at higher frequencies, times <168h, can be related to the barrier layer.

Both distributions lead to lower values than those measured by TEM for this growth condition, ~42 nm.

The NT layer grown at 10-20V (0.3M NH_4F) shows a thickness of 30.99 nm for 672h using a 2-D distribution; in this case, the thickness calculated by impedance, showed the greatest difference, when compared with the measured thickness by TEM [28], ~39 nm.

This difference between calculated and measured thicknesses for the anodic layers grown at 10-20V (0.3M NH_4F), can be attributed to the morphological characteristics of these anodic layers compared with the nanotubular layers grown at a constant voltage, 20V-60 min (0.3M NH_4F).The anodic layers grown at step voltage show a variation of intertubular space of ~21 nm in the mouth of nanotubes to ~15 nm near to bottom of these; this difference is inherent to the growth mechanism for these layers, affecting the response obtained by impedance.

These results suggest that either the native oxide layers, or the nanostructured anodic layers grown with different morphologies (NP, DU, NT), shows a surface distribution of the capacitances, and, therefore, the correct estimation of the thickness of the anodic barrier layers must be done by using the 2-D distribution. The 3-D distribution underestimates the thickness of the barrier layers of the nanostructured anodic layers grown on Ti6Al4V with different morphologies. These findings are in agreement with some results recently published by the authors in other Ti alloys [16].

4. Conclusions

The electrochemical properties of anodic layers grown on Ti6Al4V are intrinsically related to the final morphology of the anodized layer.

The polarization curves show that the anodic layers grown under different conditions, but leading to the same morphology, present similar values of i_{pass}. NP layers present the lowest ipass values. Conversely, NT layers reveal i_{pass} values on the same order of magnitude as the untreated Ti6Al4V alloy.

The impedance response corresponding to the anodic layers with NP and DU morphologies is due to the barrier layer.

Conversely, for the NT anodic layers, the impedance response shows an evolution of the diagrams, depending on the intertubular space.

For NT layer with intertubular spacing of about 30 nm, the response is controlled by the substrate, which is placed at the bottom of these spacings. On the other hand, for the NT layers having less than 30 nm, the electrochemical response evolves with the immersion time. For short immersion times, the response is due to the native oxide covering the substrate at the bottom of the intertubular spaces, while after 24h of immersion, the response shows two contributions due to the substrate (medium frequency) and the barrier layer of the nanotubes (high frequency).

Finally the electrochemical analysis of the impedance parameters indicates that either the native oxide or the anodic layers show a surface distribution of the capacitances. The thickness of the barrier layer from the C_{eff}, estimated assuming 2D-distribution, is consistent with the values measured by TEM.

Acknowledgements

This work was supported by Spanish Ministry of Science and Innovation under the Consolider-Ingenio 2010-CSD-2008-0023-FUNCOAT Project and under the MAT2013-48224-C2-1-R-MUNSUTI Project. Hernández-López J.M. is receptor of the JAE-predoc grant funded by the CSIC

References

[1] P. Roy, S. Berger, P. Schmuki, TiO_2 nanotubes: synthesis and applications, Angewandte Chemie, 50 (2011) 2904-2939.
[2] D. Kowalski, D. Kim, P. Schmuki, TiO_2 nanotubes, nanochannels and mesosponge: Self-organized formation and applications, Nano Today, 8 (2013) 235-264.
[3] C. A.Grimes, G. K.Mor, TiO_2 Nanotube Arrays: Synthesis, Properties, and Applications, in, Springer, 2009, pp. 358.
[4] H. Omidvar, S. Goodarzi, A. Seif, A.R. Azadmehr, Influence of anodization parameters on the morphology of TiO_2 nanotube arrays, Superlattices and Microstructures, 50 (2011) 26-39.
[5] K.M. Deen, A. Farooq, M.A. Raza, W. Haider, Effect of electrolyte composition on TiO_2 nanotubular structure formation and its electrochemical evaluation, Electrochimica Acta, 117 (2014) 329-335.
[6] L. Hamadou, L. Aïnouche, A. Kadri, S.A.A. Yahia, N. Benbrahim, Electrochemical impedance spectroscopy study of thermally grown oxides exhibiting constant phase element behaviour, Electrochimica Acta, 113 (2013) 99-108.
[7] S.A. Ali Yahia, L. Hamadou, A. Kadri, N. Benbrahim, E.M.M. Sutter, Effect of Anodizing Potential on the Formation and EIS Characteristics of TiO_2 Nanotube Arrays, Journal of The Electrochemical Society, 159 (2012) K83-K92.
[8] M.E.P. Souza, M. Ballester, C.M.A. Freire, EIS characterisation of Ti anodic oxide porous films formed using modulated potential, Surface and Coatings Technology, 201 (2007) 7775-7780.
[9] F. El-Taib Heakal, A.A. Ghoneim, A.S. Mogoda, K. Awad, Electrochemical behaviour of Ti–6Al–4V alloy and Ti in azide and halide solutions, Corrosion Science, 53 (2011) 2728-2737.
[10] Z. Cai, T. Shafer, I. Watanabe, M.E. Nunn, T. Okabe, Electrochemical characterization of cast titanium alloys, Biomaterials, 24 (2003) 213-218.
[11] I. Gurappa, Characterization of different materials for corrosion resistance under simulated body fluid conditions, Materials Characterization, 49 (2002) 73-79.
[12] M. Aziz-Kerrzo, K.G. Conroy, A.M. Fenelon, S.T. Farrell, C.B. Breslin, Electrochemical studies on the stability and corrosion resistance of titanium-based implant materials, Biomaterials, 22 (2001) 1531-1539.
[13] J.E.G. González, J.C. Mirza-Rosca, Study of the corrosion behavior of titanium and some of its alloys for biomedical and dental implant applications, Journal of Electroanalytical Chemistry, 471 (1999) 109-115.
[14] L. Aïnouche, L. Hamadou, A. Kadri, N. Benbrahim, D. Bradai, Interfacial Barrier Layer Properties of Three Generations of TiO_2 Nanotube Arrays, Electrochimica Acta, 133 (2014) 597-609.

[15] W.-q. Yu, J. Qiu, L. Xu, F.-q. Zhang, Corrosion behaviors of TiO_2 nanotube layers on titanium in Hank's solution, Biomedical Materials, 4 (2009) 065012.
[16] J.M. Hernández-López, A. Conde, J. de Damborenea, M.A. Arenas, Correlation of the nanostructure of the anodic layers fabricated on Ti13Nb13Zr with the electrochemical impedance response, Corrosion Science, 94 (2015) 61-69.
[17] V.S. Saji, H.C. Choe, W.A. Brantley, An electrochemical study on self-ordered nanoporous and nanotubular oxide on Ti–35Nb–5Ta–7Zr alloy for biomedical applications, Acta Biomaterialia, 5 (2009) 2303-2310.
[18] D.D.N. Singh, Passivation Behavior of Ti6Al4V Alloy in Phosphoric Acid Solution, Journal of The Electrochemical Society, 132 (1985) 378-381.
[19] V.B. Singh, S.M.A. Hosseini, Corrosion behaviour of Ti-6Al-4V in phosphoric acid, J Appl Electrochem, 24 (1994) 250-255.
[20] L.T. Duarte, S.R. Biaggio, R.C. Rocha-Filho, N. Bocchi, Surface characterization of oxides grown on the Ti–13Nb–13Zr alloy and their corrosion protection, Corrosion Science, 72 (2013) 35-40.
[21] P. Córdoba-Torres, T.J. Mesquita, R.P. Nogueira, Influence of geometry-induced current and potential distributions on the characterization of constant-phase element behavior, Electrochimica Acta, 87 (2013) 676-685.
[22] M.E. Orazem, B. Tribollet, in: Electrochemical Impedance Spectroscopy, John Wiley & Sons, Inc., 2008.
[23] B. Hirschorn, M.E. Orazem, B. Tribollet, V. Vivier, I. Frateur, M. Musiani, Constant-Phase-Element Behavior Caused by Resistivity Distributions in Films: II. Applications, Journal of The Electrochemical Society, 157 (2010) C458-C463.
[24] B. Hirschorn, M.E. Orazem, B. Tribollet, V. Vivier, I. Frateur, M. Musiani, Constant-Phase-Element Behavior Caused by Resistivity Distributions in Films: I. Theory, Journal of The Electrochemical Society, 157 (2010) C452-C457.
[25] J.-B. Jorcin, M.E. Orazem, N. Pébère, B. Tribollet, CPE analysis by local electrochemical impedance spectroscopy, Electrochimica Acta, 51 (2006) 1473-1479.
[26] I. Frateur, Characterization of oxide films by electrochemical impedance, ECS Transactions, 13 (2008) 115-128.
[27] B. Hirschorn, M.E. Orazem, B. Tribollet, V. Vivier, I. Frateur, M. Musiani, Determination of effective capacitance and film thickness from constant-phase-element parameters, Electrochimica Acta, 55 (2010) 6218-6227.
[28] J.M. Hernandez-Lopez, A. Conde, J.J. de Damborenea, M.A. Arenas, TiO_2 nanotubes with tunable morphologies, RSC Advances, 4 (2014) 62576-62585.

[29] E. Matykina, A. Conde, J. de Damborenea, D.M.y. Marero, M.A. Arenas, Growth of TiO_2-based nanotubes on Ti–6Al–4V alloy, Electrochimica Acta, 56 (2011) 9209-9218.
[30] E. Matykina, J.M. Hernandez-López, A. Conde, C. Domingo, J.J. de Damborenea, M.A. Arenas, Morphologies of nanostructured TiO_2 doped with F on Ti–6Al–4V alloy, Electrochimica Acta, 56 (2011) 2221-2229.
[31] X. Zhou, N.T. Nguyen, S. Özkan, P. Schmuki, Anodic TiO2 nanotube layers: Why does self-organized growth occur—A mini review, Electrochemistry Communications, 46 (2014) 157-162.
[32] K. Indira, S. Ningshen, U.K. Mudali, N. Rajendran, Effect of anodization parameters on the structural morphology of titanium in fluoride containing electrolytes, Materials Characterization, 71 (2012) 58-65.
[33] E.X. Sun, W.B. Nowak, Electrochemical characteristics of Ti–6Al–4V alloy in 0.2 N NaCl solution: I. Tafel slopes in quasi-passive state, Corrosion Science, 43 (2001) 1801-1816.
[34] X.L. Zhang, Z.H. Jiang, Z.P. Yao, Y. Song, Z.D. Wu, Effects of scan rate on the potentiodynamic polarization curve obtained to determine the Tafel slopes and corrosion current density, Corrosion Science, 51 (2009) 581-587.
[35] R.J. Solar, S.R. Pollack, E. Korostoff, In vitro corrosion testing of titanium surgical implant alloys: An approach to understanding titanium release from implants, Journal of Biomedical Materials Research, 13 (1979) 217-250.
[36] T.C. Niemeyer, C.R. Grandini, L.M.C. Pinto, A.C.D. Angelo, S.G. Schneider, Corrosion behavior of Ti–13Nb–13Zr alloy used as a biomaterial, Journal of Alloys and Compounds, 476 (2009) 172-175.
[37] A. Choubey, B. Basu, R. Balasubramaniam, Electrochemical behavior of Ti-based alloys in simulated human body fluid environment, Trends in Biomaterials & Artificial Organs, 18 (2005) 64-72.
[38] R. Singh, S.G. Chowdhury, S.K. Tiwari, N.B. Dahotre, Laser surface processing of Ti6Al4V in gaseous nitrogen: corrosion performance in physiological solution, Journal of Materials Science: Materials in Medicine, 19 (2007) 1363-1369.
[39] L. Mohan, C. Anandan, N. Rajendran, Electrochemical behaviour and bioactivity of self-organized TiO2 nanotube arrays on Ti-6Al-4V in Hanks' solution for biomedical applications, Electrochimica Acta, 155 (2015) 411-420.
[40] L. Mohan, C. Anandan, N. Rajendran, Electrochemical behavior and effect of heat treatment on morphology, crystalline structure of self-organized TiO2 nanotube arrays on Ti–6Al–7Nb for biomedical applications, Materials Science and Engineering: C, 50 (2015) 394-401.

[41] C. Jaeggi, P. Kern, J. Michler, J. Patscheider, J. Tharian, F. Munnik, Film formation and characterization of anodic oxides on titanium for biomedical applications, Surface and Interface Analysis, 38 (2006) 182-185.
[42] J. Pan, D. Thierry, C. Leygraf, Electrochemical impedance spectroscopy study of the passive oxide film on titanium for implant application, Electrochimica Acta, 41 (1996) 1143-1153.
[43] D.J. Blackwood, Influence of the space-charge region on electrochemical impedance measurements on passive oxide films on titanium, Electrochimica Acta, 46 (2000) 563-569.
[44] A.G. Muñoz, Q. Chen, P. Schmuki, Interfacial properties of self-organized TiO2 nanotubes studied by impedance spectroscopy, J Solid State Electrochem, 11 (2007) 1077-1084.
[45] M.E. Orazem, N. Pébère, B. Tribollet, Enhanced Graphical Representation of Electrochemical Impedance Data, Journal of The Electrochemical Society, 153 (2006) B129-B136.
[46] T. Busani, R.A.B. Devine, Dielectric and infrared properties of TiO_2 films containing anatase and rutile, Semiconductor Science and Technology, 20 (2005) 870.
[47] G. Brug, A. Van den Eeden, M. Rehbach, J. Sluyters, J Electroanal Chem 176: 275., S0022-0728 (84), (1984) 80324-80321.
[48] C. Hsu, F. Mansfeld, Technical note: concerning the conversion of the constant phase element parameter Y_0 into a capacitance, Corrosion, 57 (2001) 747-748.
[49] C.E.B. Marino, E.M.d. Oliveira, R.C. Rocha-Filho, S.R. Biaggio, On the stability of thin-anodic-oxide films of titanium in acid phosphoric media, Corrosion Science, 43 (2001) 1465-1476.
[50] E. Gemelli, N.H.A. Camargo, Oxidation kinetics of commercially pure titanium, Matéria (Rio de Janeiro), 12 (2007) 525-531.
[51] A.G. Mantzila, M.I. Prodromidis, Development and study of anodic Ti/TiO_2 electrodes and their potential use as impedimetric immunosensors, Electrochimica Acta, 51 (2006) 3537-3542.

3.4 CARACTERIZACIÓN BIOLÓGICA:

a) Doped TiO_2 anodic layers of enhanced antibacterial properties.

b) Influence of the nanostructure of F-doped TiO2 films on osteoblast growth and function.

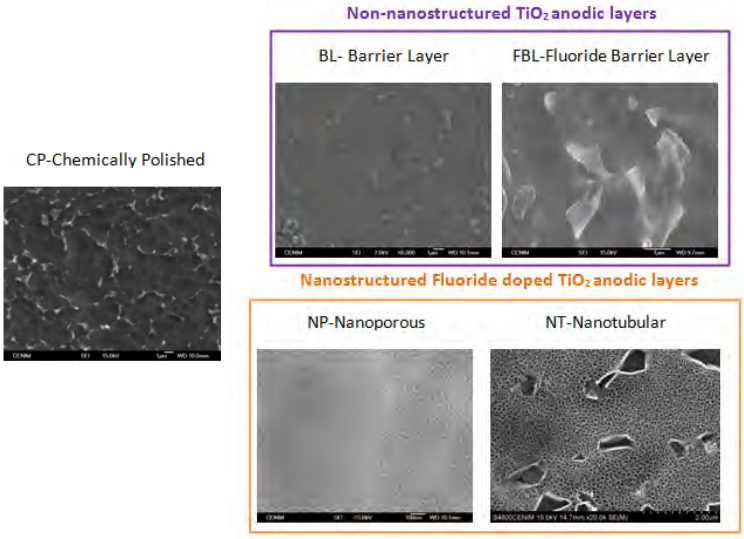

***S. aureus* clinical strains**

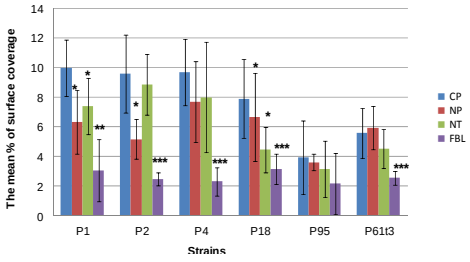

***p<0.0001 statistically significant diferences when comparing FBL with all the specimens

*P <0.0001 statistically significant diferences comparing FBL with CP sample

Células osteoblásticas de ratón, **MCT313-E1**

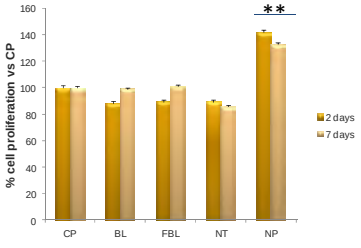

*p<0.01 statistically significant differences versus CP

**p<0.0001 statistically significant differences versus CP

CARACTERIZACIÓN BIOLÓGICA:

a) Doped TiO_2 anodic layers of enhanced antibacterial properties.
b) Influence of the nanostructure of F-doped TiO_2 films on osteoblast growth and function.

El remplazo de articulaciones mediante el uso de biomateriales como la aleación de Ti6Al4V constituye un gran avance en la cirugía ortopédica. Sin embargo, la lucha entre células y bacterias, que compiten por la colonización superficial de las prótesis durante su implantación, puede provocar problemas de infecciones difíciles de tratar, si son las bacterias las que logran llegar en primer lugar a la superficie metálica.

En trabajos previos realizados por nuestro grupo se demostró que las capas anódicas dopadas con flúor crecidas en medios que contenían HF (apartado 3.1), presentan propiedades antibacterianas tanto en ensayos realizados con cepas de colección como con cepas clínicas de dos tipos de bacterias, *S. aurius* y *S. epidermis*.

Este apartado, se ha dividido en dos partes, trata de explicar la respuesta biológica de las capas de óxido de titanio crecidas mediante anodizado en un medio ácido (H_2SO_4/HF).

En la primera parte -apartado 3.3a-, elucidando cual es el factor clave que controla la propiedad antibacteriana, discriminando entre el contenido de flúor en la capa y su morfología, es decir, su nanoestructura (Doped TiO_2 anodic layers of enhanced antibacterial properties). Para ello, en primer lugar se definieron y optimizaron las condiciones de anodizado para crecer capas barrera con flúor (BFL) y capas barrera sin flúor (BL) en su composición química, además de la generación de capas nanoestructuras. Los resultados indicaron que las capas barrera con flúor muestran una disminución estadísticamente significativa en la adhesión bacteriana en comparación con las capas barrera que no contenían flúor. Ello confirma el

papel clave del flúor en las propiedades antibacterianas de las capas anódicas frente a la nanoestructura de las capas.

Por otro lado, es importante determinar si la presencia del flúor en la superficie alterará la respuesta celular y la mineralización (Influence of the nanostructure of F-doped TiO_2 films on osteoblast growth and function). Este es el objetivo que se persigue en la segunda parte -apartado 3.3b-. Para ello, se crecieron diferentes películas anódicas: capas barrera (BL), capa barrera con flúor (FBL), capas nanotubulares (NT) y capas nanoporosas (NP), y se utilizó la línea celular osteoblástica de ratón MC3T3-E1 para determinar la proliferación celular a 2 y 7 días de crecimiento y la mineralización después de 10 días de incubación celular.

Los resultados mostraron que la presencia de flúor no altera ni impide la proliferación de células MC3T3-E1, siendo las capas con morfología nanoporosa y un contenido de flúor ~6 at.%, las que presentan la mejor respuesta celular. Además, en comparación con el Ti6Al4V sin anodizar, todas las capas anodizadas y en especial la nanoporosa, mejoran la mineralización. Por tanto, los resultados sugieren que estas películas de óxido de titanio dopado con F mejoran la función osteogénica y podrían ser adecuadas en ingeniería de tejido óseo.

Este apartado reproduce íntegramente el texto del siguiente manuscrito:

María A. Arenas, Concepción Pérez-Jorge, Ana Conde, Endzhe Matykina, Juan M. Hernández-López, Ramón Pérez-Tanoira, Juan J. de Damborenea, Enrique Gómez-Barrena, Jaime Esteba, Doped TiO_2 anodic layers of enhanced antibacterial properties, ***Colloids and Surfaces B: Biointerfaces***, Volume 105, 1 May 2013, Pages 106-112.

que se encuentra en la sección de **compendio de publicaciones** bajo el formato de la revista en la que fue publicado.

Doped TiO_2 anodic layers of enhanced antibacterial properties

María A. Arenas[a], Concepción Pérez-Jorge[b], Ana Conde[a], Endzhe Matykina[a], Juan M. Hernández-López[a], Ramón Pérez-Tanoira[b], Juan J. de Damborenea[a], Enrique Gómez-Barrena[c], Jaime Esteba[b]

[a] Centro Nacional de Investigaciones Metalúrgicas (CENIM/CSIC), Madrid, Spain

[b] Department of Clinical Microbiology, IIS-Fundación Jiménez Díaz Hospital, Madrid, Spain

[c] Department of Orthopaedics, IdiPAZ-Hospital Universitario La Paz, Madrid, Spain

Abstract

Ti–6Al–4V joint replacement implants foster uncemented fixation in orthopaedic surgery. However, bacterial colonization competes with host cells and ultimately may produce implant-related difficult-to-treat infections, justifying the efforts to obtain infection-resistant materials. In a previous work, the authors demonstrated the antibacterial properties of anodic fluoride-TiO_2 nanostructured layers on Ti–6Al–4V alloy. In this work, the anodizing bath has been modified in order to grow fluoride-TiO_2 barrier layers (FBL). A bacterial adherence protocol, run with reference and six different clinical strains of *Staphylococcus aureus* and *Staphylococcus epidermidis*, showed a statistically significant decrease in the percentage of covered surface ($p < 0.0001$, Kruskal–Wallis test) for FBL specimens when compared with non fluoride-containing specimens, *i.e.* chemically polished Ti–6Al–4V and F-free TiO_2 barrier layers. The results obtained on the F-barrier layers allowed discrimination between the effects of the presence of fluoride in the layer and the layer nanostructure on bacterial adhesion.

Keywords: Bacterial adhesion; Infection; Surface treatment; Titanium alloy

1. Introduction

Titanium and its alloys are widely used in technological applications due to their excellent mechanical properties, high corrosion resistance and biocompatibility. Broad functionality of titanium alloys is attributed to the presence of surface TiO_2 oxide layer which enhances their corrosion resistance and biological activity.

Ti–6Al–4V joint replacement implants are a great advance in orthopaedic surgery and an essential component of uncemented current joint prosthesis. However bacterial colonization of surfaces compromises the effectiveness of the implanted materials and ultimately can result in difficult-to-treat infections [1].

It is well known that most bacterial species can develop the complex structure that is known as a biofilm. It makes them less accessible to the host defence system and also decreases their antibiotic susceptibility. When the bacteria adhere to the surface before host cells do, they start to multiply and produce an extracellular matrix that constitutes the essential part of the biofilm which evolves into a clinical infection as the numbers of bacteria grow [2,3]. So, in this phenomenon, bacterial adherence to the surfaces is the first and key step in biofilm development. *Staphylococcus aureus* and *Staphylococcus epidermidis* are frequently isolated as the leading cause of biomaterial-related infections, and different authors explain this fact by the ability of these species to develop biofilms [4].

Preventing the adhesion of bacteria to the implant surfaces is a step forward in the pathogenesis of infection, because the bacteria that do not adhere are rapidly killed by the immune system [5]. According to this fact, if bacterial adherence is avoided, infection will not develop in the patient. Traditionally, prevention of bacterial adhesion has been ensured through the chemoprophylactic use of antibiotic agents before surgery, mainly administered systemically, and in some cases, even released from the implanted biomaterial. However, this latter strategy has important limitations, such as the rapid release of the adsorbed antibiotic, resistance development against the antibiotics, or systemic toxicity [6].

Development of resistance due to a broad use of antibiotics is a matter of special concern because it can limit the number of available antibiotics for treatment of infections, and even some infections can be untreatable due to the lack of useful antibiotics [7].

An interesting strategy for preventing the bacterial attachment and development of biofilm is altering the biomaterial surface properties. Surface modification techniques allow tailoring of the surface energy *via* surface chemistry and topography, showing important effects of the surface property changes on microbial colonization. Different methodologies have been used to change either the chemical composition or the microtopography of the surface and their impact on bacterial adhesion with different results [8-10].

Among the surface modification techniques, anodizing is a well known process that enables the growth of titanium oxide layer under controlled conditions. The structure of the anodic layer can be controlled by varying the electrolyte composition, the applied voltage, the time and the temperature. In general, anodic oxide layers grown in acidic, HF-containing baths have duplex structure comprising an outer nanoporous/nanotubular layer in contact with the electrolyte, and an inner compact layer (barrier layer) formed at the bottom of the nanotube/nanopore adjacent to the substrate. However, under certain conditions the growth of the nanostructured outer layer can be suppressed, promoting just the growth of the barrier layer.

In a previous work, the authors demonstrated the antibacterial properties of anodic fluoride-TiO_2 nanostructured layers on Ti–6Al–4V alloy [11-13]. The adhesion of *S. epidermidis* and *S. aureus* has been reduced by 50% due to the presence of ~5 at.% of fluorine in the oxide layer. However, as both the topography and the chemical composition were modified by the anodization process, it was difficult to elucidate which one was the major factor in the antibacterial properties: the F content in the oxide layer or the topographical features of the latter.

In this work, the anodizing bath has been modified in order to enable the growth of fluoride-containing barrier layers (FBL) for the first time. The studies performed on non-nanostructured FBL have permitted to discriminate the effect of the fluoride from the effect of the surface nanostructure on bacterial adhesion.

2. Materials and methods

2.1. Sample preparation

Ti–6Al–4V alloy specimens of ELI grade according to the standard ASTM F136-02 supplied by SURGIVAL were ground through successive grades of SiC paper to 1200 grade, degreased with a detergent and rinsed in tap water followed by deionised water. The specimens were then chemically polished (CP) in a mixture of HF (48 wt%):HNO_3 (70 wt.%):H_2O with volume ratio 1:4:5, for 5 min at room temperature under continuous agitation at 400 rpm, rinsed in distilled water and dried in cold air. The working area was 2.54 cm^2.

Fluoride-TiO_2 barrier layers (FBL) were produced in a two-electrode cell by anodizing the specimens in 1 M $NH_4H_2PO_4$/0.15 M NH_4F solution at constant voltage controlled at 20 V for 120 min and at temperature controlled at 20 °C. Platinum mesh was used as a cathode. Constant voltage was applied using LAB/SM 1300DC power supply (ET Power Systems Ltd.). Current time responses of anodizing were acquired at 0.1 Hz sampling rate using a Zero-Resistance Ammeter (ZRA) connected in series with the electrochemical cell. Fluoride-free TiO_2 barrier layers (BL) were also fabricated in 1 M H_2SO_4 electrolyte by anodizing the specimens at 15 mA cm^{-2} to 90 V. The summary of surface treatment conditions is listed in Table 1.

2.2. SEM and TEM characterization

The plan view morphology of oxide barrier layers was examined by field emission gun scanning electron microscopy (FEG-SEM) utilizing a JSM6500F JEOL instrument equipped with EDX facilities.

Electron-transparent sections, nominally 40 nm-thick, prepared by ultramicrotomy were observed by a JEOL JEM 2010 TEM instrument operated at 200 keV.

Table I. Surface treatment conditions and oxide film characteristics

Surface Treatment		Designation	Electrolyte/ Surface Treatment conditions	Film thickness (nm)	Fluorine content (at. %)
Chemically Polished	-	CP	HF (40wt %): HNO_3(70 wt%):H_2O 1:4:5 ration 5 min	No film	<0.5
Barrier layer[a]	F-free treatment	BL	1M H_2SO_4 Anodizing at 15mA/cm^2 to 90V	200	<0.3
Fluoride Barrier Layer	F-containing treatment	FBL	1M $NH_4H_2PO_4$/ 0.15M NH_4F, pH=5 Anodizing at 20V, 120min	150	12

[a]Barrier layer refers to a dense anodic oxide film without nanostructure

2.3. Surface characterization

Surface topographies were examined and roughness Ra values were obtained by using an optical imaging profilometer Plμ 2300 (Sensofar) operated at 20×. The cited Ra values are an average of five measurements.

2.4. Surface energy and contact angle

Surface contact angles were measured using distilled water and diiodomethane (from Sigma Aldrich) using Theta Attension optical tensiometer (KSV Instruments) with automatic liquid dispenser and monochromatic cold light source, operated in trigger mode with 50 video frames recorded at 112 ms interval. The measurements were performed immediately after the treatment of the surface, rinsing for 1 min in distilled water, and drying in warm air for 1 min, to avoid the adsorption of carbon-containing species from the ambience.

Contact angles were calculated using Young–Laplace drop profile fitting method. Each contact angle value is cited as an average of three measurements performed at three different locations on the specimen surface. An average of 40 frames has been used to calculate the contact angle for each drop.

Surface free energy (γ) components and work of adhesion (Wa) of the oxide layers were determined using Fowkes approach [14]:

$$W_a = \gamma_L(\cos\theta + 1) = 2(\gamma_L^D\gamma_S^D)^{1/2} + 2(\gamma_L^P\gamma_S^P)^{1/2} \quad (1)$$

$$W_a^D = 2(\gamma_L^D\gamma_S^D)^{1/2} \quad (2)$$

$$W_a^P = 2(\gamma_L^P\gamma_S^P)^{1/2} \quad (3)$$

2.5. Bacterial adhesion

Microbiology studies have been performed using two reference strains and six clinical strains of each species. The reference strains were S. aureus 15981 [15] and S. epidermidis ATCC 35984. Both strains are biofilm-producing ones. S. aureus 15981 is a clinical isolate that has been fully characterized with respect to the biofilm production. S. epidermidis ATCC 35984 is a collection strain used for biofilm studies. The clinical strains for S. aureus were P1, P2, P4, P18, P61T3 and P95 and those for S. epidermidis were P6, P33, P53B, P55, P74 and P101. The clinical strains have been isolated from patients who have had an implant-related infection using a previously described sonication procedure [16]. These strains have been characterized by phenotypic and genetic methods in a previous study. The strains were isolated from infected hip prosthesis (P2, P4, P18, P33, P53B, P55, P74 and P101), and infected osteosynthesis implants (P1, P6, P61T3 and P95). All the strains are able to form biofilm in vitro and the amount of biofilm production ranges between 1+ and 3+ according to Stepanovic method. All S. aureus strains were ica gene positive, as well as all S. epidermidis strains except the P33 and P101 [17].

In this work, the experiments on staphylococcal adhesion of reference strains were carried out on BL and FBL while the study with clinical strains

was performed on CP, and FBL. The experiments were performed following the protocol developed by Kinnari et al. [18] as previously reported by us [13]. Bacteria were inoculated in Tryptic Soy Broth (TSB, bioMérieux, Marcy L'Etoile, France) and incubated overnight at 37 °C with 5% CO_2. After culture, bacteria were centrifuged for 10 min at 3500 × g at 22 °C. Supernatant was then discarded and the pellet was washed three times with sterile phosphate buffered saline (PBS, Sigma–Aldrich Life Science). Bacteria were then suspended and diluted in PBS in order to obtain a 108 CFU/ml concentration; the bacterial concentration was determined by spectrophotometry using a visible spectrophotometer (Genesys 20, Thermo Scientific) [19]. Ten ml of this solution were used to cover the specimens in the plates. This inoculum was added onto specimens of titanium alloy (Ti–6Al–4V) with different surface treatments, and incubated for 90 min at 37 °C in order to allow adhesion in a static model.

After incubation, the samples were washed three times with PBS to remove unattached bacteria. Finally, they were stained for 2 min with Live/Dead® Bacterial Viability Kit (Backlight™) [20] and rinsed with sterile water. Eight photographs (400×, high power field) were obtained by UV microscope for each sample.

A surface of approximately 24,000 μm^2 was captured in each image. The percentage of surface area covered with adhered bacteria was calculated using ImageJ software (National Institute of Health Bethesda, MD, USA). The experiments were performed in triplicate for each strain.

The statistical analysis was performed using EPI-INFO software version 3.5.1 (CDC, Atlanta, GA, USA). The obtained results were presented comparing the mean percentage of covered biomaterial surface for CP Ti–6Al–4V specimens, and for different anodized materials, i.e. BL and FBL. In order to carry out the statistical study, non-parametric tests were performed. When more than two samples were employed, the Kruskal–Wallis test was carried out, whereas for two samples, the Mann–Whitney test was used.

3. Results

3.1. Surface characterization

The surface morphology of the CP Ti–6Al–4V reveals an α+β microstructure, comprising 2–3 μm long β-phase particles dispersed in α-phase matrix (Fig. 1(a)). Local EDX analysis disclosed that the β-phase is enriched in vanadium (up to ~14 at.%) compared with the α-phase (~2 at.%) and contains about 1 at.% of iron [21].

The Ra roughness value of CP surfaces determined over 140 μm-long profile was about 73 nm (Table 2).

The cross-section of the oxide layer prepared in 1 M H_2SO_4 (the F-free electrolyte; Fig. 1(b)) shows a 200 nm-thick barrier type layer, BL. Local crater-like irregularities are formed due to a local dielectric breakdown of the layer, Fig. 1(c). The EDX analysis performed at different sites of the layer revealed that the layer contained tracers of fluorine (≤0.3 at.%), originating from chemical etching of the substrate in $HF/HNO_3/H_2O$ solution prior to anodizing. The oxide layer formed on the β-phase still contained elevated amount of vanadium (~3.3 at.%) compared with the layer formed on α-phase (~0.7 at.%) [13].

The Ra values for the BL are slightly lower compared with CP surface, with the average Ra value of 53 nm (Table 2).

A ~150 nm-thick FBL is formed after 120 min of anodizing in $NH_4H_2PO_4/NH_4F$ electrolyte (Fig. 1(d)). The fluoride concentration and the pH of the anodizing bath strongly influence the TiO_2 layer surface morphology formed in this electrolyte [22]. Nanotubular and nanoporous structure can be also produced in this electrolyte as a consequence of the dissolution process, which is intensified at higher concentrations of F− and is inhibited by the pH increase of the electrolyte. Increasing the pH of the 1 M $NH_4H_2PO_4$/0.15 M F^- solution from 4.2 to 5.0 enabled growth of thick barrier layers instead of nanostructured layers (nanotubular layers) [22]. The TEM cross-section image of the barrier layer revealed an amorphous structure with no discernable nanocrystals (Fig. 1(d)). The oxide layer

formed on β-phase appeared nodular compared with the smooth layer generated on α-phase (Fig. 1(e)).

The chemical composition estimated by RBS revealed that the fluorine content in FBL layers is 12 at.% [22]. Lower amount of fluorine, around 4–6 at.%, has been found in the nanostructured layers described in our previous work [21].

The average roughness of the FBL surface (130 nm) is higher than that of the CP and BL specimens. The more intensive chemical dissolution of the oxide layer during the anodizing process in the fluoride-containing electrolyte results in the increased roughness on the FBL in comparison to the BL specimens.

3.2. Surface wettability

The wettability of the freshly prepared and dried surfaces was considerably high for all the treatments. FBL layer shows lower contact angle with water than CP and BL specimens, while the contact angles with diiodomethane are similar in the three types of specimens (Table 2).

Surface energy calculations from contact angle data obtained in distilled water indicated that increasing the surface roughness increased the surface energy. The calculated components of surface free energy, work of adhesion to water and solid/water interface energy are gathered in Table 2. The lowest and highest surface energies were obtained for CP and FBL specimens, respectively.

The CP and BL surface treatments had no statistically significant difference. BL layer and CP surface disclosed lower work of adhesion and higher solid/water interface energy than the FBL layer. Higher adhesion work for FBL indicates that greater separation work is required to pull a droplet of water off the surface and to create water/air and FBL/air interfaces. Respectively, lower FBL/water interface energy means that smaller work is required to create a unit of FBL/water interface.

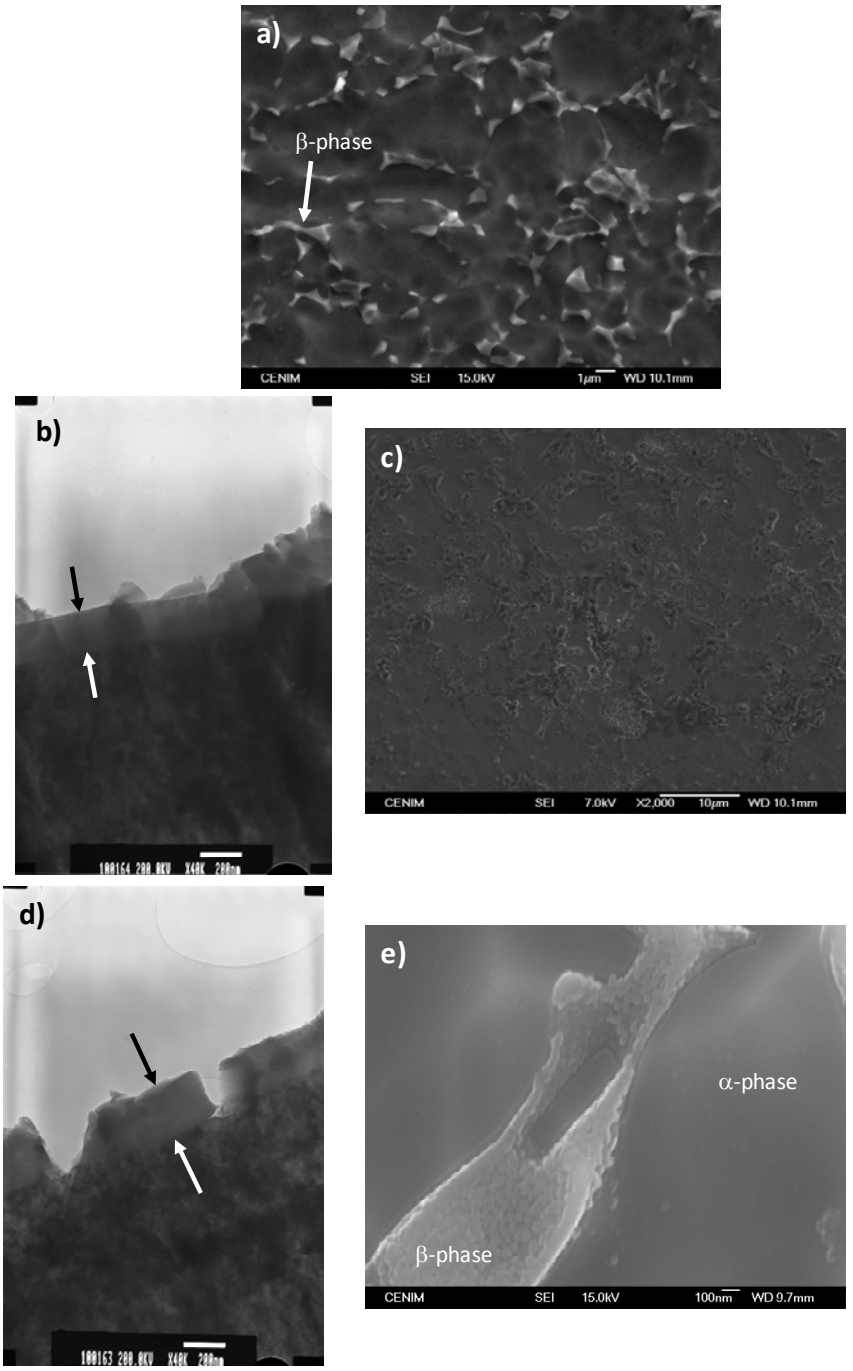

Figure 1. Surface morphology of CP Ti-6Al-4V (a); cross section and plan view of BL oxide layer prepared in 1M H_2SO_4 (b, c); cross-section and plan view of FBL formed in $NH_4H_2PO_4/NH_4F$ electrolyte for 120 min (d, e).

Table 2. Roughness and Contact angle measurements. Calculated components of surface- free energy, work of adhesion and solid/water interface energy

		Contact angle ±SE (°)		Surface-free Energy (mJ/m^2)[a]			Work of Adhesion Energy (mJ/m^2)[a]			Solid/water Interface energy (mJ/m^2)[a]
Film	**Ra (nm)**	**Water**	**Dioodomethane**	γ_s	γ^D_s	γ^P_s	W_a	W^D_a	W^P_a	γ_s
CP	53.2 ± 2.1	52.10 ± 8.2	29.05 ± 2.78	59.5	44.6	14.9	117.4	62.36	55.13	14.80
BL	73.9 ± 3.8	57.50 ±0.27	27.51 ± 1.86	58.1	45.2	12.9	114.0	62.78	51.30	16.82
FBL	130.4 ± 7.2	21.36 ± 5.18	26.16 ± 5.35	75.1	45.7	29.4	140.6	63.13	77.44	7.33
NP*	178.9 ± 8.7	29.9 ± 1.8	22.4 ± 2.11	72.5	47	25.5	136.2	64.0	72.1	9.2
NT*	168.8 ± 11.6	7.5 ± 1.58	3.98 ± 0.83	80.9	50.7	30.2	145	66.5	78.5	8.7

[a] Measured in distilled water. *Data from ref [12]

In general, the lowest surface free energy parameters were obtained for F-free surfaces –CP and BL– with the lowest roughness. Thus, in the absence of the nanostructure, the F content and the roughness alone may be considered responsible for the increase of the surface free energy parameters of FBL layers.

3.3. Adhesion studies

3.3.1. Results of reference strains

The results of the mean percentage of covered surface for reference strains are shown in Fig. 2. The response of S. aureus and S. epidermidis reveals statistically significant differences ($p < 0.0001$, Kruskal–Wallis test) when comparing FBL with CP and BL specimens. The percentage of covered surface of FBL specimens is higher for S. epidermidis than for S. aureus. However, there is no statistically significant difference between the percentage of covered surface of BL and CP specimens ($p>0.0001$, Kruskal–Wallis test).

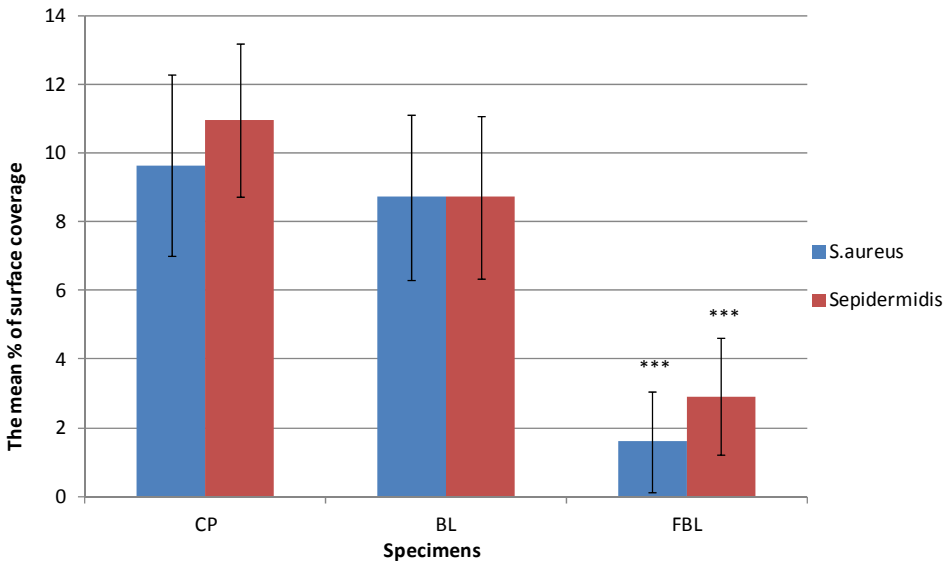

Figure 2. The mean percentage of surface coverage for *S. epidermidis.*
***Statistically significant difference with CP and BL ($p< 0.0001$)

3.3.2. Results of clinical strains

As reference bacteria did not show statistically significant difference between CP and BL treatments, further comparison of the clinical strains response was performed using just CP and FBL specimens.

Fig. 3 shows the mean percentage of covered surface for six clinical strains of S. epidermidis. For P6.2, P33.1, and P74 strains, the results showed a statistically significant decrease in the percentage of covered surface of FBL compared with the CP. Similarly, for most of the S. aureus clinical strains (P1, P2, P4, P18 and P61T3) the mean percentage of covered surface revealed a statistically significant decrease ($p<0.0001$, Kruskal–Wallis test) on FBL specimens compared with CP specimens. On the other hand, the mean percentage of covered surface of the FBL specimens is lower for S. aureus than for S. epidermidis.

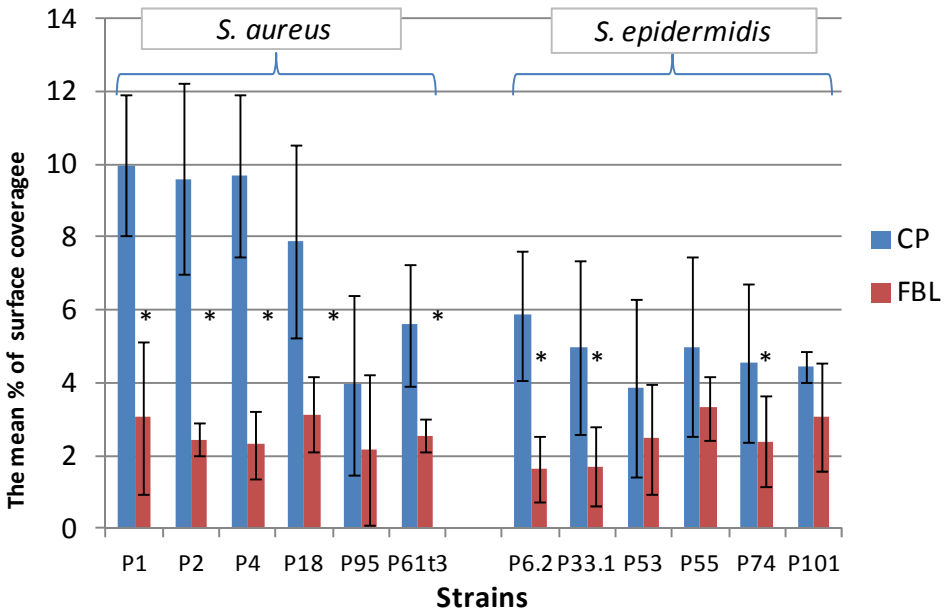

Figure 3. The mean percentage of surface coverage for S. epidermidis and S. aureus clinical strains. *statistically significant difference with CP ($p< 0.0001$).

4. Discussion

Bacterial adhesion is a complex process that depends on many factors, including some characteristics of the bacteria themselves, environmental factors and, of course, material surface properties [5].

From the perspective of the material, the chemical composition, surface charge, wettability, surface roughness and topography are important parameters influencing bacterial adhesion. Precisely, surface modification of the substratum is being studied as a potentially efficient strategy to alter surface properties (surface chemistry, topography and hence, the surface energy) of the implants and the effects of these changes on the adhesion process are being evaluated. However, although there is a lot of information on the behaviour of many bacteria on a wide variety of metals and other surfaces, still there is no a conclusive theory that explains or even summarizes all this information.

A previous study performed on specimens anodized in fluoride-containing electrolytes, using either reference strains or clinical strains, showed a decrease of bacterial adhesion on nanostructured fluoride-containing layers in comparison with the CP and BL specimens [13]. In addition, no statistically significant differences were observed between the nanostructured (nanoporous (NP) or nanotubular (NT)) specimens with respect to the adhesion of bacteria. This correlates with the fact that solid/water interface energies for both nanotubular and nanoporous specimens were very similar, despite the distinctly different microstructure (see Table 2). Hence, the observed decrease in bacterial adhesion was attributed to the presence of fluoride in the layer.

The present study compares the antibacterial properties of F-containing TiO_2 barrier layers with the non-anodized specimens, CP, and anodized specimens prepared in a F-free electrolyte which allows formation of F-free TiO_2 barrier layers, BL. Both anodized specimens (BL and FBL) have the same dense homogenous structure, i.e. both are non-nanostructured oxide layers, thus enabling to elucidate the role of the fluoride in two layers with

similar morphological features. FBL promotes the lowest bacteria attachment compared with the BL and CP treatments.

Further, FBL surface has an increased roughness and surface energy compared with the BL. Kinnari et al. [23], reported that an increase of the roughness and the surface energy leads to an increased protein adsorption, such as fibronectin, that results in a decreased bacteria attachment. So the changes both in roughness and surface energy could be the key factors responsible for the decrease in the bacterial adhesion reported for the FBL layers.

The changes in roughness and surface energy components obtained from the contact angles for the FBL are different from those for the BL specimen, but are rather similar to those reported in our previous work for the nanostructured layers, NP and NT arrays, obtained in F-containing electrolyte (Table 2) [13]. However, despite these similarities the bacterial response of the FBL is quite different in comparison with the response reported for the nanoporous and nanotubular fluoride-containing layers. While the mean percentage of surface coverage by reference S. aureus and S. epidermidis for the nanoporous, NP, and nanotubular, NT, layers is about 4 and 7%, respectively [13], for the FBL these percentages decrease to 2 and 3%, respectively.

Similarly, the mean percentage of surface coverage by clinical strains of S. aureus and S. epidermidis for the FBL specimens are much lower than observed in the F-containing nanostructured layers [13].

These differences in bacterial adhesion on FBL compared to F-nanostructured layers suggest that the surface morphology could also have a relevant effect. Merit et al. [24] found that implant site infection rates are different for porous and dense implants materials, porous material having a much higher rate of infection. However the size of the pores reported in their work is quite high, 100 μm, whereas the size of the bacteria is two orders of magnitude smaller (being 1–2 μm diameter for Staphylococcus cells). So in this case as well as in others reported on titanium for dental applications [25] and [26], the microorganisms colonize much larger pores

and cavities where they are sheltered from the host defences. Nevertheless, these pore sizes are very large compared to the pore diameter achieved in the nanoporous or nanotubular layers reported in our previous paper, whose diameter ranged from 10 to 100 nm. Thus, it appears that nanoporous features of the anodic layers have no influence on the bacterial adhesion.

Further, although porous materials or microtextured surfaces support osseonintegration, roughly textured implant substrata in dental applications are known to enhance plaque accumulation, whereas highly polished materials with reduced surface roughness limit initial biofilm formation in vivo on smooth titanium surfaces [2]. Conversely, a more recent preliminary study performed using clinical data from infected patients showed no clear differences between materials of different roughness regarding the number of bacteria present on the implant surface. Particularly, the microorganism involved in orthopaedic clinical infections in specific patients are a major factor influencing the adherence, which justifies the need to perform the studies of new materials using sufficient number of clinical strains [27]. In this sense, the use of clinical strains in adherence studies is essential, because of the potential differences in the behaviour of the different bacterial strains [28].

Moreover, Bollen et al. [29] compared the surface roughness of different materials produced by different techniques, concluding that a value of 200 nm is the average roughness threshold below which the amount of bacterial adhesion cannot be reduced any further. Therefore, as both FBL and BL layers fabricated exhibit roughness about 130 nm and 73 nm, respectively, so it appears that this parameter is not the key factor affecting the bacterial adhesion.

Thus, the findings of this work in conjunction with the previously published results [13] rule out the influence of the nanoscale roughness, the surface nanostructure and topography on the antibacterial properties of the anodic layer, suggesting that the reduction in the bacterial adhesion compared with the BL is solely due to the presence of fluoride in the layer.

In addition, the higher F– content in FBL compared with the nanostructured F-containing TiO2 layers [13] may be responsible for the enhanced antibacterial properties. The mechanism of the reduction of bacterial adhesion is thought to be related to the inhibition of their enzymatic activity by titanium-fluoride complexes, such as TiF4[30].

Although there is no material totally resistant to bacterial adhesion, certain differences exist, in this respect, among materials and surface treatments. Previous studies of the authors performed on F-containing TiO2 layers grown by anodizing show that, regardless of the surface configuration – nanoporous or nanotubular – there is a decrease in bacterial attachment on F-containing surfaces.

This paper reveals that the antibacterial properties rely on the F content in the layer rather than on the topographical properties. For the first time, bacterial adhesion studies using two reference strains and six clinical strains of S. aureus and S. epidermidis have been performed on fluoride-free TiO2 barrier layers and fluoride-TiO2 barrier layers. These results, in comparison with those previously reported in [13], discriminate between the role of the nanostructure of the layer and the F– content in the layer in bacterial adhesion, showing that the lowest bacterial adhesion is achieved on fluoride-TiO2 barrier layers due to their higher F– content compared to the nanostructured oxide layers, with no interference from other structural changes.

5. Conclusion

This paper demonstrates the enhanced antibacterial properties achieved solely by the incorporation of fluorine during the anodizing process of Ti–6Al–4V. Antibacterial properties of nanostructured anodizing layers have been recently reported by the authors. Until now, the anodizing of titanium alloys simultaneously promoted chemical and nanostructural changes of the surface. In this work, a new formulation of the anodizing bath has been developed in order to fabricate fluoride-containing barrier layers (FBL) with no change in topography. The bacterial adhesion studies performed on these non-nanostructured FBL show a statistically significant decrease

in the bacterial adhesion in comparison to fluorine-free barrier layers (BL). These results permit for first time to discriminate the effect of the fluorine from the effect of the surface nanostructure on antibacterial properties, revealing the key role of the F in the antibacterial properties.

Acknowledgements

This work was funded by a grant from the Spanish Ministry of Science and Innovation (SMOTI MAT2009-13751 and CONSOLIDER-INGENIO 2010 CSD 2008-0023 FUNCOAT). Juan Manuel Hernández López acknowledges CSIC for funding this work under the grant JAE-pre-2010.

The authors report that they have a patent for the materials regarding their antimicrobial properties PCT/ES2011/070342.

References

[1] L. Rimondini, M. Fini and R. Giardino, The microbial infection of biomaterials: A challenge for clinicians and researchers. A short review, J Appl Biomater Biomech 3(2005) 1-10.

[2] L. Hall-Stoodley, J. W. Costerton, P. Stoodley, Bacterial Biofilms: From the natural environment to infectious deasease, Nat Rev Microbiol, 2 (2004) 95-108

[3] W.Costerton, R.Veeh, M.Shirtliff, M. Pasmore, C. Post, G. Ehrlich, The application of biofilm science to the study and control of chronic bacterial infections, J. Clin. Invest. 112 (2003) 1466–1477.

[4] R.A. Brady, J.H. Calhoun, J.G. Leid and M.E. Shirtliff, Infections of Orthopaedic Implants and Devices, in: M.E. Shirtliff, J.G. Leid (Eds.) The Role of Biofilms in Device-Related Infections, Springer-Verlag, Berlin, 2009, pp. 15-56.

[5] M. Katsikogianni and Y.F. Missirlis, Concise review of mechanisms of bacterial adhesion to biomaterials and of techniques used in estimating bacteria-material interactions, Eur Cell Mater, 8 (2004) 37-57.

[6] J. Esteban, J. Cordero-Ampuero, Treatment of prosthetic osteoarticular infections, Expert Opin. Pharmacother, 12, 6 (2011) 899-912.

[7] D. Livermore, Has the era of untreatable infections arrived?, J Antimicrob Chemother. 64 (2009) i29-36.

[8] K.K. Chung, J.F. Schumacher, E.M. Sampson, R.A. Burne, P.J. Antonelli and A.B. Brennan, Impact of engineered surface microtopography on biofilm formation of Staphylococcus aureus, Biointerphases, 2 (2007) 89.

[9] M.I. Sarró, D.A. Moreno, C. Ranninger, E. King and J. Ruiz, Influence of gas nitriding of Ti6Al4V alloy at high temperature on the adhesion of Staphylococcus aureus, Surf Coat Technol, 201 (2006) 2807-2812.

[10] L. Zhao, P.K. Chu, Y. Zhang and Z. Wu, Antibacterial coatings on titanium implants, J Biomed Mater Res Part B, 91B (2009) 470-480.

[11] C.A.d.D.J. Arenas M.A., Matikyna E, Esteban J, Gomez-Barrena E, Perez-Jorge C, Perez Tanoira R, Materiales de titanio anodizado con fluor, PATENT, PCT/ES2011/070342. Spain. (2010).

[12] C.P.-J. Peremarch, R.P. Tanoira, M.A. Arenas, E. Matykina, A. Conde, J.J.D. Damborenea, E.G. Barrena and J. Esteban, Bacterial adherence to anodized titanium alloy, Journal of Physics: Conference Series, 252 (2010) 012011.

[13] C. Pérez-Jorge, A. Conde, M.A. Arenas, R. Pérez-Tanoira, E. Matykina, J.J. de Damborenea, E. Gómez-Barrena and J. Esteban, In vitro assessment of Staphylococcus epidermidis and Staphylococcus aureus adhesion on TiO2 nanotubes on Ti–6Al–4V alloy, J Biomed Mater Res Part A, 100A (2012) 1696-1705.

[14] F. Fowkes, Chemistry and Physics of Interfaces . American chemical Society, Washington, DC, 1965.

[15] J. Valle, A. Toledo-Arana, C. Berasain, J.M. Ghigo, B. Amorena, J.R. Penades and I. Lasa, SarA and not sigmaB is essential for biofilm development by Staphylococcus aureus, Mol Microbiol, 48 (2003) 1075-1087.

[16] T.J. Kinnari, A. Soininen, J. Esteban, N. Zamora, E. Alakoski, V.P. Kouri, R. Lappalainen, Y.T. Konttinen, E. Gomez-Barrena and V.M. Tiainen, Adhesion of staphylococcal and Caco-2 cells on diamond-like carbon polymer hybrid coating, J Biomed Mater Res A, 86 (2008) 760-768.

[17] J. Esteban, D. Molina-Manso, I. Spiliopoulou, J. Cordero-Ampuero, R. Fernández-Roblas, A. Foka, and E. Gómez-Barrena. Biofilm development by clinical isolates of Staphylococcus spp. from retrieved orthopedic prostheses, Acta orthop, 81 (2010) 674-679.

[18] J. Esteban, E. Gomez-Barrena, J. Cordero, N.Z. Martin-de-Hijas, T.J. Kinnari and R. Fernandez-Roblas, Evaluation of quantitative analysis of cultures from sonicated retrieved orthopedic implants in diagnosis of orthopedic infection, J Clin Microbiol, 46 (2008) 488-492.

[19] L.T. Chapin KC, Reagents, stains, and media: bacteriology, in: Manual of clinical Microbiology, ASM Press, Washington DC, 2007, pp. p 334-364.

[20] L. Boulos, M. Prevost, B. Barbeau, J. Coallier and R. Desjardins, LIVE/DEAD BacLight : application of a new rapid staining method for direct enumeration of viable and total bacteria in drinking water, J Microbiol Methods, 37 (1999) 77-86.

[21] E. Matykina, J.M. Hernandez-López, A. Conde, C. Domingo, J. De Damborenea and M.A. Arenas, Morphologies of Nanostructured TiO2 Doped with F on Ti-6Al-4V Alloy, Electrochim Acta., 56 (2011) 2221.

[22] E. Matykina, A. Conde, J. de Damborenea, D.M.y. Marero and M.A. Arenas, Growth of TiO2-based nanotubes on Ti–6Al–4V alloy, Electrochim Acta., 56 (2011) 9209-9218.

[23] T.J. Kinnari, L.I. Peltonen, P. Kuusela, J. Kivilahti, M. Könönen and J. Jero, Bacterial Adherence to Titanium Surface Coated with Human Serum Albumin, Otol Neurotol, 26 (2005) 380-384.

[24] K. Merritt, J.W. Shafer and S.A. Brown, Implant site infection rates with porous and dense materials, J Biomed Mater Res, 13 (1979) 101-108.

[25] C.B. Correa, J.R. Pires, R.B. Fernandes-Filho, R. Sartori and L.G. Vaz, Fatigue and Fluoride Corrosion onStreptococcus mutansAdherence to Titanium-Based Implant/Component Surfaces, J Prosthodont, 18 (2009) 382-387.

[26] R. Sartori, C.B. Correa, E. Marcantonio Jr and L.G. Vaz, Influence of a Fluoridated Medium with Different pHs on Commercially Pure Titanium-Based Implants, J Prosthodont, 18 (2009) 130-134.

[27] E. Gómez-Barrena, J. Esteban, F. Medel, D. Molina-Manso, A. Ortiz-Pérez, J. Cordero-Ampuero and J.A. Puértolas, Bacterial adherence to separated modular components in joint prosthesis: A clinical study, J Orthop Res, (2012) 10.1002/jor.22114.

[28] J. Esteban, D. Molina-Manso and E. Gómez-Barrena, Bacterial adherence to vitamin E UHMWPE. Considerations about in vitro studies, J Orthop Res, 30 (2012) 1181-1181.

[29] C.M.L. Bollen, P. Lambrechts and M. Quirynen, Comparison of surface roughness of oral hard materials to the threshold surface roughness for bacterial plaque retention: A review of the literature, Dent Mater, 13 (1997) 258-269.

[30] M. Yoshinari, Y. Oda, T. Kato and K. Okuda, Influence of surface modifications to titanium on antibacterial activity in vitro, Biomaterials, 22 (2001) 2043-2048.

Este apartado reproduce íntegramente el texto del siguiente manuscrito:

Lozano D, Hernández-López JM, Esbrit P, Arenas MA, Gómez-Barrena E, de Damborenea J, Esteban J, Pérez-Jorge C, Pérez-Tanoira R, Conde A. 2014. Influence of the nanostructure of F-doped TiO_2 films on osteoblast growth and function**. J Biomed Mater Res Part A**, 103A (2015) 1985-1990.

que se encuentra en la sección de **compendio de publicaciones** bajo el formato de la revista en la que fue publicado.

Influence of the nanostructure of F-doped TiO_2 films on osteoblast growth and function

Daniel Lozano[1,2], Juan M. Hernández-López[3], Pedro Esbrit[2], Maria A. Arenas[3], Enrique Gómez-Barrena[1], Juan de Damborenea[3], Jaime Esteban[4], Concepción Pérez-Jorge[4], Ramón Pérez-Tanoira[4] and Ana Conde[3].

[1]Grupo de Investigación de Cirugía OsteoArticular, Instituto de Investigación Hospital Universitario La Paz (IdiPAZ), Spain.
[2]Laboratorio de Metabolismo Mineral y Óseo, Instituto de Investigación Sanitaria (IIS)-Fundación Jiménez Díaz, Spain
[3]Centro Nacional de Investigaciones Metalúrgicas, CENIM/CSIC, Spain
[4]Departamento de Microbiología Clínica, Instituto de Investigación Sanitaria (IIS)-Fundación Jiménez Díaz, Spain

Abstract

The aim of this study was to evaluate the proliferation and mineralization ability of mouse osteoblastic MC3T3-E1 cells on F-containing TiO_2 films with different morphology and nanostructure that previously confirmed antibacterial properties. F-containing TiO_2 films were fabricated by anodizing Ti-6Al-4V alloy ELI -grade 23. By using a mixture of H_2SO4/HF acid at 20 V for 5 and 60 min, a TiO_2 film grows with nanoporous (NP) and nanotubular (NT) features, characterized with a pore diameter of 20 and 100 nm, respectively. Fluoride-TiO_2 barrier films (FBL) were produced in $1M$ $NH_4H_2PO_4$/$0.15M$ NH_4F solution at constant voltage controlled at 20 V for 120 min. The amount of F incorporated in the nanostructured oxide films was 6 at % and of 4 at %, for the NP and NT, respectively, while for the FBL film was 12 at %. MC3T3-E1 cells exhibited different behavior when seeded and grown onto these surfaces. Thus, F-doped TiO_2 films with NP structures increased proliferation as well as osteogenic gene expression and the mineralization capacity of these osteoblastic cells. These results confirm that anodizing process is suitable to fabricate multifunctional surfaces on Ti-6Al-4V alloy with improved not only antibacterial but also osteogenic properties useful for bone fixation of prosthetic devices.

Keywords: Ti-6Al-4V alloy; surface functionalization; anodizing; osteoblast growth and function

INTRODUCTION

Titanium and its alloys are widely used for orthopaedic implants and prostheses due to their inertness, biocompatibility, and satisfactory bone fixation.[1, 2] Broad functionality of titanium alloys can be related to the passive TiO_2 film that forms on the surface enhancing the corrosion resistance and biological activity. However, bacterial colonization of these titanium surfaces and defective bone formation and tissue integration compromise the effectiveness of these materials when implanted, eventually leading to implant loosening and failure.[3]

Different methods have been used to alter either the chemical composition or the topography of the titanium surface, with a different outcome in terms of bacterial and cell adhesion.[4-6] Among them, anodizing is a well known process that enables the growth of titanium oxide film under controlled conditions.[7] In previous works, the authors demonstrate that the anodizing process fabricates F-doped TiO_2 films with antibacterial properties by using the appropriate electrolyte and voltage conditions. These anodic films with different nanostructure and F content were characterized showing lower adhesion affinity to *S. aureus* and *S. epidermidis* than F-free barrier anodic films (BL) and non anodized alloy. Moreover, the comparative studies performed on F-containing TiO_2 films with and without nanostructure permitted to discriminate the effect of the fluoride from the effect of the nanostructure on bacterial adhesion, demonstrating that fluoride is the key factor which supplied enhanced antibacterial properties to TiO_2 surface films.[8-10]

The inhibition of bacterial adhesion is the most critical step to prevent implant-associated infection, but implant success requires that tissue integration occurs before appreciable bacterial colonization. Therefore, to obtain valid conclusions on the potential clinical use of the aforementioned fluoride anodic films, it is necessary to assess the effect of both fluoride content and nanostructure on cells in the bone environment.

Previous studies indicate that fluoride modifications of the Ti surface improve the bone tissue response after implantation, favoring the

osteointegration process.[11-13] Fluoride on the titanium surface is thought to be released upon phosphate exchange reaction during the initial exposure to the bone healing environment, as confirmed by several *in vitro* or *in vivo* studies on surface modified titanium alloys involving the use of HF solutions. In this way, the titanium surface acts as a site for calcium and phosphate precipitation, leading to an increased bone contact and implant stability.[14] Using murine osteoblasts on rough titanium surfaces treated with different concentrations of fluoride, or human mesenchymal stem cells on fluoride-containing modified TiO_2 surfaces, an increased cell proliferation was found to be induced by fluoride.[11, 15-18] Current data suggest that the enhancement of bone formation by this type of F-containing titanium materials might result from the right combination of several factors such as the oxide covering the surface, the presence of F, and the micro (blasting) and nanolevel topography created by the HF (acid etching).

As an initial insight into the potential ability of these unique surface modifications of titanium alloys to promote a favorable bone response, the present study evaluates *in vitro*, the influence of the nanotopography and the F content of Ti-6Al-4V alloy with different F-doped TiO_2 films on various osteoblast function features.

MATERIALS AND METHODS

Film fabrication

Surface pretreatment and anodizing process used for fabrication of TiO_2 nanostructures with different fluorine contents and controlled morphology on Ti-6Al-4V alloys have been carried out as follows.

A 18 mm diameter rod of Ti-6Al-4V alloy ELI grade according to the standard ASTMF136-02 supplied by Surgical was cut into 2-mm thick disk specimens, ground through successive grades of SiC paper to 1200 grade, degreased with a conventional detergent and rinsed in tap water followed by deionised water. The specimens were then chemically polished (CP) in a mixture of HF(48 wt %):HNO_3(70 wt %):H_2O with volume ratio 1:4:5 for 5 min at room temperature under continuous agitation at 400 rpm, rinsed in

distilled water and dried in cold air. The disks were anodized only on one side, so the treated area was 2.54 cm^2.

The anodizing treatment was performed in a two-electrode cell using a Platinum mesh as a cathode. Constant voltage was applied using LAB/SM 1300DC power supply (ET Power systems). Current-time responses of anodizing were acquired at 0.1 Hz sampling rate using a Zero-Resistance Ammeter connected in series with the electrochemical cell.

Nanoporous (NP) and nanotubular (NT) oxide films were fabricated at constant voltage controlled at 20 V in the electrolyte containing 1*M* H_2SO_4 and 0.15 wt % HF for 5 and 60 min, respectively, at temperature controlled at 20°C according to Arenas et al.[19]

Fluoride-TiO_2 barrier films (FBL) were produced in 1*M* $NH_4H_2PO_4$/0.15*M* NH_4F solution at constant voltage controlled at 20 V for 120 min and at temperature controlled at 20°C. Finally, fluoride-free barrier oxide films (BL) have been also produced by anodizing in 1*M* H_2SO_4 at 15 mA cm^{-2} to 90 V.

Cell proliferation

The materials were placed into 12-well plates before seeding MC3T3-E1 cells[20] at a density of 10,000 cells/cm^2 in 2 mL of α-minimum essential medium with 10% fetal bovine serum, 50 μg/mL ascorbic acid, 10 m*M* ß-glycerol-2-phosphate and 1% penicillin–streptomycin, followed by incubation for different times at 37°C in 5% CO_2. Medium was replaced every other day. Cell proliferation was determined by addition of Alamar Blue solution (AbD Serotec, Oxford, UK) at 10% (v/v) to the cell culture[21] at 2 and 7 days of growth, following manufacturer's instructions. Fluorescence intensity was measured with excitation and emission wavelengths of 540 and 600 nm, respectively, in an Opsys MR Reader (Dynez Techonologies, Chantilly, VA).

Cell matrix mineralization

Matrix mineralization was measured by alizarin red staining after incubating subconfluent MC3T3-E1 cells with the tested specimens in the

aforementioned medium for 10 days. The stain was dissolved with 10% cetylpyridinum chloride in 10 m*M* sodium phosphate pH 7, measuring absorbance at 620 nm.[20].

Real-time PCR

MC3T3-E1 cells were incubated with the tested specimens as described above, and 5 days thereafter, total cell RNA was extracted with Trizol (Life Technologies, Rockville, MD). Gene expression was analyzed by real-time PCR using an ABI PRISM 7500 system (Applied Biosystems, Foster City, CA) and a described protocol.[22] Unlabeled mouse specific primers for: Runx2, osteocalcin (OC) and vascular endothelial growth factor (VEGF) and TaqMan^{MGB} probes were obtained by Assay-by-Design^{SM} (Applied Biosystems). The mRNA copy numbers were calculated for each sample by using the cycle threshold (Ct) value. 18S rRNA, a housekeeping gene, was amplified in parallel with the tested genes. Fold change for the treatment was defined as the relative expression compared with that of the control and was calculated as $2^{-\Delta\Delta C}$, where $\Delta\Delta C\text{t} = \Delta C\text{treatment} - \Delta C\text{control}$.

Statistical analysis

Results are expressed as mean ± SEM. Statistical evaluation was performed through analysis of variance and Scheffé *post-hoc* test. A value of $p < 0.05$ was considered significant.

RESULTS

Film properties

Two types of nanostructure arrays have been fabricated by anodizing at 20 V for 5 and 60 min, respectively, in 1*M* H_2SO_4/0.15 wt.% HF. The morphologies of these nanostructured TiO_2 films doped with F on the Ti-6Al-4V alloy were thoroughly characterized in a previous work.[23] Short anodizing time resulted in formation of a 110-nm-thick NP oxide film with a porous diameter of 20 nm (NP). Long anodizing time produced a 300-nm-long NT oxide film with a nanotube diameter of 100 nm. The average roughness, Ra, for the NP and NT films is higher than that for CP surfaces, 53 nm, with 178 and 160 nm for NP and NT films, respectively. The

Rutherford backscattering spectroscopy (RBS) analysis revealed that these two types of films contained 6 at % for NP and 4 at % of fluorine for NT.[23] Raman spectra performed on the films formed at 20 V showed broad bands centered at 454 and 617 cm^{-1} corresponding to amorphous TiO_2. The amorphous character of the nanostructured TiO_2 deduced from Raman data also agreed with TEM observations, where, at the employed resolution, no nanocrystals were disclosed in any of the film.[23].

Two types of non nanostructured oxide films without and with fluoride have been fabricated varying the composition of the electrolyte and the electrical conditions.[23, 24] The oxide film prepared in 1*M* H_2SO_4 the F-free electrolyte is a 200-nm-thick oxide barrier type film (BL).The R_a values for the BL film are slightly higher than CP surface, with the average R_a value of 73.9 ± 3.8 nm.

Finally, a ~150 nm-thick F-barrier film, FBL, is formed after 120 min of anodizing in a $NH_4H_2PO_4/NH_4F$ electrolyte. The fluoride concentration and the pH of the anodizing bath strongly influence on the TiO_2 film surface morphology formed in this electrolyte.[24] The chemical composition estimated by RBS revealed that the fluorine content in FBL films is 12 at %.[24] The average R_a of the FBL film, 130 nm, ranges in the same order than the nanostructured oxide films NP and NT. The higher chemical dissolution process occurred during the anodizing process in the fluoride-containing electrolyte results in an increased roughness on the FBL in comparison to the BL.

Cell proliferation

When testing the different F-doped TiO_2 films in osteoblastic MC3T3-E1 cells, it was observed that the presence of F failed to affect cell proliferation (2 and 7 days) in the case of BL, BFL, NT films, but it was significantly increased on the NP specimens; thus, the mean % cell proliferation with NP versus CP specimens (normalized to 100%) was: 142 and 133%, at days 2 and 7, respectively [Fig. 1(a)].

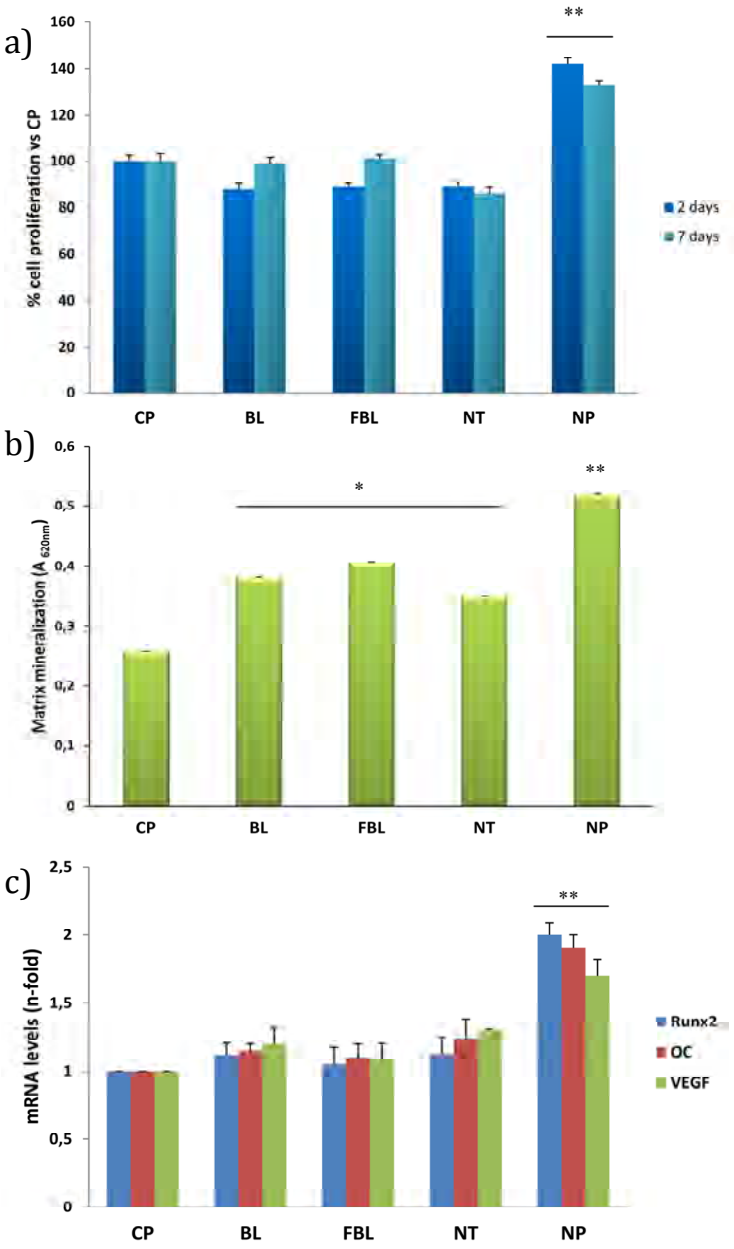

Figure 1. MCT3T3-E1 cell proliferation (measured by Alamar Blue assay) at days 2 and 7 (a); matrix mineralization at day 10 of culture (b); and gene expression of osteoblastic (Runx2 and OC) and angiogenic (VEGF) markers (c), at day 5, in the presence of Ti-6Al-4V (CP) and Ti-6Al-4V with various anodic oxide films, F-free (BL) and F-containing (FBL, NP, NT). SEMs were less than 1% in all of the experimental conditions. Results are mean ±SEM (n=4). *$p<0.01$ vs CP; **$p<0.0001$ vs CP.

Cell matrix mineralization

In addition, F-doped TiO_2 films, compared to the CP materials, significantly increased matrix mineralization in osteoblastic MC3T3-E1 cells at 10 days of culture; so that the corresponding mean A_{260nm} values for BL, FBL, and NT were: 0.38; 0.41; and 0.35, respectively, whereas that for the NP was 0.52 versus 0.26 for CP [Fig. 1(b)].

Gene expression

We analyzed the gene expression of two osteogenic markers, Runx2 and OC, corresponding to early and late osteoblast differentiation, respectively, and that of a key angiogenic factor, VEGF, in MC3T3-E1 cells exposed to the different tested specimens. It was found that NP specimens significantly increased the gene expression of all of these markers tested in MC3T3-E1 cells at day 5 [Fig. 1(c)].

DISCUSSION

The formation of bone around implants is a multistep process involving osteoblast adhesion, proliferation, differentiation, secretion of extra cellular matrix proteins, and mineralization. Yao et al.[25] evidenced an increased osteoblast adhesion on Ti and Ti-6Al-4V anodized in diluted HF, related to the surface alterations at the nanometer scale produced during short anodizing periods. Further studies by the same authors showed that the deposition of calcium by osteoblasts was increased on nanotube-like TiO_2 structures over anodized nanoparticulate structures on the titanium surface.[26] However, the osteoblast total collagen content and alkaline phosphatase activity did not show significant differences when comparing the two anodized and unanodized titanium surfaces after over 21 days. Conversely, Das et al.[27] observed an increase of both the extracellular matrix production and alkaline phosphatase expression by osteoblasts on NT oxide surface compared to unanodized titanium surfaces, suggesting that these cells mature more rapidly on a NT surface than on unanodized titanium samples.

Similarly, other authors reported that adhesion, spreading, growth, and differentiation of mesenchymal stem cells on vertically oriented TiO_2

nanotubes with defined diameters between 15 and 100 nm are critically dependent on the nanotube diameter. Thus, a diameter < 30 nm provide an effective length scale for accelerated integrin clustering/focal contact formation and enhancing cellular activities, compared to smooth TiO_2 surfaces obtained by anodization in fluoride-free H_3PO_4 electrolytes. These maximal responses were observed at 15 nm diameter, whereas cell adhesion and spreading were severely impaired on nanotube films with a nanotube diameter > 50 nm, resulting in dramatically reduced cellular activity.[28-30] However, these authors did not take into account the compositional changes induced in the oxide fabricated by the anodization in HF containing solutions together with nanometer surface features. In particular, the influence of the fluoride incorporated in the anodic film during the fabrication of the NP or NT oxide films was not considered; even though it is well known that fluorine ions induce formation of fluorapatite in the surrounding bone. The above mentioned studies conclude that the surface nano features developed in such anodizing conditions were responsible for the observed improved biological response.

The results of the present study show that the presence of F on Ti surfaces, which is responsible for the antibacterial properties, *per se* does not increase but it does not limit either osteoblastic cell growth. However, F content conferred various osteogenic features to the tested materials, as indicated by an increase in matrix mineralization and the gene expression of two osteoblastic markers, Runx2 and OC, and the angiogenic factor VEGF in MC3T3-E1 cells. Moreover, these cells exhibited improved functional parameters on F-doped TiO_2 films with NP structures [Fig. 1(a,b)] compared with NT or dense FBL structures, suggesting preferential adhesion to certain surface. The reason for this apparent preferential behavior of these osteoblastic cells is unknown. Surface roughness, however, could not explain by itself the best cell response observed on NP specimens, as the average measured roughness Ra for FBL, NP and NT specimens was similar (about 100 nm). F-containing TiO_2 anodic films FBL, NP, and NT, possess fluoride contents of 12, 6, and 4 at %, respectively. In this sense, Lamolle et al.[31] observed that small amounts of fluoride

(between 1 and 2 at %) incorporated onto the surface of metallic Ti implants have a stimulatory action on MC3T3-E1 osteoblasts. Longer immersion times in HF solutions, as used by Tiainen et al.[32] provided modified TiO_2 surfaces with 4 at % of F that induced a significantly higher osteoblastic cell number. However, they did not obtain conclusive evidence about fluoride being responsible for this cellular behavior. Moreover, they reported that a higher F content (about 9 at %) was in fact toxic to the cells. Conversely, no harmful effect was observed for the FBL film containing 12 at % of F in our study.

Even though the biological response to fluoride appears to be dose-dependent,[33] our data do not provide conclusive evidence about the concentration of fluoride being a key factor for the advantageous osteogenic properties of NP films.

Hydrophilic surfaces generally enhance protein and cell adhesion.[34-36] However, the differences in bioactivity observed in this work could not be explained by the different surface hydrophilicity of all the fabricated surfaces, all of them exhibiting high wettability with water contact angles lower than 65°.[10] In fact, NT films, with the lowest water angle contact (below 10°), was not the most effective in osteoblastic cell responses.

It is worthwhile mentioning that during the anodizing process the conditions imposed to fabricate the TiO_2 films not only influence the roughness and nanostructure of the anodic film but also its chemical composition. The latter is complex, containing TiF_4, and oxides of the alloying elements present in the titanium alloy, Al_2O_3 and V_2O_5.[23] The fluoride content and distribution are also different on each fabricated nanostructured anodic film. Habazaki et al.[37] demonstrated by GDOES analysis that fluoride ions are distributed relatively uniformly in anodic barrier films throughout the outer regions, with an accumulation of fluoride ions at the alloy/film interface. The faster inward migration rate of fluoride ions relative to that of O^{2-} ions, attributed to the smaller ionic radius of F^- ions, is the reason for such gradient distribution of fluoride. Similarly to NP films, the pore wall includes an outer pore wall that

contains TiO_2, TiF_4 and oxides of the alloying elements present in the titanium alloy, such as Al_2O_3 and V_2O_5 for Ti-6Al-4V alloy, while the inner pore wall mainly incorporates TiF_4. Longer anodizing times in the electrolyte containing HF fabricate NT anodic films, as a result of the chemical dissolution of TiF_4 placed at the inner pore wall, creating small intertubular spaces of few nm, Figure 2.

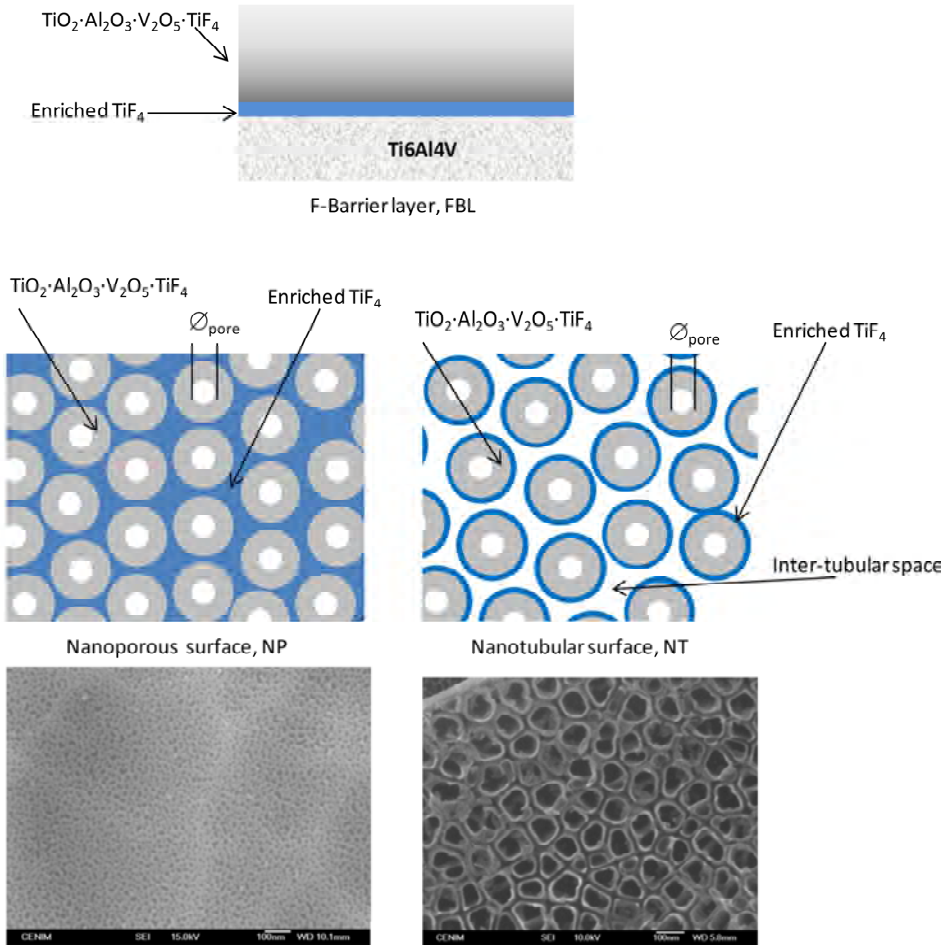

Figure 2. Scheme of TiF_4 distribution on NP, NT and FBL anodic films.

According to Ellingsen,[13] when TiF_4 contacts tissue fluids, the oxygen from phosphates present in the fluid may replace the fluoride, and phosphates become covalently bound to the titanium surface. Such reaction would also promote bone formation in bone tissue, where phosphate might

thus covalently bind to the titanium implant.[13] This study suggests that higher number of TiF_4 sites on the surface of the NP specimen, relative to that on NT and FBL specimens, might explain its improved osteogenic features. Thus, a larger TiF_4-enriched surface in contact with the physiological fluid in NP specimens than in NT would increase the capacity of NP surfaces to react with phosphate, increasing the number of preferential sites to cell attachment and bone formation. The opposite would occur in the case of FBL specimens with lower amount of titanium fluoride directly exposed to the physiological fluid, compared to NP materials. Moreover, less titanium fluoride sites available on NT and FBL, compared to NP, determine less released fluoride by the NT, which might account for their relative inefficacy to affect osteoblastic function.

In conclusion, the present findings, together with our previous results[9, 10] indicate that anodization is a quick and efficient method to form multifunctional nanostructured titanium oxide films of controllable pore size, good uniformity, and conformability over large areas. NP TiO_2 grown on Ti6Al4V can mimic constituent features of natural bone. Therefore, the observed interaction of osteoblastic cells with these materials might indicate potential impact on the bone milieu *in vivo*. Although both nanoscale topography and chemical composition are modified by the anodization process, the F content has been deemed as the major factor influencing the bacterial adhesion,[10] while parameters such as the fluoride distribution and topography appear to be paramount for osteoinduction. Furthermore, our studies provide a rationale for the development of a new kind of multifunctional prosthetic material surface based on titanium alloys with enhanced antibacterial properties, maintaining or even improving the bone formation capacity.

ACKNOLEDGMENTS

Juan Manuel Hernández López acknowledges CSIC for funding this work under the grant JAE-pre-2010. Daniel Lozano also acknowledges Comunidad Autónoma de Madrid for his post-doctoral research contract S-2009/MAT/1472. The authors report that they have a patent for the materials regarding their antimicrobial properties PCT/ES2011/070342.

REFERENCES

1. Brunette D, Tengvall P, Textor M, Thomsen M. Titanium in Medicine. Springer 2001.
2. Freese H, Volas MG, Wood J, Textor M. Titanium and its Alloys in Biomedical. Engineering. Encyclopedia of Materials: Science and Technology. Elsevier Ltd., Oxford 2001.
3. Rimondini L, Fini M, Giardino R. The microbial infection of biomaterials: A challenge for clinicians and researchers. A short review. J. Appl. Biomater. Biomech 2005;3(1):1-10.
4. Chung KK, Schumacher, James F, Sampson, Edith M, Burne, Robert A, Antonelli, Patrick J, Brennan, Anthony B. Impact of engineered surface microtopography on biofilm formation of Staphylococcus aureus. Biointerphases 2007;2(2):89-94.
5. Sarró MI, Moreno DA, Ranninger C, King E, Ruiz J. Influence of gas nitriding of Ti6Al4V alloy at high temperature on the adhesion of Staphylococcus aureus. Surf. Coat. Tech 2006;201(6):2807-2812.
6. Zhao L, Chu PK, Zhang Y, Wu Z. Antibacterial coatings on titanium implants. J. Biomed. Mater. Res B. 2009;91B(1):470-480.
7. Roy P, Berger S, Schmuki P. TiO2 Nanotubes: Synthesis and Applications. Angewe. Chem. Int. Edit. 2011;50(13):2904-2939.
8. Peremarch CP-J, Tanoira RP, Arenas MA, Matykina E, Conde A, Damborenea JJD, Barrena EG, Esteban J. Bacterial adherence to anodized titanium alloy. J. Phys: Conf. Series 2010;252(1):012011.
9. Pérez-Jorge C, Conde A, Arenas MA, Pérez-Tanoira R, Matykina E, de Damborenea JJ, Gómez-Barrena E, Esteban J. In vitro assessment of Staphylococcus epidermidis and Staphylococcus aureus adhesion on TiO2 nanotubes on Ti–6Al–4V alloy. J. Biomed. Mater. Res A 2012;100A(7):1696-1705.
10. Arenas MA, Pérez-Jorge C, Conde A, Matykina E, Hernández-López JM, Pérez-Tanoira R, de Damborenea JJ, Gómez-Barrena E, Esteba J. Doped TiO2 anodic layers of enhanced antibacterial properties. Colloids Surf B Biointerfaces 2013;105(0):106-112.
11. Monjo M, Lamolle SF, Lyngstadaas SP, Rønold HJ, Ellingsen JE. In vivo expression of osteogenic markers and bone mineral density at the surface of fluoride-modified titanium implants. Biomaterials 2008;29(28):3771-3780.
12. Lamolle S, Monjo M, Lyngstadaas S, Ellingsen J, Haugen J. Titanium implant surface modification by cathodic reduction in hydrofluoric acid: surface characterization and in vivo performance. J Biomed Mater Res A 2009;88:581-588.
13. Ellingsen JE. Pre-treatment of titanium implants with fluoride improves their retention in bone. J. Mater Sci: Mater. Med. 1995;6:749-756.

14. Isa Z, Schneider G, Zaharias R, Seabold D, Stanford C. Effects of fluoride-modified titanium surfaces on osteoblast proliferation and gene expression. Int. J. Oral. Maxillofac. Implan.t 2006;21:203-211.
15. Bellows CG, Heersche JNM, Aubin JE. The effects of fluoride on osteoblast progenitors in vitro. J. Bone. Miner. Res. 1990;5(SUPPL. 1):S101-S105.
16. Wergedal JE, Lau KHW, Baylink DJ. Fluoride and Bovine Bone Extract Influence Cell Proliferation and Phosphatase Activities in Human Bone Cell Cultures. Clin. Orthop. Relat. R. 1988;233:274-282.
17. Cooper LF, Zhou Y, Takebe J, Guo J, Abron A, Holmén A, Ellingsen JE. Fluoride modification effects on osteoblast behavior and bone formation at TiO2 grit-blasted c.p. titanium endosseous implants. Biomaterials 2006;27(6):926-936.
18. Masaki C, Schneider G, Zaharias R, Seabold D, Stanford C. Effects of implant surface microtopography onosteoblast gene expression. Clin. Ora.l Implants. Res. 2005;16:650-656.
19. Arenas M, Conde A, de Damborenea J, Matikyna E, Esteban J, Gómez-Barrena E, Pérez-Jorge C, Pérez Tanoira R. Materiales de titanio anodizado con fluor. PATENT 2010;PCT/ES2011/070342. Spain.
20. Lozano D, de Castro LF, Dapía S, Andrade-Zapata I, Manzarbeitia F, Alvarez-Arroyo MV, Gómez-Barrena E, Esbrit P. Role of Parathyroid Hormone-Related Protein in the Decreased Osteoblast Function in Diabetes-Related Osteopenia. Endocrinology 2009;150(5):2027-2035.
21. Deb S, Mandegaran R, Di Silvio L. A porous scaffold for bone tissue engineering/45S5 Bioglass® derived porous scaffolds for co-culturing osteoblasts and endothelial cells. J. Mater Sci: Mater. Med. 2010;21(3):893-905.
22. Lozano D, Feito MJ, Portal-Núñez S, Lozano RM, Matesanz MC, Serrano MC, Vallet-Regí M, Portolés MT, Esbrit P. Osteostatin improves the osteogenic activity of fibroblast growth factor-2 immobilized in Si-doped hydroxyapatite in osteoblastic cells. Acta Biomaterialia 2012;8(7):2770-2777.
23. Matykina E, Hernandez-López JM, Conde A, Domingo C, de Damborenea JJ, Arenas MA. Morphologies of nanostructured TiO2 doped with F on Ti–6Al–4V alloy. Electrochim. Acta 2011;56(5):2221-2229.
24. Matykina E, Conde A, de Damborenea J, Matín y Marero D, Arenas MA. Growth of TiO2-based nanotubes on Ti–6Al–4V alloy. Electrochim. Acta 2011;56(25):9209-9218.
25. Yao C, Perla V, Mckenzie JL, Slamovich EB, Webster TJ. Anodized Ti and Ti6Al4V Possesing Nanometer Surface Features enhances Osteoblast Adhesion. J. Biomed. Nanotechnol. 2005;2005:68-73.

26. Yao C, Slamovich EB, Webster TJ. Enhanced osteoblast functions on anodized titanium with nanotube-like structures. J. Biomed. Mater. Res A 2008;85A(1):157-166.
27. Das K, Bose S, Bandyopadhyay A. TiO2 nanotubes on Ti: Influence of nanoscale morphology on bone cell–materials interaction. J. Biomed. Mater. Res A 2009;90A(1):225-237.
28. Park J, Bauer S, von der Mark K, Schmuki P. Nanosize and Vitality: TiO2 Nanotube Diameter Directs Cell Fate. Nano Letters 2007;7(6):1686-1691.
29. Park J, Bauer S, Schlegel KA, Neukam FW, von der Mark K, Schmuki P. TiO2 Nanotube Surfaces: 15 nm—An Optimal Length Scale of Surface Topography for Cell Adhesion and Differentiation. Small 2009;5(6):666-671.
30. Zhao L, Mei S, Wang W, Chu PK, Zhang Y, Wu Z. Suppressed primary osteoblast functions on nanoporous titania surface. J. Biomed. Mater. Res A 2011;96(1):100-107.
31. Lamolle SF, Monjo M, Rubert M, Haugen HJ, Lyngstadaas SP, Ellingsen JE. The effect of hydrofluoric acid treatment of titanium surface on nanostructural and chemical changes and the growth of MC3T3-E1 cells. Biomaterials 2009;30(5):736-742.
32. Tiainen Hanna MM, Knychala J, Nilsen O, Lyngstadaas S. Petter, Ellingsen Jan Eirik, Haugen, Håvard J. The effect of fluoride surface modification of ceramic TiO2 on the surface properties and biological response of osteoblastic cells in vitro. Biomed. Maters. 2011;6.
33. Baylink D, Bernstein D. The effects of fluoride therapy on metabolic bone disease Clin. Orthop. Relat. R. 1967;55:51-85.
34.Bacakova L, Filova E, Parizek M, Ruml T, Svorcik V. Modulation of cell adhesion, proliferation and differentiation on materials designed for body implants. Biotechnol. Adv. 2011;29(6):739-767.
35. Baier R. Surface behaviour of biomaterials: The theta surface for biocompatibility. J. Mater Sci: Mater. Med. 2006;17(11):1057-1062.
36. Janssen MI, Leeuwen MBMv, Kooten TGv, Vries Jd, Dijkhuizen L, Wösten HAB. Promotion of fibroblast activity by coating with hydrophobins in the β-sheet end state. Biomaterials 2004;25(14):2731-2739.
37. Habazaki H, Fushimi K, Shimizu K, Skeldon P, Thompson G. Fast migration of fluoride ions in growing anodic titanium oxide. Electrochem. Commun. 2007;9:1222-1227.

3.5 Correlation of the nanostructure of the anodic layers fabricated on Ti13Nb13Zr with the electrochemical impedance response

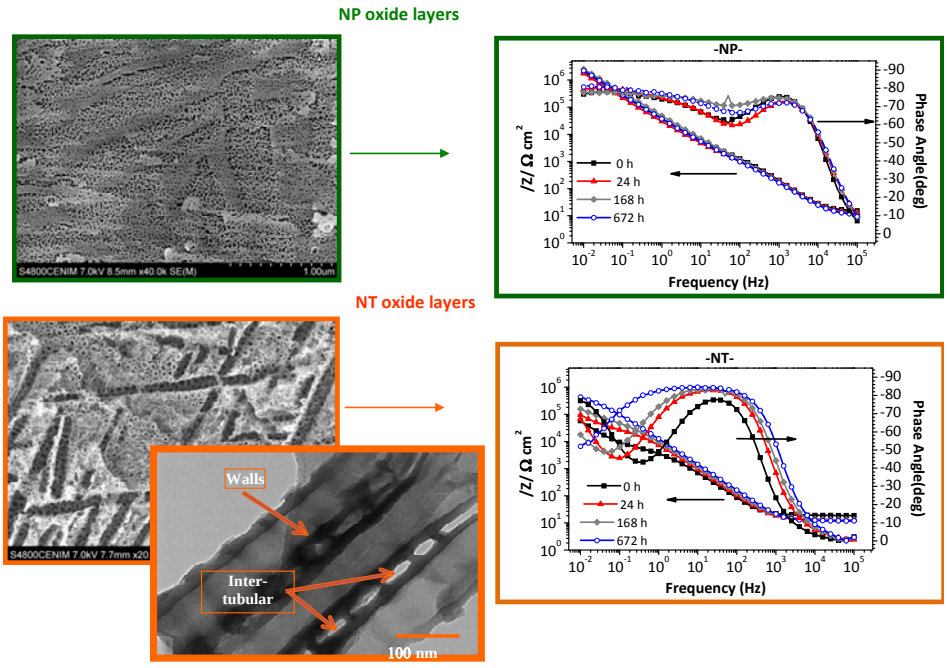

Correlation of the nanostructure of the anodic layers fabricated on Ti13Nb13Zr with the electrochemical impedance response

Como se ha mencionado a lo largo del manuscrito, la aleación Ti6Al4V ELI es ampliamente utilizado como material estructural en la mayoría de las prótesis de cadera o de rodilla. Sin embargo, la toxicidad del aluminio y el vanadio ha originado el desarrollo de aleaciones de titanio libres de estos elementos, siendo la aleación Ti13Nb13Zr una de las más prometedoras, ya que además de no poseer elementos perjudiciales para la salud humana, presenta un módulo de Young más cercano al del hueso.

En este apartado se estudia la generación de capas anódicas sobre la aleación Ti13Nb13Zr y la evaluación de su comportamiento electroquímico en una solución fisiológica simulada (PBS). Para ello, se emplea la microscopía electrónica de barrido y transmisión, la espectrometría de retrodispersión de Rutherford (RBS) y las técnicas electroquímicas de corriente continua (Curvas de polarización potenciodinámicas) y alterna (Espectroscopia de Impedancia Electroquímica -EIS-).

Los resultados muestran que la morfología de las capas anódicas depende del tiempo de anodizado, formándose una capa nanoporosa tras 5 minutos de anodizado y una capa nanotubular a los 60 minutos. La eficiencia del proceso de anodizado es superior al obtenido para la aleación Ti6Al4V bajo las mismas condiciones. Así mismo, se observó que las capas con morfología nanoporosa muestran mayor resistencia a la corrosión y estabilidad electroquímica a largos tiempos de inmersión que las capas nanotubulares. Las capas nanotubulares presentan Este comportamiento, al igual que se describió en el apartado 3.3, se debe a la separación intertubular que presentan las capas nanotubulares haciendo que la respuesta que domina sea la del sustrato expuesto. Además, se realiza un extenso análisis de la respuesta obtenida mediante EIS, calculando las

capacitancias efectivas y relacionando estas con la morfología y propiedades de las capas anódicas en cada condición estudiada.

Este comportamiento está relacionado con la morfología de las capas anódicas, debido a que en el caso de las capas nanoporosas la respuesta electroquímica del sistema está gobernada por la respuesta de la capa barrera, mientras que las capas nanotubulares, la respuesta del sistema es fundamentalmente la de la capa de óxido nativo que crece entre los espacios intertubulares.

Este apartado reproduce íntegramente el texto del siguiente manuscrito:

J.M. Hernández-López, A. Conde, J.J. de Damborenea, M.A. Arenas, Correlation of the nanostructure of the anodic layers fabricated on Ti13Nb13Zr with the electrochemical impedance response, ***Corrosion Science***,94 (2015) 61-69. doi: 10.1016/j.corsci.2015.01.041

que se encuentra en la sección de **compendio de publicaciones** bajo el formato de la revista en la que fue publicado.

Correlation of the nanostructure of the anodic layers fabricated on Ti13Nb13Zr with the electrochemical impedance response

J.M. Hernández-López[1], A. Conde[1], J.J. de Damborenea[1], M.A. Arenas[1]

[1]National Centre for Metallurgical Research (CENIM-CSIC), Avda. Gregorio del Amo 8, 28040, Madrid Spain.

Abstract

TiO_2 layers on Ti13Nb13Zr were fabricated by anodizing in acidic fluorine solution, to determine the nanostructure and electrochemical stability in a PBS solution. The anodization process showed higher growth efficiency. The morphology of nanostructured layer is more homogenous and thicker layers are obtained in shorter times regarding to organic electrolytes. Additionally, nanostructured oxide films were electrochemically studied to correlate the protective properties of the anodic films with the morphology and nanostructure developed in each anodizing condition. The anodic layers grown at short times present nanoporous structure and higher corrosion resistance than those fabricated at longer times, which possess nanotubular structure.

Keywords: TiO_2 nanotubes; Electrochemical Impedance Spectroscopy**;** RBS; Ti13Nb13Zr alloy; Corrosion.

1. Introduction

The biological response and the success of an implant depend on the physicochemical properties of the surface. Surface modification of titanium alloys is required to improve their biological activity and enhance bone formation [1, 2]. Pure titanium and Ti6Al4V ELI alloys are widely used as structural and/or functional biomaterials for artificial implants. However, the high cytotoxicity of vanadium and the relationship between aluminium and the senile dementia of Alzheimer type has promoted the need for the development of new Ti alloys for medical purposes [3].

Different alloying elements such as Fe, Cr, Mo, Nb, Sn, Ta and Zr, have been used to replace them. These alloying elements are β stabilizers. The β-

titanium alloys offer the highest strength to weight ratios and very attractive combinations of strength, toughness, and fatigue resistance at large cross sections[4, 5]. Particularly promising is the near-β Ti13Nb13Zr alloy which reduced the Young's modulus to 64-83 GPa, closer to the bone, regarding the α+β Ti6Al4V alloy -105-120 GPa- [1, 5-7].

On the other hand, as Minagar [8] pointed out, the surface of an implant needs modification to optimize the properties of the implant and to maximize its bioactivity when interfacing with natural tissue. The surface functionalization enhances both osseointegration and bioactivity, avoiding bacterial adhesion. Among other methods, anodization is a relatively simple method to fabricate a variable thickness and uniform nanostructured layer of TiO_2 on a titanium alloy surface. For titanium alloys, the oxide layer exhibits different properties depending on its microstructure as well as the processing parameters, mainly the time and potential, the electrolyte composition and the temperature. This allows the doping of the nanostructure with ions such as F which has been considered of interest as a way to provide antibacterial and osseointegration properties [1, 9-11]. Since the presence of fluoride decreases the adhesion of bacteria to the implant surface, it would increase the probability of success of the implant [12, 13].

Additionally, in order to have a long term successful implant, the electrochemical corrosion behaviour of TiO_2 anodic layers is the most important issue. Corrosion is one of the greatest challenges for ensuring the biostability and biocompatibility of metallic implants. The electrochemical behaviour of the anodic layers will depend on their interaction with the surrounding environment. It must therefore be considered the behaviour of the Ti modified surface in physiological medium to assess the nature of the passive film formed [14, 15] since a high corrosion resistance will ensure that metallic ions will not be released from implants into the bloodstream. In this sense, the β-titanium alloys, such as Ti-xZr, Ti-xNb-yZr-zTa, Ti-xNb-yTa and Ti-xNb-yZr, have been evaluated from corrosion viewpoint in different solutions. The results pointed out that these titanium alloys may show higher corrosion

resistance than CP titanium and Ti-6Al-4V alloy due to the growth of a more compact and stable native passive film composed of a mixture of protective oxides (TiO2, Nb2O5, ZrO2, Ta2O5) [15-21].

The aim of this study is to analyze the corrosion behaviour of anodic films grown on Ti13Nb13Zr in a fluoride containing solution. The samples were fully characterised by scanning electron microscope (SEM), Rutherford backscattering spectroscopy (RBS), potentiodynamic polarization and electrochemical impedance spectroscopy (EIS) to elucidate their electrochemical behaviour in a phosphate buffered saline solution (PBS).

This work shows that a thorough analysis of the impedance response supplies relevant information about the nanostructure of the anodic films, allowing the estimation of the thickness of the barrier layers and, the influence of the inter-tubular space size in the protective properties of the anodic layer. Moreover, the microstructural values obtained from the impedance measurements reveal a good correlation with the SEM and TEM microstructural examination.

2. Experimental

Rolled bars of Ti13Nb13Zr alloy were supplied by Xian Saite Metal Materials Development Co., Ltd. (China). Specimens of 28mm Ø of Ti13Nb13Zr (mass%) alloy were ground through successive grades of SiC paper up to 4000 grade. The samples were degreased with detergent and rinsed with tap water followed by deionized water.

Anodic layers were formed in a two-electrode cell by anodizing the specimens at constant voltage at 20 V in the electrolyte containing 1 M H2SO4 and 34.5 mM HF for 5 and 60 minutes at constant temperature at 20 oC. Platinum mesh was used as cathode.

The cross sections and plan views of anodic films were examined by field emission gun scanning electron microscopy (FEG-SEM) using JSM6500F Philips instrument, at 15 keV for EDS analysis and 7 keV for secondary electron imaging. Electron-transparent sections were prepared by scratching the surface of anodized specimens with a scalpel and collecting

the pieces of the oxide on a TEM grid. These pieces were observed by TEM, using a JEOL JEM 2100 instrument operated at 200 kV.

The stoichiometric composition of the oxide films was further determined by Rutherford backscattering spectrometry (RBS), using He^+ ions with the energy of 3.045 MeV (resonant energy for $^{16}O(\alpha, \alpha_0)^{16}O$ reaction), produced by the van de Graff accelerator of the Centro de Micro-Análisis de Materiales (CMAM), Madrid. The incident ion beam with the diameter of 1 mm was normal to the specimen surface with 10 μC doze scattered ions detected by a mobile detector at 165°. Data were interpreted using the SIMNRA program.

The electrochemical measurements were done in triplicate in a conventional three electrode cell. The working electrodes were the non-anodized and anodized NP and NT-specimens, with an area around to 0.32 cm2 exposed to the aggressive solution; an Ag/AgCl electrode (saturated KCl), was used as reference electrode and the counter electrode was a platinum wire with an area about 0.240 cm2. The electrolyte was a phosphate buffered saline solution (PBS), containing 150 mM NaCl, 9.99 mM KH_2PO_4, and 9.02 mM $Na_2H_2PO_4$; with a pH range between 7.2-7.4. All the tests were carried out at 37±2 °C. Corrosion behaviour was evaluated by potentiodynamic polarization and electrochemical impedance spectroscopy using a Gamry Reference 600 potentiostat. The potentiodynamic curves were conducted at a scan rate of 0.16 mV/s. Before starting the scan, the sample remained in the solution for 1 hour to stabilize the open circuit potential (OCP). The potential scan was started in the anodic direction from a potential value of −0.3 V with respect to the OCP to 3 V with respect to the Ag/AgCl electrode where the reverse scan started. A wide enough potential sweep was chosen in order to determine the breakdown potential of the specimens, to be compared with the values reported of various implant materials. For Cp-Ti and Ti-6Al-4V, the breakdown potentials of 2.4 and 2.0 V, respectively have been reported in Hank's solution [22].

EIS measurements were performed applying a sinusoidal signal of 10 mV of amplitude vs. OCP to guarantee that the electrochemical response of the system is linear. The frequency range was from 100 kHz to 10 mHz, and recording 10 points per decade was done. Measurements were carried out periodically during 4 weeks of immersion. The experimental data were analyzed using the ZVIEW software. The quality of fitting was judged by the values of the Chi-square, which is the square of the standard deviation between the original data and the calculated spectrum. It is considered a good fitting when the Chi-square was $<10^3$.

3. Results and discussion

The microstructure of the Ti13Nb13Zr alloy is martensitic with finely dispersed α-phase precipitated in a β-matrix. The microstructure within the prior beta grain boundaries is acicular, Fig. 1a [23]. The EDS analysis - Fig. 1b- shows only the peaks of Ti, Nb and Zr, with a chemical composition of 81.12 ± 2.32, 9.2 ± 1.32 and 9.68 ± 1.13 at.%, respectively. The α-phase is enriched in Zr (neutral element). The neutral elements do not have marked effect on the stability of either of the phase but form solid solutions with titanium. On the other hand, other works pointed out that the grains are refined first and then coarsened with the increase of Zr content. It is also found that Zr element added to titanium alloys has both the solution strengthening and fine-grain strengthening effect, and affects the lattice parameters. The β-matrix is enriched in Nb which is a β-stabilized element [5, 24, 25].

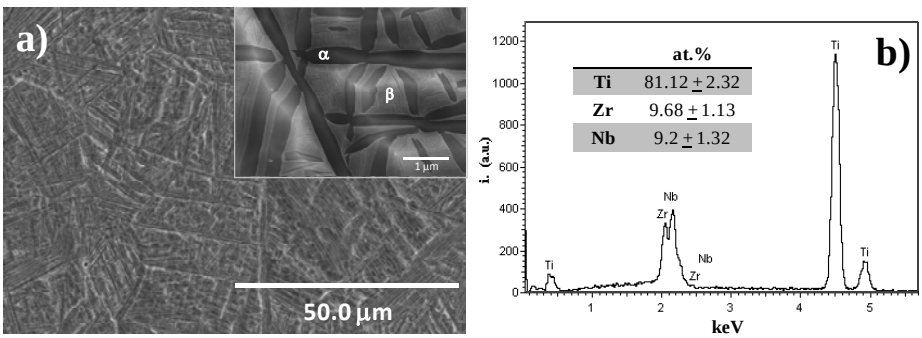

Figure 1. a) Microstructure of the Ti13Nb13Zr alloy. b) EDS analysis of the Ti13Nb13Zr alloy.

The current density transients were recorded during anodizing process at 5 and 60 minutes in H_2SO_4/HF -Fig. 2-. It can be observed that for the 60 minutes treatment the current density reaches the steady state after 9 minutes. The charge density passed during the initial surge followed by a rapid decay was 0.1308 and 0.1646 C/cm^2 for 5 and 60 minutes respectively, by applying the Faraday law and assuming 100% efficiency of the process, the estimated thickness of the amorphous barrier layer grown is 71 and 89 nm.

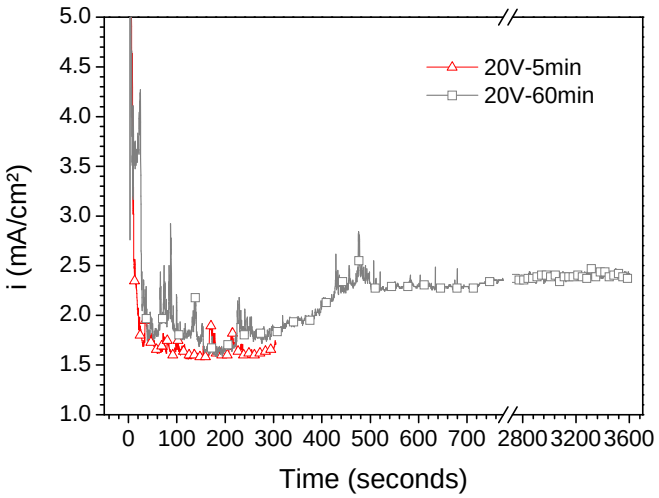

Figure 2. Current density–time response for anodizing of the Ti13Nb13Zr alloy at 20V in H_2SO_4/HF electrolyte.

Shorter anodizing times, 5 minutes, result in nanostructured layers with a porous morphology -NP- in both α and β phases, Fig. 3a, characterized by a pore diameter of ~25 nm and a total thickness around 71 ± 7 nm, Fig 3b. Conversely, the anodic film grown for 60 minutes shows a nanotubular structure -NT-, with nanotubes diameter ranging from ~75-100 nm, with inter-tubular distances about 15 nm and an average thickness about 900 ± 100 nm -Fig. 3c and d-. The variability in circumferential shape, length and diameter observed in the nanotubes depends on the phase in which the nanotubes grow. These variations can be explained by the different dissolution rates of the oxides grown in α and β phases due to their differences in chemical composition as reported for nanotubes fabricated in Ti35Nb5Zr [26] and in Ti-50Ta [27].

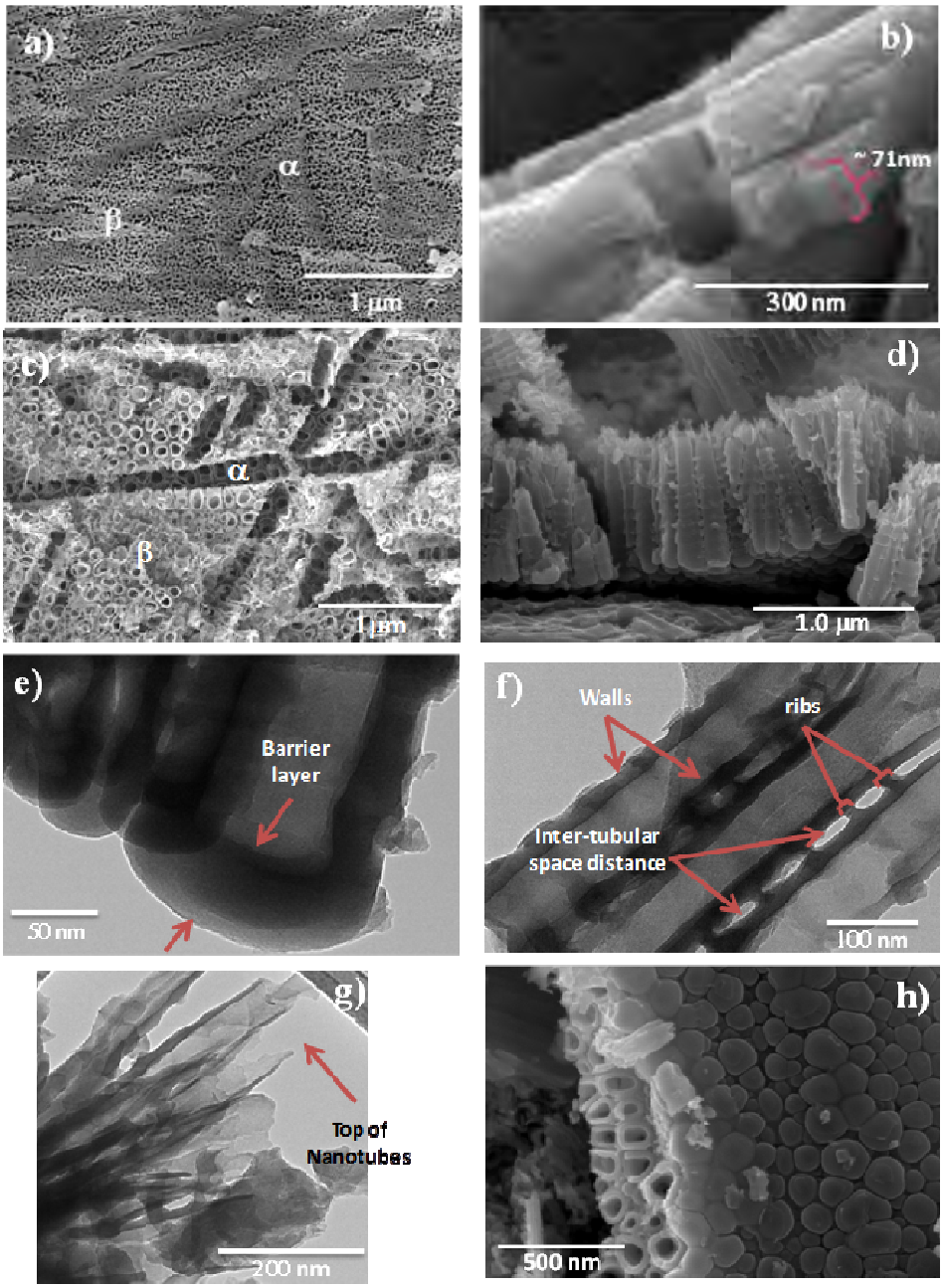

Figure 3. Morphology of the anodic layers grown at 5min -NP-(a), and 60 min -NT-(c) with its respective cross-section (b and d). TEM views of the barrier film (e), body, top and bottom of the NT layers respectively (e-h).

The thickness of the NT layer obtained in this alloy is notably higher than those obtained in Ti6Al4V alloy using the same anodizing conditions [10], and similar to those obtained in TixNbyZr alloys grown in other acidic solutions [28] and in organic electrolytes [26], but, in much shorter times as result of the higher concentration of oxygen in the aqueous solutions with respect to the organic solutions; and the higher migration rate of the anions from the electrolyte (O^{2-}, SO_4^{2-} and F^-) in presence of the electric field, which depends on the ion size and electrical conductivity of the electrolyte.

NT layers disclose a reproducible 40 nm thick barrier layer, Fig 3e, and the nanotube wall thickness was reduced from about ~15 nm at the bottom, Fig. 3f, to around 7 nm at the mouth of the nanotube, Fig. 3g. The thinning of the nanotube walls towards the outer part of the film has been previously described for nanotube formation on pure titanium [29] and Ti6Al4V alloy [10], and it is related to continuous dissolution of TiO_2 and TiF_4 along the entire nanotube length. Formation of ribs of about 13 nm thick on the nanotube walls (Fig. 3f) is also observed for the NT layers. Ribs are suggested to arise as a consequence of the dissolution of TiF_4 of the walls increasing the inter-space distance between nanotubes, subsequent access of the electrolyte in the interstice and re-growth of the barrier film in the interpore region [29-32].

The accurate elemental composition of the film was determined using RBS and average molecular compositions of the NP and NT anodic layers were derived (Table 1, Fig. 4). The spectrum for NT layer showed a steeper slope than the NP film which can be explained due to the different morphology and thickness of the layers. The composition of the anodic layer is estimated by simulating the RBS spectra using successive layers with different composition and thickness. The average molecular composition is determined with the total atoms obtained for the different elements, e.g. Ti, O, Zr, Nb and F, in all the layers used to simulate the spectrum and assuming the formation of different compounds. In the present case, the average molecular composition of the anodic layer was firstly calculated assuming the formation of TiO_x, ZrO_2, Nb_2O_5 and TiF_4. However, the amount

of oxygen in the layers did not allow forming these stoichiometric oxides and the formation of ZrF_4 and NbF_5 had to be assumed.

Film	10^{17} atoms*cm^{-2} / at%					Average molecular composition	Efficiency %
	Ti	O	F	Nb	Zr		
20V,5min NP	5.46 / 46.38	2.68 / 22.79	1.57 / 13.36	0.90 / 7.64	1.16 / 9.83	$(TiNbZr)O_{0.45}$ $0.081TiF_4$ $0.102NbF_5$ $0.081ZrF_4$	~56.57
20V,60min NT	36.07 / 42.09	24.73 / 28.86	10.26 / 11.97	8.17 / 9.54	6.47 / 7.54	$(TiNbZr)O_{0.61}$ $0.078TiF_4$ $0.098NbF_5$ $0.078ZrF_4$	~27.36

Table 1. Composition of the anodic layers formed on Ti13Nb13Zr in H_2SO_4/HF electrolyte, determined using RBS.

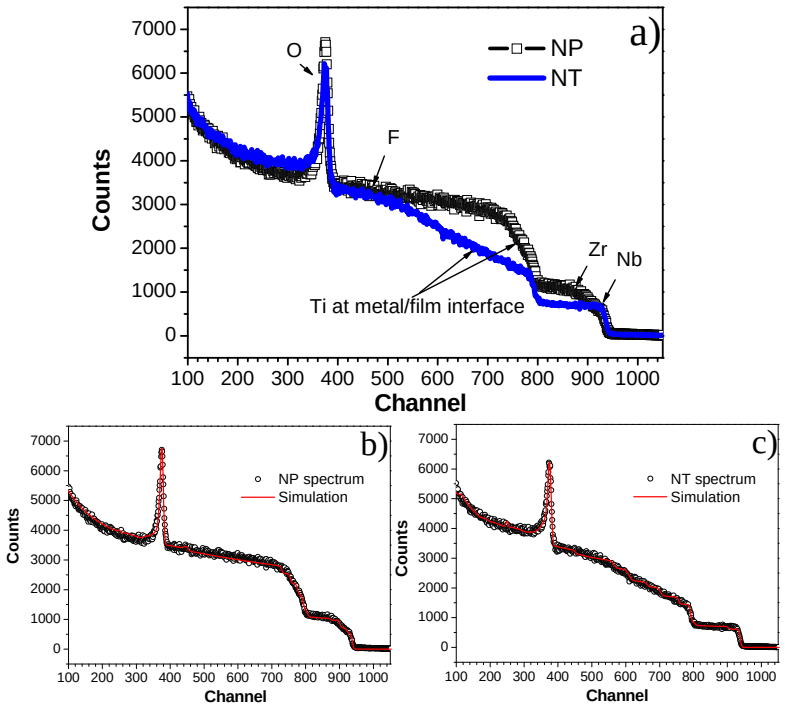

Figure 4. RBS spectra for both treatments in Ti13Nb13Zr alloy (a), anodizing to 20 V-5 minutes (experimental and simulated spectra- red line-) (b) and 20 V-60 minutes (experimental and simulated spectra-red line-) (c).

The RBS analysis indicates that the average molecular composition of the anodic film grown on Ti13Nb13Zr alloy can be expressed as

$(TiNbZrO)_{0.45}$·0.081TiF_4·0.102NbF_5·0.081ZrF_4 for NP layers and $(TiNbZrO)_{0.61}$·0.078TiF_4·0.098NbF_5·0.078ZrF_4 for NT layers -Table 1-. The presence of ZrF_4 and NbF_5 is in agreement with previously reported for the anodic films grown on TiZr and TiNb alloys in which found ZrF_4 and NbF_5, respectively [33, 34].

The RBS analysis reveals that the films contained 13.36 at.% of fluorine in NP and 11.92 at.% of fluorine in NT. This decrease in the fluorine content of the layers obtained at longer anodization time, apparently occurs due to dissolution of TiF_4 present in the walls of the nanotubes [10, 31, 32, 35]. Nevertheless, these contents are slightly higher in comparison to the anodic films grown in Ti6Al4V alloy, which showed enhanced antibacterial properties decreasing the adherence of two types of bacteria responsible for most of the prosthetic joints infections [9-11, 36].

The efficiency of the film growth was derived as a ratio of titanium ions present in the film (as determined by RBS) to titanium ions due in the film according to the charge density passed during the anodizing Table 2, assuming that all the charge was used for oxidation of titanium. The efficiency reduced drastically with increase the anodizing time from 56.6 % to 27.4 %, which is higher than those obtained for TiO_2 layers grown on Ti6Al4V under the same conditions [28] or in glycerol at similar times than those used in the present work [37].

Time Anodization (minutes)	**Charge (C/cm^2)**	**Oxidized titanium [a] (nm)**	**Total Oxide thickness (nm)**	
			Expected[b]	Experimental[c]
5	0.619	170	340	~70
60	8.471	2329	4600	~900

a Calculated for pure titanium assuming 100% current efficiency
b Calculated for compact amorphous film assuming 100% current efficiency
c Measured using SEM

Table 2. Parameters of the anodic films formed in the fluoride solution.

The electrochemical stability of the anodic films was determined by potentiodynamic polarization curves performed in PBS -Fig.5-. Before the

onset of the potential sweep, the evolution of the open circuit potential was recorded. As can be seen in Figure 5a, the OCP is stabilized after one hour of immersion for all the specimens. The non-anodized and the NT specimens disclosed similar values around -0.300 V vs. Ag/AgCl and the NP specimens show more negative values, around -0.560 V vs. Ag/AgCl. Figure 5b gathers the polarization curves of each specimen. Both the non-anodized and the NT specimens have a passive behaviour characterized by a vertical anodic branch with a passive current density -i_{pass}- of $1.1 \cdot 10^{-6}$ A/cm^2. NT revealed an increase in current density in the anodic branch until the i_{pass} is reached, consequence of the oxidation of the substrate exposed to the solution through the inter-tubular-space. Córdoba-Torres et al. [38] reported similar passive current densities for nanotubes fabricated in an organic electrolyte on pure Ti foils. Conversely, the NP layer shifted the anodic branch towards lower i_{pass} values, $2.9 \cdot 10^{-7}$ A/cm^2. This anodic layer showed a high stability along the test with a passive behaviour in the whole anodic branch and lower dissolution rates compared to both NT and non-anodized specimens, which implies a lower amount of metallic ions delivered to the solution. Moreover, the i_{pass} is one order of magnitude lower than those reported for specimens produced by different immersion treatments performed to thicken the native oxide film on Ti13Nb13Zr alloy [18, 39]. The non-anodized sample showed a slight increase of the current around to 1.3 V vs. Ag/AgCl (~1.5 V vs. ENH). This can be associated to the transpasivation behaviour of the titanium alloy. At this potential, as is observed into Pourbaix diagrams [40], the titanium oxide layer present on the surface of the alloy oxidizes forming soluble species of Ti(VI).

On the other hand, the corrosion potential, E_{corr}, of the non-anodized specimen is -0.340 V vs. Ag/AgCl. A similar value is recorded for the NT specimen, -0.363 V vs. Ag/AgCl, due to the exposure of the oxidized alloy placed at the bottom of the intertubular space. Conversely, the NP films show a E_{corr} more cathodic, about -0.459 V vs. Ag/AgCl.

Therefore, the E_{corr} and i_{pass} values of the NT specimens are similar to those recorded for the non-anodized titanium alloy suggesting that the electrochemical response of the NT is mainly due to the oxidation of the

substrate exposed through the inter-tubular spaces instead of the barrier layer at the bottom of the nanotubes. Finally, it is important to highlight that both non-anodized sample and the anodic films did not show susceptibility to localized corrosion in the whole potential sweep since there was no evidence of breakdown potential in the potentiodynamic curves.

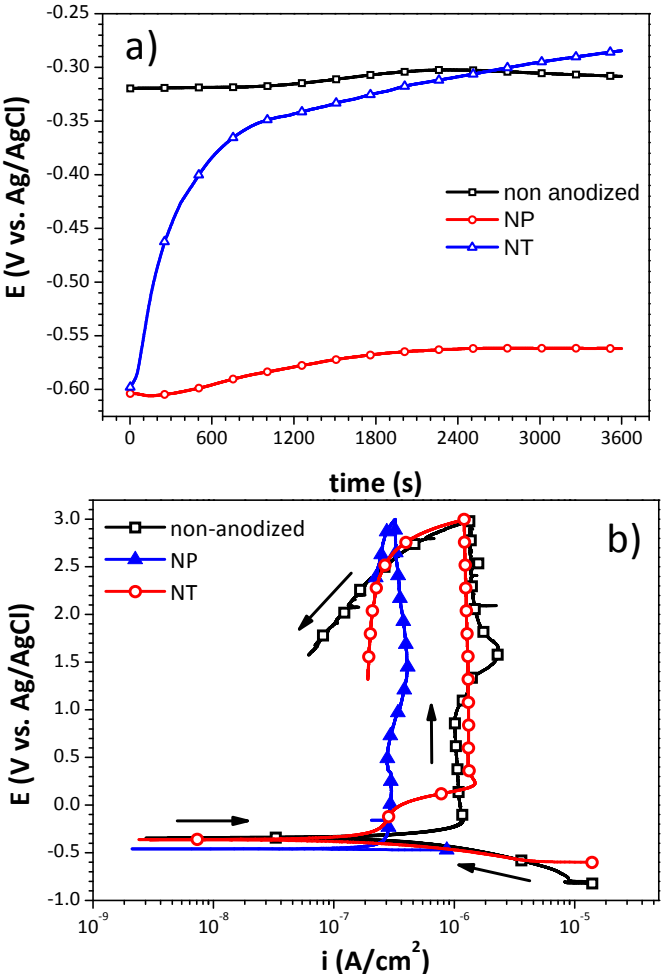

Figure 5. a) Evolution of the open circuit potential and b) potentiodynamic polarization curves for the non-anodized specimen, NP and NT layers in PBS solution at 37°C.

Impedance measurements were performed during long immersion times to study the electrochemical processes that take place during the immersion

in PBS. Fig. 6a shows the evolution of the impedance diagrams of the non-anodized specimen. At shorter immersion times, 0.25 and 24 hours, the response can be modelled by a Randles circuit, where Re is the electrolyte resistance, R_{ct} is the charge transfer resistance and C_{dl} is the capacitance of a metallic surface covered by a native oxide film. At longer immersion times, the system behaves as a blocking electrode. In this case, the response of the system can be modelled by a resistance (R_e) in series with a capacitance (C_{dl}).

Table 3 summarizes the values of these parameters. As can be seen, although the Chi-square obtained is quite high (>10^0) the capacitance values from the simulations correspond to that expected for the capacitance of an oxidized metallic surface. The use of the capacitance in the equivalent circuit, to model the response of the native oxide layer of the substrate, sheds some light on the discussion regarding to the reliability of the estimated values of the thickness of the oxide layer.

Ti13Nb13Zr (non-anodized specimen)				
Circuit parameter	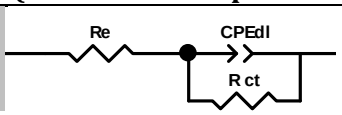		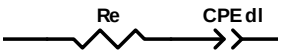	
Time (h)	0.25	24	168	672
R_e (Ω·cm²)	8.97	7.31	7.76	6.93
C_{dl} (μF/cm²)	42.58	23.85	14.99	13.68
R_{ct} (MΩ·cm²)	0.37*	1.27**	-	-
Chi-sqr (10^{-3})	370	390	5870	10640
d (nm)	0.69	1.23	1.95	2.14

*Estimated error for R_{ct} : 11%; ** Estimated error for R_{ct} : 17%

Table 3. Electrical parameters values of the unmodified specimen, including the electrical equivalent circuit used to fit the spectra.

Nevertheless, the experimental data were also simulated by the same equivalent circuits but using constant phase element, CPE, to fit the

capacitances. The quality of the fitting notably improves leading to Chi-square values about 10^{-3} (values included in Table 4).

The capacitance is related to film thickness according to [41] as:

$$C = \frac{\varepsilon\varepsilon_0}{d} \qquad [1]$$

where C is the capacitance in F/cm², ε is the dielectric constant of the surface and ε_0 is the vacuum permittivity, and d the thickness. The thickness of the native oxide film formed on the surface has been estimated assuming the value ε=33 for an amorphous TiO_2 oxide [42].

		Ti13Nb13Zr (unmodified specimen)			
	Circuit parameter	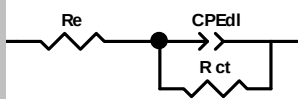		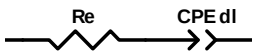	
	Time (h)	**0.25**	**24**	**168**	**672**
	R_e (Ω·cm²)	8.79	7.10	7.24	6.33
	CPE_{dl} ($\mu Ss^n/cm^2$)	54.68	29.82	19.42	20.13
	α	0.92	0.93	0.92	0.90
	R_{ct} (MΩ·cm²)	0.69	3.21	---	---
	Chi-sqr (10^{-3})	3.97	0.94	3.73	5.2
2-D distribution	**C_{eff} (μF/cm²)**	28.11	15.77	-	-
	$d_{2\text{-}D}$ (nm)	1.03	1.85	-	-
Blocking electrode	**C_{eff} (μF/cm²)**	-	-	8.98	7.43
	$d_{B\text{-}e}$ (nm)	-	-	3.25	3.93

Table 4. Electrical parameters values of the non-anodized specimen, including the electrical equivalent circuit with CPE used to fit the spectra. Thickness values of the oxide film formed on the unmodified specimen estimated from different effective capacitances, C_{eff}.

Using the values of the fitted parameters for C_{dl}, in Table 3, the thickness of the native oxide layer of the non-anodized sample showed a coarsening with immersion time, from ~0.69 nm to ~2.14 nm, after 672 h, Table 3.

However when a CPE is used to model the double layer capacitance due to the non-ideal interface conditions of the surface, attributed to roughness, non-uniform distribution of the current density on the surface, and/or a distribution of dielectric relaxation times [43, 44], the conversion to capacitance from the CPE parameters -the magnitude (Q) and the exponent (α)- is not so straightforward. In order to estimate the values of the capacitance from CPE, different approaches have been done. Hirschorn et al. published a complete study about the applicability of capacitance-CPE relations depending on the appropriate time-constant distribution function. These authors distinguished between surface and normal time-constant distributions [41]. For a surface time-constant distribution (2-D distribution), the effective capacitance, C_{eff}, associated with the CPE can be expressed as followed:

$$C_{eff} = Q^{1/\alpha}\left[{R_e}^{-1} + {R_t}^{-1}\right]^{\alpha-1/\alpha} \qquad [2]$$

when the impedance of the CPE is expressed using $Z_{CPE} = \frac{1}{Q(jw)^{\alpha}}$

where Q is the magnitude of the CPE, α is exponent of the CPE, R_e is the electrolyte resistance, and R_t is the polarization resistance. This expression is equivalent to that defined by Brug et al. [45] for a surface distribution with a different definition of the Z_{CPE} parameters, $Z_{CPE}= Q/(jw)^{1-\alpha}$.

In the limit that R_{ct} becomes infinitely large, for a blocking electrode, the equation (2) becomes:

$$C_{eff} = Q^{1/\alpha} * {R_e}^{1-\alpha/\alpha} \quad [3]$$

Table 4 shows the thickness of the native oxide layer, d_{eff}, of the non-anodized specimens using equation (2) and the C_{eff} calculated from the CPE using the equations (3) -2-D distribution- or (4) -blocking electrode-. Although the values also showed the same increasing trend, than that estimated from the C_{dl}, the thickness values calculated from C_{eff} are slightly higher and are of the same order than those reported in literature for titanium and titanium alloys[46]. Moreover, the initial values for the thickness of the native oxide are more consistent than that described using the C_{dl} parameter, which value appears to be too low, 0.69 nm.

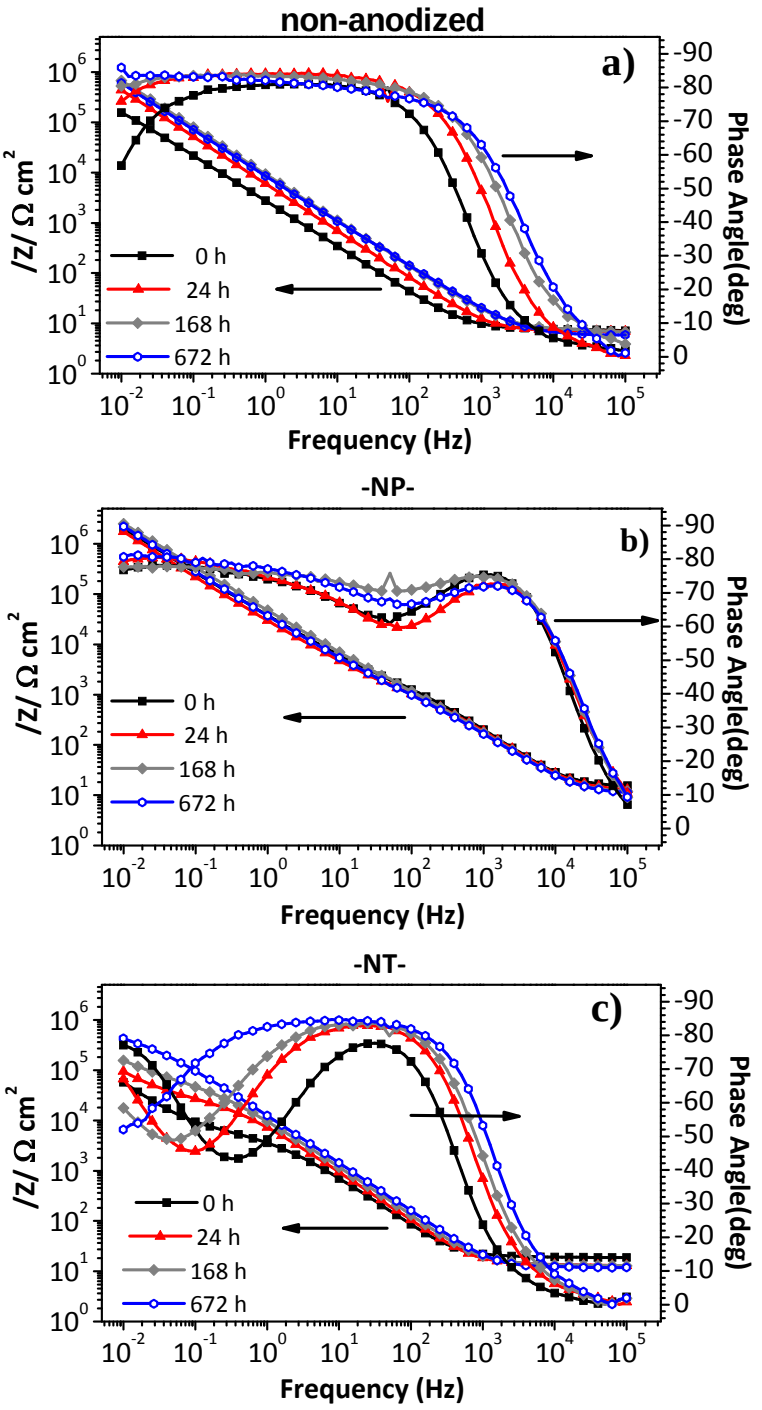

Figure 6. EIS Bode diagrams corresponding to the non-anodized specimen (a), NP (b) and NT (c) layers at different immersion times.

On the contrary, NP and NT specimens exhibit more complex impedance responses. The NP specimens -Fig. 6b- show two time-constants placed at high-medium frequencies (~10^5-10^2 Hz) related to the response of the barrier layer at the bottom of the nanopores and at low-frequencies (~10^1-10^{-2} Hz) due to the contribution of a diffusion process across the layer. Both time constants remain steady until the end of the test. This system can be modelled by a CPE_i in parallel with a resistance R_i, which is in series with a diffusional element, W. The diffusional element, W, is modelled by a CPE_w. In this NP layer, the CPE_i and R_i correspond to the electrical properties of the barrier layer.

The EIS spectra of the NT specimens -Fig. 6c- also show two time constants as the NP specimens but, they are placed in different frequency ranges suggesting that different mechanisms are occurring. An important contribution is observed at low-frequency range (~10^0-10^{-2} Hz) at early immersion times that evolves with time. The low-frequency response becomes more relevant and dominates over the time constant recorded at medium-frequency (~10^3-10^0 Hz). Both contributions correspond to the response of the substrate, which is covered by a native oxide, placed at the bottom of the inter-tubular space, Fig. 3f. As the PBS solution penetrates through the inter-tubular space and reaches the alloy, Fig. 3h, the current flows through the lower resistance path, and therefore the contribution of the substrate dominates the impedance response of the NT. The time constant at medium-frequency relates to the capacitance of the substrate covered by a native oxide film exposed at the bottom of the inter-tubular space while the low-frequency response corresponds to the diffusive behaviour. The low-frequency contribution reveals that the diffusive response is more relevant at longer immersion times, since the native oxide layer at the bottom of the inter-tubular space thickens blocking the cathodic reaction.

The impedance spectra of the NT layers were modelled with the same equivalent circuit than NP, although the electrical parameters have different physical meaning. The CPE_i, R_i corresponds to the capacitance associated with the native oxide film and the charge-transfer resistance

respectively More recently, Cordoba-Torres et al. [38] suggest that an alternative impedance representation data using the effective CPE exponent parameter allow a more accurate analysis of the TiO_2 nanotube porous layers, pointing out that a third time constant can be identified for a TiO_2 double layered interface. Nevertheless, in the work, the authors consider that further studies are still required for a in-depth characterization.

Table 5 gathers the electrical equivalent circuits used and the electrochemical parameters obtained in the simulations for the NP and NT layers.

Circuit parameter		NP				NT			
		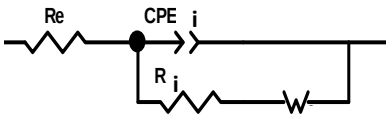							
Time (h)		**0.25**	**24**	**168**	**672**	**0**	**24**	**168**	**672**
R_e (Ω·cm²)		16.19	13.29	11.84	14.54	18.79	13.24	13.20	11.76
***CPE_i (µSs^n/cm²)**		1.37	1.08	1.28	1.54	30.55	21.70	16.81	13.62
α		0.94	0.97	0.95	0.93	0.93	0.95	0.95	0.95
***R_i (kΩ·cm²)**		1.16	0.76	1.06	1.09	5.59	25.11	46.24	145.47
W	**CPE_w(µSs^n/cm²)**	12.94	15.19	6.96	9.11	178.51	88.62	39.52	6.21
	α	0.66	0.63	0.68	0.67	0.86	0.79	0.67	0.42
Chi-sqr (10^{-3})		0.85	1.19	1.00	0.71	3.45			

*For the NP layers i means barrier layer (barrier); for the NT layers i means double layer (dl) for the CPE and charge-transfer for the resistance.

Table 5. Electrical parameters values of the NP and NT layers and electrical equivalent circuit used for simulation.

Additionally to the capacitance-CPE relations previously mentioned –2D distribution and blocking electrode-, Hirschorn et al.[41] also described that for a normal time-constant distribution (3-D distribution), the effective capacitance associated with CPE can be expressed as:

$$C_{eff} = Q^{1/\alpha} * {R_f}^{1-\alpha/\alpha} \quad [4]$$

where R_f is the film resistance. This equation is equivalent to that proposed by Hsu and Mansfeld [47] in terms of w_{max}:

$$C_{eff} = Q * {w_{max}}^{\alpha-1} \quad [5]$$

It draws attention that the equations (2), (3) and (4) have the same form, but the resistance used for the calculation of the C_{eff} is different in the three cases, being, respectively, the parallel combination of R_t and R_e for eq. (2), R_e for eq.(3) and R_f for eq. (4).

The effective capacitance (C_{eff}) calculated using equations (2) -2-D distribution- and (4) -3-D distribution- and the thickness of the oxide layers (d_{eff}) are presented in Table 6.

The determination of the oxide thickness, d_{eff}, from equation (1) has been estimated assuming that the dielectric constant of the oxide film are independent of position and ε=33 corresponding to the dielectric constant of TiO_2 amorphous has been used despite the composition of the anodic oxide is more complex, as it was obtained by RBS.

The d_{eff} of the NT and NP layers calculated using a 2-D distribution is higher than those found with a 3-D distribution, see Table 6.

		NP				NT			
	Time, h	**0.25**	**24**	**168**	**672**	**0.25**	**24**	**168**	**672**
2-D distribution	**C_{eff} (μF/cm²)**	0.68	0.73	0.75	0.72	17.39	14.13	10.8	8.6
	$d_{2\text{-}D}$ (nm)	42.98	40.06	38.85	40.5	1.68	2.07	2.71	3.4
3-D distribution	**C_{eff} (μF/cm²)**	0.9	0.98	0.93	0.98	26.7	21.02	16.59	14.12
	$d_{3\text{-}D}$ (nm)	32.53	33.37	31.28	29.85	1.09	1.39	1.76	2.07

Table 6. Thickness calculation of the oxide film of the NP and NT layers using a 2-D or 3-D time constant distributions to estimate the effective capacitance, C_{eff}.

For all immersion times, the thickness of the barrier layer of the NP specimens using the C_{eff} calculated from the 3-D distribution equation is about 32 nm and about 40 nm from the 2-D distribution equation. The latter is in agreement to that measured by SEM.

The NT layers showed thickness values of the oxide layers in the range of a few nanometers, from 1.68 to 3.40 nm using a 2-D distribution equation to estimate the C_{eff}, Table 6. Thus it is consistent with the evolution of the native oxide layer of the titanium alloy surface in the bottom of the inter-tubular space and not with the thickness of the barrier layer of the nanotube measured by TEM, about 40 nm.

A time-constant distribution on TiO_2 nanotubes has been also explored by Tsui et al. [48]. These authors have used a transmission line model to represent the electrochemical interface of TiO_2 nanotubes grown in low water content organic electrolytes. These authors evaluate the dependence of the electronic transport properties with the presence of deep level defect states.

The EIS results suggest that the assumption of a surface time-constant distribution (2- D distribution) provides satisfactory values for the thickness of the barrier layer for the NP, but also for the coarsening of the native oxide film onto the non-anodized specimens and onto the substrate placed at the bottom of the inter-tubular space in NT anodic films. This work shows that a careful analysis of the impedance response supplies relevant information about the nanostructure of the anodic films.

4. Conclusions

Anodizing of Ti-13Nb-13Zr alloy in H_2SO_4/HF electrolyte, at controlled voltage, proceeds with formation of nanostructured TiO_2 oxide either on α-phase and β-phase. The grown efficiency of the F-doped nanotubular oxide films in Ti13Nb13Zr is about 56 %, much higher efficiency than in organic electrolytes.

The composition of the nanostructured anodic layers (NP and NT) can be expressed as a oxide, $(TiNbZrO)_x$ with (x<1) and a mixture of fluoride compounds, TiF_4, NbF_5, ZrF_4.

Nanoporous anodic layers -NP- grown for 5 minutes show higher corrosion resistance than nanotubular layers, NT fabricated for 60 minutes, with superior barrier properties and long term electrochemical stability. The higher compactness of the NP layer -small pore size and the absence of interpores spaces- compared to NT layer appear to be the responsible for the better protective properties.

The impedance results show either the native oxide films or the anodic films present a two dimensional time–constant distribution. The careful analysis of the CPE supplies relevant information of the nanostructural parameters of the oxide layers, such as the barrier thickness and the presence of inter-tubular spaces through the layer that jeopardizes the protective properties.

The control of the nanostructure of the anodic layers fabricated on Ti13Nb13Zr is the key factor to fabricate oxide layers with better performance. Both the nanoporous morphology and the complex composition of the oxide, enhances the corrosion resistance.

Acknowledgements

This work was supported by Spanish Ministry of Science and Innovation under Consolider-Ingenio 2010-CSD-2008-0023-FUNCOAT Project and under the MAT2013-48224-C2-1-R-MUNSUTI Project. Hernández-López J.M. is receptor of the JAE-predoc grant funded by the CSIC.

Reference

[1] S. Bauer, P. Schmuki, K. von der Mark, J. Park, Engineering biocompatible implant surfaces: Part I: Materials and surfaces, Progress in Materials Science, 58 (2013) 261- 326.

[2] M. Peters, J. Hemptenmacher, J. Kumpfert, C. Leyens, Structure and Properties of Titanium and Titanium Alloys, in: Titanium and Titanium Alloys, Wiley-VCH 2005, pp. 1-36.

[3] A. Bigi, N. Nicoli-Aldini, B. Bracci, B. Zavan, E. Boanini, F. Sbaiz, S. Panzavolta, G. Zorzato, R. Giardino, A. Facchini, G. Abatangelo, R. Cortivo, In vitro culture of mesenchymal cells onto nanocrystalline hydroxyapatite-coated Ti13Nb13Zr alloy, Journal of Biomedical Materials Research Part A, 82A (2007) 213-221.

[4] G. Terlinde, G. Fischer, Beta Titanium Alloys, in: Titanium and Titanium Alloys. Fundamentals and Applications, Wiley-VCH Verlag GmbH & Co. KGaA, 2005, pp. 37- 57.

[5] M.T. Mohammed, Z.A. Khan, A.N. Siddiquee, Beta Titanium Alloys: The Lowest Elastic Modulus for Biomedical Applications: A Review, International Journal of Chemical, Nuclear, Metallurgical and Materials Engineering, 8 (2014) 1123-1127.

[6] M. Geetha, A.K. Singh, R. Asokamani, A.K. Gogia, Ti based biomaterials, the ultimate choice for orthopaedic implants – A review, Progress in Materials Science, 54 (2009) 397-425.

[7] I. Cvijović-Alagić, Z. Cvijović, J. Bajat, M. Rakin, Composition and processing effects on the electrochemical characteristics of biomedical titanium alloys, Corrosion Science, 83 (2014) 245-254.

[8] S. Minagar, C.C. Berndt, J. Wang, E. Ivanova, C. Wen, A review of the application of anodization for the fabrication of nanotubes on metal implant surfaces, Acta Biomaterialia, 8 (2012) 2875-2888.

[9] M. Arenas, A. Conde, J. de Damborenea, E. Matikyna, J. Esteban, E. Gómez-Barrena, C. Pérez-Jorge, R. Pérez Tanoira, Materiales de titanio anodizado con fluor, PATENT, PCT/ES2011/070342. Spain. (2010).

[10] E. Matykina, J.M. Hernandez-López, A. Conde, C. Domingo, J.J. de Damborenea, M.A. Arenas, Morphologies of nanostructured TiO_2 doped with F on Ti–6Al–4V alloy, Electrochimica Acta, 56 (2011) 2221-2229.

[11] C. Pérez-Jorge, A. Conde, M.A. Arenas, R. Pérez-Tanoira, E. Matykina, J.J. de Damborenea, E. Gómez-Barrena, J. Esteban, In vitro assessment of Staphylococcus epidermidis and Staphylococcus aureus adhesion on TiO_2 nanotubes on Ti–6Al–4V alloy, Journal of Biomedical Materials Research Part A, 100A (2012) 1696-1705.

[12] M. Quirynen, M. De Soete, D. Van Steenberghe, Infectious risks for oral implants: a review of the literature, Clinical Oral Implants Research, 13 (2002) 1-19.

[13] Z. Wang, Y. Shen, M. Haapasalo, Dental materials with antibiofilm properties, Dental Materials, 30 (2014) e1-e16.

[14] M. Aziz-Kerrzo, K.G. Conroy, A.M. Fenelon, S.T. Farrell, C.B. Breslin, Electrochemical studies on the stability and corrosion resistance of titanium-based implant materials, Biomaterials, 22 (2001) 1531-1539.

[15] V. Raman, S. Nagarajan, N. Rajendran, Electrochemical impedance spectroscopic characterisation of passive film formed over β Ti–29Nb–13Ta–4.6Zr alloy, Electrochemistry Communications, 8 (2006) 1309-1314.

[16] E.A. Ferreira, R.C. Rocha-Filho, S.R. Biaggio, N. Bocchi, Corrosion resistance of the Ti–50Zr at.% alloy after anodization in different acidic electrolytes, Corrosion Science, 52 (2010) 4058-4063.

[17] C. Vasilescu, S.I. Drob, E.I. Neacsu, J.C. Mirza Rosca, Surface analysis and corrosion resistance of a new titanium base alloy in simulated body fluids, Corrosion Science, 65 (2012) 431-440.

[18] A.K. Shukla, R. Balasubramaniam, Effect of surface treatment on electrochemical behavior of CP Ti, Ti–6Al–4V and Ti–13Nb–13Zr alloys in simulated human body fluid, Corrosion Science, 48 (2006) 1696-1720.

[19] S. Ningshen, U. Kamachi Mudali, P. Mukherjee, A. Sarkar, P. Barat, N. Padhy, B. Raj, Influence of oxygen ion irradiation on the corrosion aspects of Ti-5%Ta-2%Nb alloy and oxide coated titanium, Corrosion Science, 50 (2008) 2124-2134.

[20] J.M. Calderon Moreno, E. Vasilescu, P. Drob, P. Osiceanu, C. Vasilescu, S.I. Drob, M. Popa, Surface and electrochemical characterization of a new ternary titanium based alloy behaviour in electrolytes of varying pH, Corrosion Science, 77 (2013) 52-63.

[21] L.T. Duarte, S.R. Biaggio, R.C. Rocha-Filho, N. Bocchi, Surface characterization of oxides grown on the Ti–13Nb–13Zr alloy and their corrosion protection, Corrosion Science, 72 (2013) 35-40.

[22] M. Peters, J. Hemptenmacher, J. Kumpfert, C. Leyens, Structure and Properties of Titanium and Titanium Alloys, in: Titanium and Titanium Alloys. Fundamentals and Applications. Wiley-VCH Verlag GmbH & Co. KGaA, 2005, pp. 20.

[23] ASTM F1713-08(2013), Standard Specification for Wrought Titanium-13Niobium-13Zirconium Alloy for Surgical Implant Applications (UNS R58130), in, ASTM International, West Conshohocken, 2013.

[24] M. Geetha, A.K. Singh, K. Muraleedharan, A.K. Gogia, R. Asokamani, Effect of thermomechanical processing on microstructure of a Ti–13Nb–13Zr alloy, Journal of Alloys and Compounds, 329 (2001) 264-271.

[25] Y. Okazaki, Y. Ito, A. Ito, T. Tateishi, Effect of alloying elements on mechanical properties of titanium alloys for medical implants, Mater. Trans., JIM, 34 (1993) 1217-1222.

[26] S. Bai, D. Ding, C. Ning, R. Qin, L. Huang, M. Li, D. Mao, Anodic growth of uniform nanotube arrays on biphase Ti35Nb5Zr alloy, Electrochemistry Communications, 12 (2010) 152-155.

[27] H. Tsuchiya, T. Akaki, J. Nakata, D. Terada, N. Tsuji, Y. Koizumi, Y. Minamino, P. Schmuki, S. Fujimoto, Anodic oxide nanotube layers on Ti–Ta

alloys: Substrate composition, microstructure and self-organization on two-size scales, Corrosion Science, 51 (2009) 1528-1533.

[28] V. Saji, H. Choe, W. Brantley, Nanotubular oxide layer formation on Ti–13Nb–13Zr alloy as a function of applied potential, J Mater Sci, 44 (2009) 3975-3982.

[29] A. Valota, D.J. LeClere, P. Skeldon, M. Curioni, T. Hashimoto, S. Berger, J. Kunze, P. Schmuki, G.E. Thompson, Influence of water content on nanotubular anodic titania formed in fluoride/glycerol electrolytes, Electrochimica Acta, 54 (2009) 4321-4327.

[30] D. Regonini, C.R. Bowen, A. Jaroenworaluck, R. Stevens, A review of growth mechanism, structure and crystallinity of anodized TiO_2 nanotubes, Materials Science and Engineering: R: Reports, 74 (2013) 377-406.

[31] P. Roy, S. Berger, P. Schmuki, TiO_2 nanotubes: synthesis and applications, Angewandte Chemie, 50 (2011) 2904-2939.

[32] C.A. Grimes, G.K. Mor, TiO_2 Nanotube Arrays: Synthesis, Properties, and Applications, in, Springer, 2009, pp. 358.

[33] S. Minagar, C.C. Berndt, T. Gengenbach, C. Wen, Fabrication and characterization of TiO_2-ZrO_2-$ZrTiO_4$ nanotubes on TiZr alloy manufactured via anodization, Journal of Materials Chemistry B, 2 (2014) 71-83.

[34] J. Fornell, N.T.C. Oliveira, E. Pellicer, N. Van Steenberge, M.D. Baró, C. Bolfarini, J. Sort, Anodic formation of self-organized Ti(Nb,Sn) oxide nanotube arrays with tuneable aspect ratio and size distribution, Electrochemistry Communications, 33 (2013) 84-87.

[35] E. Matykina, A. Conde, J. de Damborenea, D.M.y. Marero, M.A. Arenas, Growth of TiO_2-based nanotubes on Ti–6Al–4V alloy, Electrochimica Acta, 56 (2011) 9209-9218.

[36] M.A. Arenas, C. Pérez-Jorge, A. Conde, E. Matykina, J.M. Hernández-López, R. Pérez-Tanoira, J.J. de Damborenea, E. Gómez-Barrena, J. Esteba, Doped TiO_2 anodic layers of enhanced antibacterial properties, Colloids and surfaces. B, Biointerfaces, 105 (2013) 106-112.

[37] A. Valota, D.J. Leclere, T. Hashimoto, P. Skeldon, G.E. Thompson, S. Berger, J. Kunze, P. Schmuki, The efficiency of nanotube formation on titanium anodized under voltage and current control in fluoride/glycerol electrolyte, Nanotechnology, 19 (2008) 355701.

[38] P. Córdoba-Torres, N.T.C. Oliveira, C. Bolfarini, V. Roche, R.P. Nogueira, Electrochemical impedance analysis of TiO_2 nanotube porous layers based on an alternative representation of impedance data, Journal of Electroanalytical Chemistry (2014), doi:10.1016/j.elechem.2014.06.034.

[39] M.A. Baker, S.L. Assis, O.Z. Higa, I. Costa, Nanocomposite hydroxyapatite formation on a Ti–13Nb–13Zr alloy exposed in a MEM cell

culture medium and the effect of H_2O_2 addition, Acta Biomaterialia, 5 (2009) 63-75.

[40] M. Pourbaix, Atlas of electrochemical equilibrium in aqueous solutions, NACE, USA, 1974.

[41] B. Hirschorn, M.E. Orazem, B. Tribollet, V. Vivier, I. Frateur, M. Musiani, Determination of effective capacitance and film thickness from constant-phase-element parameters, Electrochimica Acta, 55 (2010) 6218-6227.

[42] T. Busani, R.A.B. Devine, Dielectric and infrared properties of TiO_2 films containing anatase and rutile, Semiconductor Science and Technology, 20 (2005) 870.

[43] J.-B. Jorcin, M.E. Orazem, N. Pébère, B. Tribollet, CPE analysis by local electrochemical impedance spectroscopy, Electrochimica Acta, 51 (2006) 1473-1479.

[44] B. Hirschorn, M.E. Orazem, B. Tribollet, V. Vivier, I. Frateur, M. Musiani, Constant-Phase-Element Behavior Caused by Resistivity Distributions in Films: I. Theory, Journal of The Electrochemical Society, 157 (2010) C452-C457.

[45] G.J. Brug, A.L.G. van den Eeden, M. Sluyters-Rehbach, J.H. Sluyters, The analysis of electrode impedances complicated by the presence of a constant phase element, Journal of Electroanalytical Chemistry and Interfacial Electrochemistry, 176 (1984) 275-295.

[46] C.E.B. Marino, E.M.d. Oliveira, R.C. Rocha-Filho, S.R. Biaggio, On the stability of thin-anodic-oxide films of titanium in acid phosphoric media, Corrosion Science, 43 (2001) 1465-1476.

[47] C. Hsu, F. Mansfeld, Technical note: concerning the conversion of the constant phase element parameter Y0 into a capacitance, Corrosion, 57 (2001) 747-748.

[48]. L. -K. Tsui, G. Zangari, Water Content in the anodization electrolyte affects the electrochemical and electronic transport properties of TiO_2 nanotubes: a study by electrochemical impedance spectroscopy, Electrochimica Acta, 121 (2014) 203-209.

Capítulo 4

Resultados y Discusión

Los resultados de esta tesis han permitido entender la estrecha relación que guardan la morfología de las capas anódicas de óxido de titanio con las condiciones de crecimiento, como: la composición del baño, el voltaje aplicado y el tiempo del proceso tanto para la aleación Ti6Al4V como para la aleación Ti13Nb13Zr. Además, se han diseñado estructuras de óxido de titanio a medida (apartados 3.1, 3.2 y 3.5) mediante la selección adecuada de los parámetros del proceso de anodizado. Así mismo, se han determinado los factores clave que controlan tanto la respuesta biológica de las superficies modificadas mediante anodizado (apartado 3.4) como la respuesta electroquímica (apartados 3.3 y 3.5) de las películas de óxido de titanio crecidas.

4.1 Crecimiento y caracterización superficial de capas anódicas crecidas sobre Ti6Al4V en medio H_2SO_4/HF

En primer lugar, el trabajo se centró en la obtención de capas anódicas nanoestructuradas de óxido de titanio dopadas con flúor (apartado 3.1), ya que diferentes estudios en la bibliografía mostraban que pre-tratamientos con soluciones que contenían fluoruros estimulaban la respuesta ósea alrededor del implante de titanio, tanto en ensayos *in vitro* como *in vivo* [1-4], además de que la presencia de este elemento en la superficie del titanio podría proporcionar a la superficie propiedades antibacterianas [5]. El crecimiento de capas nanoestructuradas de TiO_2 parece ser una vía adecuada para funcionalizar la superficie de las aleaciones de titanio empleadas en aplicaciones biomédicas ya que la mayoría de los electrolitos que permiten crecer capas nanoestructuradas contienen fluoruros que se incorporarían a la capa durante el proceso de crecimiento.

En una primera etapa se crecieron capas anódicas sobre Ti6Al4V empleando una mezcla de ácidos (H_2SO_4/HF), a dos condiciones de voltaje (20 y 60 V) y tiempo (5 y 60 minutos), con el fin de obtener estructuras nanotubulares dopadas con flúor y optimizar la morfología, composición y espesor de las capas anódicas. En estas condiciones de generación del

óxido se observó que el crecimiento de las capas anódicas está claramente influenciado por la microestructura de la aleación base, encontrándose una disolución preferencial del óxido que crece en la fase β en comparación con el que crece en la fase α, debido a la mayor solubilidad de los óxidos de vanadio que crecen en la fase β [6, 7].

Las capas anódicas crecidas a 20 V y 5 minutos de anodizado presentaron una estructura nanoporosa con un diámetro de poro de ~20 nm y un espesor de capa de ~110 nm, de los cuales ~45 nm son de capa barrera. Mientras que a 20 V y 60 minutos de anodizado la morfología de la capa evoluciona y se forman estructuras nanotubulares que crecen sobre la fase α con un diámetro de ~100 nm y un espaciamiento entre nanotubos de ~30 nm. El espesor de la capa anódica es de ~230 nm, de los cuales ~25 nm corresponden al espesor de la capa barrera.

Las capas crecidas a 60 V y 5 minutos muestran una morfología nanoporosa caracterizada por una capa barrera más grande, ~140 nm, que la obtenida a 20 V para el mismo tiempo de anodizado, con un diámetro de poro de ~15 nm y un espesor total de capa de ~200 nm. A tiempos de anodizado más largos (60 minutos), la capa presenta una estructura desordenada sin una morfología definida, similar a una esponja, con un espesor de ~500 nm, de los cuales ~75 nm corresponden a la capa barrera.

Estas capas anódicas fueron analizadas mediante espectroscopía Raman y los resultados revelaron que las capas anódicas crecidas sobre la aleación de Ti6Al4V presentan una estructura amorfa de TiO_2 con V_2O_5 y Al_2O_3 con nanocristales de rutilo, tanto para 20 V como 60 V, a diferencia de lo indicado en la bibliografía para las capas anódicas crecidas sobre titanio puro en una solución de 1M H_2SO_4 y 0.15 wt% HF. En este caso, los análisis de difracción de rayos X, indicaban la presencia de anatasa y de rutilo en diferentes proporciones en las capas anódicas crecidas en voltajes comprendidos entre los 25 V y los 40 V [8].

La determinación de la composición y la eficiencia del proceso de anodizado se realizó mediante espectroscopía de retrodispersión de Rutherford (RBS) revelando que las capas anódicas formadas a 20 V contienen entre ~6 y ~4 % at. de flúor en su estructura para 5 y 60 minutos, respectivamente. Esta disminución en la concentración de flúor en las capas generadas a mayores tiempos de anodizado está asociada a la intensa disolución química durante el proceso de anodizado del TiF_4 que se encuentra en las zonas externas de las paredes de los nanotubos. Las capas crecidas a 60 V muestran un contenido de flúor de ~6 y ~13 % at. para 5 y 60 minutos, respectivamente. En este caso, el aumento de flúor estaría relacionado con el mayor espesor de la capa anódica crecida a 60 minutos.

La eficiencia en la formación de las capas anódicas disminuye con el tiempo de anodizado en ambas condiciones de voltaje, de 39.7 para 5 minutos a 1.3 % para 60 minutos a 20 V y de 79.8 para 5 minutos a 5.3 % para 60 minutos a 60 V. La disminución en la eficiencia del proceso se debe fundamentalmente al proceso de disolución química observada en la formación de estructuras nanoporosas/nanotubulares sobre titanio y sus aleaciones en medios acuosos ácidos que contienen fluoruros [9, 10]. Además de determinar la eficiencia del proceso de anodizado, se estimó la composición molecular media de los distintos óxidos crecidos a lo largo de la capa anódica, obteniendo que las capas crecidas a 20 V presentan una composición molecular media de $TiO_{1.6}{\cdot}0.06TiF_4{\cdot}0.12Al_2O_3{\cdot}0.033V_2O_5$ y $TiO_{1.44}{\cdot}0.036TiF_4{\cdot}0.11Al_2O_3{\cdot}0.034V_2O_5$ para 5 y 60 minutos respectivamente, mientras que a 60 V presentan una composición de $TiO_{1.47}{\cdot}0.05TiF_4{\cdot}0.105Al_2O_3{\cdot}0.035V_2O_5$ para 5 minutos y $TiO_{1.5}{\cdot}0.13TiF_4{\cdot}0.12Al_2O_3{\cdot}0.04V_2O_5$ para 60 minutos. En todos los casos se forma un TiO_x con $x<2$.

4.2 Crecimiento y caracterización superficial de capas anódicas crecidas sobre Ti6Al4V en medio $NH_4H_2PO_4/NH_4F$

Sin embargo, el principal inconveniente que presentan las capas nanoestructuradas crecidas en H_2SO_4/HF son la baja relación espesor/diámetro de poro. Este hecho motivó la búsqueda y optimización de condiciones de crecimiento que permitieran generar capas anódicas con una relación espesor/diámetro de poro alta (high-aspect ratio) para aumentar la funcionalidad de las nanoestructuras de óxido de titanio crecidas, por ejemplo para ser empleadas como reservorio de medicamentos que pudieran ser liberados in-situ ante una posible infección. Los primeros resultados obtenidos en nuestro grupo se recogieron en el trabajo "Growth of TiO_2-based nanotubes on Ti–6Al–4V alloy". En este trabajo se empleó un baño de anodizado que contenía una solución buffer de $NH_4H_2PO_4$ con diferentes concentraciones de sales de fluoruro, desde 0.15 M, 0.3 M a 0.45 M de NH_4F. A un voltaje constante de 20 V y tras 60 minutos de anodizado, se obtienen capas anódicas con un espesor de ~320, ~1250 y ~1750 nm y un diámetro de poro de ~20, ~44 y ~80 nm, para las distintas concentraciones de NH_4F estudiadas, 0.15, 0.3 y 0.45 M, respectivamente. Por tanto, en estas condiciones de anodizado se consiguen capas con una mayor relación diámetro del poro/espesor a las crecidas en medios ácidos con HF, además de incorporar en la capa una concentración de flúor del orden de ~12 % at., que no había sido descrito en la bibliografía hasta el momento.

Por tanto, los resultados revelan que el espesor de las películas nanotubulares crecidas en la aleación Ti6Al4V puede ser controlado adaptando la composición del baño, concentración de iones fluoruro y los aditivos presentes en el electrolito (H_2SO_4, $NH_4H_2PO_4$, etc.), y el control del pH [11].

Estos resultados son similares a los obtenidos para capas anódicas crecidas en titanio puro empleando distintas mezclas de electrolitos como

Na_2SO_4/NaF, $(NH_4)_2SO_4$/NH_4F, donde determinaron que la clave para la obtención de estructuras con un "high-aspect ratio", es el control del pH del baño de anodizado y en especial de la acidificación localizada que se produce en el fondo de los nanotubos debido a los mecanismos que controlan la formación de la capa y a las reacciones químicas que se producen durante el crecimiento de las capas nanotubulares/nanoporosas [12, 13], figura 4.1.

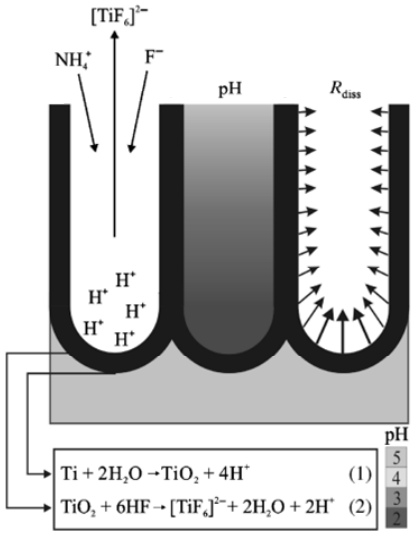

Figura 4.1. Representación esquemática de las reacciones químicas y mecanismos de disolución en baños que contienen sales de fluoruro [13].

Además de poder aumentar el espesor de las capas anódicas, también es posible modificar el diámetro de los nanotubos variando el voltaje aplicado. Mor y col.[14] fabricaron capas nanoestructuras de TiO_2 con forma cónica y espesor de 200 nm sobre titanio puro mediante la aplicación de rampas de voltaje en soluciones de HF. Estas geometrías podrían resultar interesantes desde el punto de vista biomédico ya que podrían servir como sistemas liberadores de fármacos de forma controlada. Por ello, se decidió estudiar si mediante la aplicación de diferentes escalones de voltaje se podía conseguir variar el diámetro de los nanotubos durante el crecimiento de las capas anódicas con el fin de obtener capas nanotubulares con forma de botella (apartado 3.2).

Como habíamos visto en trabajos previos [11, 15], la composición del baño de anodizado influye de forma determinante en las características finales de las capas anódicas (morfología, espesor, diámetro de poro, etc.). Por tanto, en primer lugar se determinó la influencia de la concentración de fluoruros en el baño incorporados mediante una sal, NH_4F, (0.15, 0.3 y 0.45M) en la morfología de las capas anódicas crecidas mediante la aplicación de un escalón de voltaje, 10-20 V, 10 V durante 30 minutos seguido de un segundo tramo a 20 V durante 60 minutos.

Un aumento en la concentración de NH_4F provoca el aumento del diámetro de las bocas de los nanoporos/nanotubos formados, variando desde los ~15 nm para una concentración de 0.15 M NH_4F hasta los ~63 nm para una concentración de 0.45 M NH_4F. Esto es debido a la mayor disolución de las paredes de las capas nanotubulares, tanto por el proceso de disolución química asociado al aumento de la concentración de los iones fluoruro en el baño de anodizado como a la disolución asistida por el campo eléctrico. Por otra parte, se consiguen espesores entorno a los ~661 nm hasta los ~1585 nm para 0.15 M y 0.45 M de NH_4F, respectivamente, que son del mismo orden que el obtenido en capas anódicas crecidas en baños de anodizado con composición similar aplicando un potencial constante de 20 V [11].

Además de las diferencias en el espesor y en el diámetro del poro, las capas anódicas crecidas presentan morfología diferente dependiendo de la concentración de iones fluoruro del medio. Para 0.15 M NH_4F, las capas presentan una estructura dual, nanoporosa de ~180 nm de espesor en la interfase electrolito/óxido y nanotubular de ~480 nm en la intercara óxido/metal. Esta morfología de capa ha sido también encontrada por otros autores tanto para titanio puro como para Ti6Al4V [11, 16]. Sin embargo, el mecanismo que explica la transición de una capa nanoporosa a nanotubular no está aún claro [17]. A mayores concentraciones de iones fluoruro en el medio, 0.3 y 0.45 M NH_4F, se favorece la disolución química de la capa anódica por la presencia de una mayor concentración de F^- en el

baño, y se obtienen estructuras nanotubulares a lo largo de toda la capa de óxido.

El espesor de la capa barrera en las capas anódicas crecidas aplicando el escalón de potencial 10-20 V es de ~40 nm para todos los medios estudiados lo que sugiere un factor de crecimiento de 2 nm/V en el segundo tramo del escalón 20 V durante 60 minutos) ya que el último voltaje aplicado (20 V) determina las características de la capa de óxido en la intercara óxido/metal [18-22].

Finalmente, para estudiar la influencia del campo eléctrico en la nanoestructura de las capas anódicas crecidas se varió la magnitud de los escalones de potencial para una concentración de fluoruros en el medio de 0.3M NH_4F. A esta concentración de fluoruros y para el escalón 10-20 V, las capas anódicas mostraron un poro en forma de botella mejor definido que el generado para las otras dos concentraciones analizadas.

Las diferentes valores de potencial aplicado en el escalón promueven cambios significativos en la morfología de las estructuras nanotubulares, que en el caso del escalón 20-40 V, primer tramo a 20 V durante 30 minutos seguido de 40 V durante 60 minutos, conducen a la pérdida de la integridad y al colapso de la capa anódica.

Las medidas de los diámetros internos de las estructuras nanotubulares en la parte superior del nanotubo muestran que éstos dependen principalmente del potencial aplicado, ya que éste determina la fuerza del campo eléctrico a través de la capa de óxido. Así, capas anódicas crecidas a un potencial inicial de 20 V (20-30 V y 20-40 V) tienen un diámetro de poro más grande de ~63-67 nm, en comparación con las capas crecidas con un potencial inicial de 10 V (10-20 V y 10-30 V) con diámetros entre ~39-47 nm, respectivamente.

Los espesores de las capas anódicas crecidas con los diferentes escalones de potencial son superiores al micrómetro, siendo las capas fabricadas a 20-40 V las que presentan un menor espesor, del orden de ~1187 nm. Esta

disminución del espesor se debe a que las capas están sometidas a una mayor disolución asistida por el campo dado que uno de los votajes aplicados, 40 V, es mayor que en las otras condiciones estudiadas.

Los resultados obtenidos están de acuerdo con las curvas de densidad de corriente vs tiempo recogidas durante el proceso de anodizado. En estas condiciones de anodizado, el mecanismo que gobierna el crecimiento de las capas anódicas es la disolución asistida por el campo eléctrico junto con la disolución química, en lugar del mecanismo de flujo asistido por el campo eléctrico.

La composición de las capas anódicas crecidas a un escalón de potencial de 10-20 V, y con diferentes concentraciones de NH_4F, revela un contenido similar de flúor para todas las capas, del orden de ~9 - 10 % at. y una composición molecular media de $TiO_{1.24}{\cdot}0.080TiF_4{\cdot}0.067Al_2O_3{\cdot}0.044V_2O_5$ para una concentración de 0.15 M NH_4F, mientras que las capas crecidas a 0.3 y 0.45 M NH_4F muestran una disminución en la estequiometria del óxido de titanio, $TiO_{0.92}$ y $TiO_{0.98}$, respectivamente , y contenidos similares de TiF_4, Al_2O_3 y V_2O_5.

Las capas crecidas en 1M $NH_4H_2PO_4$/0.3 M NH_4F y diferentes escalones de potencial, muestran contenidos de flúor entre ~9 - 12 % at. y una composición molecular media de $TiO_{0.87}{\cdot}0.073TiF_4{\cdot}0.098Al_2O_3{\cdot}0.039V_2O_5$ para la capa anódica crecida a 20-40 V y $TiO_{0.98}{\cdot}0.094TiF_4{\cdot}0.111Al_2O_3{\cdot}0.045V_2O_5$ para la capa crecida a 20-30 V.

La eficiencia del proceso de anodizado de las capas crecidas a un mismo escalón de potencial (10-20 V) disminuye conforme aumenta la concentración de NH_4F en el medio, desde 34.24 % para 0.15 M NH_4F a 12.42 % para 0.45 M NH_4F. Ello es debido a un aumento de la disolución de las capas anódicas debido al incremento de los iones fluoruro en el baño de anodizado, tal y como se observó en las capas crecidas en un medio similar pero a voltaje constante, 20 V, durante 60 minutos [11].

Las capas crecidas aplicando distintos escalones de potencial muestran una eficiencia del proceso de anodizado del orden de 22 - 26 %, lo que sugiere que la eficiencia del proceso no depende de la magnitud del voltaje aplicado sino que está asociada principalmente a la disolución química del óxido debido a la presencia de iones fluoruro.

La caracterización estructural y composicional de las capas anódicas crecidas tanto en H_2SO_4/HF como en $NH_4H_2PO_4$/NH_4F mediante distintas técnicas de análisis superficial: RBS, espectroscopía fotoelectrónica de rayos X (XPS) y espectrometría de masas de iones secundarios (SIMS) [23] (los resultados de estas dos últimas técnicas no se recogen en la presente tesis doctoral) nos ha permitido proponer el esquema de crecimiento de la capa que se muestra en la figura 4.2. En la figura 4.2a se recoge el movimiento y la distribución de los iones en la capa y en la figura 4.2 b se presenta la composición de las capas anódicas crecidas sobre la aleación Ti6Al4V. Este esquema nos permitirá explicar las propiedades biológicas que presentan estas capas anódicas, y que se discutirán en esta sección más adelante.

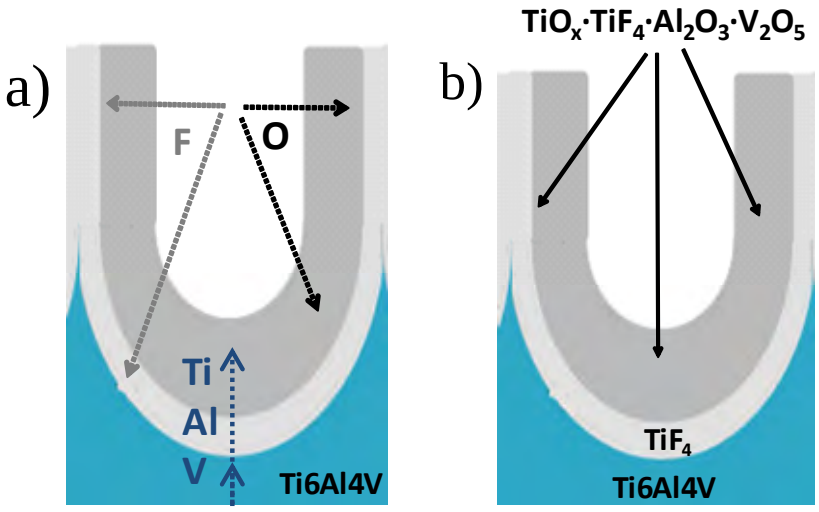

Figura 4.2 Distribución esquemática de los iones (a) y composición (b) de las capas anódicas crecidas tanto en medios con fluoruros.

4.3 Caracterización electroquímica de las capas anódicas

La caracterización de las capas anódicas crecidas sobre la aleación Ti6Al4V, se ha completado con la evaluación de su comportamiento frente a la corrosión mediante curvas de polarización potenciodinámicas (CP) y espectroscopía de impedancia electroquímica (EIS). Estos resultados se presentan en el apartado 3.3.

El comportamiento electroquímico de las capas anódicas dependerá de su interacción con el entorno circundante, por lo que una alta resistencia a la corrosión asegurará que el número de iones metálicos liberados desde el implante al torrente sanguíneo será muy bajo o prácticamente nulo.

Las capas anódicas crecidas en la presente tesis se pueden clasificar en tres morfologías distintas: nanoporosa(NP), dual (DU) (nanoporosa en la parte externa y nanotubular en la parte interna de la capa) y nanotubular (NT), las cuales han sido descritas en trabajos previos [11, 15, 24], tabla 4.1.

Las curvas de polarización tanto de las capas anódicas como de la muestra de referencia describen el comportamiento típico de un material pasivo, presentando todas las capas anódicas, independientemente de su morfología, una densidad de corriente de pasivación (i_{pass}) menor o del mismo orden que la muestra de referencia.

La i_{pass} depende de la morfología de las capas anódicas, presentando valores de menor a mayor en el siguiente orden: NP<DU<NT<Ti6Al4V sin tratamiento, con valores mínimos de i_{pass} de 1.9E-9, 4.0E-8, 1.1E-7 y 6.9E-7 A/cm^2, respectivamente.

La muestra de referencia presenta un potencial de picadura de ~2.28 V vs. AgAgCl. Este comportamiento no se observa en las capas NP, DU o incluso en las muestras NT crecidas en un electrolito con NH_4F. Únicamente la capa nanotubular crecida a 20V-60 min (HF), con unas características morfológicas determinadas, exhibe un potencial de picadura a valores similares. El electrolito penetra a través de los espacios intertubulares

originando la aparición de picaduras. Estas capas NT presentan un espaciado de ~30 nm, el mayor de todas las capas NT estudiadas, tabla 4.1.

Condiciones experimentales			Espacio Inter-tubular (nm)	Capa barrera (nm)	Espesor (nm)
Morfología	**Composición del baño/ V, t**	**Acrónimo**			
Nanoporosa (NP)	1M H_2SO_4/0.15 % peso HF; 20 V, 5 min	20V-5 min (HF)	---	~45	~110
	1M $NH_4H_2PO_4$/0.15M NH_4F; 10 V, 30 min	10V-30 min (0.15M NH_4F)	---	---	~105
Dual (DU)	1M $NH_4H_2PO_4$/0.15M NH_4F; 20 V, 60 min	20V-60 min (0.15M NH_4F)	---	~45	~320
	1M $NH_4H_2PO_4$/0.3M NH_4F; 10 V, 30 min	10V-30 min (0.3M NH_4F)	---	---	~540
Nanotubular (NT)	1M H_2SO_4/0.15 % peso HF; 20 V, 60 min	20V-60 min (HF)	~30	~25	~230
	1M $NH_4H_2PO_4$/0.3M NH_4F; 20 V, 60 min	20V-60 min (0.3M NH_4F)	~15	~42	~1250
	1M $NH_4H_2PO_4$/0.3M NH_4F; 10 V, 30 min + 20 V, 60 min	10-20V (0.3M NH_4F)	~15	~40	~1355

Tabla 4.1 Condiciones de crecimiento de las capas anódicas para su caracterización electroquímica.

Además de analizar las capas anódicas empleando curvas de polarización potenciodinámicas, se estudió su estabilidad química a tiempos de inmersión más largos utilizando la técnica de espectroscopía de impedancia electroquímica.

Las capas con morfología nanoporosa, NP, y dual, DU, muestran una gran estabilidad durante las 4 semanas de ensayo. Los diagramas de impedancia revelan la presencia de dos contantes de tiempo, estando la constante de tiempo que aparece en el rango de frecuencias de 10^5 a ~10^0 Hz asociada a

la respuesta de la capa barrera y la constante de tiempo localizada entre los $\sim 10^{0}$ a 10^{-2} Hz relacionada con un proceso de difusión.

Por el contrario, las capas con estructura nanotubular, NT, presentan dos comportamientos distintos asociados al espaciamiento intertubular que presentan estas capas.

Capas NT con espaciamiento intertubular inferior a ~30 nm, muestran una respuesta electroquímica que evoluciona con el tiempo de inmersión. A tiempos cortos de inmersión, se aprecian dos constantes de tiempo, estando la constante de tiempo de altas frecuencias asociada a la capa nativa de óxido que crece en el sustrato expuesto a través de los espacios intertubulares y la constante de tiempo a bajas frecuencias relacionada con los procesos de difusión ocurridos en la capa barrera. En este caso, las constantes de tiempo se localizan en los mismos intervalos de frecuencia en los que aparecían las constantes observadas en los espectros de las capas NP y DU.

A partir de las 24 horas de inmersión y hasta finalizar el ensayo a las 672 horas, los espectros de las capas NT crecidas a 20V-60 min (0.3M NH_4F) y 10-20V (0.3M NH_4F) presentan 3 constantes de tiempo, asociadas a la respuesta de la capa barrera del nanotubo (10^{5} - $\sim 10^{2}$ Hz), al óxido nativo que crece en el sustrato expuesto a través de los espacios inter-tubulares ($\sim 10^{2}$ - $\sim 5 \cdot 10^{-1}$ Hz) y a un proceso de difusión ($\sim 5 \cdot 10^{-1}$ - 10^{-2} Hz).

Mientras que las capas NT con un espaciamiento de ~30 nm no presentan la tercera constante de tiempo a 24 horas, por lo que la respuesta electroquímica de estas capas es debida únicamente a la capa nativa de óxido que crece sobre el sustrato en el fondo de los espaciamientos intertubulares y a los procesos difusivos a través de estas capas, durante todos los tiempos de inmersión estudiados.

Los circuitos equivalentes propuestos para simular los espectros de impedancia son distintos a los descritos en la bibliografía para explicar el comportamiento de capas anódicas.

En la bibliografía se asocian las dos constantes de tiempo con la respuesta de la parte porosa externa y la respuesta de la capa barrera interna de las capas anódicas, respectivamente (fig. 4.3 a). Cuando aparecen tres constantes de tiempo, la constante de tiempo a bajas frecuencias se asocia a procesos de difusión (fig. 4.3 b) [25-28].

Por el contrario, en nuestros resultados cuando los espectros revelan tres constantes de tiempo dichas constantes se asocian a la respuesta de la capa barrera, la respuesta del sustrato expuesto entre los espacios intertubulares y a los procesos difusivos, tal y como se describió anteriormente (fig. 4.3 e).

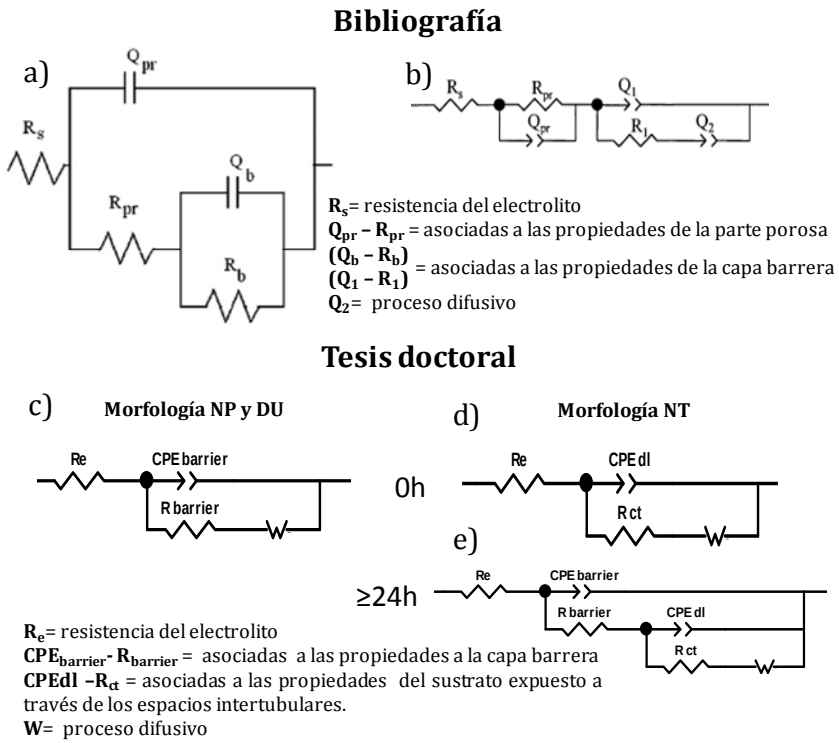

Figura 4.3 Circuitos equivalentes propuestos en la bibliografía (a y b) [25, 28] y en la presente tesis doctoral (c, d y e), para simular los espectros de las capas anódicas obtenidos mediante EIS.

La simulación de los espectros de impedancia empleando los circuitos equivalentes propuestos para las distintas morfologías de las capas

anódicas (fig. 4.3 c-e) proporcionan un buen acuerdo entre los datos experimentales y los simulados, pudiéndose correlacionar las características morfológicas de las capas anódicas, como el espesor de la capa barrera, con los datos medidos mediante otras técnicas como TEM.

Para llevar a cabo las simulaciones se han empleado elementos de fase constante -CPE-, que son considerados un promedio estadístico de las componentes resistivas y capacitivas existentes sobre la superficie del electrodo de trabajo.

La determinación de la capacidad del sistema a partir de los CPE no se puede realizar de manera directa. Recientemente, en la bibliografía se muestra que la capacidad podría deberse a una distribución de capacidades como resultado de la presencia de heterogeneidades en la superficie como fronteras de grano u otras variaciones. En estos casos, se define el concepto de capacidad efectiva, C_{eff}, para referirse a la capacidad resultante de una superficie, y puede ser debida a una distribución de constantes de tiempo a lo largo de la superficie (2-D) o en la dirección normal a ésta (3-D) [29-31].

Diferentes investigadores han desarrollado modelos para estimar la capacidad efectiva -C_{eff}- del sistema para una distribución de constantes de tiempo 2D o 3D, empleando los distintos parámetros eléctricos obtenidos en las simulaciones [29, 30, 32, 33].

En el presente trabajo, se calcularon los valores de C_{eff} para cada una de las capas anódicas estudiadas, considerando tanto una distribución 2-D como una 3-D, y se determinó a partir de dicho valor, el espesor de las capas barrera y el espesor del óxido nativo de la muestra de referencia según la siguiente ecuación:

$$d = {}^{\varepsilon\varepsilon_0}/_{C_{eff}} \quad (4.1)$$

donde ε es la constante dieléctrica y ε_0 es la permitividad del vacío, 8.85E-14 F/cm.

La muestra sin anodizar presenta un óxido cuyo espesor es entorno a los 1 - 3 nm, estando estos valores de acuerdo con los descritos en la bibliografía para capas nativas de TiO_2 [34-36].

Las capas anódicas con morfología nanoporosa crecidas a 20V-5 min (HF), presentan valores de la capa barrera de 47.97 ± 0.98 y 28 ± 5.81 nm asumiendo una distribución 2-D y 3-D, respectivamente. Las capas NP crecidas a 10V-30 min (0.15M NH_4F) presentan espesores de 25.27 ± 0.86 nm para una distribución 2-D y de 17.66 ± 0.96 nm para una distribución 3-D.

Las capas con morfología dual presentan espesores de la capa barrera similares, siendo para una distribución 2-D de 50.89 ± 2.96 nm para la capa crecida a 20V-60 min (0.15M NH4F) y de 25.65 ± 0.67 nm para la capa crecida a 10V-30 min (0.3M NH4F).

Por otra lado, las capas con morfología nanotubular crecidas a 20V-60 min (HF) muestran valores de espesor similares a los de la muestra de referencia, tanto para una distribución 2-D como 3D entorno a 3.72 ± 1.36 y 1.99 ± 0.31 nm, respectivamente. Mientras que las otras dos capas NT crecidas a 20V-60 min (0.3M NH_4F) y a 10-20V (0.3M NH_4F) muestran un incremento del espesor en función del tiempo de inmersión.

Las capas crecidas a 20V-60 min (0.3M NH_4F) presentan un aumento de espesor desde 6.38 nm a las 0 horas, 31.94 nm a las 24 horas, hasta 38.39 nm al final del ensayo, 672 horas, para una distribución 2-D; mientras que usando una distribución 3-D, se observa la misma tendencia, pero los valores de espesor son menores, 18.27 nm a las 672 horas de inmersión.

El espesor de las estructuras nanotubulares crecidas a 10-20V (0.3M NH_4F) crecen de 6.40 a las 0 horas hasta valores de 31 nm a las 672 horas para una distribución 2-D y alcanza un valor máximo de 22.3 nm cuando se emplea una distribución 3-D. En ambos casos, son espesores inferiores a los medidos mediante TEM [24], estas diferencias se pueden atribuir a la variación intertubular que muestran estas capas a lo largo de su espesor

(~21 nm en la boca de los nanotubos y ~15 nm cerca de la parte inferior de estos), en comparación a las capas nanotubulares crecidas a voltaje constante 20V-60 min (0.3M NH_4F), que presentan un espaciamiento intertubular de ~15 nm a lo largo de todo el espesor de la capa anódica.

El espesor de la capa barrera de todas las capas anódicas estudiadas determinado a partir de la capacidad efectiva obtenida al suponer una distribución de constantes de tiempo superficial (2D) es del mismo orden al medido mediante TEM [11, 15, 24]. Por lo tanto, la distribución 2-D describe de manera más adecuada el comportamiento de las capas anódicas que la 3D, análogamente a lo que se indica en la bibliografía para capas anódicas crecidas sobre Ti [37] y Ti13Nb13Zr [38].

La caracterización electroquímica mediante EIS permitió discernir que la respuesta electroquímica está gobernada por el espaciamiento intertubular que muestran las capas anódicas crecidas sobre Ti6Al4V.

4.4 Caracterización biológica de las capas crecidas sobre Ti6Al4V

Los primeros estudios realizados para evaluar la respuesta biológica de las capas de TiO_2 dopadas con flúor fueron ensayos de adhesión bacteriana sobre las capas anódicas crecidas a 20 V- 5 y 60 minutos, respectivamente, en una solución con HF. Los resultados muestran una disminución de la adherencia tanto con cepas de colección como con cepas clínicas de dos especies de bacterias, *Staphylococcus epidermis* y *Staphylococcus aureus*, siendo las capas crecidas a 20 V - 5 minutos las que presentaron una menor adherencia para todas las cepas estudiadas, figura 4.4 [39].

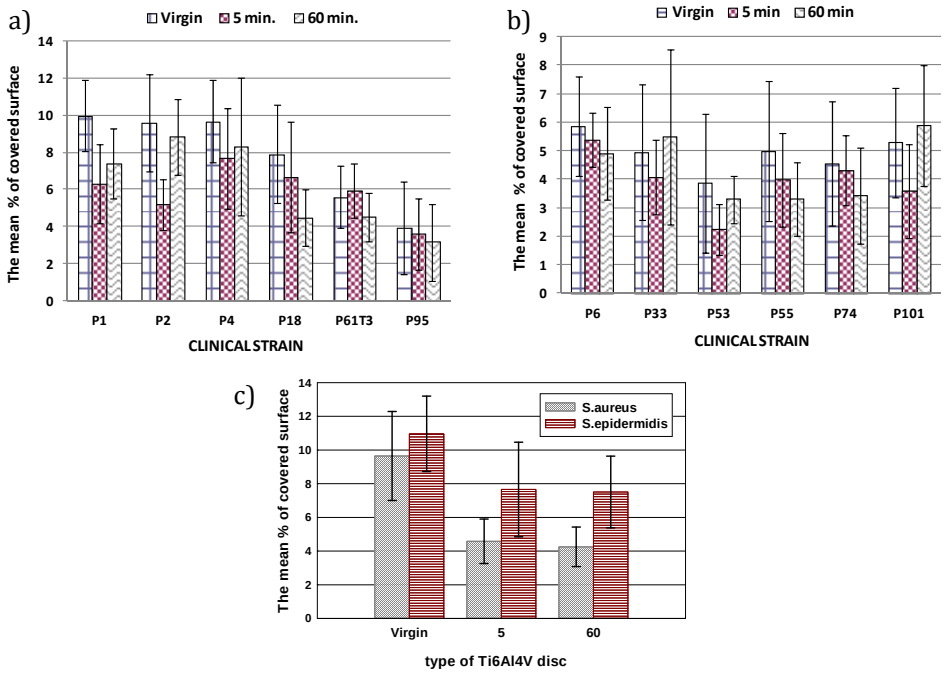

Figura 4.4 Resultados de adherencia bacteriana en discos de Ti6Al4V sin tratamiento de anodizado (Virgin) y con tratamiento de anodizado 20V durante 5minutos (5 min.) y 60minutos (60min.), empleando cepas clínicas de *S.aureus* (a) *S.epidermidis* (b) y cepas de colección (c) [39].

Sin embargo, ya que tanto la topografía como la composición química de la superficie han sido modificadas por el proceso de anodizado, es difícil *a priori* determinar cuál es el factor principal que controla las propiedades antibacterianas de las superficies modificadas. Por esta razón, el apartado 3.4a se centra en identificar cual es el factor responsable de la disminución de la adherencia bacteriana sobre la superficie de las capas anódicas crecidas, si es el contenido de flúor en la capa de óxido o las características topográficas de las capas.

Para ello, se crecieron dos capas anódicas barrera, con y sin flúor (FBL y BL, respectivamente) en su composición química. Las capas sin flúor (BL) se crecen en un baño de 1M H_2SO_4 a 15 mA/cm^2 hasta llegar a 90 V, y presentan un espesor de ~200 nm. Mientras que las capas barrera dopadas con flúor (FBL) se crecen en una solución de 0.15M $NH_4F/NH_4H_2PO_4$ a 20 V

durante 120 minutos y un pH igual a 5 [11], obteniendo un espesor de ~150 nm con un contenido de flúor de ~12 at. %.

El ensayo de de mojabilidad superficial mostro que las capas FBL presentaban el menor ángulo de contacto usando agua, en comparación con las capas BL y la muestra de referencia (CP), con valores de 21.36°, 57.50° y 52.10° y, respectivamente.

Además, las capas anódicas FBL presentaron los valores más altos de rugosidad (Ra) y de energía libre superficial, que las demás condiciones estudiadas, pero del mismo orden que las capas anódicas con estructuras nanoporosa y nanotubular descritas en la bibliografía [40].

Los resultados de adherencia bacteriana de *S. aureus* y *S. epidermidis* muestran que existen diferencias estadísticamente significativas entre la capa barrera dopada con flúor y la capa barrera sin flúor, siendo las FBL las que muestran el menor porcentaje de superficie cubierta, tanto para cepas de colección como con clínicas.

Estos resultados permiten concluir que la disminución en la adherencia bacteriana es debido a la presencia de flúor en las capas anódicas más que a la morfología de la capa anódica (barrera o nanotubular/nanoporosa).

Por otro lado, es importa evaluar si la presencia de flúor en las capas anódicas altera la respuesta celular y la mineralización en comparación con la aleación Ti6Al4V sin anodizar. Por ello, se llevó a cabo el estudio de la capacidad de proliferación y mineralización de células osteoblásticas de ratón MC3T3-E1, apartado 3.4b, en las películas anódicas con diferente morfología y concentración de flúor, Tabla 4.2.

Los resultados de proliferación celular mostraron que solo las capas anódicas NP presentan un aumento estadísticamente significativo tanto a 2 como a 7 días con respecto a las demás muestras analizadas. Mientras que los ensayos de mineralización de la matriz celular mostraron que todas las capas anódicas presentan un aumento de la mineralización de la matriz

celular estadísticamente significativo a los 10 días de cultivo, en comparación con la muestra CP. Además, los análisis de la expresión génica de dos marcadores osteogénicos, revelaron que las muestras NP aumentan significativamente la expresión génica de todos los marcadores.

Condiciones experimentales			**$\varnothing_{poro}$ (nm)**	**Espesor (nm)**	**[F] (% at.)**
Nombre	**Acrónimo**	Composición del baño/ V, t			
Pulida Químicamente	**CP**	$HF:HNO_3:H_2O$; 5 min	-	-	-
Capa barrera sin flúor	**BL**	1M H_2SO_4; 15mA/cm^2 a 90 V	-	200	-
Capa barrera con flúor	**FBL**	1M $NH_4H_2PO_4$ / 0.15M NH_4F; 20V, 120min, pH:5	-	150	12
Capa nanoporosa	**NP**	H_2SO_4 / HF; 20 V, 5 min	20	110	6.4
Capa nanotubular	**NT**	H_2SO_4/ HF; 20 V, 60 min	100	300	4.2

Tabla 4.2 Condiciones de crecimiento de las capas anódicas, empleadas para estudiar *in vitro* sus propiedades de mineralización y crecimiento celular.

El motivo por el cual estas células osteoblásticas proliferan preferencialmente sobre las muestras NP no está claro. Los diferentes trabajos en la bibliografía sobre crecimiento y diferenciación celular, con resultados similares, atribuyen esta mejora a diferentes factores, entre los que se encuentran: alteraciones superficiales a la escala nanométrica producida durante períodos cortos de anodización [41], diferencias en el diámetro de poro de las capas dúplex [41-45] y a la presencia de pequeñas cantidades de flúor (<5 % at.) en la superficie del titanio [46, 47]. En este sentido, Ellingsen y col. [2], propusieron que la mejora de las propiedades osteogénicas presentada por superficies pre-tratadas con fluoruros se debe a que los fluoruros se liberan de la superficie del titanio mediante una reacción de intercambio iónico con los fosfatos, formándose una unión

covalente entre el titanio y el fosfato promoviéndose así la formación de hueso [2, 48-50], figura 4.5.

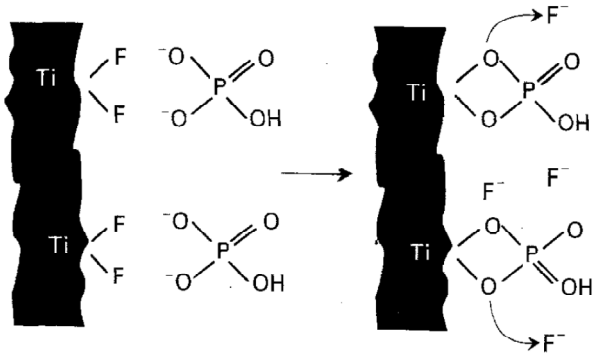

Figura 4.5 Esquema del mecanismo propuesto por Ellingsen para la formación de hueso después de la implantación de un implante de titanio pre-tratado con fluoruros [2].

Todo parece indicar que la composición química de las capas de óxido crecidas, así como la distribución de los iones en la capa, y fundamentalmente en la superficie, pueden ser la clave de la mejora en la respuesta osteogénica. Ello explicaría el comportamiento preferencial de mineralización que se observa sobre las muestras NP, debido a un mayor número de sitios de TiF_4 disponibles en la superficie en comparación con las capas anódicas nanotubulares, NT, y con la capa barrera con flúor, FBL.

Por tanto, los resultados obtenidos sobre la aleación de titanio Ti6Al4V indican que la anodización es un método rápido y eficaz para formar películas multifuncionales de óxido de titanio nanoestructurado, uniformes, con una composición química controlada y una buena estabilidad química, que muestra propiedades antibacterianas y que favorecen la mineralización y el crecimiento celular en ensayos *in vitro*.

4.5 Crecimiento, caracterización superficial y electroquímica de capas anódicas crecidas sobre Ti13Nb13Zr

Sin embargo, uno de los problemas que presenta el uso de la aleación Ti6Al4V como biomaterial, es debido a los posibles efectos tóxicos

asociados a la lixiviación del aluminio o el vanadio dentro del cuerpo humano [51, 52]. En este sentido, se utilizan diferentes elementos de aleación como Fe, Nb, Ta, Mo, Zr, de menor toxicidad para reemplazarlos. De entre todas las aleaciones desarrolladas, la aleación Ti13Nb13Zr casi beta, que presenta una microestructura α martensítica precipitada en una matriz β, es una de las candidatas más prometedoras para sustituir a la aleación Ti6Al4V en los implantes ortopédicos, ya que presenta una alta resistencia a la corrosión, buena biocompatibilidad y un reducido módulo de Young (64-83 GPa), más cercano al hueso (10-30 GPa) que la aleación Ti6Al4V (105-120 GPa) [51, 53, 54].

Por este motivo, en la última parte del trabajo desarrollado en la presente tesis doctoral se decidió llevar a cabo el crecimiento de capas anódicas sobre la aleación Ti13Nb13Zr, apartado 3.5, empleando un medio acuoso de H_2SO_4/HF y aplicando un voltaje constante de 20 V (condiciones de crecimiento similares a las usadas en el apartado 3.1 para la aleación de Ti6Al4V).

Las capas anódicas crecidas a tiempos cortos de anodizado (5 minutos) muestran una estructura nanoporosa con un diámetro de poro de ~25 nm y un espesor de ~71nm. Mientras que a tiempos más largos de anodizado (60 minutos), las capas presentan una estructura nanotubular con un diámetro de poro entre ~75 - 100 nm, un espaciamiento intertubular de ~15 nm y un espesor de ~900 ± 100 nm. Las variaciones de espesor y diámetro de poro observado en las capas nanotubulares depende principalmente de la fase en la que crecen los nanotubos debido a las diferentes velocidades de disolución de los óxidos que crecen en cada fase [55, 56].

La eficiencia del proceso de anodizado en esta aleación disminuye conforme aumenta el tiempo de anodizado de ~56 a ~27 %, para 5 y 60 minutos, respectivamente. Este hecho está asociado principalmente a la disolución química de las capas anódicas para tiempos largos de anodizado.

Los análisis de la composición química de las capas relevan la presencia de flúor en una concentración del orden del 13 a 11 % at. para las capas nanoporosas y nanotubulares, respectivamente. Estos valores son superiores a los obtenidos para las capas anódicas crecidas en Ti6Al4V empleando las mismas condiciones, lo que está relacionado tanto con el mayor espesor de las capas anódicas crecidas en Ti13Nb13Zr como con su composición molecular media obtenida mediante RBS. En este caso, la composición molecular media puede expresarse como una mezcla de compuestos de fluoruro, TiF_4, NbF_5 y ZrF_4, y un óxido principal de todos los elementos de la aleación, $(TiNbZrO)_x$ con $x<1$. Estos resultados están de acuerdo a lo indicado en la bibliografía para capas anódicas crecidas en aleaciones binarias de TiZr y TiNb [57, 58].

Además de estudiar las características morfológicas de las capas anódicas crecidas sobre esta aleación, se realizó su caracterización electroquímica empleando curvas de polarización potenciodinámica y espectroscopía de impedancia electroquímica, al igual que en el apartado 3.3.

Las curvas de polarización muestran una densidad de corriente de pasivación de ~1.1E-6 A/cm^2 tanto para las muestras de referencia (no anodizada) como para las capas nanotubulares, NT, exhibiendo una disminución de la densidad de corriente de pasivación a ~2.9E-7 A/cm^2 para las capas nanoporosas. A diferencia de lo que se observó en la aleación Ti6Al4V y para una de las capas con morfología nanotubular (20 V-60min (HF)), la muestra de referencia y las capas NT no presentan un potencial de picadura.

Los resultados de impedancia revelaron que tanto la aleación de referencia como los dos tipos de capa anódica estudiadas son muy estables durante todo el tiempo de evaluación estudiado.

Ambas capas anódicas muestran dos constantes de tiempo bien definidas a lo largo del tiempo de inmersión. Las capas con estructura nanoporosa muestran las constantes de tiempo en los intervalos de frecuencia de 10^5 -

$\sim 10^{2}$ Hz a y de $\sim 10^{1}$ - 10^{-2} Hz, mientras que las capas nanotubulares presentan las constantes de tiempo en otros rangos de frecuencia. Para las capas nanotubulares, la constante de tiempo situada entre 10^{5} - $\sim 10^{-1}$ Hz a 0.25h de inmersión se desplaza hacia ligeramente con el tiempo de inmersión en el rango de 10^{5} - $\sim 10^{0}$ Hz a las 672h y la segunda constante de tiempo se sitúa en 10^{-1} - $\sim 10^{-2}$ al inicio del ensayo y se desplaza hasta frecuencias de 10^{0} - $\sim 10^{-2}$ tras 672h de inmersión.

El análisis de los espectros de impedancia de las capas anódicas se realizó empleando el mismo circuito equivalente (fig. 4.6), pero los elementos del circuito tienen diferente significado según la morfología evaluada. Para las capas con morfología nanoporosa las constantes de tiempo son simuladas asumiendo que la respuesta es asociada a la capa barrera de las estructuras nanoporosas y a los procesos de difusión que ocurren a través de la capa. Y para las capas nanotubulares son simulados asumiendo que la respuesta es debido a la señal del sustrato expuesto a través de los espacios intertubulares de las capas anódicas, lo cual estaría de acuerdo con el comportamiento observado en las curvas de polarización.

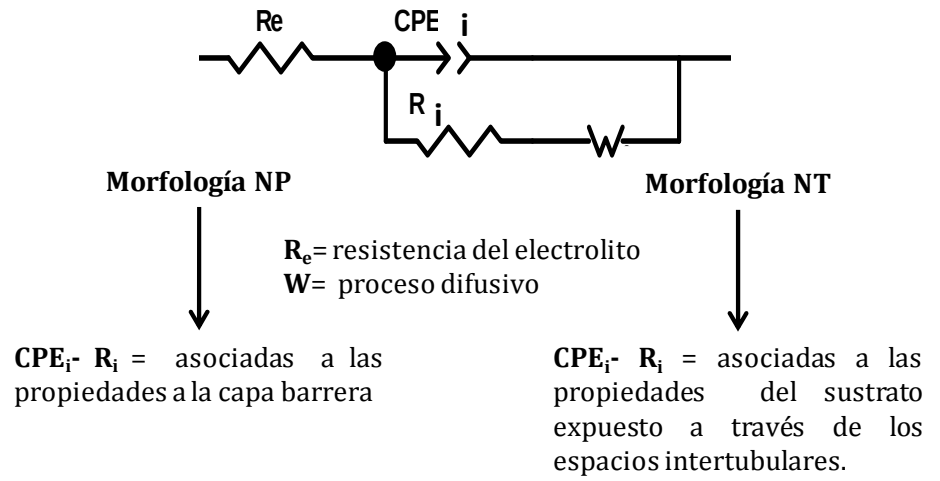

Figura 4.6 Circuito equivalente empleado para simular los espectros de las capas anódicas crecidas sobre Ti13Nb13Zr.

De la misma forma que en el apartado 3.3, se calcularon las capacidades efectivas a partir del elemento de fase constante, CPE, asumiendo una distribución 2-D o 3-D de las constantes de tiempo y a partir de estos valores se determinaron los espesores de la capa barrera y del óxido que crece sobre el sustrato que queda expuesto a través de los espacios intertubulares.

Los espesores de la capa barrera de las capas anódicas con morfología nanoporosa variaron entorno a los 40.60±1.73 y 31.76±1.53 nm dependiendo si se supone una distribución 2-D o una 3-D, respectivamente. Al comparar estos valores con los medidos mediante SEM -~40nm-, es evidente que la determinación del espesor de las capas barrera mediante una distribución 2-D es la que ofrece valores más cercanos a los medidos experimentalmente.

Los valores determinados para las capas nanotubulares se encuentran en el rango de los 1.68 nm para tiempos iniciales hasta 3.40 nm a las 672h para una distribución 2-D y de 1.09 nm a 2.07 nm a las 672 h para una distribución 3-D. Estos valores corresponden al espesor de la capa de óxido que crece sobre la superficie de la aleación en el fondo de los espacios intertubulares.

Por tanto, los resultados permiten concluir que la caracterización electroquímica y en especial la espectroscopía de impedancia electroquímica es una herramienta muy potente en la caracterización de capas anódicas de titanio.

REFERENCIAS

[1] J.E. Ellingsen, C.B. Johansson, A. Wennerberg, A. Holmén, Improved retention and bone-to-implant contact with fluoride-modified titanium implants, The International journal of oral & maxillofacial implants., 19 (2004) 659-666.
[2] J.E. Ellingsen, Pre-treatment of titanium implants with fluoride improves their retention in bone, J Mater Sci: Mater Med, 6 (1995) 749-753.
[3] J. Guo, R. Padilla, W. Ambrose, I. De Kok, L. Cooper, The effect of hydrofluoric acid treatment of TiO_2 grit blasted titanium implants on adherent osteoblast gene expression in vitro and in vivo., Biomaterials, 28 (2007) 5418-5425.
[4] L.F. Cooper, Y. Zhou, J. Takebe, J. Guo, A. Abron, A. Holmén, J.E. Ellingsen, Fluoride modification effects on osteoblast behavior and bone formation at TiO_2 grit-blasted c.p. titanium endosseous implants, Biomaterials, 27 (2006) 926-936.
[5] M. Yoshinari, Y. Oda, T. Kato, K. Okuda, Influence of surface modifications to titanium on antibacterial activity in vitro, Biomaterials, 22 (2001) 2043-2048.
[6] J.M. Macak, H. Tsuchiya, L. Taveira, A. Ghicov, P. Schmuki, Self-organized nanotubular oxide layers on Ti-6Al-7Nb and Ti-6Al-4V formed by anodization in NH_4F solutions, Journal of biomedical materials research. Part A, 75 (2005) 928-933.
[7] V. Zwilling, E. Darque-Ceretti, A. Boutry-Forveille, D. David, M.Y. Perrin, M. Aucouturier, Structure and physicochemistry of anodic oxide films on titanium and TA6V alloy, Surface and Interface Analysis, 27 (1999) 629-637.
[8] M. Bestetti, S. Franz, M. Cuzzolin, P. Arosio, P.L. Cavallotti, Structure of nanotubular titanium oxide templates prepared by electrochemical anodization in H_2SO_4/HF solutions, Thin Solid Films, 515 (2007) 5253-5258.
[9] L.V. Taveira, J.M. Macak, K. Sirotna, L.F.P. Dick, P. Schmuki, Voltage Oscillations and Morphology during the Galvanostatic Formation of Self-Organized TiO_2 Nanotubes, Journal of The Electrochemical Society, 153 (2006) B137-B143.
[10] J.M. Macak, H. Tsuchiya, A. Ghicov, K. Yasuda, R. Hahn, S. Bauer, P. Schmuki, TiO_2 nanotubes: Self-organized electrochemical formation, properties and applications, Current Opinion in Solid State and Materials Science, 11 (2007) 3-18.
[11] E. Matykina, A. Conde, J. de Damborenea, D.M.y. Marero, M.A. Arenas, Growth of TiO_2-based nanotubes on Ti–6Al–4V alloy, Electrochimica Acta, 56 (2011) 9209-9218.

[12] J.M. Macak, K. Sirotna, P. Schmuki, Self-organized porous titanium oxide prepared in Na_2SO_4/NaF electrolytes, Electrochimica Acta, 50 (2005) 3679-3684.
[13] J.M. Macák, H. Tsuchiya, P. Schmuki, High-aspect-ratio TiO_2 nanotubes by anodization of titanium, Angewandte Chemie - International Edition, 44 (2005) 2100-2102.
[14] G.K. Mor, O.K. Varghese, M. Paulose, N. Mukherjee, C.A. Grimes, Fabrication of tapered, conical-shaped titania nanotubes, Journal of Materials Research, 18 (2003) 2588-2593.
[15] E. Matykina, J.M. Hernandez-López, A. Conde, C. Domingo, J.J. de Damborenea, M.A. Arenas, Morphologies of nanostructured TiO_2 doped with F on Ti–6Al–4V alloy, Electrochimica Acta, 56 (2011) 2221-2229.
[16] G.A. Crawford, N. Chawla, Porous hierarchical TiO_2 nanostructures: Processing and microstructure relationships, Acta Materialia, 57 (2009) 854-867.
[17] D. Regonini, C.R. Bowen, A. Jaroenworaluck, R. Stevens, A review of growth mechanism, structure and crystallinity of anodized TiO_2 nanotubes, Materials Science and Engineering: R: Reports, 74 (2013) 377-406.
[18] D. Guan, P.J. Hymel, Y. Wang, Growth mechanism and morphology control of double-layer and bamboo-type TiO_2 nanotube arrays by anodic oxidation, Electrochimica Acta, 83 (2012) 420-429.
[19] X. Wang, S. Zhang, L. Sun, A Two-step anodization to grow high-aspect-ratio TiO_2 nanotubes, Thin Solid Films, 519 (2011) 4694-4698.
[20] X. Wang, R. Chen, J. Zheng, P. Nie, H. Xie, X. Zhao, Two-step anodization of maltilayer TiO_2 nanotube and its photocatalytic activity under UV light, J. Wuhan Univ. Technol.-Mat. Sci. Edit., 27 (2012) 866-870.
[21] D. Guan, Y. Wang, Synthesis and growth mechanism of multilayer TiO_2 nanotube arrays, Nanoscale, 4 (2012) 2968-2977.
[22] J.M. Macak, S. Albu, D.H. Kim, I. Paramasivam, S. Aldabergerova, P. Schmuki, Multilayer TiO_2–Nanotube Formation by Two-Step Anodization, Electrochemical and Solid-State Letters, 10 (2007) K28-K31.
[23] J.M. Hernández-López, M.Á. Arenas Vara, J.J. de Damborenea González, D. Gamarra Sanchez, F. Yubero Valencia, J.P. Espinós Manzorro, A. Conde del Campo, Incorporación de aniones en las capas anódicas de TiO_2: potenciales aplicaciones en medicina, in: XIII Congreso Nacional de Materiales, Barcelona, 2014.
[24] J.M. Hernandez-Lopez, A. Conde, J.J. de Damborenea, M.A. Arenas, TiO_2 nanotubes with tunable morphologies, RSC Advances, 4 (2014) 62576-62585.
[25] M.E.P. Souza, M. Ballester, C.M.A. Freire, EIS characterisation of Ti anodic oxide porous films formed using modulated potential, Surface and Coatings Technology, 201 (2007) 7775-7780.

[26] J. Pan, D. Thierry, C. Leygraf, Electrochemical impedance spectroscopy study of the passive oxide film on titanium for implant application, Electrochimica Acta, 41 (1996) 1143-1153.
[27] S.A. Fadl-allah, Q. Mohsen, Characterization of native and anodic oxide films formed on commercial pure titanium using electrochemical properties and morphology techniques, Applied Surface Science, 256 (2010) 5849-5855.
[28] M. Aziz-Kerrzo, K.G. Conroy, A.M. Fenelon, S.T. Farrell, C.B. Breslin, Electrochemical studies on the stability and corrosion resistance of titanium-based implant materials, Biomaterials, 22 (2001) 1531-1539.
[29] B. Hirschorn, M.E. Orazem, B. Tribollet, V. Vivier, I. Frateur, M. Musiani, Determination of effective capacitance and film thickness from constant-phase-element parameters, Electrochimica Acta, 55 (2010) 6218-6227.
[30] B. Hirschorn, M.E. Orazem, B. Tribollet, V. Vivier, I. Frateur, M. Musiani, Constant-Phase-Element Behavior Caused by Resistivity Distributions in Films: I. Theory, Journal of The Electrochemical Society, 157 (2010) C452-C457.
[31] L. Hamadou, L. Aïnouche, A. Kadri, S.A.A. Yahia, N. Benbrahim, Electrochemical impedance spectroscopy study of thermally grown oxides exhibiting constant phase element behaviour, Electrochimica Acta, 113 (2013) 99-108.
[32] C. Hsu, F. Mansfeld, Technical note: concerning the conversion of the constant phase element parameter Y_0 into a capacitance, Corrosion, 57 (2001) 747-748.
[33] G.J. Brug, A.L.G. van den Eeden, M. Sluyters-Rehbach, J.H. Sluyters, The analysis of electrode impedances complicated by the presence of a constant phase element, Journal of Electroanalytical Chemistry and Interfacial Electrochemistry, 176 (1984) 275-295.
[34] D.R. Buddy, S.H. Allan, J.S. Frederick, E.L. Jack, Biomaterials science: An Introduction to Materials in Medicine, Academic Press, 2004.
[35] V.A. Alves, R.Q. Reis, I.C.B. Santos, D.G. Souza, T. de F. Gonçalves, M.A. Pereira-da-Silva, A. Rossi, L.A. da Silva, In situ impedance spectroscopy study of the electrochemical corrosion of Ti and Ti–6Al–4V in simulated body fluid at 25°C and 37°C, Corrosion Science, 51 (2009) 2473-2482.
[36] C.E.B. Marino, E.M.d. Oliveira, R.C. Rocha-Filho, S.R. Biaggio, On the stability of thin-anodic-oxide films of titanium in acid phosphoric media, Corrosion Science, 43 (2001) 1465-1476.
[37] L. Aïnouche, L. Hamadou, A. Kadri, N. Benbrahim, D. Bradai, Interfacial Barrier Layer Properties of Three Generations of TiO_2 Nanotube Arrays, Electrochimica Acta, 133 (2014) 597-609.
[38] J.M. Hernández-López, A. Conde, J. de Damborenea, M.A. Arenas, Correlation of the nanostructure of the anodic layers fabricated on

Ti13Nb13Zr with the electrochemical impedance response, Corrosion Science, 94 (2015) 61-69.
[39] C.P.-J. Peremarch, R.P. Tanoira, M.A. Arenas, E. Matykina, A. Conde, J.J. De Damborenea, E.G. Barrena, J. Esteban, Bacterial adherence to anodized titanium alloy, Journal of Physics: Conference Series, 252 (2010) 012011.
[40] C. Pérez-Jorge, A. Conde, M.A. Arenas, R. Pérez-Tanoira, E. Matykina, J.J. de Damborenea, E. Gómez-Barrena, J. Esteban, In vitro assessment of Staphylococcus epidermidis and Staphylococcus aureus adhesion on TiO_2 nanotubes on Ti–6Al–4V alloy, Journal of Biomedical Materials Research Part A, 100A (2012) 1696-1705.
[41] C. Yao, V. Perla, J.L. Mckenzie, E.B. Slamovich, T.J. Webster, Anodized Ti and Ti6Al4V Possesing Nanometer Surface Features enhances Osteoblast Adhesion, Journal of Biomedical Nanotechnology, 2005 (2005) 68-73.
[42] K. Das, S. Bose, A. Bandyopadhyay, TiO_2 nanotubes on Ti: Influence of nanoscale morphology on bone cell–materials interaction, Journal of Biomedical Materials Research Part A, 90A (2009) 225-237.
[43] J. Park, S. Bauer, K. von der Mark, P. Schmuki, Nanosize and Vitality: TiO_2 Nanotube Diameter Directs Cell Fate, Nano Letters, 7 (2007) 1686-1691.
[44] J. Park, S. Bauer, K.A. Schlegel, F.W. Neukam, K. von der Mark, P. Schmuki, TiO_2 Nanotube Surfaces: 15 nm—An Optimal Length Scale of Surface Topography for Cell Adhesion and Differentiation, Small, 5 (2009) 666-671.
[45] L. Zhao, S. Mei, W. Wang, P.K. Chu, Y. Zhang, Z. Wu, Suppressed primary osteoblast functions on nanoporous titania surface, Journal of Biomedical Materials Research A, 96 (2011) 100-107.
[46] S.F. Lamolle, M. Monjo, M. Rubert, H.J. Haugen, S.P. Lyngstadaas, J.E. Ellingsen, The effect of hydrofluoric acid treatment of titanium surface on nanostructural and chemical changes and the growth of MC3T3-E1 cells, Biomaterials, 30 (2009) 736-742.
[47] M.M. Tiainen Hanna, Knychala J, Nilsen O, Lyngstadaas S. Petter, Ellingsen Jan Eirik, Haugen, Håvard J, The effect of fluoride surface modification of ceramic TiO_2 on the surface properties and biological response of osteoblastic cells in vitro, Biomedical materials, 6 (2011).
[48] M. Monjo, S.F. Lamolle, S.P. Lyngstadaas, H.J. Rønold, J.E. Ellingsen, In vivo expression of osteogenic markers and bone mineral density at the surface of fluoride-modified titanium implants, Biomaterials, 29 (2008) 3771-3780.
[49] S. Lamolle, M. Monjo, S. Lyngstadaas, J. Ellingsen, J. Haugen, Titanium implant surface modification by cathodic reduction in hydrofluoric acid: surface characterization and in vivo performance., J Biomed Mater Res A 88 (2009) 581-588.

[50] Z. Isa, G. Schneider, R. Zaharias, D. Seabold, C. Stanford, Effects of fluoride-modified titanium surfaces on osteoblast proliferation and gene expression, Int J Oral Maxillofac Implant, 21 (2006) 203-211.
[51] L.T. Duarte, S.R. Biaggio, R.C. Rocha-Filho, N. Bocchi, Surface characterization of oxides grown on the Ti–13Nb–13Zr alloy and their corrosion protection, Corrosion Science, 72 (2013) 35-40.
[52] M.A. Khan, R.L. Williams, D.F. Williams, The corrosion behaviour of Ti–6Al–4V, Ti–6Al–7Nb and Ti–13Nb–13Zr in protein solutions, Biomaterials, 20 (1999) 631-637.
[53] S. Bauer, P. Schmuki, K. von der Mark, J. Park, Engineering biocompatible implant surfaces: Part I: Materials and surfaces, Progress in Materials Science, 58 (2013) 261-326.
[54] M. Geetha, A.K. Singh, R. Asokamani, A.K. Gogia, Ti based biomaterials, the ultimate choice for orthopaedic implants – A review, Progress in Materials Science, 54 (2009) 397-425.
[55] S. Bai, D. Ding, C. Ning, R. Qin, L. Huang, M. Li, D. Mao, Anodic growth of uniform nanotube arrays on biphase Ti35Nb5Zr alloy, Electrochemistry Communications, 12 (2010) 152-155.
[56] H. Tsuchiya, T. Akaki, J. Nakata, D. Terada, N. Tsuji, Y. Koizumi, Y. Minamino, P. Schmuki, S. Fujimoto, Anodic oxide nanotube layers on Ti–Ta alloys: Substrate composition, microstructure and self-organization on two-size scales, Corrosion Science, 51 (2009) 1528-1533.
[57] S. Minagar, C.C. Berndt, T. Gengenbach, C. Wen, Fabrication and characterization of TiO_2-ZrO_2-$ZrTiO_4$ nanotubes on TiZr alloy manufactured via anodization, Journal of Materials Chemistry B, 2 (2014) 71-83.
[58] J. Fornell, N.T.C. Oliveira, E. Pellicer, N. Van Steenberge, M.D. Baró, C. Bolfarini, J. Sort, Anodic formation of self-organized Ti(Nb,Sn) oxide nanotube arrays with tuneable aspect ratio and size distribution, Electrochemistry Communications, 33 (2013) 84-87.

Capítulo 5

Conclusiones

De los resultados de la presente tesis doctoral, se puede concluir que la técnica de anodizado permite diseñar capas de óxido de titanio con morfología, espesor y composición controlada sobre las aleaciones de titanio Ti6Al4V y Ti13Nb13Zr.

Crecimiento de capas anódicas sobre Ti6Al4V

- Medio H_2SO_4/HF-

- El crecimiento de capas anódicas sobre la aleación Ti6Al4V empleando electrolitos ácidos y voltaje constante de 20 V permite la formación de estructuras nanoporosas y nanotubulares en función del tiempo de anodizado con espesores que no superan los ~230 nm. Las capas anódicas crecidas a voltajes de 60 V presentan una morfología poco definida con espesores superiores a los obtenidos a 20 V a tiempos similares.
- La determinación de la fórmula molecular media de las capas anódicas permitió establecer que el óxido que crece no es TiO_2 sino un óxido no estequiométrico de TiO_x con $x<2$ junto con una mezcla de óxidos de Al_2O_3, V_2O_5, y el compuesto TiF_4. La concentración de flúor es del 4-6 % at. para las capas crecidas a 20 V y de 6-13 % at. para aquellas fabricadas a 60 V.

-Medio $NH_4H_2PO_4$/NH_4F-

- El empleo de baños de anodizado de $NH_4H_2PO_4$/NH_4F favorece el crecimiento de estructuras anódicas con espesores superiores al micrómetro y la aplicación de un escalón de potencial permite el diseño de estructuras nanotubulares con diámetro de poro variable.
- Las capas anódicas nanotubulares crecidas aplicando un escalón de potencial, 10 V durante 30 minutos seguido por 20 V durante 60 minutos, en un baño que contiene 1M $NH_4H_2PO_4$/0.3M NH_4F, presentan una mejor definición de la forma de botella buscada, con un diámetro de nanotubo de ~47 nm en la zona externa y ~69 nm en

la intercara óxido/metal. El espesor de la capa es de ~1355 nm y la concentración de flúor de ~9 % at.

Caracterización electroquímica

- La resistencia frente a la corrosión electroquímica de las capas anódicas depende de su morfología. Las capas anódicas con morfología nanoporosa presentan los menores valores de $i_{pasivación}$, mientras que las capas con estructura nanotubular presenta valores de $i_{pasivación}$ del mismo orden que la aleación Ti6Al4V sin anodizar.
- Los ensayos de impedancia electroquímica revelan que las capas anódicas con morfología dual (nanoporosa+nanotubular) muestran la misma respuesta electroquímica que las capas con morfología nanoporosa y una gran estabilidad con el tiempo de inmersión.
- La respuesta electroquímica de las capas nanotubulares depende del tamaño del espaciado intertubular. Espacios intertubulares del orden de 30 nm, determinan que la respuesta electroquímica está gobernada por el sustrato expuesto a través de los mismos, mientras que en capas con espacios intertubulares ≤ 15 nm, la respuesta está determinada tanto por la contribución de la capa barrera de los nanotubos como la del óxido que cubre al sustrato expuesto en el fondo de los mismos.
- El análisis cuidadoso de los espectros de impedancia permite la determinación de los espesores de la capa barrera a partir de los valores de la capacidad efectiva calculada suponiendo una distribución de constantes de tiempo en superficie (2D).

Caracterización biológica

- La incorporación de flúor en las capas de óxido crecidas sobre la aleación Ti6Al4V mediante anodizado es el factor clave que promueve la disminución de la adherencia bacteriana en comparación con la aleación sin tratar o respecto a capas anódicas que no contienen flúor en su composición.

- La presencia de flúor en las capas anódicas reduce la adherencia bacteriana de *Staphylococcus aureus y Staphylococcus epidermidis,* hasta en un 50 %, tanto en cepas de colección como cepas clínicas extraídas de pacientes que habían desarrollado infección.
- En general, las capas anódicas con propiedades antibacterianas no alteran la respuesta celular ni la mineralización en comparación con la aleación Ti6Al4V sin anodizar.
- En algunos casos, la distribución del flúor en las capas anódicas mejora la respuesta a la mineralización y proliferación celular, como es el caso de las capas anódicas con morfología nanoporosa generadas en un baño de H_2SO_4/HF a 20 V durante 5 minutos.

Crecimiento y caracterización de capas anódicas sobre Ti13Nb13Zr

- Las capas anódicas fabricadas sobre la aleación Ti13Nb13Zr en baños de H_2SO_4/HF presentan espesores cercanos al micrómetro y una concentración de flúor entorno al 12 % at. para las capas crecidas a 20V y 60 minutos en comparación a las capas obtenidas sobre Ti6Al4V a las mismas condiciones de crecimiento.
- La respuesta electroquímica de las capas anódicas crecidas sobre esta aleación muestran el mismo comportamiento que las capas crecidas sobre Ti6Al4V. La $i_{pasivación}$ es menor para las capas anódicas nanoporosas que para las nanotubulares.
- Los ensayos de espectroscopía de impedancia electroquímica revelaron que estas capas anódicas presentan una gran estabilidad a lo largo del tiempo -672h-.
- La respuesta electroquímica de las capas nanoporosas está dominada por la señal de la capa barrera localizada en el fondo de los poros, mientras que en las capas con morfología nanotubular la respuesta está controlada por la respuesta del óxido nativo que crece sobre el sustrato expuesto al medio a través de los espacios intertubulares.

Capítulo 6

Compendio de publicaciones

Electrochimica Acta 56 (2011) 2221–2229

Contents lists available at ScienceDirect

Electrochimica Acta

journal homepage: www.elsevier.com/locate/electacta

Morphologies of nanostructured TiO_2 doped with F on Ti–6Al–4V alloy

E. Matykina [a], J.M. Hernandez-López [a], A. Conde [a], C. Domingo [b], J.J. de Damborenea [a], M.A. Arenas [a,*]

[a] Departamento de Corrosión y Protección, Centro Nacional de Investigaciones Metalúrgicas (CENIM-CSIC), Avda. Gregorio del Amo 8, 28040 Madrid, Spain
[b] Instituto de Estructura de la Materia, CSIC, Serrano 123, 28006 Madrid, Spain

ARTICLE INFO

Article history:
Received 17 September 2010
Received in revised form
16 November 2010
Accepted 20 November 2010
Available online 29 November 2010

Keywords:
Ti–6Al–4V alloy
Nanotubes
Anodizing
Fluorine

ABSTRACT

The formation of nanotubes in sulphuric/hydrofluoric acid electrolyte at controlled voltage is investigated on Ti–6Al–4V alloy used for load-bearing prosthetic applications. The effects of anodizing time and voltage on film morphology, composition and microstructure are studied by scanning and transmission electron microscopy, Rutherford backscattering spectroscopy (RBS), and Raman spectroscopy. Fluorine content in the films was of a particular interest for enhancement of antibacterial properties of the surface. The efficiencies of film formation are determined as about 40% and 80% for anodizing at 20 V and 60 V respectively for shorter anodizing time and as about 1 and 5% for longer anodizing time. For 5 min of anodizing, higher voltage conditions results in a thicker barrier layer. At extended anodizing time a further disruption of the nanotubular morphology and formation of approximately 1.5 μm-thick nanoporous film is promoted. The films grown at 20 V contain from 4 at.% to 6 at.% of fluorine. RBS detects about 13 at.% of fluorine incorporated in the film formed at 60 V for 60 min, possibly associated with a greater film thickness. The oxide film material consists of amorphous titania matrix doped with V_2O_5 and Al_2O_3.

1. Introduction

Titanium and its alloys are widely used as biomaterials for dental implant and orthopaedic prosthesis applications due to their high strength-to-weight ratio, corrosion resistance and bio-inertness [1,2]. However, the thin, air-formed oxides present on the metal surfaces do not promote a direct chemical bond with bone tissue, thus surface modifications, altering topography and chemical composition of these materials, are required to enhance direct structural and functional anchoring of the prosthesis to the living bone (osseointegration). The most common surface treatments of commercially available implants and prosthesis encompass pickling [3], sandblasting [4], plasma spraying [5,6], anodizing [7], micro-arc oxidation [8,9].

For decades, until recently, cell interactions and bone response were studied on implant surfaces with micrometer-scale topography. Latest researches have shown that nanoscale topography as well as the order of the nanofeatures organisation is a critical factor promoting early cell responses to the implant surface [10–15]. Hence the fabrication of highly ordered TiO_2 nanotube films for biomedical applications is attracting much attention.

The advantages of the method are easy control of the nanotube diameter and thickness by use of adequate electrolyte and anodizing regime parameters, such as voltage and time [16]. Typically TiO_2 nanotubes as-formed on pure titanium are amorphous, however their crystal structure can be influenced by alloying elements [17,18] or radically modified by post-annealing [19–23].

Although the majority of TiO_2 nanotube research has been done on c.p. titanium and regularities and mechanisms of film formation have been well enough elucidated [24–31], the formation of TiO_2 nanotubes on titanium alloys has been also reported [18,23,32–42]. High strength titanium alloys are used for load-bearing prosthetic applications [43–46], where the reduction of the probability of infection during surgery and healing process is one of the primary goals. Ion incorporation (e.g. silver, fluorine) into titanium surface has been shown as effective method of providing antibacterial properties [47]. Additionally, fluoride ions are known to induce formation of fluorapatite in the surrounding bone and thus improve the bone anchorage to titanium implant [48–51].

In this connection TiO_2 nanotubes are of particular interest, as majority of the electrolytes used for anodizing are fluoride-based, hence the nanotubes always contain a certain amount of incorporated fluorine. Fluorine content in the nanotubes may vary depending on the electrolyte and anodizing conditions [26,28].

The present work investigates the development of self-organised TiO_2 nanotubes with sufficient fluorine content on Ti–6Al–4V alloy and aims for optimisation of the nanotube layer thickness, morphology and composition.

* Corresponding author at: Departamento de Corrosión y Protección, Centro Nacional de Investigaciones Metalúrgicas (CENIM-CSIC), Avda. Gregorio del Amo 8, 28040 Madrid, Spain. Tel.: +34 91 5538900x292; fax: +34 915743425.
E-mail address: geles@cenim.csic.es (M.A. Arenas).

0013-4686/$ – see front matter © 2010 Elsevier Ltd. All rights reserved.
doi:10.1016/j.electacta.2010.11.069

2. Experimental

A 18 mm ⌀ rod of Ti–6Al–4V alloy ELI grade according to the standard ASTM F136-02 supplied by SURGIVAL was cut into 2 mm thick disk specimens, ground through successive grades of SiC paper to 1200 grade, degreased with a detergent and rinsed in tap water followed by deionised water. The specimens were then chemically polished in a mixture of HF (48 wt.%):HNO_3 (70 wt.%):H_2O with volume ratio 1:4:5 for 5 min at room temperature under continuous agitation at 400 rpm, rinsed in distilled water and dried in cold air. The working area was 2.54 cm^2.

Nanotubes were formed in a two-electrode cell by anodizing the specimens at constant voltage controlled at 20 V and 60 V in the electrolyte containing 1 M H_2SO_4 and 0.15 wt.% HF for 5 and 60 min at temperature controlled at 20 °C according to the patent described elsewhere [52]. Platinum mesh was used as a cathode. Voltage–time and current–time responses of anodizing were acquired at 0.1 Hz sampling rate using a zero-ohm ammeter.

The plan view morphology of nanotubular oxide films was examined by field emission gun scanning electron microscopy (FEG–SEM) utilizing JSM6500F JEOL instrument equipped with EDX facilities, operated at 15 keV for EDX analysis and 7 keV for secondary electron imaging. Each of the area and local EDX analysis results are quoted as an average of 3 measurements.

Electron-transparent sections, nominally 40 nm thick, were prepared by ultramicrotomy and observed by a JEOL JEM 2010 TEM, instrument operated at 200 keV. Other sections were also prepared by scratching the surface of anodized specimens with a scalpel and collecting them on a TEM grid.

The presence of fluorine in the oxide films was first assessed semiquantitatively by EDX. The stoichiometric composition of the oxide films was further determined by Rutherford backscattering spectrometry (RBS), using 3.045 MeV (resonant energy for $^{16}O(a, a_0)^{16}O$ reaction) He^+ ions produced by the van de Graff accelerator of the Centro de Micro-Analisis de Materiales (CMAM), Madrid. The incident ion beam was normal to the specimen surface with 10 μC dose scattered ions detected at 170°. Data were interpreted using the SIMNRA program.

Raman spectra were obtained with a Renishaw Raman System RM2000 equipped with a Leica microscope (using magnification 50×), an electrically refrigerated CCD camera and an Ar^+ laser at 514.5 nm with exit power of 3 mW as excitation source, The spectra were taken with a spectral resolution of 4 cm^{-1} and acquisition times of 100 s. Raman spectra of the films annealed at 400 °C for 2 h were also measured.

3. Results and discussion

3.1. Current response during anodizing

In all experiments current transients showed good reproducibility. Typical current density–time responses for anodizing of Ti–6Al–4V alloy in mixed sulphuric/hydrofluoric acid electrolyte at constant voltage (Fig. 1) comprised three stages: (i) an initial surge to ~27.3 mA cm^{-2} and ~104 mA cm^{-2} for anodizing at 20 V and 60 V, respectively, followed by a rapid decay to a minimum of ~0.5 mA cm^{-2} and ~0.6 mA cm^{-2} respectively, (ii) a plateau at the minimum current density for a period of ~500 s and ~950 s, respectively, and (iii) further progressive increase to ~1.7 mA cm^{-2} and ~1.8 mA cm^{-2} until anodizing ends after 3600 s.

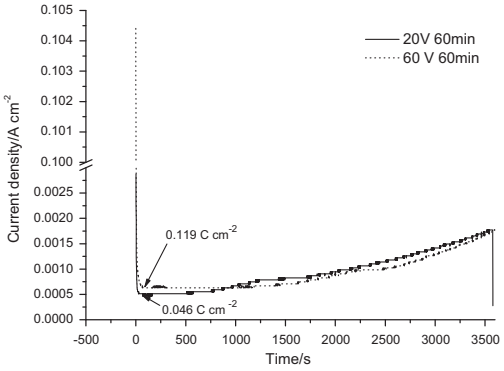

Fig. 1. Current density–time responses for anodizing of Ti–6Al–4V in sulphuric/hydrofluoric acid electrolyte at 20 and 60 V for 60 min at 20 °C.

Stage (i) is typically ascribed to growth of barrier layer, hence the associated resistance increase and current decay. The charge densities passed during stage (i) in the present work were ~0.046 and ~0.119 C cm^{-2} for 20 V and 60 V, respectively, (Table 1) that is equivalent to the growth of 25 and 64 nm of barrier amorphous layer at 100% efficiency. Notably, no stabilisation of current density has occurred at the stage (iii), unlike observed by Macak et al. [30] for nanotube formation on pure titanium in H_2SO_4/HF electrolyte and on Ti–6Al–4V in $(NH_4)_2SO_4/NH_4F$ electrolyte [32]. Typically, such stabilisation of current density following an increase from some minimum is associated with self-organisation of the nanotubes and their steady state growth, where electrochemical oxidation (barrier film growth) and chemical dissolution are balanced.

The charge densities passed following 5 min of anodizing at 20 V and at 60 V (Table 1) were sufficient to oxidize 43 nm and 70 nm of pure titanium, presuming that oxidation occurs with 100% efficiency. With the same assumption, the expected thicknesses of compact amorphous titanium oxide are 85 and 138 nm, respectively.

Table 1
Parameters of the porous films formed on Ti–6Al–4V in sulphuric/hydrofluoric acid electrolyte.

Film	Charge (A s cm^{-2})	Oxidized titanium[a] (nm)	Expected oxide thickness[b] (nm)	Barrier part thickness[c] (nm)	Total thickness[c] (nm)
20 V 5 min	0.156	43	85	~45	~110
20 V 60 min	3.45	949	1876	~25	~230
60 V 5 min	0.254	70	138	~140	~200
60 V 60 min	3.38	930	1838	~75	~500

[a] Calculated for pure titanium assuming 100% current efficiency.
[b] Calculated for compact amorphous film assuming 100% current efficiency.
[c] Measured using TEM.

Table 2
Results of area EDX analysis at.% of Ti–6Al–4V anodized in sulphuric/hydrofluoric acid electrolyte.

Film	Area/point	Ti	O	F	Al	V	S	Fe	Al/Ti	V/Ti	F/Ti
Before anodizing	A	77.35	–	–	6.9	14.43	–	1.32	0.09	0.19	–
	B	85.97	–	1.04	10.95	2.04	–	–	0.13	0.02	–
	C	86.17	–	–	10.15	3.67	–	–	0.12	0.04	–
20 V 5 min	A	55.58	31.66	4.23	6.5	1.98	0.05	–	0.12	0.04	0.08
20 V 60 min	A	63.35	23.01	3.97	8.27	1.36	0.05	–	0.13	0.02	0.06
	B	80.4	–	0.47	7.62	10.43	0.03	1.04	0.09	0.13	0.01
60 V 5 min	A	38.90	50.92	3.96	4.37	1.61	0.25	–	0.11	0.04	0.10
60 V 60 min	A	43.17	44.83	5.0	5.24	1.74	0.02	–	0.12	0.04	0.12

3.2. Film morphology and compositions

3.2.1. Nanotubes formed at 20 V

Before anodizing the chemically polished substrate was examined by FEG–SEM and its general composition as well as the local compositions of α- and β-phase were analysed by EDX. Fig. 2 shows typical morphology of Ti–6Al–4V alloy with dispersed 2–3 μm long β-phase particles of irregular shapes (point A). Local composition analysis of the particles disclosed that they are enriched in vanadium and deficient in aluminium compared with the composition of the α-phase (point B) (Table 2). Further, β-phase particles contained about 1.3 at.% of iron, which was absent in the α-phase. About 1 at.% of fluorine was found in the α-phase, that apparently originated from etching solution.

Five minutes of anodizing at 20 V resulted in oxidation of the α-phase with formation of randomly arranged nanotubes of about 20 nm in diameter (Fig. 3(a) and (b)). The area EDX analysis of the porous film formed on α-phase detected about 4.2 at.% of fluorine and traces of sulphur (Table 2). No nanotubular film was formed on β-phase grains, which appeared recessed, compared with the surrounding α-matrix and revealed a nanoscale irregular surface topography. Following anodizing at 20 V for 60 min

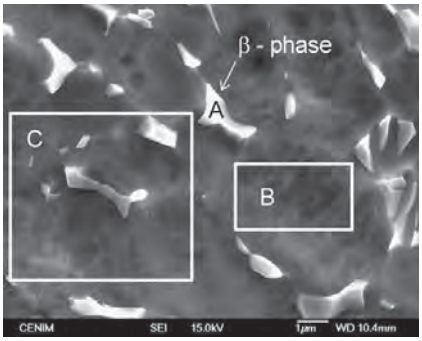

Fig. 2. Secondary electron micrograph of Ti–6Al–4V chemically polished in HNO_3/HF mixture.

the oxide film exhibits a clear self-organised morphology with the nanotube diameter increased to ~100 nm and approximately 30 nm inter-spacing. The nanotubular oxide contains about 4 at.% of fluorine (area A, Fig. 3(c)) and less than 0.1 at.% of sulphur; the flu-

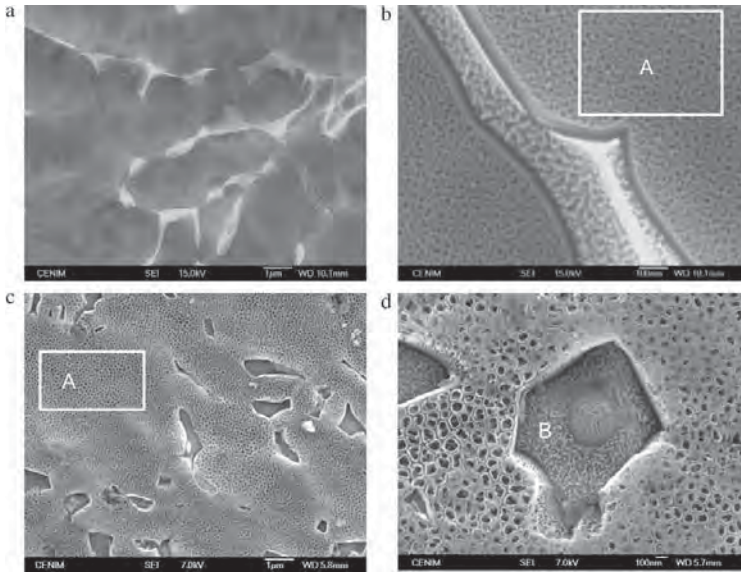

Fig. 3. Plan-view secondary electron micrographs of anodic oxide films formed on Ti–6Al–4V in sulphuric/hydrofluoric acid electrolyte at 20 V for 5 min (a and b) and 60 min (c and d) at 20 °C.

orine content in the film appeared to decrease with anodizing time from 0.08 to 0.06 of F/Ti ratio. The Al/Ti and V/Ti ratios remained unchanged (0.13 and 0.02, respectively) compared with chemically polished substrate. The dissolution of the β-phase becomes obvious (Fig. 3(c) and (d)) which is in agreement with [32] and occurs due to high solubility of vanadium oxides, β-phase being rich in vanadium. However, whether the dissolution of the β-phase is partial or complete could not be confirmed by the utilised characterisation methodology. The local EDX analysis of the β-phase (point B, Fig. 3d) revealed no oxygen presence; traces of fluorine (<0.5 at.%) and sulphur (<0.05 at.%). The dissolution of the β-phase during anodizing led to its depletion in vanadium: V/Ti ratio decreased from 0.19 to 0.13 compared with local β-phase composition of the chemically polished substrate; the Al/Ti ratio remained unaffected at 0.09 (Table 2).

In some areas of the surface a deposit is visible on the surface of the nanotubular film (Fig. 3d), which has been identified previously as titanium (IV) oxyhydroxide $TiO(OH)_2$, or $Ti(OH)_4$ [30,53]. It may be associated with relatively high current density that leads to local concentration of hydrated species at the mouth of the pore exceeding the precipitation threshold. Precipitation of $TiO(OH)_2$ and/or $Ti(OH)_4$ typically occur on pure titanium as a result of hydrolysis of TiO_2 at the pore initiation stage when current densities are sufficiently high; further, chemical dissolution of TiF_4 also proceeds with formation of $Ti(OH)_4$. The precipitate then re-dissolves with increased anodizing times and following current decay. In the present case however a continuous current increase was observed, thus the conditions for re-dissolution of hydrolysed species have never been reached. The precipitate of hydrolysis products can be discerned in transmission electron micrographs (Fig. 4(b) and (d)) as substance with grainy appearance, often blocking the mouth of the nanotubes (Fig. 4(c-inset)).

The transmission electron micrograph of a scraped material in Fig. 4(a) shows a detached nanotubular oxide film formed for 5 min, comprising a ~45 nm-thick barrier layer and a ~55 nm-thick porous part that reveals a well-defined tubular microstructure with

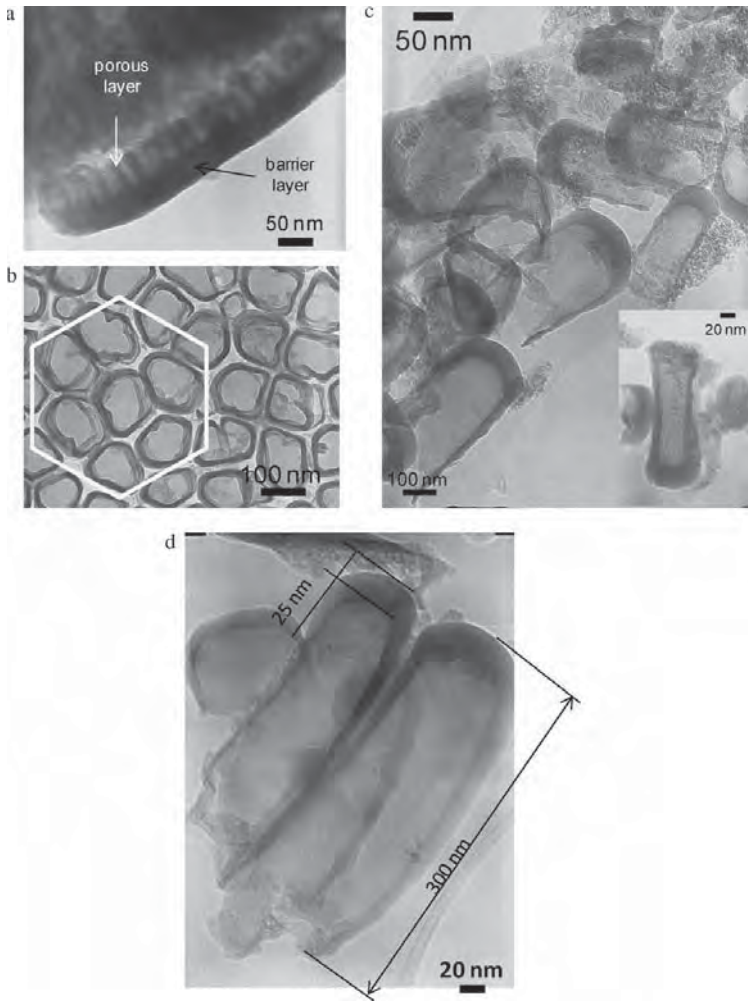

Fig. 4. Transmission electron micrographs of anodic oxide films formed on Ti–6Al–4V in sulphuric/hydrofluoric acid electrolyte at 20 V for 5 min (a) and 60 min (b–d) at 20 °C.

both internal tube diameter and tube wall thickness being about 20–25 nm. The nanotubes formed by anodizing for 60 min disclose variability in circumferential shape (Fig. 4(b)), length and diameter (Fig. 4(c) and (d)). The average length of the nanotubes appears to be ~230 nm, the maximum length being ~300 nm. The variability in nanotube internal diameter (100–200 nm) apparent in Fig. 4(b) may however arise from a different angle of cross-sectional view, as the nanotubes are not of perfect cylindrical shape. All micrographs of the nanotubes formed for 60 min disclosed a reproducible 25 nm-thick barrier layer that corresponds to the charge passed at the stage (i) of current response. The nanotube wall thickness was reduced from ~13 nm at the bottom to ~6 nm at the mouth of the nanotube. The thinning of the nanotube walls towards the outer part of the film is a well known fact for nanotube formation on pure titanium, related to continuous dissolution of TiO_2 and TiF_4 along the entire nanotube length [28], and a new material being formed at the metal/film interface.

Using the nanotube geometry and assuming that nanotubes are cylinders sealed at one end (with 25 nm-thick bottom, 112 nm average external diameter and 9 nm-thick average wall) and arranged in hexagonal arrays (Fig. 4(b)), the volume porosity of the film formed for 60 min is estimated as 83.4%.

3.2.2. Nanotubes formed at 60 V

The morphology of the porous film formed at 60 V for 5 min (Fig. 5(a) and (b)) was largely similar to the one formed at 20 V for 5 min and disclosed analogous dissolution of the β-phase. The general area composition of the film (area A, Fig. 5(a)) disclosed F/Ti ratio of 0.1, slightly higher than in the films formed at 20 V (Table 2). TEM micrographs of the ultramicrotomed sections of the film disclosed a ~180 nm-thick film with a well developed ~140 nm-thick barrier layer and initiating nanotubes with ~15 nm of internal diameter (Fig. 6(a–c)). The anodizing for extended time resulted in disruption of order and tubular morphology and formation of a sponge-like nanoporous material, with a nanopore size varying from ~15 nm to ~100 nm (Fig. 5(c) and (d)). Relatively deep cavities appear to form in the places of β-phase, the mouth of the cavities seem to narrow due to the overflow of the surrounding oxide film. The 30° tilted view of the fractured film disclosed a variation of the film thickness in the range of 0.4–0.85 μm. The general composition of the film indicates the highest F/Ti ratio of 0.12 of all four coatings. No continuous barrier layer could be discerned at the given resolution. TEM micrographs of the scraped film indicate that the inner part of the film possibly retains nanotubular morphology, with the variation of the thickness of the barrier layer in the range of 50–125 nm (Fig. 6(f) and (g)).

The formation ratio of the barrier layer for short anodizing times was found as 2.25 and 2.33 nm V^{-1} for 20 and 60 V films respectively. At the extended anodizing times both ratios decreased to 1.25 nm V^{-1} (assuming the average thickness of the barrier layer of the film formed at 60 V as 75 nm). This drastic drop in the formation ratio is associated with the chemical dissolution process which strongly affects the structure and composition of the anodic layers. Previously the formation ratio of the nanotubes on pure titanium in non-aqueous electrolyte at 20 V for 2000 s was estimated at 1.35 nm V^{-1} [23], whereas a formation ratio of a typical barrier titania film grown at constant current in aqueous electrolyte is about 2.2 nm V^{-1} [54].

The ratio of the real thickness of the film to the expected thickness of titanium oxidized with 100% current efficiency was 2.56 and 2.86 for films formed for 5 min at 20 V and 60 V, respectively. The value of 2.54 was reported for titanium anodized at constant voltage in glycerol electrolyte [26], whereas calculations for compact amorphous formed with 100% efficiency produce a ratio of 1.95. Evidently, measured thickness of the films formed for short times exceeds the expected thickness of the oxide by approximately 30% (Table 1). This length expansion may occur as a result of (i) incorporation of fluoride, aluminium and vanadium species into the oxide and (ii) flow of the growing oxide up the walls due to the plasticity of the film material under the electric field and the film growth

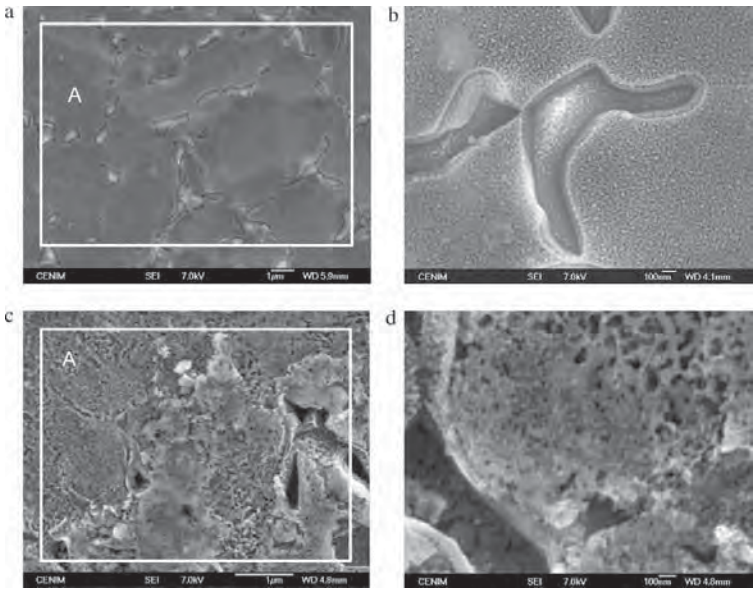

Fig. 5. Plan-view secondary electron micrographs of anodic oxide films formed on Ti–6Al–4V in sulphuric/hydrofluoric acid electrolyte at 60 V for 5 min (a and b) and 60 min (c and d) at 20 °C.

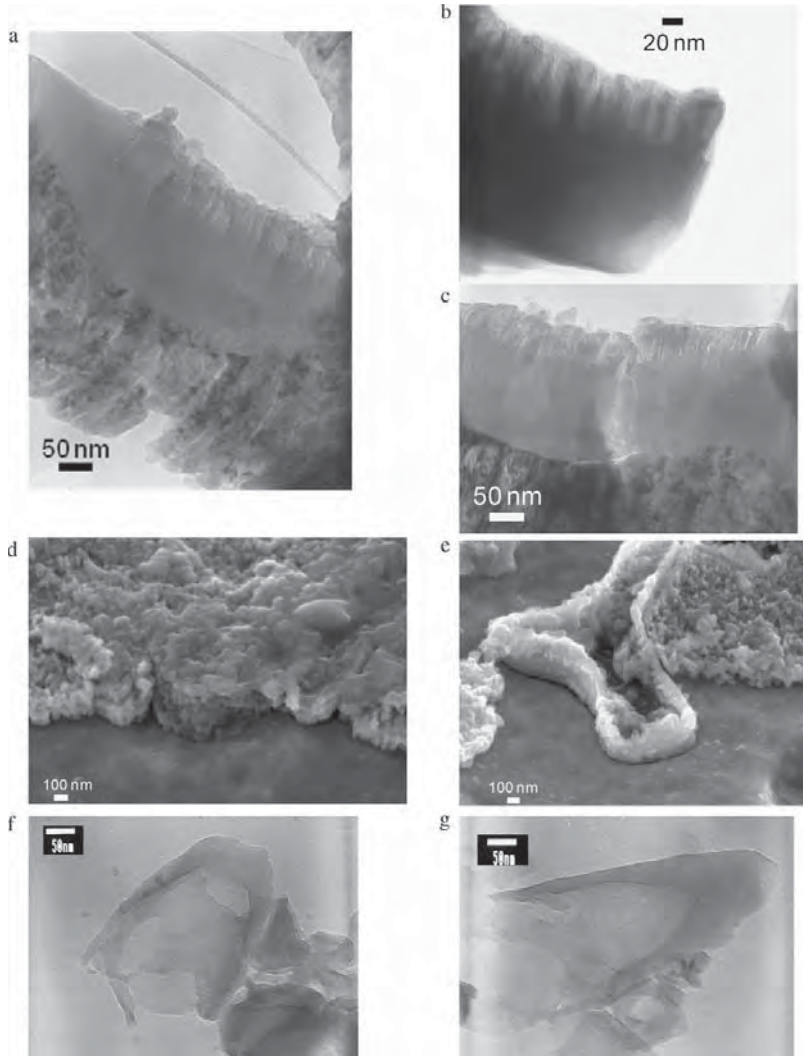

Fig. 6. Transmission electron micrographs (a–c, f and g) and secondary electron micrographs (d and e) of anodic oxide films formed on Ti–6Al–4V in sulphuric/hydrofluoric acid electrolyte at 60 V for 5 min (a–c) and 60 min (d–f) at 20 °C.

stresses as demonstrated previously on pure titanium by Berger and LeClere [27,55]. Originally a flow dependent formation has been developed for porous alumina [56–60].

3.3. Film microstructure

Raman spectra of the films formed both at 20 and 60 V are presented in Fig. 7 (Ib–Ie). The broad bands centered at 454 and 617 cm^{-1} correspond to amorphous TiO_2 [61]. The third very broad band centered at 850–890 cm^{-1} should arise from V–O–R (R = Ti, Al) bonds, as it has been shown that both, V_2O_5–TiO_2 doped [62] and V_2O_5–Al_2O_3 doped compounds [63] exhibit Raman bands around 860 cm^{-1}. The Raman intensity of the 20 V films is much weaker than for 60 V, possibly associated with lower thickness of the films formed at low voltage. The amorphous character of the TiO_2 nanotubes deduced from Raman data agrees with TEM observations, where, at the employed resolution, no nanocrystals were disclosed in any of the examined films.

This result is in apparent contradiction with other results previously reported on titanium anodized in a mixture of sulphuric/hydrofluoric acid electrolyte [64]. There, higher voltages result in formation of mixed anatase–rutile structure with anatase/rutile ratio increasing with voltage. No such effect is observed in our case.

Raman spectra of the films annealed at 400 °C for 2 h (Fig. 7(IIb′) and (IIe′)), show narrower bands at 397, 514 and 638 cm^{-1} corresponding to anatase, as well as a band centered at 830 cm^{-1} which indicates the presence of V–O–Ti bonds.

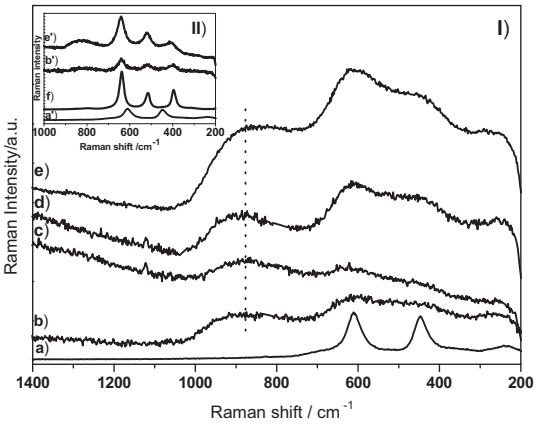

Fig. 7. (I) Raman spectra of anodic oxide films formed on Ti–6Al–4V in sulphuric/hydrofluoric acid electrolyte at 20 °C, at controlled voltage and time: (b) 20 V 5 min; (c) 20 V 60 min; (d) 60 V 5 min; (e) 60 V 60 min. Spectrum (e) here presented is divided by 3. Raman spectrum of rutile (a) is included for comparison. (II) (b′) and (e′): Raman spectra of films (Ib) and (Ie), respectively, annealed at 400 °C during 120 min. Raman spectra of pure rutile (a′) and anatase (f) TiO_2 phases are also shown for comparison.

3.4. Efficiencies of film formation

In addition to semi-quantitative EDX the oxide films were examined by RBS in order to determine the composition of the film and efficiency of the nanotube formation. RBS spectra for the different samples are shown in (Fig. 8(a)). The fittings of the spectra for all the specimens except the one obtained at 60 V for 60 min were performed as a monolayer of the oxide with uniformly distributed species. The thickness of the film formed at 60 V for 60 min exceeded the depth detection limit for RBS; the accuracy of fitting was further affected by the increased roughness of the film, compared to other specimens, and therefore the simulation of the spectrum was performed as a multilayered fitting, with the yield of the outermost layer quoted. The effects of the roughness of the metal/film and film/air interfaces, non-uniformity of the film thickness and film porosity are reflected in the sloping edges of the spectra corresponding to titanium yield from the metal/film interface. Vanadium manifested itself as a small slope of the edge of the spectra at ~800 channel. The presence of aluminium was indicated by a small step in the overall spectrum yield. Fluorine did not yield a prominent peak due to its relatively low content and the fact that RBS is less sensitive to the light elements than to the heavy elements because the scattering cross-section is proportional to the square of atomic number of the detected species. However due to a large yield from oxygen at its resonant scattering energy it was possible to simulate the total composition with reasonable accuracy, as fitting of the oxygen peak was very sensitive to the presence of fluorine in the total balance.

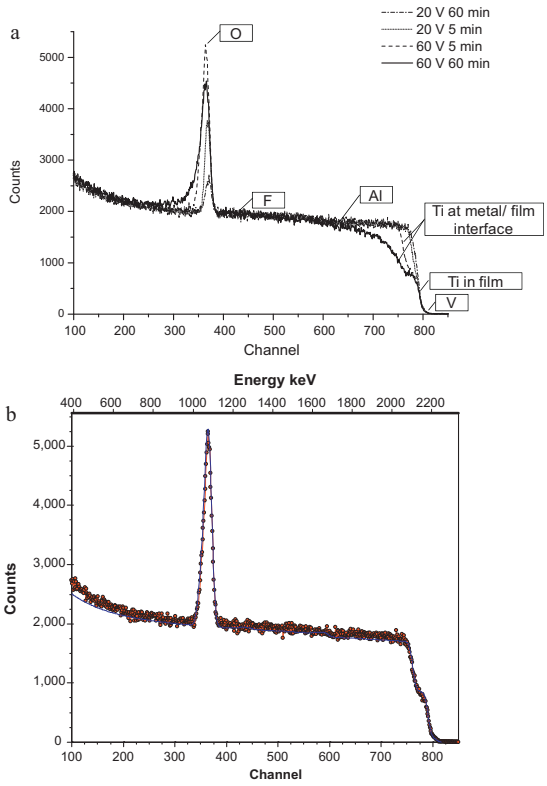

Fig. 8. Rutherford backscattering analysis spectra for anodic oxide films formed on Ti–6Al–4V in sulphuric/hydrofluoric acid electrolyte (a) and fitting of the spectra for the film formed at 60 V for 5 min (b): dotted line – original data; solid line – simulation.

The compositions of the films and current efficiencies are given in Table 3. The nanotubes formed at 20 V contained ~6 at.% and ~4 at.% of fluorine after 5 and 60 min of anodizing respectively, which is in agreement with the values determined by XPS for nanotubes formed on Ti–6Al–4V alloys in mildly acidic electrolyte in [32]. The decrease in the fluorine content apparently occurs due to intensive dissolution of TiF_4 in the walls of the nanotubes. First studies performed to evaluate the adhesion of bacteria revealed a decrease of adherence either for collections or clinical strains of two species of bacteria *Staphylococcus epidermis* and *Staphylococcus aureus*. This decrease occurs for any of the F contents obtained under these anodizing conditions [65].

Table 3
Composition of the porous films ($\times 10^{15}$ atoms cm^{-2}) formed on Ti–6Al–4V in sulphuric acid/hydrofluoric acid electrolyte, determined using RBS.

Film	Ti	O	F	Al	V	Average molecular composition	Efficiency (%)
20 V 5 min	96.56	193.8	21.6	21.6	6.25	$TiO_{1.6}0.06TiF_4 0.12Al_2O_3 0.033V_2O_5$	39.7
20 V 60 min	68.32	128.24	9.42	14.49	4.53	$TiO_{1.44}0.036TiF_4 0.11Al_2O_3 0.034V_2O_5$	1.3
60 V 5 min	316.0	596.9	62.78	63.84	24.3	$TiO_{1.47}0.05TiF_4 0.105Al_2O_3 0.035V_2O_5$	79.8
60 V 60 min	280.06	510.12	130.03	60.0	20.0	$TiO_{1.5}0.13TiF_4 0.12Al_2O_3 0.04V_2O_5$	5.3

On the other hand, the nanotubes formed at 60 V revealed an increases of fluorine from ~6 at.% to ~13 at.% with anodizing time. Notably, fluorine content in the film formed at 60 V for 5 min was similar to that of the film formed at 20 V for 5 min, despite almost twice lower thickness of the latter. Since the length of the nanoporous part of the film is approximately the same in both cases, it is possible that fluorine is mostly incorporated into the porous part of the film, as thickness of the barrier layer for the 60 V is nearly 3 times of that for the 20 V. However barrier and porous parts of the films could not be discriminated by RBS, and the spectra were best fitted in a single-layer simulation. Similarly, the increase of fluorine with time for anodizing at 60 V can be explained by a greater thickness of the nanoporous film. The average stoichiometric composition estimated from the RBS fitting is gathered in Table 3.

The real density of the 20 V 60 min film material composed of $Ti_2O_30.11Al_2O_3$ (molar mass 137.55 g M^{-1}) with the film thicknesses derived from RBS (225×10^{15} atoms cm^{-2}) and TEM (~300 nm) was determined as 0.571 g cm^{-3}. Assuming a calculated material density for a non-porous oxide with composition $Ti_2O_30.11Al_2O_3$ as 4.28 g cm^{-3} the volume porosity of the film was found as 86.6%, which is in good agreement with the one calculated previously from film geometry.

The efficiencies were derived using ratio of titanium ions determined by RBS in each film and titanium ions due in the film if all the charge passed during film formation was spent on oxidation of titanium (Table 1). Calculations were made using the electrochemical equivalent and density of pure titanium. The efficiency of the film formation both at 20 V and 60 V dropped remarkably with extended anodizing times from original ~40% and ~80%, respectively to ~1% and ~5%, respectively. Typically about 48–50% efficiency is reported for nanotubes formed in glycerol [26] and H_2SO_4/HF electrolytes [30] at 20 V and 20 °C for 40–60 min of anodizing.

Conventional formation of anodic titania proceeds with outward migration of Ti^{4+} and inward migration of O^{2-} ions through the film thickness with the transport numbers of ~0.4 and 0.6 respectively [66]. The growth of TiO_2 nanotubes is a result of competing electrochemical oxidation of titanium

$$Ti + 2H_2O \rightarrow TiO_2 + 4H^+ + 4e^- \quad (1)$$

and chemical dissolution of the anodic film material.

$$TiO_2 + 6HF \rightarrow [TiF_6]^{2-} + 2H^+ + 2H_2O \quad (2)$$

Thus the film develops at the titanium/film interface due to the inward migration of O^{2-} ions. Oxygen evolution may be one of the factors determining the efficiency loss. Although no visible oxygen evolution has been observed in the present work at any conditions, and Raman Spectroscopy did not detected the presence of nanocrystalline rutile in the present films, oxygen evolution, associated with nanocrystallisation of the film, may take place [67]. The reduced efficiency is largely attributed to chemical dissolution of the film, dissolution of TiF_4, according to reaction

$$TiF_4 + 4H_2O = Ti(OH)_4 + 4HF; \quad (3)$$

field-assisted ejection of outwardly migrating Ti^{4+}, field-assisted dissolution of the film, dissolution due to increased acidification of the bottom of the pore and physical loss due to detachment of the film at high current densities [68].

4. Conclusions

(1) Anodizing of Ti–6Al–4V alloy in sulphuric/hydrofluoric acid electrolyte at controlled voltage proceeds with formation of nanotubes on α-phase and recession of β-phase due to partial or complete dissolution.
(2) Anodizing for 5 min at 20 V and 60 V results in formation of 40–50 nm-long nanotubes of 15–20 nm in diameter. Self-organised nanotubes of 100 nm in diameter and about 230 nm-long with about 86% volume porosity are formed following anodizing at 20 V for 60 min. Disruption of self-ordering and of tubular morphology occurs with the voltage increase, while thickness of the film formed at 60 V achieves in the average 1 μm after 60 min of anodizing.
(3) Twice higher efficiency of film formation is achieved at 60 V anodizing compared with 20 V anodizing for shorter anodizing times (5 min). The efficiency of film formation decreases with time from about 40% and 80% to about 1 and 5% for anodizing at 20 V and 60 V respectively.
(4) Fluorine content decreases with anodizing time from ~6 at.% to ~4 at.% in the nanotubes formed at 20 V and increases from ~6 at.% to ~13 at.% in the nanotubes formed at 60 V, the latter associated with a greater film thickness.
(5) The microstructure of the nanotubes determined by Raman spectroscopy comprises an amorphous matrix and vanadium and aluminium oxides. According to the relative peak intensity the amount of the nanocrystalline material increases at higher anodizing voltage and time.

Acknowledgement

The authors thank Spanish Ministry of Science and Innovation for support of this work (SMOTI MAT2009-13751, FUNCOAT Consolider-Ingenio 2010 CSD2008-00023).

References

[1] D.M. Brunette, P. Tengvall, M. Textor, P. Thomsen, Titanium in Medicine, Springer, 2001.
[2] H.L. Freese, M.G. Volas, J.R. Wood, M. Textor, Titanium and its Alloys in Biomedical Engineering. Encyclopedia of Materials: Science and Technology, Elsevier Ltd., Oxford, 2001, p. 9374.
[3] M. Browne, P.J. Gregson, Biomaterials 15 (1994) 894.
[4] T. Albrektsson, A. Wennerberg, Int. J. Prosthodont. 17 (2004) 536.
[5] C. Sittig, M. Textor, N.D. Spencer, M. Wieland, P.H. Vallotton, J. Mater. Sci. Mater. Med. 10 (1999) 35.
[6] M. Taborelli, M. Jobin, P. Francois, P. Vaudaux, M. Tonetti, S. Szmukler-moncler, J.P. Simpson, P. Descouts, Clin. Oral Implant. Res. 8 (1997) 208.
[7] J.A. Disegi, Anodizing treatments for titanium implants, in: Proceedings of the Sixteenth Southern Biomedical Engineering Conference, Biloxi, MS, USA, 1997, 4–6 April.
[8] Y. Tanaka, J. Mater. Sci. 40 (2005) 3081.
[9] Y.-T. Sul, C.B. Johansson, Y. Jeong, A. Wennerberg, T. Albrektsson, Clin. Oral Implant. Res. 13 (2002) 252.
[10] M.M. Stevens, J.H. George, Science 310 (2005) 1135.
[11] J. Park, S. Bauer, K. Von Der Mark, P. Schmuki, Nano Lett. 7 (2007) 1686.
[12] F. Barrère, T.A. Mahmood, K. de Groot, C.A. van Blitterswijk, Mater. Sci. Eng. R: Report 59 (2008) 38.
[13] G. Mendonça, D.B.S. Mendonça, F.J.L. Aragao, L.F. Cooper, Biomaterials 29 (2008) 3822.
[14] K. Das, S. Bose, A. Bandyopadhyay, J. Biomed. Mater. Res. A 90A (2009) 225.
[15] J. Park, S. Bauer, K.A. Schlegel, F.W. Neukam, K.v.d. Mark, P. Schmuki, Small 5 (2009) 666.
[16] J.M. Macak, H. Tsuchiya, A. Ghicov, K. Yasuda, R. Hahn, S. Bauer, P. Schmuki, Curr. Opin. Solid State Mater. Sci. 11 (2007) 3.
[17] S.B. Aldabergenova, A. Ghicov, S. Albu, J.M. Macak, P. Schmuki, Non-Cryst. Solids 354 (2008) 2190.
[18] X.J. Feng, J.M. Macak, S.P. Albu, P. Schmuki, Acta Biomater. 4 (2008) 318.
[19] A. Ghicov, H. Tsuchiya, J.M. Macak, P. Schmuki, Phys. Stat. Sol. (A) 203 (4) (2006) R28.
[20] J.M. Macak, S. Aldabergerova, A. Ghicov, P. Schmuki, Phys. Stat. Sol. (A) 203 (10) (2006) R67.
[21] B. Luo, H. Yang, S. Liu, W. Fu, P. Sun, M. Yuan, Y. Zhang, Z. Liu, Mater. Lett. 62 (2008) 4512.
[22] S.-J. Cho, K.-S. Mun, D.-J. Yang, H.-P. Hun-Park, Y.-J. Park, J.-O. Kim, W.-Y. Choi, Ceram. Process Res. 9 (2008) 449.
[23] S. Sreekantan, Z. Lockman, R. Hazan, M. Tasbihi, L.K. Tong, A.R. Mohamed, J. Alloy Compd. 485 (2009) 478.
[24] J.M. Macak, K. Sirotna, P. Schmuki, Electrochim. Acta 50 (2005) 3679.

[25] A. Ghicov, H. Tsuchiya, J.M. Macak, P. Schmuki, Electrochem. Commun. 7 (2005) 505.
[26] A. Valota, D.J. LeClere, T. Hashimoto, P. Skeldon, G.E. Thompson, S. Berger, J. Kunze, P. Schmuki, Nanotechnology 19 (2008) 355701.
[27] S. Berger, J. Kunze, P. Schmuki, D. LeClere, A.T. Valota, P. Skeldon, G.E. Thompson, Electrochim. Acta 54 (2009) 5942.
[28] A. Valota, D.J. LeClere, P. Skeldon, M. Curioni, T. Hashimoto, S. Berger, J. Kunze, P. Schmuki, G.E. Thompson, Electrochim. Acta 54 (2009) 4321.
[29] H. Tsuchiya, J.M. Macak, A. Ghicov, A.S. RÃ¤der, L. Taveira, P. Schmuki, Corros. Sci. 49 (2007) 203.
[30] J.M. Macak, H. Tsuchiya, S. Berger, S. Bauer, S. Fujimoto, P. Schmuki, Chem. Phys. Lett. 428 (2006) 421.
[31] S. Bauer, S. Kleber, P. Schmuki, Electrochem. Commun. 8 (2006) 132.
[32] J.M. Macak, H. Tsuchiya, L. Taveira, A. Ghicov, P. Schmuki, J. Biomed. Mater. Res. Part A 75 (2005) 928.
[33] A. Ghicov, S. Aldabergenova, H. Tsuchiya, P. Schmuki, Angew. Chem. Int. Ed. 45 (2006) 6993.
[34] H. Tsuchiya, S. Berger, J.M. Macak, A. Ghicov, P. Schmuki, Electrochem. Commun. 9 (2007) 2397.
[35] K. Yasuda, P. Schmuki, Electrochim. Acta 52 (2007) 4053.
[36] K. Yasuda, P. Schmuki, Adv. Mater. 19 (2007) 1757.
[37] K. Yasuda, J.M. Macak, S. Berger, A. Ghicov, P. Schmuki, J. Electrochem. Soc. 154 (2007) C472.
[38] A. Ghicov, M. Yamamoto, P. Schmuki, Angew. Chem. Int. Ed. 47 (2008) 7934.
[39] S. Berger, H. Tsuchiya, P. Schmuki, Chem. Mater. 20 (2008) 3245.
[40] Y -C. Nah, A. Ghicov, D. Kim, S. Berger, P. Schmuki, J. Am. Chem. Soc. 130 (2008) 16154.
[41] V.S. Saji, H.C. Choe, W.A. Brantley, Acta Biomater. 5 (2009) 2303–2310.
[42] H. Tsuchiya, T. Akaki, J. Nakata, D. Terada, N. Tsuji, Y. Koizumi, Y. Minamino, P. Schmuki, S. Fujimoto, Corros. Sci. 51 (2009) 1528.
[43] B.C. Carr, T. Goswami, Mater. Des. 30 (2009) 398.
[44] M. Long, H.J. Rack, J. Biomater. 19 (1998) 1621.
[45] D.O. Meredith, M.O. Riehle, A.S.G. Curtis, R.G. Richards, J. Mater. Sci. Mater. Med. 18 (2007) 405.
[46] M. Geetha, A.K. Singh, R. Asokamani, A.K. Gogia, Prog. Mater. Sci. 54 (2009) 397.
[47] M. Yoshinari, Y. Oda, T. Kato, K. Okuda, Biomaterials 22 (2001) 2043.
[48] J.E. Ellingsen, J. Mater. Sci. Mater. Med. 6 (1995) 749.
[49] J. Guo, R.J. Padilla, W. Ambrose, I.J. De Kok, L.F. Cooper, Biomaterials 28 (2007) 5418.
[50] Z.M. Isa, G.B. Schneider, R. Zaharias, D. Seabold, C.M. Stanford, Int. J. Oral Maxillofac. Implant. 21 (2006) 203.
[51] L.F. Cooper, Y. Zhou, J. Takebe, J. Guo, A. Abron, A. Holmeïn, J.E. Ellingsen, Biomaterials 27 (2006) 926.
[52] M.A. Arenas, A. Conde, J. de Damborenea, E. Matykina, J.M. Esteban Moreno, E. Gomez Barrena, C. Perez-Jorge- Permarch, R. Perez Tanoira, Patent. Application number: P201030720, Spain, (14-05-2010).
[53] L.V. Taveira, J.M. Macak, H. Tsuchiya, L.F.P. Dick, P. Schmuki, J. Electrochem. Soc. 152 (2005) B405.
[54] H. Habazaki, K. Shimizu, S. Nagata, P. Skeldon, G.E. Thompson, G.C. Wood, J. Electrochem. Soc. 149 (2002) B70.
[55] D.J. LeClere, A. Velota, P. Skeldon, G.E. Thompson, S. Berger, J. Kunze, P. Schmuki, H. Habazaki, S. Nagata, J. Electrochem. Soc. 155 (2008) C487.
[56] S.J. Garcia-Vergara, L. Iglesias-Rubianes, C.E. Blanco-Pinzon, P. Skeldon, G.E. Thompson, P. Campestrini, Proc. R. Soc. A 462 (2006) 2345.
[57] S.J. Garcia-Vergara, P. Skeldon, G.E. Thompson, H. Habakaki, Appl. Surf. Sci. 254 (2007) 1534.
[58] S.J. Garcia-Vergara, P. Skeldon, G.E. Thompson, H. Habazaki, Corros. Sci. 49 (2007) 3772.
[59] S.J. Garcia-Vergara, P. Skeldon, G.E. Thompson, T. Hashimoto, H. Habazaki, J. Electrochem. Soc. 154 (2007) C540.
[60] S.J. Garcia-Vergara, P. Skeldon, G.E. Thompson, H. Habazaki, Electrochim. Acta 52 (2006) 681.
[61] A.G. Gaynor, R.J. Gonzalez, R.M. Davis, R.J. Zallen, J. Mater. Res. 12 (7) (1997) 1755.
[62] G.N. Kryukova, G.A. Zenkovets, G. Mestl, R. Schlögl, React. Kinet. Catal. L 80 (2003) 161.
[63] K. Scheurell, G. Scholz, E. Kemnitz, J. Solid State Chem. 180 (2007) 749–758.
[64] M. Bestetti, S. Franz, M. Cuzzolin, P. Arosio, P.L. Cavallotti, Thin Solid Films 515 (2007) 5253.
[65] C. Pérez-Jorge Peremarch, R. Pérez Tanoira, M.A. Arenas, E. Matykina, A. Conde, J.J. de Damborenea, E. Gómez Barrena, J. Esteban, J. Phys.: Conf. Ser. (2010) Pending of publication.
[66] H. Habazaki, K. Fushimi, K. Shimizu, P. Skeldon, G.E. Thompson, Electrochem. Commun. 9 (2007) 1222.
[67] H. Habazaki, M. Uozumi, H. Konno, K. Shimizu, S. Nagata, K. Takayama, Y. Oda, P. Skeldon, G.E. Thompson, J. Electrochem. Soc. 152 (2005) B263.
[68] L.V. Taveira, J.M. Macak, K. Sirotna, L.F.P. Dick, P. Schmuki, J. Electrochem. Soc. 153 (2006) B137.

RSC Advances

PAPER

View Article Online
View Journal | View Issue

Cite this: *RSC Adv.*, 2014, **4**, 62576

TiO_2 nanotubes with tunable morphologies

J. M. Hernández-López, A. Conde, J. J. de Damborenea and M. A. Arenas*

Received 29th September 2014
Accepted 6th November 2014

DOI: 10.1039/c4ra11457d

www.rsc.org/advances

Titanium anodic oxide layers with a bottle shaped nanotubular structure have been grown in an electrolyte containing NH_4F, applying voltage steps. The grown layers were analyzed using scanning and transmission electron microscopy (SEM and TEM), and Rutherford backscattering spectroscopy (RBS). The results show that a concentration of 0.15 M of NH_4F in the anodizing bath, and a step of 10 to 20 V produces an oxide with a double morphology comprised of nanotubes at the oxide/metal interface and nanopores at the oxide/electrolyte interface of the anodic layer. Higher concentration of F^- in the bath, 0.3 and 0.45 M NH_4F, enhanced the chemical dissolution of the anodic layer resulting in nanotubular structures along the oxide layer. Therefore, the bottle shaped nanotubular structures that show a well defined morphology are obtained in a bath containing a concentration of 0.3 M NH_4F and applying a voltage step of 10–20 V.

1. Introduction

In recent years, the growth and/or deposition of titanium thin films and titanium oxide layers have received considerable attention in a variety of fields of endeavour such as: tissue engineering, drug delivery systems, orthopaedic implants, gas sensors, lithium ion batteries, solar cells, photovoltaic devices and have therefore encouraged its study and development.[1–7] Different techniques such as laser, sputtering, sol–gel, thermal oxidation, electrophoresis and electroplating have been used to obtain TiO_2 layers. Nevertheless, these techniques are limited when it comes to controlling the thickness of TiO_2 and/or when dealing with the lack of uniformity in the grown layer.[8,9]

By contrast, the anodizing process allows the fabrication of uniform TiO_2 layers with a controlled thickness and a variety of nanostructures that differs from barrier to porous layers, depending on the composition of the electrolyte used and the growth conditions (temperature, stirring, voltage and/or current applied).[10,11] Zwilling *et al.* in 1999 obtained self-organized TiO_2 nanoporous structures using diluted hydrofluoric acid solutions.[12] Subsequent works showed that in these HF containing solutions, the thickness of TiO_2 anodic layer was limited to 500–600 nm. The chemical dissolution resulting from the high acidity of the bath and the presence of fluorides,[13] is responsible for this limitation in thickness. This drawback is overcome by the use of buffer solutions containing NaF or NH_4F (where the chemical dissolution is decreased), along with pH control of the anodizing bath, leading to TiO_2 layers up to 2 μm thick.[14,15] It was precisely this increase in the thickness of the nanostructured TiO_2 layers which made it possible to expand the niche of applications of TiO_2 layers in those uses in which the nanostructure and thickness are critical, such as TiO_2 fuel cells, which have improved their efficiency and service life by increasing the surface area.[16,17]

However, in addition to thickness, it is also possible to modify the diameter of the nanotubes by varying the applied voltage. Mor *et al.*,[5] fabricated porous TiO_2 layers with conical structures on titanium applying voltage ramps in an HF solution. The conical nanotubular layers had variable inner diameters throughout but the thickness of the oxide layer was limited to 200 nm. Similar nanostructures were obtained in organic electrolytes by applying ramps with ascending and descending voltages, leading to thicker anodic oxide layers and, therefore, greater surface areas of interest in the photocatalytic applications.[18–22] Liu *et al.*[23] fabricated TiO_2 nanotubes with periodically changing morphology by using periodic pulses consisting of high and low voltages. However, the main drawbacks are either the instability of the organic baths, or the longer times required to achieve the desired thicknesses. In addition, most of the works are focused on pure titanium or titanium binary alloys and few papers are devoted to fabricate tailored nanotubes in the micrometer range on technologically relevant substrates such as Ti6Al4V alloy.

The objective of the present work is the growth of thick anodic layers in the micrometer range, with bottle shaped nanotubular structures in Ti6Al4V alloy in short times, less than two hours, and in aqueous anodizing baths that could be of interest for drug delivery control systems in orthopaedic prostheses. The work correlates the influence of the anodizing process parameters: the concentration of fluoride in the bath and the application of increasing voltage steps on the fabricated nanostructures.

Centro Nacional de Investigaciones Metalúrgicas (CENIM-CSIC), Avda. Gregorio del Amo, 8, 28040 Madrid, Spain. E-mail: geles@cenim.csic.es

2. Experimental procedure

Ti6Al4V alloy specimens of ELI grade according to the standard ASTM F136-02 supplied by SURGIVAL were ground using successive grades of SiC paper to 1200 grade, degreased with a detergent and rinsed in tap water followed by deionised water.

The specimens were then chemically polished in a mixture of HF(40 wt%) : HNO_3(70 wt%) : H_2O with a volume ratio of 1 : 4 : 5 for 5 min, at room temperature under continuous agitation at 400 rpm, rinsed in distilled water and dried in cold air. The working area was 2.54 cm^2. Electrolytes containing 1 M $NH_4H_2PO_4$ and 0.15, 0.3 and 0.45 M NH_4F were prepared. Bottle shaped nanotubes were formed in a two-electrode cell. The specimens were anodized at stepped voltage with the first voltage (V_1) applied for 30 min followed by a second voltage step (V_2) applied for 60 min, as seen in Fig. 1. The temperature was controlled at 20 °C. Platinum mesh was used as a cathode. The voltages were applied using LAB/SM 1300 DC power supply (ET Power Systems Ltd). Current-time responses of anodizing were acquired at 0.1 Hz sampling rate using a zero-ohm ammeter connected in series with the electrochemical cell.

The plan-view morphology of the nanotubular oxide films was examined by field emission gun scanning electron microscopy (FEG-SEM) utilizing JSM6500F Philips instrument equipped with EDX facilities and a ZEISS Ultra 55 scanning electron microscope. Electron-transparent sections were prepared by scratching the surface of the anodized specimens with a scalpel and collecting the pieces of the oxide on a TEM grid. TEM grids were observed using a JEOL JEM 2010 instrument operated at 200 keV.

The stoichiometric composition of the oxide films was further determined by Rutherford backscattering spectroscopy (RBS), using the following non-Rutherford elastic backscattering cross sections: He^+ ions with the energy of 3.045 MeV (resonant energy for $^{16}O(\alpha,\alpha_0)^{16}O$ reaction), 3.777 MeV (resonant energy for $^{19}F(\alpha,\alpha_0)^{19}F$ reaction) and 5.725 MeV (resonant energy for $^{27}Al(\alpha,\alpha_0)^{27}Al$ reaction) were produced by the van de Graff accelerator located at the Centro de Micro-Análisis de Materiales (CMAM), Madrid. The incident ion beam was normal to the surface of the specimen with 10 μC dose scattered ions detected by a mobile detector at 165°. Data were interpreted using the SIMNRA program.

3. Results and discussion

3.1. Current density *versus* time response

In the following sections, the current transients recorded during anodizing process were evaluated to determine the influence of the composition of the anodizing bath and voltage steps applied, *i.e.* electric field, on the anodic layers grown.

3.1.1. Influence of the composition of the anodizing bath. The current density *versus* time curves collected during the anodizing of Ti and its alloys, show significant growth aspects of the anodic oxide layer and its morphology.[8,18,21,24] Fig. 2 shows the evolution of the current density *versus* time during the anodizing of the Ti6Al4V alloy in a 1 M $NH_4H_2PO_4$ bath with different concentrations of NH_4F applying voltage steps. In this figure, it is observed that the current-time transient, recorded for the different concentrations of NH_4F used, is similar to that described by other authors for the anodizing of Ti and its alloys in aqueous media.[5,8] Three different stages are distinguished:

Electrolyte		time (min)		Voltage (V)		Nomenclature
		t_1	t_2	V_1	V_2	
1M $NH_4H_2PO_4$	0.15M NH_4F	30	60	10	20	10-20V
	0.3M NH_4F			10	20	10-20V
				20	30	20-30V
				20	40	20-40V
	0.45M NH_4F			10	20	10-20V

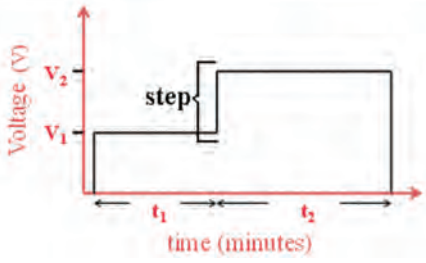

Fig. 1 Fabrication conditions of nanotubes grown on Ti6Al4V.

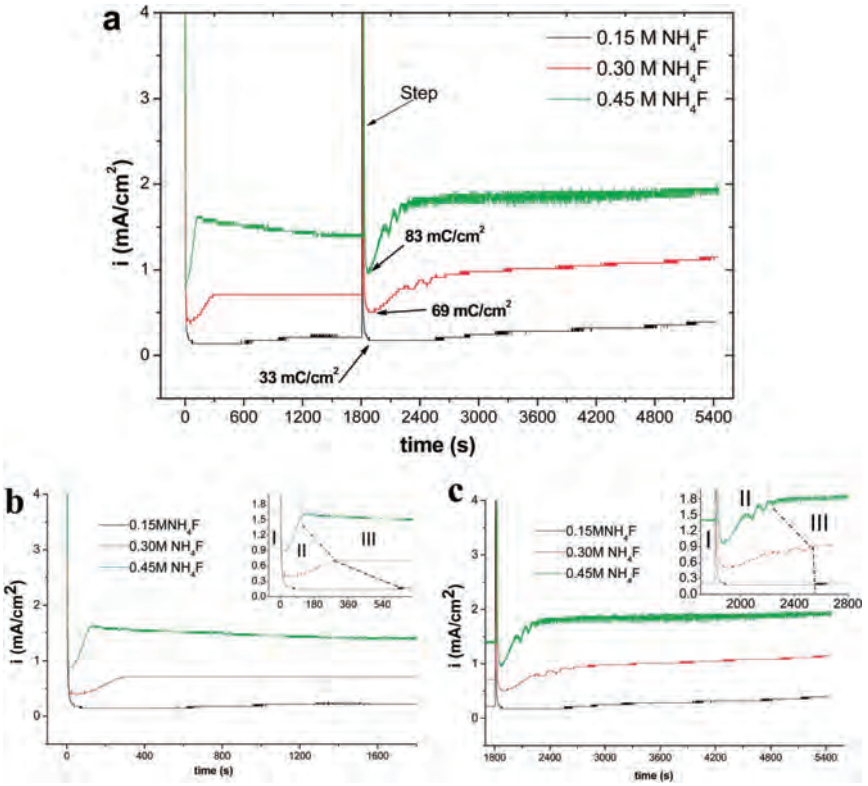

Fig. 2 Current density–time responses of anodizing of Ti6Al4V at 10 V for 30 minutes followed by second voltage step at 20 V for 60 minutes (a), *i vs. t* response related to $V_1 = 10$ V for 30 minutes (b) and $V_2 = 20$ V for 60 minutes (c).

the growth of the high resistance oxide barrier layer – stage I; pores nucleation – stage II; and the steady state (growth of nanotubes)-stage III.

In this electrolyte, the pore initiation stage can be attributed to both the field-assisted ejection of Ti^{4+} ions into the electrolyte and the chemical dissolution of the oxide due to the presence of fluoride ions readily forming cavities within the oxide.

The three stages plotted in the current density *versus* time response are observed for each applied step voltage, $V_1 = 10$ V for 30 minutes and $V_2 = 20$ V for 60 minutes, Fig. 2b and c. The steady state current density recorded on stage III corresponding to the first applied voltage, $V_1 = 10$ V, is 0.2 mA cm^{-2} for the bath containing 0.15 M NH_4F and increases to 1.5 mA cm^{-2} for 0.45 M NH_4F, Fig. 2b. The steady current density recorded for the second voltage step, $V_2 = 20$ V, increases approximately 0.2 mA cm^{-2} compared to the values showed for the first voltage step for all the NH_4F concentrations studied, Fig. 2c.

The increase in steady current density depending on the fluoride concentration in the bath indicates a greater chemical dissolution of the anodic layers with the fluoride content in the electrolyte.

The value of the final voltage (V_2) determines the features of the anodic oxide layer grown on the oxide/metal interface.[18–21,25] Therefore, the charge density related to the thickness of the barrier layer is calculated by integrating the stage I from the current density *vs.* time response corresponding to the second voltage step. These values vary between 33–83 mC cm^{-2} depending on the fluoride concentration in the bath, Table 1. Assuming that all the charge are only employed to form a dense layer of amorphous TiO_2,[21] the thickness of barrier layer varies from 18 to 45 nm, Table 1.

Similarly, by calculating the total charge density used in the anodizing process, it can be seen that the total charge density increases with the fluoride content in the bath, from 1.393 to 9.322 mC cm^{-2} (Table 1). Assuming an efficiency of 100% for the titanium anodizing process, the thickness of the anodic layer would be 758 nm for a concentration of 0.15 M NH_4F, 2615 nm for 0.3 M NH_4F, and 5071 nm for 0.45 M NH_4F, Table 1. However, as expected, the thickness values of the TiO_2 layers measured by SEM differ significantly from the theoretical values calculated, Table 1, as it will be discussed later. This difference is increased with the fluoride content in the bath due to the higher chemical dissolution of the anodic layer which occurs in

Table 1 Parameters of nanotubes formed in 1 M $NH_4H_2PO_4$/[X] M NH_4F

[X] M NH_4F	Step (30–60 min)	Barrier film charge mC cm^{-2}	Expected barrier oxide thickness, nm[a]	Charge C cm^{-2}	Expected oxide thickness, nm[a]	NT inner diameter mouth[b]/bottom[c], nm	Barrier layer thickness[c], nm	Total thickness[b], nm
0.15	10–20 V	33	18	1.393	758	~15/53	41	~661
0.3		69	38	4.807	2615	~47/69	39	~1355
0.45		83	45	9.322	5071	~63/65	40	~1585

[a] Calculate for compact amorphous film assuming 100% current efficiency. [b] Measured by SEM. [c] Measured by TEM.

presence of fluorides since the dissolution rate of the oxide layer increases considerably with the F^- content.[26]

3.1.2. Influence of the electric field. To study the influence of the electric field on the nanostructure of the anodic layers, the magnitude of the voltage steps was varied for a specific concentration of fluorides, 0.3 M NH_4F.

Fig. 3 shows the anodizing curves obtained for 0.3 M NH_4F solution using different voltage steps. The evolution of the *i vs. t* curves is similar to those described in Fig. 2. Thus, after applying a voltage step of 10 V, an abrupt decrease in the current density related to the formation of the oxide barrier layer is observed, followed by the nucleation of the pores which does not exceed 300 seconds. Finally, the current density is maintained constant indicating that the steady state, in which the growth of the nanotubes takes place, has been reached (Fig. 3).

Upon applying the second voltage step, either 20 or 30 V, the current density at the steady state depicts higher oscillations than during the first voltage step of 10 V. This is due to the increase of the field-assisted dissolution of the anodic layer at voltages higher than 10 V, unbalancing the formation and dissolution of the anodic oxide layer.

The current density evolution at the steady state for a given $\Delta V = V_2 - V_1$, indicates that the current density depends primarily on the applied ΔV rather than on the absolute values of each step, V_1 and V_2, see Fig. 3b and c.

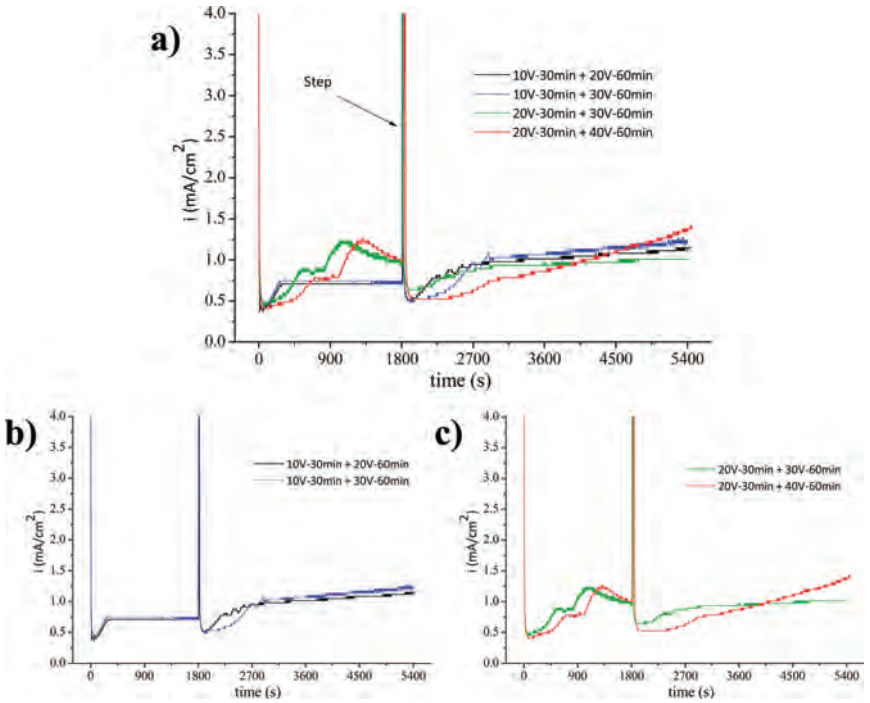

Fig. 3 Current density–time responses of anodizing of Ti6Al4V in 1 M $NH_4FH_2PO_4$/0.3 M NH_4F at different voltage steps (a), with $V_1 = 10$ V (b), with $V_1 = 20$ V (c).

Nevertheless, in the last 30 minutes of the 20–40 V treatment, the current density increases continuously, without actually reaching any steady state, thus revealing a greater field-assisted dissolution of the anodic layer at high voltages.

The results suggest that the main process occurring at stage III (constant nanotubular layer thickness over time) is field-assisted dissolution instead of "flow assisted" due to the significant level of dissolution of the oxide layer in this aqueous media.

3.2. Film morphology

In this section, the film morphology of the anodic layers fabricated using different anodizing conditions were characterized using scanning electron microscopy and transmission electron microscopy.

The morphology of the nanotubular layers fabricated in Ti6Al4V alloy by applying 10–20 V voltage steps in baths containing different NH_4F concentrations is shown in Fig. 4. In all cases the formation of nanotubes preferentially grown in the α-phase, enriched in aluminium, along with the dissolution of the oxides in β-phase is observed. Such morphology has been widely described for F^- containing aqueous electrolytes. The absence of porous structures in the β-phase relates to the high solubility of vanadium oxides formed on this phase.[5,8,12,15,27,28]

The micrographs gathered in Fig. 4 show the influence of the NH_4F concentration in the nanotube inner diameter in the mouth, which varies from 15–63 nm for 0.15 M and 0.45 M NH_4F, respectively, Table 1. This increase in the inner diameter of the nanotube is a result of the chemical dissolution of the nanotube walls due to the presence of fluorides in the electrolyte,[27,29] according to the following reaction:

$$TiO_2 + 6F^- + 4H^+ \rightarrow TiF_6^{2-} + 2H_2O \quad (1)$$

This reaction may be further enhanced by the weakness of the bond between adjacent Ti and O due to the electric field (field-assisted dissolution).

Additionally in Fig. 4b and c it can be observed that in some areas the mouths of nanotubes appear to be plugged by a white oxide. This oxide is the result of the solubilization of the titanium and precipitation in form of hydrated species ($TiO(OH)_2$ or $Ti(OH)_4$).[24,28,30,31]

The thickness of the grown layers measured by SEM varies from 661 nm for the anodic layer fabricated in the bath with the lowest concentration of fluoride, up to 1585 nm approximately, for the layer obtained in a bath with the highest concentration, 0.45 M NH_4F, Table 1.

Fig. 5a–f show the cross section of the anodic layers. Nanotubular structure can be distinguished in α-phase, while cavities caused by the preferential dissolution of the oxide formed in β-phase are observed.

It is important to highlight that the lowest concentration of fluoride, 0.15 M NH_4F, promotes a layer with double nanoporous-nanotubular structure, Fig. 5a–b. This complex morphology comprises an outer nanoporous part (~180 nm thick) and inner nanotubular part. In the literature this bi-layered structure has been reported on pure titanium[32] but also on Ti6Al4V.[27] The explanation about the mechanism for the

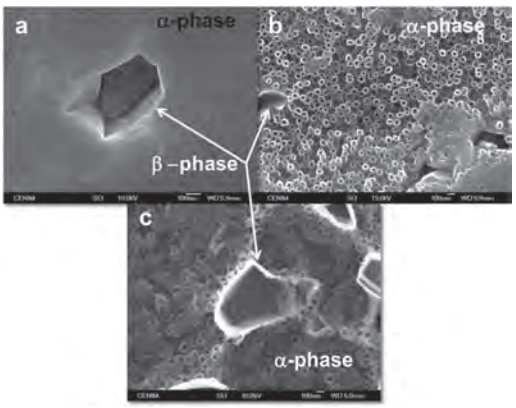

Fig. 4 Scanning electron micrographs. Morphology of the anodic layers grown at $V_1 = 10$ V for 30 minutes and $V_2 = 20$ V for 60 minutes on Ti6Al4V using (a) 0.15 M, (b) 0.3 M and (c) 0.45 M NH_4F.

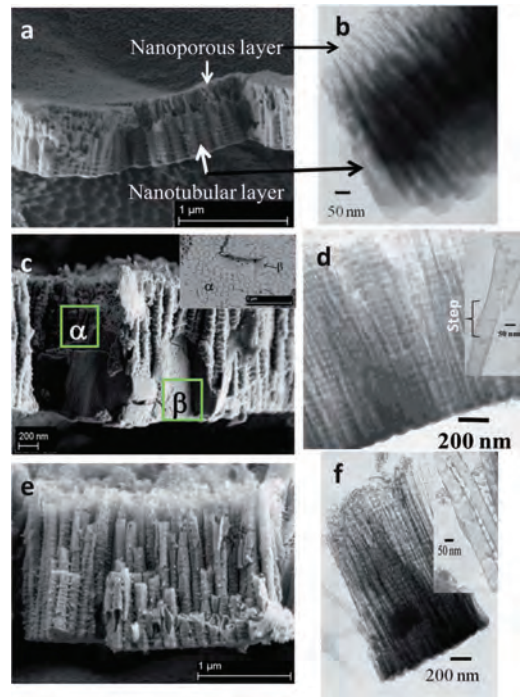

Fig. 5 Cross sections of anodic layers fabricated at 10–20 V in 1 M $NH_4H_2PO_4$ with (a and b) 0.15 M, (c and d) 0.3 M and (e and f) 0.45 M of NH_4F.

transition from nanoporous to nanotubular structure is unclear. According to Crawford *et al.*,[32] the nanotubes grow deeper into the alloy due to the competition of oxide growth and chemical dissolution at the bottom of the nanotube. As nanotubes continue to grow, the nanoporous layer is subjected to chemical dissolution, resulting in thinning and eventual disappearance.

Conversely, the layers grown in baths with 0.3 M and 0.45 M NH_4F have just a nanotubular structure throughout the thickness, Fig. 5c–f. The nanoporous layer disappears at higher concentration of fluorides in the bath, 0.3 and 0.45 M, since the nanoporous layer is subjected to a most intense chemical dissolution due to the higher fluorides presence in the bath.

The thickness of the barrier layer at the bottom of the nanotubes is about 40 nm, Table 1, suggesting an oxide growth rate of 2 nm V^{-1} within 60 min of anodizing.

The images of the cross-section of the anodic layers obtained by TEM clearly show the change in the nanotube inner diameter from the bottom to the mouth with the applied voltage step, Fig. 5d and f. Table 1, shows the inner diameters of the mouth and of the bottom of the nanotubes grown applying the stepped voltage, 10–20 V for the three anodizing baths. It can be seen that the best defined bottle shaped nanotubular structures are obtained for the bath containing 0.3 M NH_4F. The design of bottle-shaped nanotubes with thicknesses greater than micrometer, is specially interesting for controlled drug delivery systems in orthopaedic prostheses.[33]

In addition, by applying different voltage steps, in a bath containing 0.3 M NH_4F promotes changes in the nanotubular structures with regard to those previously described, Fig. 6a–h. The anodizing process performed at 10–30 V, Fig. 6c–d, shows poorly defined pores throughout the surface area, while the layers grown at 20–30 V Fig. 6e, show better defined nanotubular structures, similar to those obtained at 10–20 V, Fig. 6a. In the 20–40 V treatment, Fig. 6g, the formation of the nanotubes is not homogeneous over the entire surface, showing that the film looses integrity and collapses.

Values of the inner diameter in the mouth and in the bottom of the nanotubes are included in Table 2.

Nanotubes inner diameter depends primarily on the applied voltage since the voltage determines the electric field strength across the oxide, thus affecting the migration of ions and ultimately the nanotube inner diameter. The upper diameter (mouth diameter) is related to the value of the first applied voltage during the growth of the anodic layers. Layers which are grown with an initial voltage of 20 V (20–30 V and 20–40 V) have a larger pore diameter, in the range of 63–67 nm, compared to layers grown with an initial voltage of 10 V (10–20 V and 10–30 V) with diameters comprises between 39–47 nm, Table 2. Nanotubes bottom diameter depends on the second applied voltage. Values vary from 69 nm for 20 V to 90 nm for 40 V.

Assuming an efficiency of 100% for the titanium anodizing process, the thickness of the anodic layer fabricated using the different voltage steps applied ranges between 2600 and 2800 nm, Table 2. The thickness of the anodic layers measured by SEM are about 1400 nm for all anodic layers except for the layer grown at 20–40 V, which showed a smaller thickness, 1187 nm,

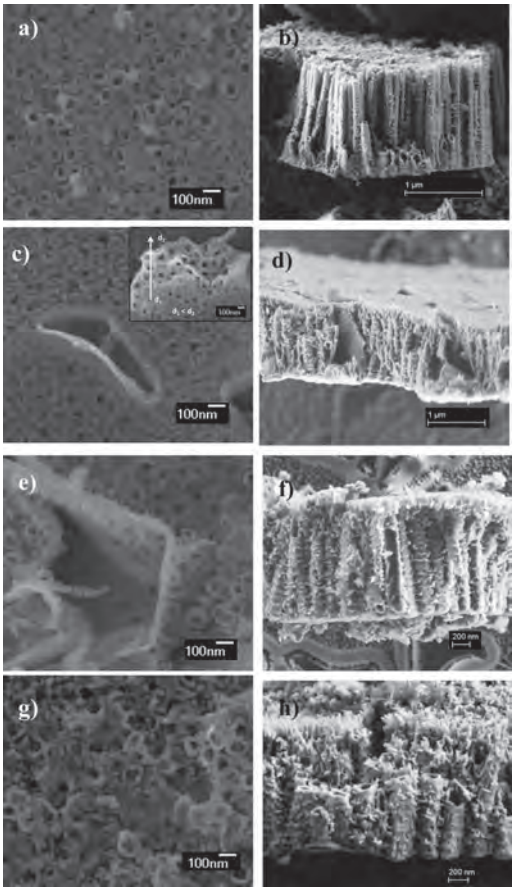

Fig. 6 Scanning electron micrographs. Morphology of the anodic layers grown in 1 M $NH_4H_2PO_4$ + 0.3 M NH_4F at (a and b) 10–20 V, (c and d) 10–30 V, (e and f) 20–30 V, (g and h) 20–40 V.

Table 2. This difference can be attributed to the stronger electric field at 40 V compared to that obtained at lower applied voltages. This implies that there is a higher dissolution rate for the oxide being formed. This is clearly revealed in the anodizing curves, by the increasing current density recorded at stage III pointing out that a steady state is not reached, Fig. 3.

For the oxide layers fabricated, either in the solutions containing different fluoride concentrations, or varying the voltage steps, Fig. 5 and 6, the formation of ribs on the wall of the nanotubes is observed. Ribs have been widely described in the literature in aqueous electrolytes and organic electrolytes with a water content higher than 5%.[18,34–36] Its formation occurs in a non-continuous way and is due to several factors such as the aggressiveness of the anodizing bath; mechanical stress generated during the growth of nanotubular oxide; the expansion factor; and the electric field generated by applying high voltage.

Table 2 Parameters of nanotubes formed at different voltage steps

Electrolyte	Step V_1 30 min	Step V_2 60 min	Charge (C cm^{-2})	Expected oxide thickness[a], nm	NT inner diameter mouth/bottom, nm	Total thickness[b], nm	Name
1 M $NH_4H_2PO_4$ + 0.3 M NH_4F	10 V	20 V	4.807	2615	~47/69	~1355	10–20 V
	10 V	30 V	4.946	2690	~39/57[c]	~1383	10–30 V
	20 V	30 V	4.999	2720	~67/90	~1450	20–30 V
	20 V	40 V	5.207	2839	~63/90[c]	~1187	20–40 V

[a] Calculate for compact amorphous film assuming 100% current efficiency. [b] Measured by SEM. [c] Measured at half of the oxide.

The inward migration of O^{2-} ions during anodization fills the volume of metal consumed, but the outward migrating Ti^{4+} ions do not contribute to growth at the metal/oxide interface but pass directly into the solution. Fluoride ions migrate inward at twice the rate of oxygen ions across the layer and form a fluoride-rich layer at the metal/oxide interface. This fluoride-rich layer is more soluble in the anodizing electrolyte than the relatively pure TiO_2 forming the majority of the layer thickness. The dissolution of the fluoride rich layer placed between the nanotubes walls (TiF_4), according to reactions (2) and (3), increases the inter-space distance between the nanotubes. Therefore, the electrolyte accesses throughout the inter-space, and promotes the growth of a new barrier layer between the walls of adjacent nanotubes to form the ribs, in accordance with reaction (4):[27,35,37]

$$TiF_4 + 2H_2O \rightarrow H^+ + [TiF_4(OH)H_2O]^- \quad (2)$$

$$[TiF_4(OH)H_2O]^- + HF \rightarrow [TiF_5 \cdot H_2O]^- \quad (3)$$

$$Ti + 2H_2O \rightarrow TiO_2 + 4H^+ + 4e^- \quad (4)$$

Fig. 6h shows that the greater amplitude of the voltage step, *i.e.* 20–40 V, favours the formation of ribs along the nanotube to a greater extent than the other conditions studied. Moreover, in this case it appears that the inter-space distance is greater than at lower voltages thus indicating greater field-assisted dissolution of the nanotube walls at the highest applied voltages.

3.3. Efficiency of film formation and composition

In order to determine the composition of the anodic layers and estimate the efficiency of the anodizing process, the oxide layers were analysed by means of Rutherford Backscattering Spectroscopy (RBS).

Fig. 7a presents the RBS spectra corresponding to the anodic layers grown at voltage steps 10–20 V in electrolytes with different NH_4F concentrations. All the spectra show a well-defined peak in channel 475 associated with oxygen, with the same number of counts, but with different width. The most significant difference among the spectra collected in Fig. 7a, is depicted in the slope plotted between channels 850 and 950 and is related to the presence of titanium in the anodic layer. As the concentration of fluoride in the electrolyte increases, the formation of a more pronounced step is observed. This step is related to the different thickness of the anodic layers, while the slope can be attributed to: differences in the roughness of the metal/oxide and oxide/surface interfaces; porosity of the grown layer; and heterogeneity of the oxide formed.

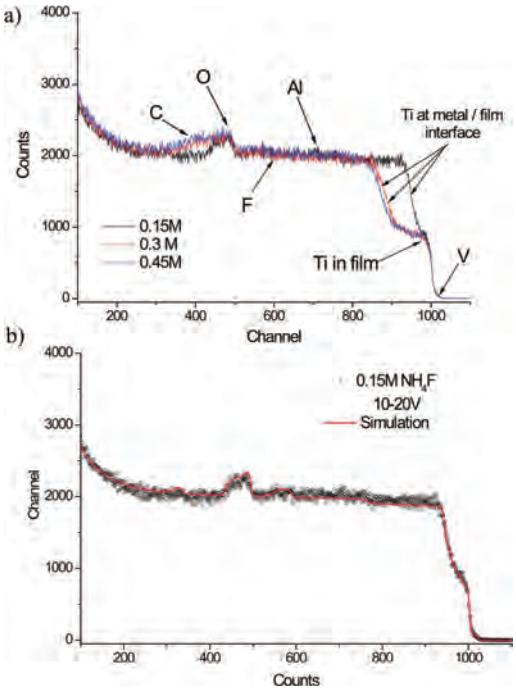

Fig. 7 Rutherford backscattering analysis spectra for anodic oxide films formed on Ti-6Al-4V in 1 M $NH_4FH_2PO_4$ + [x] M NH_4F electrolyte at 10 V for 30 min and 20 V for 60 min, acquired at 3.777 MeV (a) and fitting of the spectra for the film formed in 0.15 M NH_4F (b) circles-original data, solid line-simulation.

RBS spectra show a similar trend in the thickness of the anodic layers in relation to that measured by SEM. The layer fabricated in 0.15 M NH_4F has the lowest thickness, while those grown in 0.3 M and 0.45 M NH_4F are thicker and similar between them.

In order to determine the composition and thickness of the oxides grown, the simulation of RBS spectra was conducted

using the SIMRA software, Fig. 7b and 8b. In order to simulate these complex oxide layers, the fitting of the spectra was performed assuming various layers of varying composition and thicknesses. The results show good agreement between the fitted and experimental data, for all cases.

The composition of the anodic layers in 10^{15} atoms per cm^2 and at.% is gathered in Table 3. It can be observed that the chemical composition for the layers fabricated in solutions containing different NH_4F concentrations are similar among them, showing 33 to 34 at.% for oxygen, 47 to 51 at.% for titanium, 4 to 7 at.% for aluminium, 3 at.% for vanadium and fluorine contents about 9–10 at.%, Table 3.

The composition of the layers was determined assuming the stoichiometric formation of V_2O_5, Al_2O_3 and TiF_4. The average molecular composition of the nanotubes formed on Ti6Al4V alloys can be expressed as $TiO_{1.24}\cdot 0.080TiF_4\cdot 0.067Al_2O_3\cdot 0.044V_2O_5$ for the layer grown in 0.15 M NH_4F while for the layers grown at 0.3 and 0.45 M NH_4F, the titanium oxide is composed of $TiO_{0.92}$ and $TiO_{0.98}$, respectively, Table 3. Similar contents of TiF_4, Al_2O_3 and V_2O_5 are found for layers fabricated with 0.3 M and 0.45 M NH_4F.

RBS spectra for layers grown in an electrolyte with 0.3 M of NH_4F and different voltage steps, Fig. 8a, are similar to those obtained for the anodic layers grown with different concentrations of NH_4F. A well-defined oxygen peak of similar width is observed in all growth conditions. There are no great differences in thickness between the layers. The anodic oxide layer fabricated at 20–30 V is slightly thicker, while the layer grown at 20–40 V, has the lowest thickness. These results are in agreement with those measured in the SEM images as is summarised in Table 2.

The composition of the titanium oxide layers is similar in all cases, showing 33 to 36 at.% for oxygen, 45 to 47 at.% for titanium, 7 at.% for aluminium, 2 to 3 at.% for vanadium and fluorine contents about 9–12 at.%, Table 4. The layer grown at 20–30 V presents a slightly higher Ti/O ratio, showing an average molecular composition expressed as $TiO_{0.98}$ $0.094TiF_4$ $0.111Al_2O_3$ $0.045V_2O_5$, while the oxide grown at 20–40 V, revealing a lower ratio of Ti/O, is composed of $TiO_{0.87}\cdot 0.073TiF_4\cdot 0.098Al_2O_3\cdot 0.039V_2O_5$, Table 4.

The efficiency of the anodizing process has been estimated using the expression that relates the concentration of titanium obtained from RBS spectra (concentration of Titanium in 10^{15} atoms per cm^2, second column in Tables 3 and 4) and the calculated from the charge recorded during the anodizing (Tables 1 and 2), assuming that all the charge is consumed to oxidize titanium (100% efficiency):

$$\text{Efficiency} = \frac{\text{Ti atoms per cm}^2\text{(RBS)}}{\text{Ti atoms per cm}^2\text{(current} - \text{time curves)}} \times 100 \quad (5)$$

where the Ti atoms per cm^2 are estimated as follows:

$$\text{Ti atoms per cm}^2\ \text{(current} - \text{time curves)} = \text{charge recorded} \times 1.5597 \times 10^{18}\ \text{at C}^{-1} \quad (6)$$

$$1.5597 \times 10^{18}\ \text{at C}^{-1} = 275\ \text{nm C}^{-1} \times \frac{\rho N_A}{W_M} \quad (7)$$

being 275 nm cm^2 C^{-1} the titanium consumed by charge unit, ρ the titanium density, N_A the Avogadro's number and W_M the titanium molecular weight.

The results reveal an efficiency about 34.2% for the bath containing 0.15 M NH_4F, and 12.4% for the bath with 0.45 M NH_4F, Table 3. The efficiency decreases with the fluoride concentration in the bath despite the influence of the F^- content on the charge, as can be seen in the increasing current density response described in the curves in Fig. 2. This means that not all the collected charge is used to grow the titanium oxide, but that part of it is due to either the dissolution of both the nanotubes formed in the α phase and the oxidation of the β-phase, or to the oxygen evolution at the anode. The higher the fluoride concentration in the anodizing electrolyte, the lower the process efficiency. This response has been also described for TiO_2 anodic layers fabricated in similar electrolytes at constant voltages.[27,28]

The efficiency of the anodizing process performed in the present work, applying voltage steps, Table 4, is 22–25%. It appears that efficiency of the anodizing process is not influenced by the voltages or by the ΔV applied. The results suggest that the growth efficiency depends mainly on the chemical dissolution of the oxide due to the fluoride presence in the

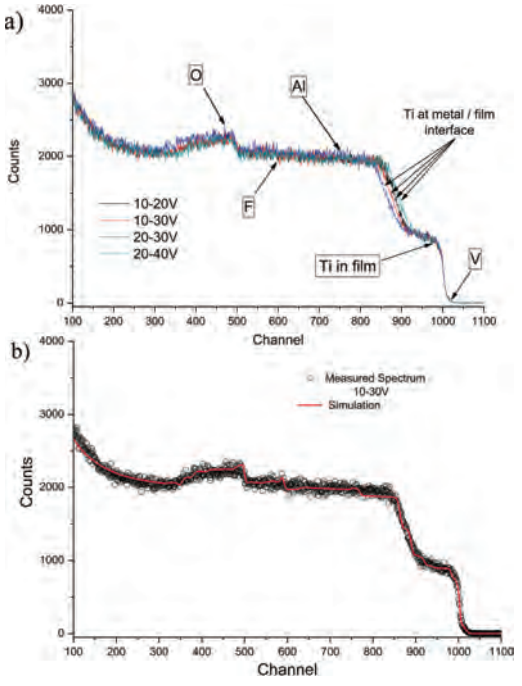

Fig. 8 Rutherford backscattering analysis spectra for anodic oxide films formed on Ti-6Al-4V in 1 M $NH_4FH_2PO_4$ + 0.3 M NH_4F electrolyte at different voltage steps, acquired at 3.777 MeV (a), fitting of the spectra for the film formed at 10–30 V, (b) circles-original data, solid line-simulation.

Table 3 Composition of the nanotubular films ($\times 10^{15}$ atoms cm^{-2}), and at.% of each element, formed on Ti6Al4V in 1 M $NH_4H_2PO_4$ electrolyte containing different NH_4F concentrations, applying a voltage step of 10 V for 30 minutes and 20 V for 60 minutes

	Ti	O	F	Al	V		
Film NH_4F	($\times 10^{15}$ at cm^{-2}/at.%)					Average molecular composition	Efficiency (%)
0.15 M	743/33	1142/51	221/10	92/4	60/3	$TiO_{1.24}\cdot 0.080TiF_4\cdot 0.067Al_2O_3\cdot 0.044V_2O_5$	34.24
0.30 M	1760/34	2389/47	485/9	346/7	145/3	$TiO_{0.92}\cdot 0.074TiF_4\cdot 0.106Al_2O_3\cdot 0.044V_2O_5$	23.53
0.45 M	1802/33	2594/47	536/10	383/7	156/3	$TiO_{0.98}\cdot 0.080TiF_4\cdot 0.115Al_2O_3\cdot 0.047V_2O_5$	12.42

Table 4 Composition of the nanotubular films ($\times 10^{15}$ atoms cm^{-2}), and at.% of each element, formed on Ti6Al4V in 1 M $NH_4H_2PO_4$ + 0.3 M NH_4F, at different voltage steps

	Ti	O	F	Al	V		
Film	($\times 10^{15}$ at cm^{-2}/at.%)					Average molecular composition	Efficiency (%)
10–20 V	1760/34	2389/47	485/9	346/7	145/3	$TiO_{0.92}\cdot 0.074TiF_4\cdot 0.106Al_2O_3\cdot 0.044V_2O_5$	23.53
10–30 V	1842/34	2429/45	630/12	372/7	132/2	$TiO_{0.93}\cdot 0.093TiF_4\cdot 0.109Al_2O_3\cdot 0.037V_2O_5$	25.73
20–30 V	1938/33	2724/46	668/11	387/7	158/3	$TiO_{0.98}\cdot 0.094TiF_4\cdot 0.111Al_2O_3\cdot 0.045V_2O_5$	24.72
20–40 V	1674/36	2121/45	447/10	303/7	124/3	$TiO_{0.87}\cdot 0.073TiF_4\cdot 0.098Al_2O_3\cdot 0.039V_2O_5$	22.13

electrolyte more than the field-assisted dissolution of the oxide and field-assisted ejection of Ti ions into the electrolyte.

4. Conclusions

In this paper it has been demonstrated that it is possible to design TiO_2 oxide layers with bottle-shaped nanostructures by controlling the anodizing electrolyte and the applied voltage steps.

For the anodic layer fabricated applying voltage steps of 10–20 V, the F^- concentration mainly influenced the inner nanotubes diameter, which also depends on the value of the voltage applied. Electrolytes with low fluoride concentration, 0.15 M NH_4F, lead to anodic layers with double morphology, nanoporous on the oxide/solution interface and nanotubular on the metal/oxide interface. Conversely, at higher fluoride concentrations, 0.3 M and 0.45 M NH_4F, only a nanotubular oxide layer with variable inner diameter along the layer is fabricated. Therefore, the growth of bottle-shaped nanotubular oxide layers is achieved only when apply a voltage steps using the adequate fluoride concentration in the electrolyte. The best bottle-shaped morphology is obtained in the anodizing bath containing 0.3 M NH_4F with a inner diameter about 47 nm at the mouth and about 69 nm at the bottom. This anodic layer is homogeneous and thicker than one micrometer.

Other voltage steps, 10–30 V, 20–30 V or 20–40 V, applied in the same anodizing bath-0.3 M NH_4F – lead to oxide layers thicker than the micrometer but their nanostructures are not well defined.

Ribs on the wall of the nanotubes are observed for the oxide layers fabricated, either in the solutions containing different fluoride concentrations, or varying the voltage steps. Nevertheless, the formation of ribs are favoured for the greater amplitude of the voltage step, *i.e.* 20–40 V, than the other conditions studied. Additionally, the inter-space distance is also greater at 40 V than at lower voltages thus indicating greater field-assisted dissolution of the nanotube walls at the highest applied voltages.

The efficiency of the anodizing process decreases with the fluorides concentration in the bath, from 34.2% for 0.15 M NH_4F, 22% for 0.3 M NH_4F to 12.4% for 0.45 M NH_4F, and is practically constant for the different voltages applied, about 22–25 %. It appears that efficiency of the anodizing process depends mainly on the chemical dissolution of the oxide due to the fluoride concentration in the electrolyte more than the field-assisted dissolution of the oxide and field-assisted ejection of Ti ions into the electrolyte.

Acknowledgements

The authors acknowledge to the Spanish Ministry of Science and Innovation-under Consolider-Ingenio 2010 CSD 2008-0023 FUNCOAT Project and to the Spanish Ministry of Economy and Competitiveness-under MUNSUTI Project – MAT2013-48224-C2-1-R-. Mr J. M.Hernández-López wishes to thank to CSIC for his PhD grant JAE-predoc.

References

1 S. Minagar, C. C. Berndt, J. Wang, E. Ivanova and C. Wen, *Acta Biomater.*, 2012, **8**, 2875–2888.
2 M. Geetha, A. K. Singh, R. Asokamani and A. K. Gogia, *Prog. Mater. Sci.*, 2009, **54**, 397–425.
3 B. M. Holzapfel, J. C. Reichert, J. T. Schantz, U. Gbureck, L. Rackwitz, U. Noth, F. Jakob, M. Rudert, J. Groll and D. W. Hutmacher, *Adv. Drug Delivery Rev.*, 2013, **65**, 581–603.

4 L. Zhao, P. K. Chu, Y. Zhang and Z. Wu, *J. Biomed. Mater. Res., Part B*, 2009, **91**, 470–480.
5 G. K. Mor, O. K. Varghese, M. Paulose, K. Shankar and C. A. Grimes, *Sol. Energy Mater. Sol. Cells*, 2006, **90**, 2011–2075.
6 E. Gultepe, D. Nagesha, S. Sridhar and M. Amiji, *Adv. Drug Delivery Rev.*, 2010, **62**, 305–315.
7 O. R. Brian and G. Michael, *Nature*, 1991, **353**, 737–740.
8 P. Roy, S. Berger and P. Schmuki, *Angew. Chem., Int. Ed.*, 2011, **50**, 2904–2939.
9 T. Goto, *Int. Congr. Ser.*, 2005, **1284**, 248–256.
10 Y.-T. Sul, C. B. Johansson, Y. Jeong and T. Albrektsson, *Med. Eng. Phys.*, 2001, **23**, 329–346.
11 G. Liu, K. Wang, N. Hoivik and H. Jakobsen, *Sol. Energy Mater. Sol. Cells*, 2012, **98**, 24–38.
12 V. Zwilling, E. Darque-Ceretti, A. Boutry-Forveille, D. David, M. Y. Perrin and M. Aucouturier, *Surf. Interface Anal.*, 1999, **27**, 629–637.
13 C. A. Grimes and G. K. Mor, *TiO_2 Nanotube Arrays, Synthesis, Properties, and Applications*, Springer, 2009, p. 358.
14 A. Ghicov, H. Tsuchiya, J. M. Macak and P. Schmuki, *Electrochem. Commun.*, 2005, **7**, 505–509.
15 J. M. Macak, H. Tsuchiya, L. Taveira, A. Ghicov and P. Schmuki, *J. Biomed. Mater. Res., Part A*, 2005, **75**, 928–933.
16 Y. Li, H. Yu, W. Song, G. Li, B. Yi and Z. Shao, *Int. J. Hydrogen Energy*, 2011, **36**, 14374–14380.
17 J. Lin, J. Chen and X. Chen, *Nanoscale Res. Lett.*, 2011, **6**, 1–5.
18 D. Guan, P. J. Hymel and Y. Wang, *Electrochim. Acta*, 2012, **83**, 420–429.
19 X. Wang, S. Zhang and L. Sun, *Thin Solid Films*, 2011, **519**, 4694–4698.
20 X. Wang, R. Chen, J. Zheng, P. Nie, H. Xie and X. Zhao, *J. Wuhan Univ. Technol., Mater. Sci. Ed.*, 2012, **27**, 866–870.
21 D. Guan and Y. Wang, *Nanoscale*, 2012, **4**, 2968–2977.
22 D. Wang, Y. Liu, B. Yu, F. Zhou and W. Liu, *Chem. Mater.*, 2009, **21**, 1198–1206.
23 Y. Liu, D. Wang, L. Cao and S. Chen, *Electrochem. Commun.*, 2012, **23**, 68–71.
24 L. V. Taveira, J. M. Macák, H. Tsuchiya, L. F. P. Dick and P. Schmuki, *J. Electrochem. Soc.*, 2005, **152**, B405.
25 J. M. Macak, S. Albu, D. H. Kim, I. Paramasivam, S. Aldabergerova and P. Schmuki, *Electrochem. Solid-State Lett.*, 2007, **10**, K28–K31.
26 J. M. Macak, H. Hildebrand, U. Marten-Jahns and P. Schmuki, *J. Electroanal. Chem.*, 2008, **621**, 254–266.
27 E. Matykina, A. Conde, J. de Damborenea, D. M. y. Marero and M. A. Arenas, *Electrochim. Acta*, 2011, **56**, 9209–9218.
28 E. Matykina, J. M. Hernandez-López, A. Conde, C. Domingo, J. J. de Damborenea and M. A. Arenas, *Electrochim. Acta*, 2011, **56**, 2221–2229.
29 K. Yasuda and P. Schmuki, *Electrochim. Acta*, 2007, **52**, 4053–4061.
30 J. M. Macak, H. Tsuchiya, A. Ghicov, K. Yasuda, R. Hahn, S. Bauer and P. Schmuki, *Curr. Opin. Solid State Mater. Sci.*, 2007, **11**, 3–18.
31 K. Yasuda, J. M. Macak, S. Berger, A. Ghicov and P. Schmuki, *J. Electrochem. Soc.*, 2007, **154**, C472–C478.
32 G. A. Crawford and N. Chawla, *Acta Mater.*, 2009, **57**, 854–867.
33 J. M. Hernández López, M. A. Arenas, A. L. Doadrio, A. Conde, C. Pérez-Jorge, J. J. de Damborenea, M. Vallet-Regi, E. Gómez-Barrena and J. Esteban. *Proceedings of the 22nd Annual Meeting of the European Orthophaedic Research Sociaty*, Nantes, France, 2014.
34 Y. A. Buslaev and V. A. Shcherbakov, *J. Struct. Chem.*, 1966, **7**, 332–336.
35 A. Valota, D. J. LeClere, P. Skeldon, M. Curioni, T. Hashimoto, S. Berger, J. Kunze, P. Schmuki and G. E. Thompson, *Electrochim. Acta*, 2009, **54**, 4321–4327.
36 J. M. Macak, H. Tsuchiya, L. Taveira, S. Aldabergerova and P. Schmuki, *Angew. Chem., Int. Ed.*, 2005, **44**, 7463–7465.
37 C. Lin, S. Chen and L. Cao, *Mater. Sci. Semicond. Process.*, 2013, **16**, 154–159.

Colloids and Surfaces B: Biointerfaces 105 (2013) 106–112

Contents lists available at SciVerse ScienceDirect

Colloids and Surfaces B: Biointerfaces

journal homepage: www.elsevier.com/locate/colsurfb

Doped TiO_2 anodic layers of enhanced antibacterial properties

María A. Arenas[a], Concepción Pérez-Jorge[b], Ana Conde[a,*], Endzhe Matykina[a], Juan M. Hernández-López[a], Ramón Pérez-Tanoira[b], Juan J. de Damborenea[a], Enrique Gómez-Barrena[c], Jaime Esteba[b]

[a] Centro Nacional de Investigaciones Metalúrgicas (CENIM/CSIC), Madrid, Spain
[b] Department of Clinical Microbiology, IIS-Fundación Jiménez Díaz Hospital, Madrid, Spain
[c] Department of Orthopaedics, IdiPAZ-Hospital Universitario La Paz, Madrid, Spain

ARTICLE INFO

Article history:
Received 7 November 2012
Received in revised form
17 December 2012
Accepted 21 December 2012
Available online 5 January 2013

Keywords:
Bacterial adhesion
Infection
Surface treatment
Titanium alloy

ABSTRACT

Ti–6Al–4V joint replacement implants foster uncemented fixation in orthopaedic surgery. However, bacterial colonization competes with host cells and ultimately may produce implant-related difficult-to-treat infections, justifying the efforts to obtain infection-resistant materials. In a previous work, the authors demonstrated the antibacterial properties of anodic fluoride-TiO_2 nanostructured layers on Ti–6Al–4V alloy. In this work, the anodizing bath has been modified in order to grow fluoride-TiO_2 barrier layers (FBL). A bacterial adherence protocol, run with reference and six different clinical strains of *Staphylococcus aureus* and *Staphylococcus epidermidis*, showed a statistically significant decrease in the percentage of covered surface ($p < 0.0001$, Kruskal–Wallis test) for FBL specimens when compared with non fluoride-containing specimens, *i.e.* chemically polished Ti–6Al–4V and F-free TiO_2 barrier layers. The results obtained on the F-barrier layers allowed discrimination between the effects of the presence of fluoride in the layer and the layer nanostructure on bacterial adhesion.

1. Introduction

Titanium and its alloys are widely used in technological applications due to their excellent mechanical properties, high corrosion resistance and biocompatibility. Broad functionality of titanium alloys is attributed to the presence of surface TiO_2 oxide layer which enhances their corrosion resistance and biological activity.

Ti–6Al–4V joint replacement implants are a great advance in orthopaedic surgery and an essential component of uncemented current joint prosthesis. However bacterial colonization of surfaces compromises the effectiveness of the implanted materials and ultimately can result in difficult-to-treat infections [1].

It is well known that most bacterial species can develop the complex structure that is known as a biofilm. It makes them less accessible to the host defence system and also decreases their antibiotic susceptibility. When the bacteria adhere to the surface before host cells do, they start to multiply and produce an extracellular matrix that constitutes the essential part of the biofilm which evolves into a clinical infection as the numbers of bacteria grow [2,3]. So, in this phenomenon, bacterial adherence to the surfaces is the first and key step in biofilm development. *Staphylococcus aureus* and *Staphylococcus epidermidis* are frequently isolated as the leading cause of biomaterial-related infections, and different authors explain this fact by the ability of these species to develop biofilms [4].

Preventing the adhesion of bacteria to the implant surfaces is a step forward in the pathogenesis of infection, because the bacteria that do not adhere are rapidly killed by the immune system [5]. According to this fact, if bacterial adherence is avoided, infection will not develop in the patient. Traditionally, prevention of bacterial adhesion has been ensured through the chemoprophylactic use of antibiotic agents before surgery, mainly administered systemically, and in some cases, even released from the implanted biomaterial. However, this latter strategy has important limitations, such as the rapid release of the adsorbed antibiotic, resistance development against the antibiotics, or systemic toxicity [6].

Development of resistance due to a broad use of antibiotics is a matter of special concern because it can limit the number of available antibiotics for treatment of infections, and even some infections can be untreatable due to the lack of useful antibiotics [7].

An interesting strategy for preventing the bacterial attachment and development of biofilm is altering the biomaterial surface properties. Surface modification techniques allow tailoring of the surface energy *via* surface chemistry and topography, showing important effects of the surface property changes on microbial

* Corresponding author at: Centro Nacional de Investigaciones Metalúrgicas (CENIM-CSIC), Avenida Gregorio del Amo, 8, 28040 Madrid, Spain. Tel.: +34 915538900; fax: +34 915347425.
E-mail address: a.conde@cenim.csic.es (A. Conde).

0927-7765/$ – see front matter © 2013 Elsevier B.V. All rights reserved.
http://dx.doi.org/10.1016/j.colsurfb.2012.12.051

colonization. Different methodologies have been used to change either the chemical composition or the microtopography of the surface and their impact on bacterial adhesion with different results [8–10].

Among the surface modification techniques, anodizing is a well known process that enables the growth of titanium oxide layer under controlled conditions. The structure of the anodic layer can be controlled by varying the electrolyte composition, the applied voltage, the time and the temperature. In general, anodic oxide layers grown in acidic, HF-containing baths have duplex structure comprising an outer nanoporous/nanotubular layer in contact with the electrolyte, and an inner compact layer (barrier layer) formed at the bottom of the nanotube/nanopore adjacent to the substrate. However, under certain conditions the growth of the nanostructured outer layer can be suppressed, promoting just the growth of the barrier layer.

In a previous work, the authors demonstrated the antibacterial properties of anodic fluoride-TiO_2 nanostructured layers on Ti–6Al–4V alloy [11–13]. The adhesion of *S. epidermidis* and *S. aureus* has been reduced by 50% due to the presence of ~5 at.% of fluorine in the oxide layer. However, as both the topography and the chemical composition were modified by the anodization process, it was difficult to elucidate which one was the major factor in the antibacterial properties: the F content in the oxide layer or the topographical features of the latter.

In this work, the anodizing bath has been modified in order to enable the growth of fluoride-containing barrier layers (FBL) for the first time. The studies performed on non-nanostructured FBL have permitted to discriminate the effect of the fluoride from the effect of the surface nanostructure on bacterial adhesion.

2. Materials and methods

2.1. Sample preparation

Ti–6Al–4V alloy specimens of ELI grade according to the standard ASTM F136-02 supplied by SURGIVAL were ground through successive grades of SiC paper to 1200 grade, degreased with a detergent and rinsed in tap water followed by deionised water. The specimens were then chemically polished (CP) in a mixture of HF (48 wt%):HNO_3 (70 wt.%):H_2O with volume ratio 1:4:5, for 5 min at room temperature under continuous agitation at 400 rpm, rinsed in distilled water and dried in cold air. The working area was 2.54 cm^2.

Fluoride-TiO_2 barrier layers (FBL) were produced in a two-electrode cell by anodizing the specimens in 1 M $NH_4H_2PO_4$/0.15 M NH_4F solution at constant voltage controlled at 20 V for 120 min and at temperature controlled at 20 °C. Platinum mesh was used as a cathode. Constant voltage was applied using LAB/SM 1300DC power supply (ET Power Systems Ltd.). Current time responses of anodizing were acquired at 0.1 Hz sampling rate using a Zero-Resistance Ammeter (ZRA) connected in series with the electrochemical cell. Fluoride-free TiO_2 barrier layers (BL) were also fabricated in 1 M H_2SO_4 electrolyte by anodizing the specimens at 15 mA cm^{-2} to 90 V. The summary of surface treatment conditions is listed in Table 1.

2.2. SEM and TEM characterization

The plan view morphology of oxide barrier layers was examined by field emission gun scanning electron microscopy (FEG-SEM) utilizing a JSM6500F JEOL instrument equipped with EDX facilities.

Electron-transparent sections, nominally 40 nm-thick, prepared by ultramicrotomy were observed by a JEOL JEM 2010 TEM instrument operated at 200 keV.

2.3. Surface characterization

Surface topographies were examined and roughness R_a values were obtained by using an optical imaging profilometer Plμ 2300 (Sensofar) operated at 20×. The cited R_a values are an average of five measurements.

2.4. Surface energy and contact angle

Surface contact angles were measured using distilled water and diiodomethane (from Sigma Aldrich) using Theta Attension optical tensiometer (KSV Instruments) with automatic liquid dispenser and monochromatic cold light source, operated in trigger mode with 50 video frames recorded at 112 ms interval. The measurements were performed immediately after the treatment of the surface, rinsing for 1 min in distilled water, and drying in warm air for 1 min, to avoid the adsorption of carbon-containing species from the ambience.

Contact angles were calculated using Young–Laplace drop profile fitting method. Each contact angle value is cited as an average of three measurements performed at three different locations on the specimen surface. An average of 40 frames has been used to calculate the contact angle for each drop.

Surface free energy (γ) components and work of adhesion (W_a) of the oxide layers were determined using Fowkes approach [14]:

$$W_a = \gamma_L(\cos\theta + 1) = 2(\gamma_L^D\gamma_S^D)^{1/2} + 2(\gamma_L^P\gamma_S^P)^{1/2} \quad (1)$$

$$W_a^D = 2(\gamma_L^D\gamma_S^D)^{1/2} \quad (2)$$

$$W_a^P = 2(\gamma_L^P\gamma_S^P)^{1/2} \quad (3)$$

2.5. Bacterial adhesion

Microbiology studies have been performed using two reference strains and six clinical strains of each species. The reference strains were *S. aureus* 15981 [15] and *S. epidermidis* ATCC 35984. Both strains are biofilm-producing ones. *S. aureus* 15981 is a clinical isolate that has been fully characterized with respect to the biofilm production. *S. epidermidis* ATCC 35984 is a collection strain used for biofilm studies. The clinical strains for *S. aureus* were P1, P2, P4, P18, P61T3 and P95 and those for *S. epidermidis* were P6, P33,

Table 1
Surface treatment conditions and oxide film characteristics.

Surface treatment		Designation	Electrolyte/surface treatment conditions	Film thickness (nm)	Fluorine content (at.%)
Chemically polished	–	CP	HF (40 wt%):HNO_3 (70 wt%):H_2O 1:4:5 ratio 5 min	No film	<0.5
Barrier layer[a]	F-free treatment	BL	1 M H_2SO_4 anodizing at 15 mA/cm^2 to 90 V	200	<0.3
Fluoride barrier layer	F-containing treatment	FBL	1 M $NH_4H_2PO_4$/0.15 M NH_4F, pH = 5 Anodizing at 20 V, 120 min	150	12

[a] Barrier layer refers to a dense anodic oxide film without nanostructure.

P53B, P55, P74 and P101. The clinical strains have been isolated from patients who have had an implant-related infection using a previously described sonication procedure [16]. These strains have been characterized by phenotypic and genetic methods in a previous study. The strains were isolated from infected hip prosthesis (P2, P4, P18, P33, P53B, P55, P74 and P101), and infected osteosynthesis implants (P1, P6, P61T3 and P95). All the strains are able to form biofilm *in vitro* and the amount of biofilm production ranges between 1+ and 3+ according to Stepanovic method. All *S. aureus* strains were *ica* gene positive, as well as all *S. epidermidis* strains except the P33 and P101 [17].

In this work, the experiments on staphylococcal adhesion of reference strains were carried out on BL and FBL while the study with clinical strains was performed on CP, and FBL. The experiments were performed following the protocol developed by Kinnari et al. [18] as previously reported by us [13]. Bacteria were inoculated in Tryptic Soy Broth (TSB, bioMérieux, Marcy L'Etoile, France) and incubated overnight at 37 °C with 5% CO_2. After culture, bacteria were centrifuged for 10 min at 3500 × *g* at 22 °C. Supernatant was then discarded and the pellet was washed three times with sterile phosphate buffered saline (PBS, Sigma–Aldrich Life Science). Bacteria were then suspended and diluted in PBS in order to obtain a 10^8 CFU/ml concentration; the bacterial concentration was determined by spectrophotometry using a visible spectrophotometer (Genesys 20, Thermo Scientific) [19]. Ten ml of this solution were used to cover the specimens in the plates. This inoculum was added onto specimens of titanium alloy (Ti–6Al–4V) with different surface treatments, and incubated for 90 min at 37 °C in order to allow adhesion in a static model.

After incubation, the samples were washed three times with PBS to remove unattached bacteria. Finally, they were stained for 2 min with Live/Dead® Bacterial Viability Kit (Backlight™) [20] and rinsed with sterile water. Eight photographs (400×, high power field) were obtained by UV microscope for each sample.

A surface of approximately 24,000 μm^2 was captured in each image. The percentage of surface area covered with adhered bacteria was calculated using ImageJ software (National Institute of Health Bethesda, MD, USA). The experiments were performed in triplicate for each strain.

The statistical analysis was performed using EPI-INFO software version 3.5.1 (CDC, Atlanta, GA, USA). The obtained results were presented comparing the mean percentage of covered biomaterial surface for CP Ti–6Al–4V specimens, and for different anodized materials, *i.e.* BL and FBL. In order to carry out the statistical study, non-parametric tests were performed. When more than two samples were employed, the Kruskal–Wallis test was carried out, whereas for two samples, the Mann–Whitney test was used.

3. Results

3.1. Surface characterization

The surface morphology of the CP Ti–6Al–4V reveals an α + β microstructure, comprising 2–3 μm long β-phase particles dispersed in α-phase matrix (Fig. 1(a)). Local EDX analysis disclosed that the β-phase is enriched in vanadium (up to ~14 at.%) compared with the α-phase (~2 at.%) and contains about 1 at.% of iron [21].

The R_a roughness value of CP surfaces determined over 140 μm-long profile was about 73 nm (Table 2).

The cross-section of the oxide layer prepared in 1 M H_2SO_4 (the F-free electrolyte; Fig. 1(b)) shows a 200 nm-thick barrier type layer, BL. Local crater-like irregularities are formed due to a local dielectric breakdown of the layer, Fig. 1(c). The EDX analysis performed at different sites of the layer revealed that the layer contained tracers of fluorine (≤0.3 at.%), originating from chemical etching of the substrate in $HF/HNO_3/H_2O$ solution prior to anodizing. The oxide layer formed on the β-phase still contained elevated amount of vanadium (~3.3 at.%) compared with the layer formed on α-phase (~0.7 at.%) [13].

The R_a values for the BL are slightly lower compared with CP surface, with the average R_a value of 53 nm (Table 2).

A ~150 nm-thick FBL is formed after 120 min of anodizing in $NH_4H_2PO_4/NH_4F$ electrolyte (Fig. 1(d)). The fluoride concentration and the pH of the anodizing bath strongly influence the TiO_2 layer surface morphology formed in this electrolyte [22]. Nanotubular and nanoporous structure can be also produced in this electrolyte as a consequence of the dissolution process, which is intensified at higher concentrations of F^- and is inhibited by the pH increase of the electrolyte. Increasing the pH of the 1 M $NH_4H_2PO_4$/0.15 M F^- solution from 4.2 to 5.0 enabled growth of thick barrier layers instead of nanostructured layers (nanotubular layers) [22]. The TEM cross-section image of the barrier layer revealed an amorphous structure with no discernable nanocrystals (Fig. 1(d)). The oxide layer formed on β-phase appeared nodular compared with the smooth layer generated on α-phase (Fig. 1(e)).

The chemical composition estimated by RBS revealed that the fluorine content in FBL layers is 12 at.% [22]. Lower amount of fluorine, around 4–6 at.%, has been found in the nanostructured layers described in our previous work [21].

The average roughness of the FBL surface (130 nm) is higher than that of the CP and BL specimens. The more intensive chemical dissolution of the oxide layer during the anodizing process in the fluoride-containing electrolyte results in the increased roughness on the FBL in comparison to the BL specimens.

3.2. Surface wettability

The wettability of the freshly prepared and dried surfaces was considerably high for all the treatments. FBL layer shows lower contact angle with water than CP and BL specimens, while the contact angles with diiodomethane are similar in the three types of specimens (Table 2).

Surface energy calculations from contact angle data obtained in distilled water indicated that increasing the surface roughness increased the surface energy. The calculated components of surface free energy, work of adhesion to water and solid/water interface energy are gathered in Table 2. The lowest and highest surface energies were obtained for CP and FBL specimens, respectively.

The CP and BL surface treatments had no statistically significant difference. BL layer and CP surface disclosed lower work of adhesion and higher solid/water interface energy than the FBL layer. Higher adhesion work for FBL indicates that greater separation work is required to pull a droplet of water off the surface and to create water/air and FBL/air interfaces. Respectively, lower FBL/water interface energy means that smaller work is required to create a unit of FBL/water interface.

In general, the lowest surface free energy parameters were obtained for F-free surfaces – CP and BL with the lowest roughness. Thus, in the absence of the nanostructure, the F content and the roughness alone may be considered responsible for the increase of the surface free energy parameters of FBL layers.

3.3. Adhesion studies

3.3.1. Results of reference strains

The results of the mean percentage of covered surface for reference strains are shown in Fig. 2. The response of *S. aureus* and *S. epidermidis* reveals statistically significant differences ($p < 0.0001$, Kruskal–Wallis test) when comparing FBL with CP and BL specimens. The percentage of covered surface of FBL specimens is

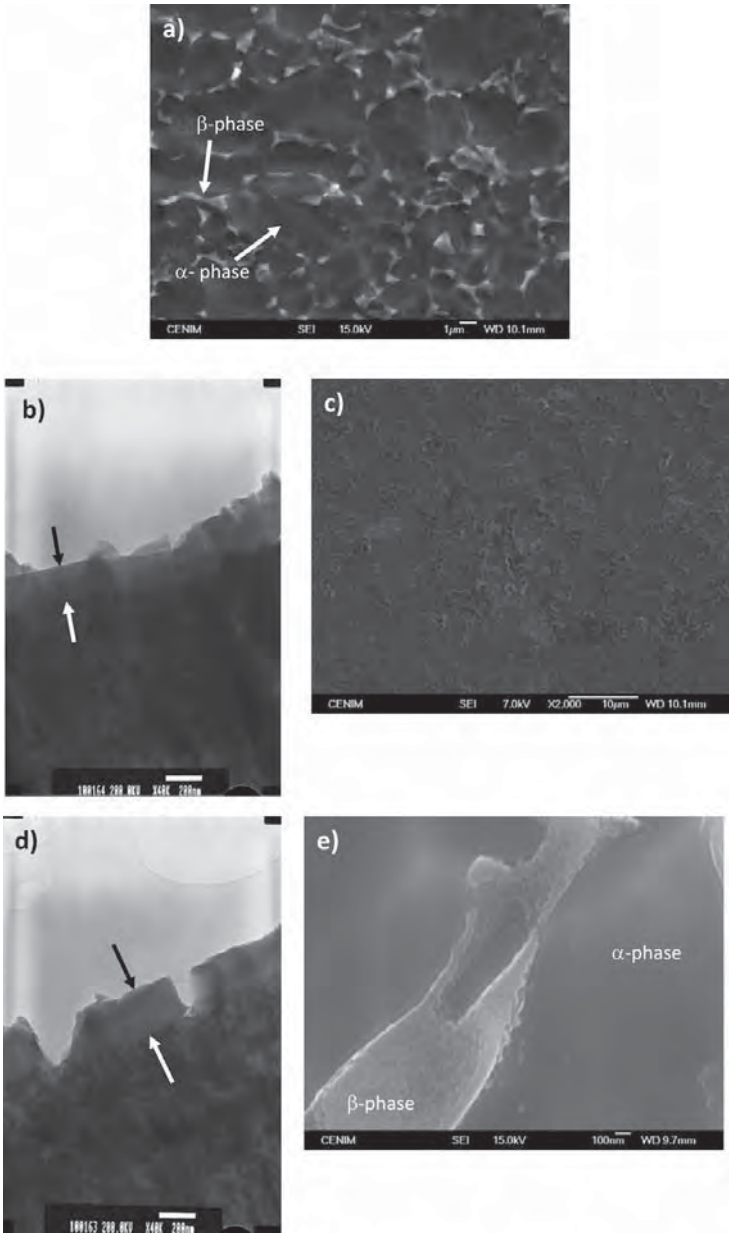

Fig. 1. Surface morphology of CP Ti–6Al–4V (a); cross-section and plan view of BL oxide layer prepared in 1 M H_2SO_4 (b, c); cross-section and plan view of FBL formed in $NH_4H_2PO_4/NH_4F$ electrolyte for 120 min (d, e).

higher for *S. epidermidis* than for *S. aureus*. However, there is no statistically significant difference between the percentage of covered surface of BL and CP specimens ($p > 0.0001$, Kruskal–Wallis test).

3.3.2. Results of clinical strains

As reference bacteria did not show statistically significant difference between CP and BL treatments, further comparison of the clinical strains response was performed using just CP and FBL specimens.

Fig. 3 shows the mean percentage of covered surface for six clinical strains of *S. epidermidis*. For P6.2, P33.1, and P74 strains, the results showed a statistically significant decrease in the percentage of covered surface of FBL compared with the CP. Similarly, for most of the *S. aureus* clinical strains (P1, P2, P4, P18 and P61T3) the

Table 2
Roughness and contact angle measurements. Calculated components of surface-free energy, work of adhesion and solid/water interface energy.

Film	R_a (nm)	Contact angle ± SE (°)		Surface-free energy (mJ/m^2)[a]			Work of adhesion energy (mJ/m^2)[a]			Solid/water interface energy (mJ/m^2)[a]
		Water	Dioodomethane	γ_S	γ_S^D	γ_S^P	W_a	W_a^D	W_a^P	γ_S
CP	53.2 ± 2.1	52.10 ± 8.2	29.05 ± 2.78	59.5	44.6	14.9	117.4	62.36	55.13	14.80
BL	73.9 ± 3.8	57.50 ± 0.27	27.51 ± 1.86	58.1	45.2	12.9	114.0	62.78	51.30	16.82
FBL	130.4 ± 7.2	21.36 ± 5.18	26.16 ± 5.35	75.1	45.7	29.4	140.6	63.13	77.44	7.33
NP[b]	178.9 ± 8.7	29.9 ± 1.8	22.4 ± 2.11	72.5	47	25.5	136.2	64.0	72.1	9.2
NT[b]	168.8 ± 11.6	7.5 ± 1.58	3.98 ± 0.83	80.9	50.7	30.2	145	66.5	78.5	8.7

[a] Measured in distilled water.
[b] Data from Ref. [12].

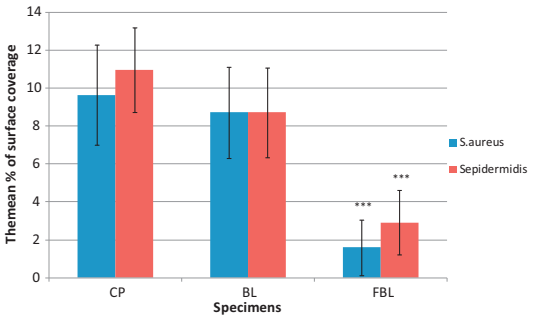

Fig. 2. The mean percentage of surface coverage for *S. epidermidis*. ***Statistically significant difference with CP and BL ($p < 0.0001$).

mean percentage of covered surface revealed a statistically significant decrease ($p < 0.0001$, Kruskal–Wallis test) on FBL specimens compared with CP specimens. On the other hand, the mean percentage of covered surface of the FBL specimens is lower for *S. aureus* than for *S. epidermidis*.

4. Discussion

Bacterial adhesion is a complex process that depends on many factors, including some characteristics of the bacteria themselves, environmental factors and, of course, material surface properties [5].

From the perspective of the material, the chemical composition, surface charge, wettability, surface roughness and topography are important parameters influencing bacterial adhesion.

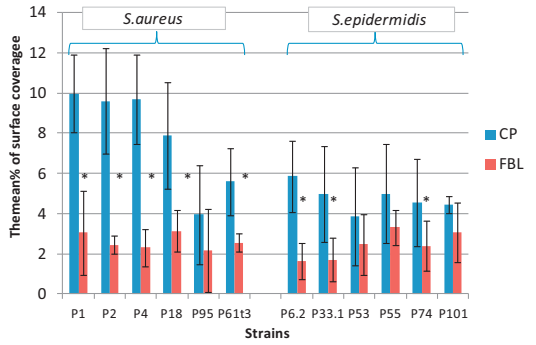

Fig. 3. The mean percentage of surface coverage for *S. epidermidis* and *S. aureus* clinical strains. *Statistically significant difference with CP ($p < 0.0001$).

Precisely, surface modification of the substratum is being studied as a potentially efficient strategy to alter surface properties (surface chemistry, topography and hence, the surface energy) of the implants and the effects of these changes on the adhesion process are being evaluated. However, although there is a lot of information on the behaviour of many bacteria on a wide variety of metals and other surfaces, still there is no a conclusive theory that explains or even summarizes all this information.

A previous study performed on specimens anodized in fluoride-containing electrolytes, using either reference strains or clinical strains, showed a decrease of bacterial adhesion on nanostructured fluoride-containing layers in comparison with the CP and BL specimens [13]. In addition, no statistically significant differences were observed between the nanostructured (nanoporous (NP) or nanotubular (NT)) specimens with respect to the adhesion of bacteria. This correlates with the fact that solid/water interface energies for both nanotubular and nanoporous specimens were very similar, despite the distinctly different microstructure (see Table 2). Hence, the observed decrease in bacterial adhesion was attributed to the presence of fluoride in the layer.

The present study compares the antibacterial properties of F-containing TiO_2 barrier layers with the non-anodized specimens, CP, and anodized specimens prepared in a F-free electrolyte which allows formation of F-free TiO_2 barrier layers, BL. Both anodized specimens (BL and FBL) have the same dense homogenous structure, *i.e.* both are non-nanostructured oxide layers, thus enabling to elucidate the role of the fluoride in two layers with similar morphological features. FBL promotes the lowest bacteria attachment compared with the BL and CP treatments.

Further, FBL surface has an increased roughness and surface energy compared with the BL. Kinnari et al. [23], reported that an increase of the roughness and the surface energy leads to an increased protein adsorption, such as fibronectin, that results in a decreased bacteria attachment. So the changes both in roughness and surface energy could be the key factors responsible for the decrease in the bacterial adhesion reported for the FBL layers.

The changes in roughness and surface energy components obtained from the contact angles for the FBL are different from those for the BL specimen, but are rather similar to those reported in our previous work for the nanostructured layers, NP and NT arrays, obtained in F-containing electrolyte (Table 2) [13]. However, despite these similarities the bacterial response of the FBL is quite different in comparison with the response reported for the nanoporous and nanotubular fluoride-containing layers. While the mean percentage of surface coverage by reference *S. aureus* and *S. epidermidis* for the nanoporous, NP, and nanotubular, NT, layers is about 4 and 7%, respectively [13], for the FBL these percentages decrease to 2 and 3%, respectively.

Similarly, the mean percentage of surface coverage by clinical strains of *S. aureus* and *S. epidermidis* for the FBL specimens are much lower than observed in the F-containing nanostructured layers [13].

These differences in bacterial adhesion on FBL compared to F-nanostructured layers suggest that the surface morphology could also have a relevant effect. Merit et al. [24] found that implant site infection rates are different for porous and dense implants materials, porous material having a much higher rate of infection. However the size of the pores reported in their work is quite high, 100 μm, whereas the size of the bacteria is two orders of magnitude smaller (being 1–2 μm diameter for *Staphylococcus* cells). So in this case as well as in others reported on titanium for dental applications [25,26], the microorganisms colonize much larger pores and cavities where they are sheltered from the host defences. Nevertheless, these pore sizes are very large compared to the pore diameter achieved in the nanoporous or nanotubular layers reported in our previous paper, whose diameter ranged from 10 to 100 nm. Thus, it appears that nanoporous features of the anodic layers have no influence on the bacterial adhesion.

Further, although porous materials or microtextured surfaces support osseonintegration, roughly textured implant substrata in dental applications are known to enhance plaque accumulation, whereas highly polished materials with reduced surface roughness limit initial biofilm formation *in vivo* on smooth titanium surfaces [2]. Conversely, a more recent preliminary study performed using clinical data from infected patients showed no clear differences between materials of different roughness regarding the number of bacteria present on the implant surface. Particularly, the microorganism involved in orthopaedic clinical infections in specific patients are a major factor influencing the adherence, which justifies the need to perform the studies of new materials using sufficient number of clinical strains [27]. In this sense, the use of clinical strains in adherence studies is essential, because of the potential differences in the behaviour of the different bacterial strains [28].

Moreover, Bollen et al. [29] compared the surface roughness of different materials produced by different techniques, concluding that a value of 200 nm is the average roughness threshold below which the amount of bacterial adhesion cannot be reduced any further. Therefore, as both FBL and BL layers fabricated exhibit roughness about 130 nm and 73 nm, respectively, so it appears that this parameter is not the key factor affecting the bacterial adhesion.

Thus, the findings of this work in conjunction with the previously published results [13] rule out the influence of the nanoscale roughness, the surface nanostructure and topography on the antibacterial properties of the anodic layer, suggesting that the reduction in the bacterial adhesion compared with the BL is solely due to the presence of fluoride in the layer. In addition, the higher F^- content in FBL compared with the nanostructured F-containing TiO_2 layers [13] may be responsible for the enhanced antibacterial properties. The mechanism of the reduction of bacterial adhesion is thought to be related to the inhibition of their enzymatic activity by titanium-fluoride complexes, such as TiF_4 [30].

Although there is no material totally resistant to bacterial adhesion, certain differences exist, in this respect, among materials and surface treatments. Previous studies of the authors performed on F-containing TiO_2 layers grown by anodizing show that, regardless of the surface configuration – nanoporous or nanotubular – there is a decrease in bacterial attachment on F-containing surfaces.

This paper reveals that the antibacterial properties rely on the F content in the layer rather than on the topographical properties. For the first time, bacterial adhesion studies using two reference strains and six clinical strains of *S. aureus* and *S. epidermidis* have been performed on fluoride-free TiO_2 barrier layers and fluoride-TiO_2 barrier layers. These results, in comparison with those previously reported in [13], discriminate between the role of the nanostructure of the layer and the F^- content in the layer in bacterial adhesion, showing that the lowest bacterial adhesion is achieved on fluoride-TiO_2 barrier layers due to their higher F^- content compared to the nanostructured oxide layers, with no interference from other structural changes.

5. Conclusion

This paper demonstrates the enhanced antibacterial properties achieved solely by the incorporation of fluorine during the anodizing process of Ti–6Al–4V. Antibacterial properties of nanostructured anodizing layers have been recently reported by the authors. Until now, the anodizing of titanium alloys simultaneously promoted chemical and nanostructural changes of the surface. In this work, a new formulation of the anodizing bath has been developed in order to fabricate fluoride-containing barrier layers (FBL) with no change in topography. The bacterial adhesion studies performed on these non-nanostructured FBL show a statistically significant decrease in the bacterial adhesion in comparison to fluorine-free barrier layers (BL). These results permit for first time to discriminate the effect of the fluorine from the effect of the surface nanostructure on antibacterial properties, revealing the key role of the F in the antibacterial properties.

Acknowledgements

This work was funded by a grant from the Spanish Ministry of Science and Innovation (SMOTI MAT2009-13751 and CONSOLIDER-INGENIO 2010 CSD 2008-0023 FUNCOAT). Juan Manuel Hernández López acknowledges CSIC for funding this work under the grant JAE-pre-2010.

The authors report that they have a patent for the materials regarding their antimicrobial properties PCT/ES2011/070342.

References

[1] L. Rimondini, M. Fini, R. Giardino, The microbial infection of biomaterials: a challenge for clinicians and researchers. A short review, J. Appl. Biomater. Biomech. 3 (2005) 1–10.
[2] L. Hall-Stoodley, J.W. Costerton, P. Stoodley, Bacterial biofilms: from the natural environment to infectious deasease, Nat. Rev. Microbiol. 2 (2004) 95–108.
[3] W. Costerton, R. Veeh, M. Shirtliff, M. Pasmore, C. Post, G. Ehrlich, The application of biofilm science to the study and control of chronic bacterial infections, J. Clin. Invest. 112 (2003) 1466–1477.
[4] R.A. Brady, J.H. Calhoun, J.G. Leid, M.E. Shirtliff, Infections of orthopaedic implants and devices, in: M.E. Shirtliff, J.G. Leid (Eds.), The Role of Biofilms in Device-related Infections, Springer-Verlag, Berlin, 2009, pp. 15–56.
[5] M. Katsikogianni, Y.F. Missirlis, Concise review of mechanisms of bacterial adhesion to biomaterials and of techniques used in estimating bacteria–material interactions, Eur. Cell Mater. 8 (2004) 37–57.
[6] J. Esteban, J. Cordero-Ampuero, Treatment of prosthetic osteoarticular infections, Expert Opin. Pharmacother. 12 (6) (2011) 899–912.
[7] D. Livermore, Has the era of untreatable infections arrived? J. Antimicrob. Chemother. 64 (2009) i29–i36.
[8] K.K. Chung, J.F. Schumacher, E.M. Sampson, R.A. Burne, P.J. Antonelli, A.B. Brennan, Impact of engineered surface microtopography on biofilm formation of *Staphylococcus aureus*, Biointerphases 2 (2007) 89.
[9] M.I. Sarró, D.A. Moreno, C. Ranninger, E. King, J. Ruiz, Influence of gas nitriding of Ti6Al4V alloy at high temperature on the adhesion of *Staphylococcus aureus*, Surf. Coat. Technol. 201 (2006) 2807–2812.
[10] L. Zhao, P.K. Chu, Y. Zhang, Z. Wu, Antibacterial coatings on titanium implants, J. Biomed. Mater. Res. B 91B (2009) 470–480.
[11] M. A. Arenas Vara, A. Conde del Campo, J. J. de Damborenea González, E. Matykina, J. Esteban Moreno, E. Gómez Barrena, C. Pérez- Jorge Permach, R. Pérez Tanoira, Materiales de titanio anodizado con fluor, PATENT, PCT/ES2011/070342, Spain, 2010.
[12] C. Pérez-Jorge Peremach, R. Pérez Tanoira, M.A. Arenas, E. Matykina, A. Conde, J.J.D. Damborenea, E.G. Barrena, J. Esteban, Bacterial adherence to anodized titanium alloy, J. Phys.: Conf. Ser. 252 (2010) 012011.
[13] C. Pérez-Jorge, A. Conde, M.A. Arenas, R. Pérez-Tanoira, E. Matykina, J.J. de Damborenea, E. Gómez-Barrena, J. Esteban, In vitro assessment of *Staphylococcus epidermidis* and *Staphylococcus aureus* adhesion on TiO_2 nanotubes on Ti–6Al–4V alloy, J. Biomed. Mater. Res. A 100A (2012) 1696–1705.
[14] F. Fowkes, Chemistry and Physics of Interfaces, American Chemical Society, Washington, DC, 1965.
[15] J. Valle, A. Toledo-Arana, C. Berasain, J.M. Ghigo, B. Amorena, J.R. Penades, I. Lasa, SarA and not sigmaB is essential for biofilm development by *Staphylococcus aureus*, Mol. Microbiol. 48 (2003) 1075–1087.

[16] T.J. Kinnari, A. Soininen, J. Esteban, N. Zamora, E. Alakoski, V.P. Kouri, R. Lappalainen, Y.T. Konttinen, E. Gómez-Barrena, V.M. Tiainen, Adhesion of staphylococcal and Caco-2 cells on diamond-like carbon polymer hybrid coating, J. Biomed. Mater. Res. A 86 (2008) 760–768.
[17] J. Esteban, D. Molina-Manso, I. Spiliopoulou, J. Cordero-Ampuero, R. Fernández-Roblas, A. Foka, E. Gómez-Barrena, Biofilm development by clinical isolates of *Staphylococcus* spp. from retrieved orthopedic prostheses, Acta Orthop. 81 (2010) 674–679.
[18] J. Esteban, E. Gómez-Barrena, J. Cordero, N.Z. Martin-de-Hijas, T.J. Kinnari, R. Fernandez-Roblas, Evaluation of quantitative analysis of cultures from sonicated retrieved orthopedic implants in diagnosis of orthopedic infection, J. Clin. Microbiol. 46 (2008) 488–492.
[19] K.C. Chapin, Reagents, stains, and media: bacteriology, in: Manual of Clinical Microbiology, ASM Press, Washington, DC, 2007, pp. 334–364.
[20] L. Boulos, M. Prevost, B. Barbeau, J. Coallier, R. Desjardins, LIVE/DEAD BacLight: application of a new rapid staining method for direct enumeration of viable and total bacteria in drinking water, J. Microbiol. Methods 37 (1999) 77–86.
[21] E. Matykina, J.M. Hernández-López, A. Conde, C. Domingo, J. De Damborenea, M.A. Arenas, Morphologies of nanostructured TiO_2 doped with F on Ti–6Al–4V alloy, Electrochim. Acta 56 (2011) 2221.
[22] E. Matykina, A. Conde, J. de Damborenea, D. Martín y Marero, M.A. Arenas, Growth of TiO_2-based nanotubes on Ti–6Al–4V alloy, Electrochim. Acta 56 (2011) 9209–9218.
[23] T.J. Kinnari, L.I. Peltonen, P. Kuusela, J. Kivilahti, M. Könönen, J. Jero, Bacterial adherence to titanium surface coated with human serum albumin, Otol. Neurotol. 26 (2005) 380–384.
[24] K. Merritt, J.W. Shafer, S.A. Brown, Implant site infection rates with porous and dense materials, J. Biomed. Mater. Res. 13 (1979) 101–108.
[25] C.B. Correa, J.R. Pires, R.B. Fernandes-Filho, R. Sartori, L.G. Vaz, Fatigue and fluoride corrosion on streptococcus mutans adherence to titanium-based implant/component surfaces, J. Prosthodont. 18 (2009) 382–387.
[26] R. Sartori, C.B. Correa, E. Marcantonio Jr., L.G. Vaz, Influence of a fluoridated medium with different pHs on commercially pure titanium-based implants, J. Prosthodont. 18 (2009) 130–134.
[27] E. Gómez-Barrena, J. Esteban, F. Medel, D. Molina-Manso, A. Ortiz-Pérez, J. Cordero-Ampuero, J.A. Puértolas, Bacterial adherence to separated modular components in joint prosthesis: a clinical study, J. Orthop. Res. 30 (2012) 1634–1639.
[28] J. Esteban, D. Molina-Manso, E. Gómez-Barrena, Bacterial adherence to vitamin E UHMWPE. Considerations about in vitro studies, J. Orthop. Res. 30 (2012) 1181.
[29] C.M.L. Bollen, P. Lambrechts, M. Quirynen, Comparison of surface roughness of oral hard materials to the threshold surface roughness for bacterial plaque retention: a review of the literature, Dent. Mater. 13 (1997) 258–269.
[30] M. Yoshinari, Y. Oda, T. Kato, K. Okuda, Influence of surface modifications to titanium on antibacterial activity in vitro, Biomaterials 22 (2001) 2043–2048.

Society For Biomaterials

Influence of the nanostructure of F-doped TiO_2 films on osteoblast growth and function

Daniel Lozano,[1,2] Juan M. Hernández-López,[3] Pedro Esbrit,[2] Maria A. Arenas,[3] Enrique Gómez-Barrena,[1] Juan de Damborenea,[3] Jaime Esteban,[4] Concepción Pérez-Jorge,[4] Ramón Pérez-Tanoira,[4] Ana Conde[3]

[1]Grupo de Investigación de Cirugía OsteoArticular, Instituto de Investigación Hospital Universitario La Paz (IdiPAZ), 28046 Madrid, Spain
[2]Laboratorio de Metabolismo Mineral y Óseo, Instituto de Investigación Sanitaria (IIS)-Fundación Jiménez Díaz, UAM, 28040 Madrid, Spain, and RETICEF, Instituto de Salud Carlos III, 28029 Madrid, Spain
[3]Centro Nacional de Investigaciones Metalúrgicas, CENIM/CSIC, Madrid, Avda. Gregorio del Amo 8, 28040, Spain
[4]Departamento de Microbiología Clínica, Instituto de Investigación Sanitaria (IIS)-Fundación Jiménez Díaz, 28040 Madrid, Spain

Received 28 July 2014; revised 3 September 2014; accepted 15 September 2014
Published online 25 September 2014 in Wiley Online Library (wileyonlinelibrary.com). DOI: 10.1002/jbm.a.35337

Abstract: The aim of this study was to evaluate the proliferation and mineralization ability of mouse osteoblastic MC3T3-E1 cells on F-containing TiO_2 films with different morphology and nanostructure that previously confirmed antibacterial properties. F-containing TiO_2 films were fabricated by anodizing Ti-6Al-4V alloy ELI -grade 23. By using a mixture of H_2SO4/HF acid at 20 V for 5 and 60 min, a TiO_2 film grows with nanoporous (NP) and nanotubular (NT) features, characterized with a pore diameter of 20 and 100 nm, respectively. Fluoride-TiO_2 barrier films (FBL) were produced in 1*M* $NH_4H_2PO_4$/0.15*M* NH_4F solution at constant voltage controlled at 20 V for 120 min. The amount of F incorporated in the nanostructured oxide films was 6 at % and of 4 at %, for the NP and NT, respectively, while for the FBL film was 12 at %. MC3T3-E1 cells exhibited different behavior when seeded and grown onto these surfaces. Thus, F-doped TiO_2 films with NP structures increased proliferation as well as osteogenic gene expression and the mineralization capacity of these osteoblastic cells. These results confirm that anodizing process is suitable to fabricate multifunctional surfaces on Ti-6Al-4V alloy with improved not only antibacterial but also osteogenic properties useful for bone fixation of prosthetic devices © 2014 Wiley Periodicals, Inc. J Biomed Mater Res Part A: 103A: 1985–1990, 2015.

Key Words: Ti-6Al-4V alloy, surface functionalization, anodizing, osteoblast growth and function

How to cite this article: Lozano D, Hernández-López JM, Esbrit P, Arenas MA, Gómez-Barrena E, de Damborenea J, Esteban J, Pérez-Jorge C, Pérez-Tanoira R, Conde A. 2015. Influence of the nanostructure of F-doped TiO_2 films on osteoblast growth and function. J Biomed Mater Res Part A 2015:103A:1985–1990.

INTRODUCTION

Titanium and its alloys are widely used for orthopaedic implants and prostheses due to their inertness, biocompatibility, and satisfactory bone fixation.[1,2] Broad functionality of titanium alloys can be related to the passive TiO_2 film that forms on the surface enhancing the corrosion resistance and biological activity. However, bacterial colonization of these titanium surfaces and defective bone formation and tissue integration compromise the effectiveness of these materials when implanted, eventually leading to implant loosening and failure.[3]

Different methods have been used to alter either the chemical composition or the topography of the titanium surface, with a different outcome in terms of bacterial and cell adhesion.[4–6] Among them, anodizing is a well known process that enables the growth of titanium oxide film under controlled conditions.[7] In previous works, the authors demonstrate that the anodizing process fabricates F-doped TiO_2 films with antibacterial properties by using the appropriate electrolyte and voltage conditions. These anodic films with different nanostructure and F content were characterized showing lower adhesion affinity to *S. aureus* and *S. epidermidis* than F-free barrier anodic films (BL) and non anodized alloy. Moreover, the comparative studies performed on F-containing TiO_2 films with and without nanostructure permitted to discriminate the effect of the fluoride from the effect of the nanostructure on bacterial adhesion,

Correspondence to: A. Conde; e-mail: a.conde@cenim.csic.es
Contract grant sponsor: Spanish Ministry of Science and Innovation; contract grant numbers: MAT2009-13751 SMOTI and CONSOLIDER-INGENIO 2010 CSD 2008-0023 FUNCOAT
Contract grant sponsor: Spanish Ministry of Economy; contract grant number: MAT2013-48224-C2
Contract grant sponsor: Comunidad Autónoma de Madrid; contract grant number: S-2009/MAT/1472
Contract grant sponsor: RED TEMÁTICA DE INVESTIGACIÓN COOPERATIVA EN ENVEJECIMIENTO Y FRAGILIDAD (RETICEF); contract grant number: RD12/0043/0008

demonstrating that fluoride is the key factor which supplied enhanced antibacterial properties to TiO_2 surface films.[8–10]

The inhibition of bacterial adhesion is the most critical step to prevent implant-associated infection, but implant success requires that tissue integration occurs before appreciable bacterial colonization. Therefore, to obtain valid conclusions on the potential clinical use of the aforementioned fluoride anodic films, it is necessary to assess the effect of both fluoride content and nanostructure on cells in the bone environment.

Previous studies indicate that fluoride modifications of the Ti surface improve the bone tissue response after implantation, favoring the osteointegration process.[11–13] Fluoride on the titanium surface is thought to be released upon phosphate exchange reaction during the initial exposure to the bone healing environment, as confirmed by several *in vitro* or *in vivo* studies on surface modified titanium alloys involving the use of HF solutions. In this way, the titanium surface acts as a site for calcium and phosphate precipitation, leading to an increased bone contact and implant stability.[14] Using murine osteoblasts on rough titanium surfaces treated with different concentrations of fluoride, or human mesenchymal stem cells on fluoride-containing modified TiO_2 surfaces, an increased cell proliferation was found to be induced by fluoride.[11,15–18] Current data suggest that the enhancement of bone formation by this type of F-containing titanium materials might result from the right combination of several factors such as the oxide covering the surface, the presence of F, and the micro (blasting) and nanolevel topography created by the HF (acid etching).

As an initial insight into the potential ability of these unique surface modifications of titanium alloys to promote a favorable bone response, the present study evaluates *in vitro*, the influence of the nanotopography and the F content of Ti-6Al-4V alloy with different F-doped TiO_2 films on various osteoblast function features.

MATERIALS AND METHODS

Film fabrication

Surface pretreatment and anodizing process used for fabrication of TiO_2 nanostructures with different fluorine contents and controlled morphology on Ti-6Al-4V alloys have been carried out as follows.

A 18 mm diameter rod of Ti-6Al-4V alloy ELI grade according to the standard ASTMF136-02 supplied by Surgical was cut into 2-mm thick disk specimens, ground through successive grades of SiC paper to 1200 grade, degreased with a conventional detergent and rinsed in tap water followed by deionised water. The specimens were then chemically polished (CP) in a mixture of HF(48 wt %):HNO_3(70 wt %):H_2O with volume ratio 1:4:5 for 5 min at room temperature under continuous agitation at 400 rpm, rinsed in distilled water and dried in cold air. The disks were anodized only on one side, so the treated area was 2.54 cm^2.

The anodizing treatment was performed in a two-electrode cell using a Platinum mesh as a cathode. Constant voltage was applied using LAB/SM 1300DC power supply (ET Power systems). Current-time responses of anodizing were acquired at 0.1 Hz sampling rate using a Zero-Resistance Ammeter connected in series with the electrochemical cell.

Nanoporous (NP) and nanotubular (NT) oxide films were fabricated at constant voltage controlled at 20 V in the electrolyte containing 1*M* H_2SO_4 and 0.15 wt % HF for 5 and 60 min, respectively, at temperature controlled at 20°C according to Arenas et al.[19]

Fluoride-TiO_2 barrier films (FBL) were produced in 1*M* $NH_4H_2PO_4$/0.15*M* NH_4F solution at constant voltage controlled at 20 V for 120 min and at temperature controlled at 20°C. Finally, fluoride-free barrier oxide films (BL) have been also produced by anodizing in 1*M* H_2SO_4 at 15 mA cm^{-2} to 90 V.

Cell proliferation

The materials were placed into 12-well plates before seeding MC3T3-E1 cells[20] at a density of 10,000 cells/cm^2 in 2 mL of α-minimum essential medium with 10% fetal bovine serum, 50 μg/mL ascorbic acid, 10 m*M* ß-glycerol-2-phosphate and 1% penicillin–streptomycin, followed by incubation for different times at 37°C in 5% CO_2. Medium was replaced every other day. Cell proliferation was determined by addition of Alamar Blue solution (AbD Serotec, Oxford, UK) at 10% (v/v) to the cell culture[21] at 2 and 7 days of growth, following manufacturer's instructions. Fluorescence intensity was measured with excitation and emission wavelengths of 540 and 600 nm, respectively, in an Opsys MR Reader (Dynez Techonologies, Chantilly, VA).

Cell matrix mineralization

Matrix mineralization was measured by alizarin red staining after incubating subconfluent MC3T3-E1 cells with the tested specimens in the aforementioned medium for 10 days. The stain was dissolved with 10% cetylpyridinum chloride in 10 m*M* sodium phosphate pH 7, measuring absorbance at 620 nm.[20]

Real-time PCR

MC3T3-E1 cells were incubated with the tested specimens as described above, and 5 days thereafter, total cell RNA was extracted with Trizol (Life Technologies, Rockville, MD). Gene expression was analyzed by real-time PCR using an ABI PRISM 7500 system (Applied Biosystems, Foster City, CA) and a described protocol.[22] Unlabeled mouse specific primers for: Runx2, osteocalcin (OC) and vascular endothelial growth factor (VEGF) and TaqMan^{MGB} probes were obtained by Assay-by-Design^{SM} (Applied Biosystems). The mRNA copy numbers were calculated for each sample by using the cycle threshold (Ct) value. 18S rRNA, a housekeeping gene, was amplified in parallel with the tested genes. Fold change for the treatment was defined as the relative expression compared with that of the control and was calculated as $2^{-\Delta\Delta C}$, where $\Delta\Delta C\mathrm{t} = \Delta C\mathrm{treatment} - \Delta C\mathrm{control}$.

Statistical analysis

Results are expressed as mean ± SEM. Statistical evaluation was performed through analysis of variance and Scheffé *post-hoc* test. A value of $p < 0.05$ was considered significant.

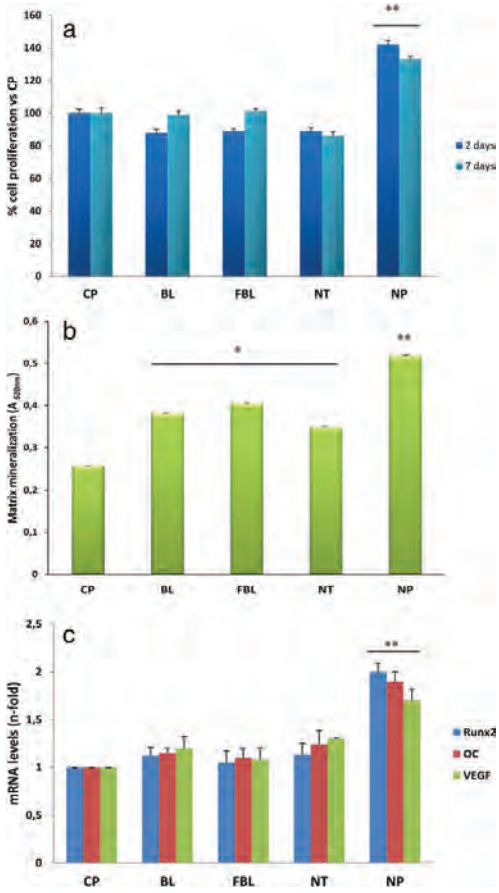

FIGURE 1. MCT3T3-E1 cell proliferation (measured by Alamar Blue assay) at days 2 and 7 (**a**); matrix mineralization at day 10 of culture (**b**); and gene expression of osteoblastic (Runx2 and OC) and angiogenic (VEGF) markers (**c**), at day 5, in the presence of Ti-6Al-4V (CP) and Ti-6Al-4V with various anodic oxide films, F-free (BL) and F-containing (FBL, NP, NT). SEMs were less than 1% in all of the experimental conditions. Results are mean ± SEM ($n = 4$). *$p < 0.01$ versus CP; **$p < 0.0001$ versus CP. [Color figure can be viewed in the online issue, which is available at wileyonlinelibrary.com.]

RESULTS

Film properties

Two types of nanostructure arrays have been fabricated by anodizing at 20 V for 5 and 60 min, respectively, in 1*M* H_2SO_4/0.15 wt.% HF. The morphologies of these nanostructured TiO_2 films doped with F on the Ti-6Al-4V alloy were thoroughly characterized in a previous work.[23] Short anodizing time resulted in formation of a 110-nm-thick NP oxide film with a porous diameter of 20 nm (NP). Long anodizing time produced a 300-nm-long NT oxide film with a nanotube diameter of 100 nm. The average roughness, Ra, for the NP and NT films is higher than that for CP surfaces, 53 nm, with 178 and 160 nm for NP and NT films, respectively. The Rutherford backscattering spectroscopy (RBS) analysis revealed that these two types of films contained 6 at % for NP and 4 at % of fluorine for NT.[23] Raman spectra performed on the films formed at 20 V showed broad bands centered at 454 and 617 cm^{-1} corresponding to amorphous TiO_2. The amorphous character of the nanostructured TiO_2 deduced from Raman data also agreed with TEM observations, where, at the employed resolution, no nanocrystals were disclosed in any of the film.[23]

Two types of non nanostructured oxide films without and with fluoride have been fabricated varying the composition of the electrolyte and the electrical conditions.[23,24] The oxide film prepared in 1*M* H_2SO_4 the F-free electrolyte is a 200-nm-thick oxide barrier type film (BL).The R_a values for the BL film are slightly higher than CP surface, with the average R_a value of 73.9 ± 3.8 nm.

Finally, a ~150 nm-thick F-barrier film, FBL, is formed after 120 min of anodizing in a $NH_4H_2PO_4/NH_4F$ electrolyte. The fluoride concentration and the pH of the anodizing bath strongly influence on the TiO_2 film surface morphology formed in this electrolyte.[24] The chemical composition estimated by RBS revealed that the fluorine content in FBL films is 12 at %.[24] The average R_a of the FBL film, 130 nm, ranges in the same order than the nanostructured oxide films NP and NT. The higher chemical dissolution process occurred during the anodizing process in the fluoride-containing electrolyte results in an increased roughness on the FBL in comparison to the BL.

Cell proliferation

When testing the different F-doped TiO_2 films in osteoblastic MC3T3-E1 cells, it was observed that the presence of F failed to affect cell proliferation (2 and 7 days) in the case of BL, BFL, NT films, but it was significantly increased on the NP specimens; thus, the mean % cell proliferation with NP versus CP specimens (normalized to 100%) was: 142 and 133%, at days 2 and 7, respectively [Fig. 1(a)].

Cell matrix mineralization

In addition, F-doped TiO_2 films, compared to the CP materials, significantly increased matrix mineralization in osteoblastic MC3T3-E1 cells at 10 days of culture; so that the corresponding mean A_{260nm} values for BL, FBL, and NT were: 0.38; 0.41; and 0.35, respectively, whereas that for the NP was 0.52 versus 0.26 for CP [Fig. 1(b)].

Gene expression

We analyzed the gene expression of two osteogenic markers, Runx2 and OC, corresponding to early and late osteoblast differentiation, respectively, and that of a key angiogenic factor, VEGF, in MC3T3-E1 cells exposed to the different tested specimens. It was found that NP specimens significantly increased the gene expression of all of these markers tested in MC3T3-E1 cells at day 5 [Fig. 1(c)].

DISCUSSION

The formation of bone around implants is a multistep process involving osteoblast adhesion, proliferation,

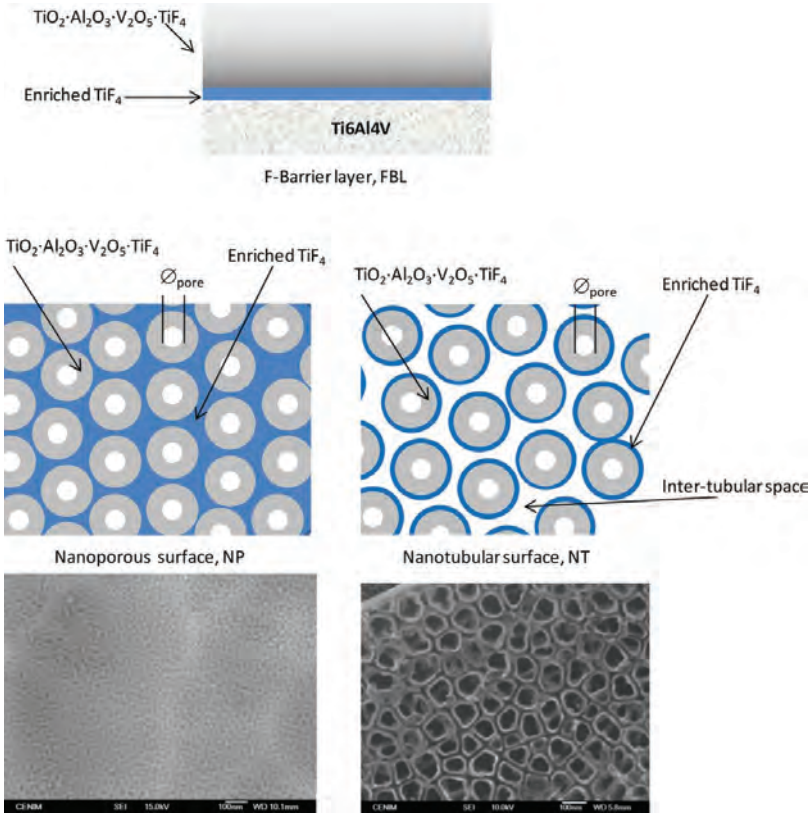

FIGURE 2. Scheme of TiF_4 distribution on NP, NT, and FBL anodic films. [Color figure can be viewed in the online issue, which is available at wileyonlinelibrary.com.]

differentiation, secretion of extra cellular matrix proteins, and mineralization. Yao et al.[25] evidenced an increased osteoblast adhesion on Ti and Ti-6Al-4V anodized in diluted HF, related to the surface alterations at the nanometer scale produced during short anodizing periods. Further studies by the same authors showed that the deposition of calcium by osteoblasts was increased on nanotube-like TiO_2 structures over anodized nanoparticulate structures on the titanium surface.[26] However, the osteoblast total collagen content and alkaline phosphatase activity did not show significant differences when comparing the two anodized and unanodized titanium surfaces after over 21 days. Conversely, Das et al.[27] observed an increase of both the extracellular matrix production and alkaline phosphatase expression by osteoblasts on NT oxide surface compared to unanodized titanium surfaces, suggesting that these cells mature more rapidly on a NT surface than on unanodized titanium samples.

Similarly, other authors reported that adhesion, spreading, growth, and differentiation of mesenchymal stem cells on vertically oriented TiO_2 nanotubes with defined diameters between 15 and 100 nm are critically dependent on the nanotube diameter. Thus, a diameter < 30 nm provide an effective length scale for accelerated integrin clustering/focal contact formation and enhancing cellular activities, compared to smooth TiO_2 surfaces obtained by anodization in fluoride-free H_3PO_4 electrolytes. These maximal responses were observed at 15 nm diameter, whereas cell adhesion and spreading were severely impaired on nanotube films with a nanotube diameter > 50 nm, resulting in dramatically reduced cellular activity.[28–30] However, these authors did not take into account the compositional changes induced in the oxide fabricated by the anodization in HF containing solutions together with nanometer surface features. In particular, the influence of the fluoride incorporated in the anodic film during the fabrication of the NP or NT oxide films was not considered; even though it is well known that fluorine ions induce formation of fluorapatite in the surrounding bone. The above mentioned studies conclude that the surface nano features developed in such anodizing conditions were responsible for the observed improved biological response.

The results of the present study show that the presence of F on Ti surfaces, which is responsible for the antibacterial properties, *per se* does not increase but it does not limit either osteoblastic cell growth. However, F content conferred various osteogenic features to the tested materials, as indicated by an increase in matrix mineralization and the gene expression of two osteoblastic markers, Runx2 and OC, and the angiogenic factor VEGF in MC3T3-E1 cells. Moreover, these cells exhibited improved functional parameters on F-doped TiO_2 films with NP structures [Fig. 1(a,b)] compared with NT or dense FBL structures, suggesting preferential adhesion to certain surface. The reason for this apparent preferential behavior of these osteoblastic cells is unknown. Surface roughness, however, could not explain by itself the best cell response observed on NP specimens, as the average measured roughness Ra for FBL, NP and NT specimens was similar (about 100 nm). F-containing TiO_2 anodic films FBL, NP, and NT, possess fluoride contents of 12, 6, and 4 at %, respectively. In this sense, Lamolle et al.[31] observed that small amounts of fluoride (between 1 and 2 at %) incorporated onto the surface of metallic Ti implants have a stimulatory action on MC3T3-E1 osteoblasts. Longer immersion times in HF solutions, as used by Tiainen et al.[32] provided modified TiO_2 surfaces with 4 at % of F that induced a significantly higher osteoblastic cell number. However, they did not obtain conclusive evidence about fluoride being responsible for this cellular behavior. Moreover, they reported that a higher F content (about 9 at %) was in fact toxic to the cells. Conversely, no harmful effect was observed for the FBL film containing 12 at % of F in our study.

Even though the biological response to fluoride appears to be dose-dependent,[33] our data do not provide conclusive evidence about the concentration of fluoride being a key factor for the advantageous osteogenic properties of NP films.

Hydrophilic surfaces generally enhance protein and cell adhesion.[34–36] However, the differences in bioactivity observed in this work could not be explained by the different surface hydrophilicity of all the fabricated surfaces, all of them exhibiting high wettability with water contact angles lower than 65°.[10] In fact, NT films, with the lowest water angle contact (below 10°), was not the most effective in osteoblastic cell responses.

It is worthwhile mentioning that during the anodizing process the conditions imposed to fabricate the TiO_2 films not only influence the roughness and nanostructure of the anodic film but also its chemical composition. The latter is complex, containing TiF_4, and oxides of the alloying elements present in the titanium alloy, Al_2O_3 and V_2O_5.[23] The fluoride content and distribution are also different on each fabricated nanostructured anodic film. Habazaki et al.[37] demonstrated by GDOES analysis that fluoride ions are distributed relatively uniformly in anodic barrier films throughout the outer regions, with an accumulation of fluoride ions at the alloy/film interface. The faster inward migration rate of fluoride ions relative to that of O^{2-} ions, attributed to the smaller ionic radius of F^- ions, is the reason for such gradient distribution of fluoride. Similarly to NP films, the pore wall includes an outer pore wall that contains TiO_2, TiF_4 and oxides of the alloying elements present in the titanium alloy, such as Al_2O_3 and V_2O_5 for Ti-6Al-4V alloy, while the inner pore wall mainly incorporates TiF_4. Longer anodizing times in the electrolyte containing HF fabricate NT anodic films, as a result of the chemical dissolution of TiF_4 placed at the inner pore wall, creating small intertubular spaces of few nm, Figure 2.

According to Ellingsen,[13] when TiF_4 contacts tissue fluids, the oxygen from phosphates present in the fluid may replace the fluoride, and phosphates become covalently bound to the titanium surface. Such reaction would also promote bone formation in bone tissue, where phosphate might thus covalently bind to the titanium implant.[13] This study suggests that higher number of TiF_4 sites on the surface of the NP specimen, relative to that on NT and FBL specimens, might explain its improved osteogenic features. Thus, a larger TiF_4-enriched surface in contact with the physiological fluid in NP specimens than in NT would increase the capacity of NP surfaces to react with phosphate, increasing the number of preferential sites to cell attachment and bone formation. The opposite would occur in the case of FBL specimens with lower amount of titanium fluoride directly exposed to the physiological fluid, compared to NP materials. Moreover, less titanium fluoride sites available on NT and FBL, compared to NP, determine less released fluoride by the NT, which might account for their relative inefficacy to affect osteoblastic function.

In conclusion, the present findings, together with our previous results[9,10] indicate that anodization is a quick and efficient method to form multifunctional nanostructured titanium oxide films of controllable pore size, good uniformity, and conformability over large areas. NP TiO_2 grown on Ti6Al4V can mimic constituent features of natural bone. Therefore, the observed interaction of osteoblastic cells with these materials might indicate potential impact on the bone milieu *in vivo*. Although both nanoscale topography and chemical composition are modified by the anodization process, the F content has been deemed as the major factor influencing the bacterial adhesion,[10] while parameters such as the fluoride distribution and topography appear to be paramount for osteoinduction. Furthermore, our studies provide a rationale for the development of a new kind of multifunctional prosthetic material surface based on titanium alloys with enhanced antibacterial properties, maintaining or even improving the bone formation capacity.

ACKNOWLEDGMENTS

Juan Manuel Hernández López acknowledges CSIC for funding this work under the grant JAE-pre-2010. Daniel Lozano also acknowledges Comunidad Autónoma de Madrid for his postdoctoral research contract S-2009/MAT/1472. The authors report that they have a patent for the materials regarding their antimicrobial properties PCT/ES2011/070342.

REFERENCES

1. Brunette D, Tengvall P, Textor M, Thomsen M. Titanium in Medicine. Springer-Verlag, Berlin Heidelberg GmbH; 2001.
2. Freese H, Volas MG, Wood J, Textor M. Titanium and its alloys in biomedical. engineering. In: Encyclopedia of Materials: Science and Technology. Oxford: Elsevier; 2001.

3. Rimondini L, Fini M, Giardino R. The microbial infection of biomaterials: A challenge for clinicians and researchers. A short review. J Appl Biomater Biomech 2005;3:1–10.
4. Chung KK, Schumacher JF, Sampson, EM, Burne, RA, Antonelli, PJ, Brennan, AB. Impact of engineered surface microtopography on biofilm formation of Staphylococcus aureus. Biointerphases 2007;2:89–94.
5. Sarró MI, Moreno DA, Ranninger C, King E, Ruiz J. Influence of gas nitriding of Ti6Al4V alloy at high temperature on the adhesion of Staphylococcus aureus. Surf Coat Tech 2006;201:2807–2812.
6. Zhao L, Chu PK, Zhang Y, Wu Z. Antibacterial coatings on titanium implants. J Biomed Mater Res B 2009;91B:470–480.
7. Roy P, Berger S, Schmuki P. TiO2 Nanotubes: Synthesis and Applications. Angew Chem Int Ed 2011;50:2904–2939.
8. Peremarch CP-J, Tanoira RP, Arenas MA, Matykina E, Conde A, Damborenea JJD, Barrena EG, Esteban J. Bacterial adherence to anodized titanium alloy. J Phys Conf Series 2010;252:012011.
9. Pérez-Jorge C, Conde A, Arenas MA, Pérez-Tanoira R, Matykina E, de Damborenea JJ, Gómez-Barrena E, Esteban J. In vitro assessment of Staphylococcus epidermidis and Staphylococcus aureus adhesion on TiO2 nanotubes on Ti–6Al–4V alloy. J Biomed Mater Res A 2012;100A:1696–1705.
10. Arenas MA, Pérez-Jorge C, Conde A, Matykina E, Hernández-López JM, Pérez-Tanoira R, de Damborenea JJ, Gómez-Barrena E, Esteba J. Doped TiO2 anodic layers of enhanced antibacterial properties. Colloids Surf B Biointerfaces 2013;105:106–112.
11. Monjo M, Lamolle SF, Lyngstadaas SP, Rønold HJ, Ellingsen JE. In vivo expression of osteogenic markers and bone mineral density at the surface of fluoride-modified titanium implants. Biomaterials 2008;29:3771–3780.
12. Lamolle S, Monjo M, Lyngstadaas S, Ellingsen J, Haugen J. Titanium implant surface modification by cathodic reduction in hydrofluoric acid: surface characterization and in vivo performance. J Biomed Mater Res A 2009;88:581–588.
13. Ellingsen JE. Pre-treatment of titanium implants with fluoride improves their retention in bone. J Mater Sci Mater Med 1995;6:749–756.
14. Isa Z, Schneider G, Zaharias R, Seabold D, Stanford C. Effects of fluoride-modified titanium surfaces on osteoblast proliferation and gene expression. Int J Oral Maxillofac Implant 2006;21:203–211.
15. Bellows CG, Heersche JNM, Aubin JE. The effects of fluoride on osteoblast progenitors in vitro. J Bone Miner Res 1990;5(SUPPL. 1):S101–S105.
16. Wergedal JE, Lau KHW, Baylink DJ. Fluoride and bovine bone extract influence cell proliferation and phosphatase activities in human bone cell cultures. Clin Orthop Relat Res 1988;233:274–282.
17. Cooper LF, Zhou Y, Takebe J, Guo J, Abron A, Holmén A, Ellingsen JE. Fluoride modification effects on osteoblast behavior and bone formation at TiO2 grit-blasted c.p. titanium endosseous implants. Biomaterials 2006;27:926–936.
18. Masaki C, Schneider G, Zaharias R, Seabold D, Stanford C. Effects of implant surface microtopography onosteoblast gene expression. Clin Oral Implants Res 2005;16:650–656.
19. Arenas M, Conde A, de Damborenea J, Matikyna E, Esteban J, Gómez-Barrena E, Pérez-Jorge C, Pérez Tanoira R. Materiales de titanio anodizado con fluor. PATENT 2010; PCT/ES2011/070342. Spain.
20. Lozano D, de Castro LF, Dapía S, Andrade-Zapata I, Manzarbeitia F, Alvarez-Arroyo MV, Gómez-Barrena E, Esbrit P. Role of parathyroid hormone-related protein in the decreased osteoblast function in diabetes-related osteopenia. Endocrinology 2009;150:2027–2035.
21. Deb S, Mandegaran R, Di Silvio L. A porous scaffold for bone tissue engineering/45S5 Bioglass® derived porous scaffolds for co-culturing osteoblasts and endothelial cells. J Mater Sci Mater Med 2010;21:893–905.
22. Lozano D, Feito MJ, Portal-Núñez S, Lozano RM, Matesanz MC, Serrano MC, Vallet-Regí M, Portolés MT, Esbrit P. Osteostatin improves the osteogenic activity of fibroblast growth factor-2 immobilized in Si-doped hydroxyapatite in osteoblastic cells. Acta Biomater 2012;8:2770–2777.
23. Matykina E, Hernandez-López JM, Conde A, Domingo C, de Damborenea JJ, Arenas MA. Morphologies of nanostructured TiO2 doped with F on Ti–6Al–4V alloy. Electrochim Acta 2011;56:2221–2229.
24. Matykina E, Conde A, de Damborenea J, Matín y Marero D, Arenas MA. Growth of TiO2-based nanotubes on Ti–6Al–4V alloy. Electrochim Acta 2011;56:9209–9218.
25. Yao C, Perla V, Mckenzie JL, Slamovich EB, Webster TJ. Anodized Ti and Ti6Al4V possesing nanometer surface features enhances osteoblast adhesion. J Biomed Nanotechnol 2005;2005:68–73.
26. Yao C, Slamovich EB, Webster TJ. Enhanced osteoblast functions on anodized titanium with nanotube-like structures. J Biomed Mater Res A 2008;85A:157–166.
27. Das K, Bose S, Bandyopadhyay A. TiO2 nanotubes on Ti: Influence of nanoscale morphology on bone cell–materials interaction. J Biomed Mater Res A 2009;90A:225–237.
28. Park J, Bauer S, von der Mark K, Schmuki P. Nanosize and vitality: TiO2 nanotube diameter directs cell fate. Nano Lett 2007;7:1686–1691.
29. Park J, Bauer S, Schlegel KA, Neukam FW, von der Mark K, Schmuki P. TiO2 nanotube surfaces: 15 nm—An optimal length scale of surface topography for cell adhesion and differentiation. Small 2009;5:666–671.
30. Zhao L, Mei S, Wang W, Chu PK, Zhang Y, Wu Z. Suppressed primary osteoblast functions on nanoporous titania surface. J Biomed Mater Res A 2011;96:100–107.
31. Lamolle SF, Monjo M, Rubert M, Haugen HJ, Lyngstadaas SP, Ellingsen JE. The effect of hydrofluoric acid treatment of titanium surface on nanostructural and chemical changes and the growth of MC3T3-E1 cells. Biomaterials 2009;30:736–742.
32. Tiainen Hanna MM, Knychala J, Nilsen O, Petter LS, Eirik EJ, Haugen HJ. The effect of fluoride surface modification of ceramic TiO2 on the surface properties and biological response of osteoblastic cells in vitro. Biomed Mater 2011;6.
33. Baylink D, Bernstein D. The effects of fluoride therapy on metabolic bone disease. Clin Orthop Relat Res 1967;55:51–85.
34. Bacakova L, Filova E, Parizek M, Ruml T, Svorcik V. Modulation of cell adhesion, proliferation and differentiation on materials designed for body implants. Biotechnol Adv 2011;29:739–767.
35. Baier R. Surface behaviour of biomaterials: The theta surface for biocompatibility. J Mater Sci Mater Med 2006;17:1057–1062.
36. Janssen MI, Leeuwen MBMv, Kooten TGv, Vries Jd, Dijkhuizen L, Wösten HAB. Promotion of fibroblast activity by coating with hydrophobins in the β-sheet end state. Biomaterials 2004;25:2731–2739.
37. Habazaki H, Fushimi K, Shimizu K, Skeldon P, Thompson G. Fast migration of fluoride ions in growing anodic titanium oxide. Electrochem Commun 2007;9:1222–1227.

Corrosion Science 94 (2015) 61–69

Contents lists available at ScienceDirect

Corrosion Science

journal homepage: www.elsevier.com/locate/corsci

Correlation of the nanostructure of the anodic layers fabricated on Ti13Nb13Zr with the electrochemical impedance response

J.M. Hernández-López, A. Conde, J. de Damborenea, M.A. Arenas *

National Centre for Metallurgical Research (CENIM-CSIC), Avda. Gregorio del Amo 8, 28040 Madrid, Spain

ARTICLE INFO

Article history:
Received 31 October 2014
Accepted 23 January 2015
Available online 31 January 2015

Keywords:
A. Titanium alloy
B. EIS
B. RBS
B. Polarization
C. Anodic films
C. Corrosion

ABSTRACT

TiO_2 layers on Ti13Nb13Zr were fabricated by anodizing in acidic fluorine solution, to determine the nanostructure and electrochemical stability in a PBS solution. The anodization process showed higher growth efficiency. The morphology of nanostructured layer is more homogenous and thicker layers are obtained in shorter times regarding to organic electrolytes. Additionally, nanostructured oxide films were electrochemically studied to correlate the protective properties of the anodic films with the morphology and nanostructure developed in each anodizing condition. The anodic layers grown at short times present nanoporous structure and higher corrosion resistance than those fabricated at longer times, which possess nanotubular structure.

1. Introduction

The biological response and the success of an implant depend on the physicochemical properties of the surface. Surface modification of titanium alloys is required to improve their biological activity and enhance bone formation [1,2]. Pure titanium and Ti6Al4V ELI alloys are widely used as structural and/or functional biomaterials for artificial implants. However, the high cytotoxicity of vanadium and the relationship between aluminum and the senile dementia of Alzheimer type has promoted the need for the development of new Ti alloys for medical purposes [3].

Different alloying elements such as Fe, Cr, Mo, Nb, Sn, Ta and Zr, have been used to replace them. These alloying elements are β stabilizers. The β-titanium alloys offer the highest strength to weight ratios and very attractive combinations of strength, toughness, and fatigue resistance at large cross sections [4,5]. Particularly promising is the near-β Ti13Nb13Zr alloy which reduced the Young's modulus to 64–83 GPa, closer to the bone, regarding the α + β Ti6Al4V alloy – 105–120 GPa – [1,5–7].

On the other hand, as Minagar [8] pointed out, the surface of an implant needs modification to optimize the properties of the implant and to maximize its bioactivity when interfacing with natural tissue. The surface functionalization enhances both osseointegration and bioactivity, avoiding bacterial adhesion. Among other methods, anodization is a relatively simple method to fabricate a variable thickness and uniform nanostructured layer of TiO_2 on a titanium alloy surface. For titanium alloys, the oxide layer exhibits different properties depending on its microstructure as well as the processing parameters, mainly the time and potential, the electrolyte composition and the temperature. This allows the doping of the nanostructure with ions such as F which has been considered of interest as a way to provide antibacterial and osseointegration properties [1,9–11]. Since the presence of fluoride decreases the adhesion of bacteria to the implant surface, it would increase the probability of success of the implant [12,13].

Additionally, in order to have a long term successful implant, the electrochemical corrosion behavior of TiO_2 anodic layers is the most important issue. Corrosion is one of the greatest challenges for ensuring the biostability and biocompatibility of metallic implants. The electrochemical behavior of the anodic layers will depend on their interaction with the surrounding environment. It must therefore be considered the behavior of the Ti modified surface in physiological medium to assess the nature of the passive film formed [14,15] since a high corrosion resistance will ensure that metallic ions will not be released from implants into the bloodstream. In this sense, the β-titanium alloys, such as Ti–*x*Zr, Ti–*x*Nb–*y*Zr–*z*Ta, Ti–*x*Nb–*y*Ta and Ti–*x*Nb–*y*Zr, have been evaluated from corrosion viewpoint in different solutions. The results pointed out that these titanium alloys may show higher corrosion resistance than CP titanium and Ti6Al4V alloy due to the growth of a more compact and stable native passive film composed of a mixture of protective oxides (TiO_2, Nb_2O_5, ZrO_2 and Ta_2O_5) [15–21].

* Corresponding author.
E-mail address: geles@cenim.csic.es (M.A. Arenas).

http://dx.doi.org/10.1016/j.corsci.2015.01.041
0010-938X/

The aim of this study is to analyze the corrosion behavior of anodic films grown on Ti13Nb13Zr in a fluoride containing solution. The samples were fully characterized by scanning electron microscope (SEM), Rutherford backscattering spectroscopy (RBS), potentiodynamic polarization and electrochemical impedance spectroscopy (EIS) to elucidate their electrochemical behavior in a phosphate buffered saline solution (PBS).

This work shows that a thorough analysis of the impedance response supplies relevant information about the nanostructure of the anodic films, allowing the estimation of the thickness of the barrier layers and, the influence of the inter-tubular space size in the protective properties of the anodic layer. Moreover, the microstructural values obtained from the impedance measurements reveal a good correlation with the SEM and TEM microstructural examination.

2. Experimental

Rolled bars of Ti13Nb13Zr alloy were supplied by Xian Saite Metal Materials Development Co., Ltd. (China). Specimens of 28 mm of Ti13Nb13Zr (mass%) alloy were ground through successive grades of SiC paper up to 4000 grade. The samples were degreased with detergent and rinsed with tap water followed by deionized water. Anodic layers were formed in a two-electrode cell by anodizing the specimens at constant voltage at 20 V in the electrolyte containing 1 M H_2SO_4 and 34.5 mM HF for 5 and 60 min at constant temperature at 20 °C. Platinum mesh was used as cathode.

The cross sections and plan views of anodic films were examined by field emission gun scanning electron microscopy (FEG-SEM) using JSM6500F Philips instrument, at 15 keV for EDS analysis and 7 keV for secondary electron imaging.

Electron-transparent sections were prepared by scratching the surface of anodized specimens with a scalpel and collecting the pieces of the oxide on a TEM grid. These pieces were observed by TEM, using a JEOL JEM 2100 instrument operated at 200 kV.

The stoichiometric composition of the oxide films was further determined by Rutherford backscattering spectrometry (RBS), using He^+ ions with the energy of 3.045 MeV (resonant energy for $^{16}O(\alpha, \alpha_0)^{16}O$ reaction), produced by the van de Graff accelerator of the Centro de Micro-Análisis de Materiales (CMAM), Madrid. The incident ion beam with the diameter of 1 mm was normal to the specimen surface with 10 μC doze scattered ions detected by a mobile detector at 165°. Data were interpreted using the SIMNRA program.

The electrochemical measurements were done in triplicate in a conventional three-electrode cell. The working electrodes were the non-anodized and anodized NP and NT-specimens, with an area around to 0.32 cm^2 exposed to the aggressive solution; an Ag/AgCl electrode (saturated KCl), was used as reference electrode and the counter electrode was a platinum wire with an area about 0.240 cm^2. The electrolyte was a phosphate buffered saline solution (PBS), containing 150 mM NaCl, 9.99 mM KH_2PO_4, and 9.02 mM $Na_2H_2PO_4$; with a pH range between 7.2 and 7.4. All the tests were carried out at 37 ± 2 °C. Corrosion behavior was evaluated by potentiodynamic polarization and electrochemical impedance spectroscopy using a Gamry Reference 600 potentiostat. The potentiodynamic curves were conducted at a scan rate of 0.16 mV/s. Before starting the scan, the sample remained in the solution for 1 h to stabilize the open circuit potential (OCP). The potential scan was started in the anodic direction from a potential value of −0.3 V with respect to the OCP to 3 V with respect to the Ag/AgCl electrode where the reverse scan started. A wide enough potential sweep was chosen in order to determine the breakdown potential of the specimens, to be compared with the values reported of various implant materials. For Cp-Ti and Ti6Al4V, the breakdown potentials of 2.4 and 2.0 V, respectively have been reported in Hank's solution [22].

EIS measurements were performed applying a sinusoidal signal of 10 mV of amplitude vs. OCP to guarantee that the electrochemical response of the system is linear. The frequency range was from 100 kHz to 10 mHz, and recording 10 points per decade was done. Measurements were carried out periodically during 4 weeks of immersion. The experimental data were analyzed using the ZVIEW software. The quality of fitting was judged by the values of the Chi-square, which is the square of the standard deviation between the original data and the calculated spectrum. It is considered a good fitting when the Chi-square was $<10^3$.

3. Results and discussion

The microstructure of the Ti13Nb13Zr alloy is martensitic with finely dispersed α-phase precipitated in a β-matrix. The microstructure within the prior beta grain boundaries is acicular, Fig. 1a [23]. The EDS analysis – Fig. 1b – shows only the peaks of Ti, Nb and Zr, with a chemical composition of 81.12 ± 2.32, 9.2 ± 1.32 and 9.68 ± 1.13 at.%, respectively. The α-phase is enriched in Zr (neutral element). The neutral elements do not have marked effect on the stability of either of the phase but form solid solutions with titanium. On the other hand, other works pointed out that the grains are refined first and then coarsened with the increase of Zr content. It is also found that Zr element added to titanium alloys has both the solution strengthening and fine-grain strengthening effect, and affects the lattice parameters. The β-matrix is enriched in Nb which is a β-stabilized element [5,24,25].

The current density transients were recorded during anodizing process at 5 and 60 min in H_2SO_4/HF – Fig. 2. It can be observed that for the 60 min treatment the current density reaches the steady state after 9 min. The charge density passed during the initial surge followed by a rapid decay was 0.1308 and 0.1646 C/cm^2

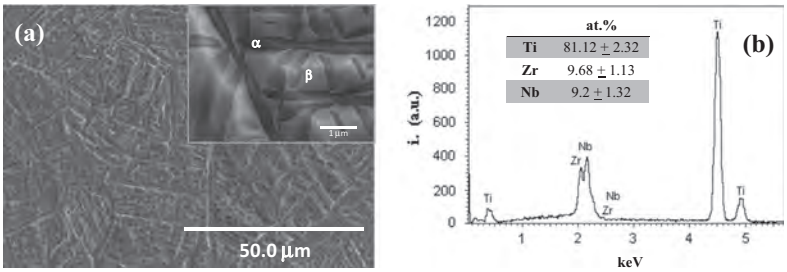

Fig. 1. (a) Microstructure of the Ti13Nb13Zr alloy. (b) EDS analysis of the Ti13Nb13Zr alloy.

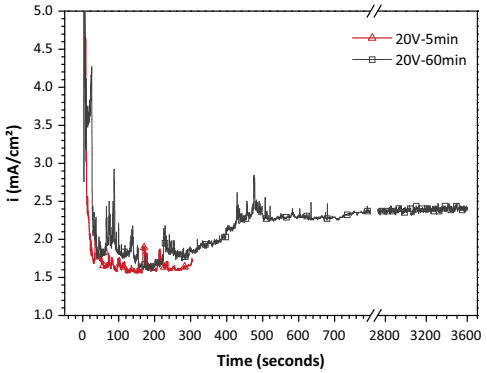

Fig. 2. Current density–time response for anodizing of the Ti13Nb13Zr alloy at 20 V in H_2SO_4/HF electrolyte.

for 5 and 60 min respectively, by applying the Faraday law and assuming 100% efficiency of the process, the estimated thickness of the amorphous barrier layer grown is 71 and 89 nm.

Shorter anodizing times, 5 min, result in nanostructured layers with a porous morphology – NP – in both α and β phases, Fig. 3a, characterized by a pore diameter of ~25 nm and a total thickness around 71 ± 7 nm, Fig 3b. Conversely, the anodic film grown for 60 min shows a nanotubular structure – NT, with nanotubes diameter ranging from ~75 to 100 nm, with inter-tubular distances about 15 nm and an average thickness about 900 ± 100 nm – Fig. 3c and d. The variability in circumferential shape, length and diameter observed in the nanotubes depends on the phase in which the nanotubes grow. These variations can be explained by the different dissolution rates of the oxides grown in α and β phases due to their differences in chemical composition as reported for nanotubes fabricated in Ti35Nb5Zr [26] and in Ti–50Ta [27]. The thickness of the NT layer obtained in this alloy is notably higher than those obtained in Ti6Al4V alloy using the same anodizing conditions [10], and similar to those obtained in TixNbyZr alloys grown in other acidic solutions [28] and in organic electrolytes [26], but, in much shorter times as result of the higher concentration of oxygen in the aqueous solutions with respect to the organic solutions; and the higher migration rate of the anions from the electrolyte (O^{2-}, SO_4^{2-} and F^-) in presence of the electric field, which depends on the ion size and electrical conductivity of the electrolyte.

NT layers disclose a reproducible 40 nm thick barrier layer, Fig 3e, and the nanotube wall thickness was reduced from about ~15 nm at the bottom, Fig. 3f, to around 7 nm at the mouth of the nanotube, Fig. 3g. The thinning of the nanotube walls toward the outer part of the film has been previously described for nanotube formation on pure titanium [29] and Ti6Al4V alloy [10], and it is related to continuous dissolution of TiO_2 and TiF_4 along the entire nanotube length.

Formation of ribs of about 13 nm thick on the nanotube walls (Fig. 3f) is also observed for the NT layers. Ribs are suggested to arise as a consequence of the dissolution of TiF_4 of the walls increasing the inter-space distance between nanotubes, subsequent access of the electrolyte in the interstice and re-growth of the barrier film in the inter-pore region [29–32].

The accurate elemental composition of the film was determined using RBS and average molecular compositions of the NP and NT anodic layers were derived (Table 1, Fig. 4). The spectrum for NT layer showed a steeper slope than the NP film which can be explained due to the different morphology and thickness of the layers. The composition of the anodic layer is estimated by simulating the RBS spectra using successive layers with different composition and thickness. The average molecular composition is determined with the total atoms obtained for the different elements, e.g. Ti, O, Zr, Nb and F, in all the layers used to simulate the spectrum and assuming the formation of different compounds. In the present case, the average molecular composition of the anodic layer was firstly calculated assuming the formation of TiO_x, ZrO_2, Nb_2O_5 and TiF_4. However, the amount of oxygen in the layers did not allow forming these stoichiometric oxides and the formation of ZrF_4 and NbF_5 had to be assumed.

The RBS analysis indicates that the average molecular composition of the anodic film grown on Ti13Nb13Zr alloy can be expressed as $(TiNbZrO)_{0.45}{\cdot}0.081TiF_4{\cdot}0.102NbF_5{\cdot}0.081ZrF_4$ for NP layers and $(TiNbZrO)_{0.61}{\cdot}0.078TiF_4{\cdot}0.098NbF_5{\cdot}0.078ZrF_4$ for NT layers – Table 1. The presence of ZrF_4 and NbF_5 is in agreement with previously reported for the anodic films grown on TiZr and TiNb alloys in which found ZrF_4 and NbF_5, respectively [33,34].

The RBS analysis reveals that the films contained 13.36 at.% of fluorine in NP and 11.92 at.% of fluorine in NT. This decrease in the fluorine content of the layers obtained at longer anodization time, apparently occurs due to dissolution of TiF_4 present in the walls of the nanotubes [10,31,32,35]. Nevertheless, these contents are slightly higher in comparison to the anodic films grown in Ti6Al4V alloy, which showed enhanced antibacterial properties decreasing the adherence of two types of bacteria responsible for most of the prosthetic joints infections [9–11,36].

The efficiency of the film growth was derived as a ratio of titanium ions present in the film (as determined by RBS) to titanium ions due in the film according to the charge density passed during the anodizing Table 2, assuming that all the charge was used for oxidation of titanium. The efficiency reduced drastically with increase the anodizing time from 56.6% to 27.4%, which is higher than those obtained for TiO_2 layers grown on Ti6Al4V under the same conditions [28] or in glycerol at similar times than those used in the present work [37].

The electrochemical stability of the anodic films was determined by potentiodynamic polarization curves performed in PBS – Fig. 5. Before the onset of the potential sweep, the evolution of the open circuit potential was recorded. As can be seen in Fig. 5a, the OCP is stabilized after one hour of immersion for all the specimens. The non-anodized and the NT specimens disclosed similar values around −0.300 V vs. Ag/AgCl and the NP specimens show more negative values, around −0.560 V vs. Ag/AgCl. Fig. 5b gathers the polarization curves of each specimen. Both the non-anodized and the NT specimens have a passive behavior characterized by a vertical anodic branch with a passive current density – i_{pass} – of $1.1 \cdot 10^{-6}$ A/cm^2. NT revealed an increase in current density in the anodic branch until the i_{pass} is reached, consequence of the oxidation of the substrate exposed to the solution through the inter-tubular-space. Córdoba-Torres et al. [38] reported similar passive current densities for nanotubes fabricated in an organic electrolyte on pure Ti foils. Conversely, the NP layer shifted the anodic branch toward lower i_{pass} values, $2.9 \cdot 10^{-7}$ A/cm^2. This anodic layer showed a high stability along the test with a passive behavior in the whole anodic branch and lower dissolution rates compared to both NT and non-anodized specimens, which implies a lower amount of metallic ions delivered to the solution. Moreover, the i_{pass} is one order of magnitude lower than those reported for specimens produced by different immersion treatments performed to thicken the native oxide film on Ti13Nb13Zr alloy [18,39].

The non-anodized sample showed a slight increase of the current around to 1.3 V vs. Ag/AgCl (~1.5 V vs. ENH). This can be associated to the transpassivation behavior of the titanium alloy. At this potential, as is observed into Pourbaix diagrams [40], the titanium oxide layer present on the surface of the alloy oxidizes forming soluble species of Ti(VI).

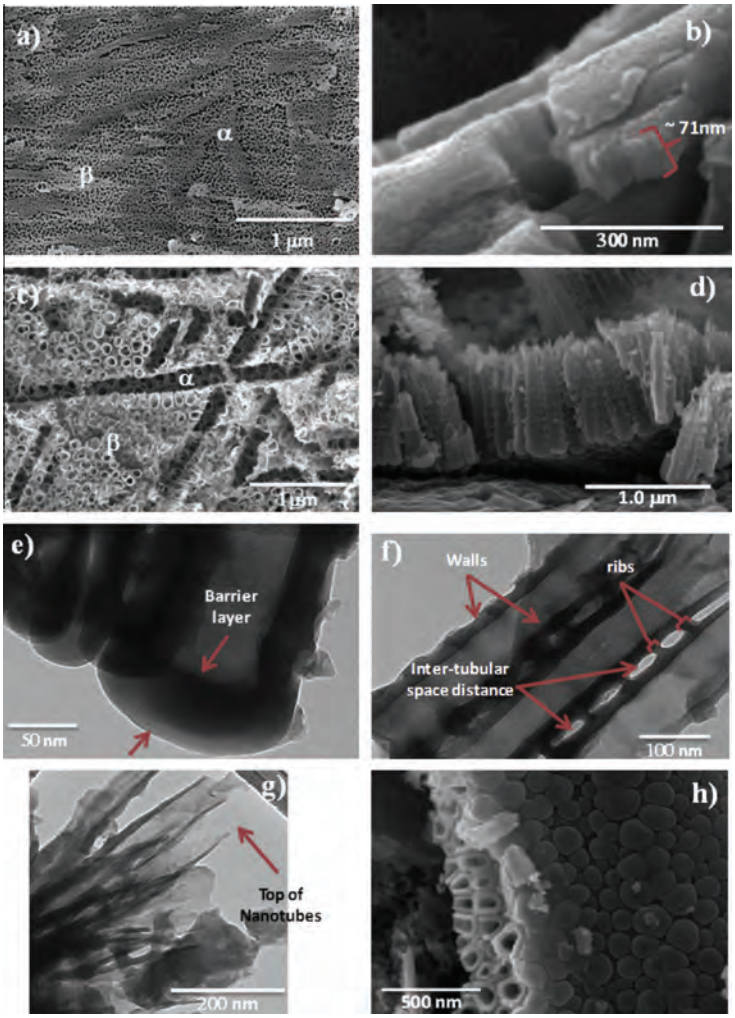

Fig. 3. Morphology of the anodic layers grown at 5 min – NP – (a), and 60 min – NT – (c) with its respective cross-section (b) and (d). TEM views of the barrier film (e), body, top and bottom of the NT layers respectively (e)–(h).

Table 1
Composition of the anodic layers formed on Ti13Nb13Zr in H_2SO_4/HF electrolyte, determined using RBS.

Film	10^{17} atoms cm^{-2}/at.%					Average molecular composition	Efficiency %
	Ti	O	F	Nb	Zr		
20V, 5 min NP	5.46/46.38	2.68/22.79	1.57/13.36	0.90/7.64	1.16/9.83	$(TiNbZr)O_{0.45}$ $0.081TiF_4$ $0.102NbF_5$ $0.081ZrF_4$	~56.57
20V, 60 min NT	36.07/42.09	24.73/28.86	10.26/11.97	8.17/9.54	6.47/7.54	$(TiNbZr)O_{0.61}$ $0.078TiF_4$ $0.098NbF_5$ $0.078ZrF_4$	~27.36

On the other hand, the corrosion potential, E_{corr}, of the non-anodized specimen is −0.340 V vs. Ag/AgCl. A similar value is recorded for the NT specimen, −0.363 V vs. Ag/AgCl, due to the exposure of the oxidized alloy placed at the bottom of the inter-tubular space. Conversely, the NP films show a E_{corr} more cathodic, about −0.459 V vs. Ag/AgCl.

Therefore, the E_{corr} and i_{pass} values of the NT specimens are similar to those recorded for the non-anodized titanium alloy suggesting that the electrochemical response of the NT is mainly due to the oxidation of the substrate exposed through the inter-tubular spaces instead of the barrier layer at the bottom of the nanotubes.

Finally, it is important to highlight that both non-anodized sample and the anodic films did not show susceptibility to localized corrosion in the whole potential sweep since there was no evidence of breakdown potential in the potentiodynamic curves.

Impedance measurements were performed during long immersion times to study the electrochemical processes that take place

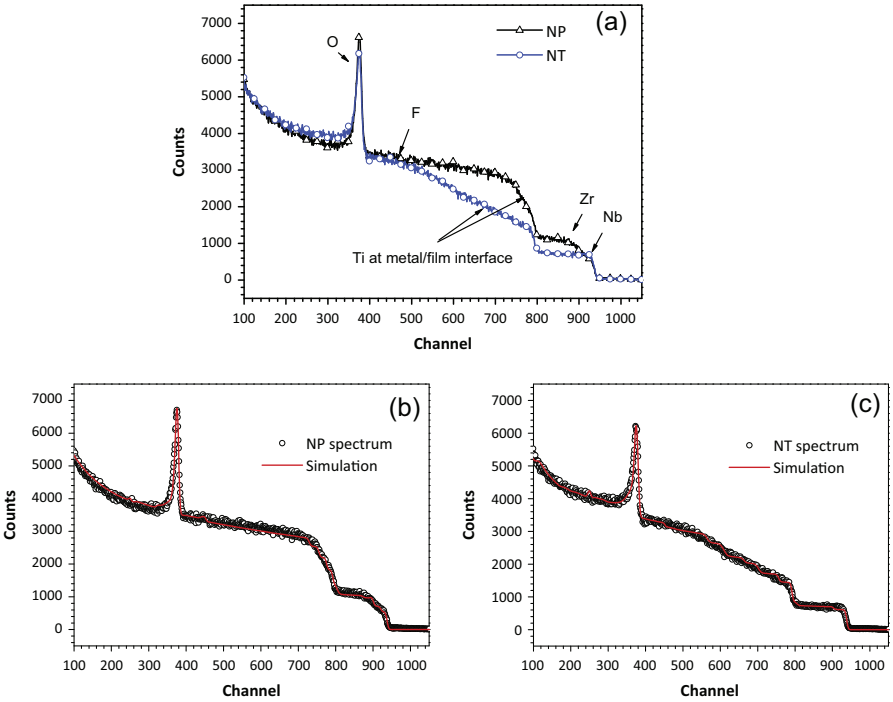

Fig. 4. RBS spectra for both treatments in Ti13Nb13Zr alloy (a), anodizing to 20 V–5 min (experimental and simulated spectra-red line) (b) and 20 V–60 min (experimental and simulated spectra-red line) (c). (For interpretation of the references to color in this figure legend, the reader is referred to the web version of this article.)

Table 2
Parameters of the anodic films formed in the fluoride solution.

Time anodization (min)	Charge (C/cm^2)	Oxidized titanium[a] (nm)	Total oxide thickness (nm)	
			Expected[b]	Experimental[c]
5	0.619	170	340	~70
60	8.471	2329	4600	~900

[a] Calculated for pure titanium assuming 100% current efficiency.
[b] Calculated for compact amorphous film assuming 100% current efficiency.
[c] Measured using SEM.

during the immersion in PBS. Fig. 6a shows the evolution of the impedance diagrams of the non-anodized specimen. At shorter immersion times, 0.25 and 24 h, the response can be modelled by a Randles circuit, where R_e is the electrolyte resistance, R_{ct} is the charge transfer resistance and C_{dl} is the capacitance of a metallic surface covered by a native oxide film. At longer immersion times, the system behaves as a blocking electrode. In this case, the response of the system can be modelled by a resistance (R_e) in series with a capacitance (C_{dl}).

Table 3 summarizes the values of these parameters. As can be seen, although the Chi-square obtained is quite high (>10^0) the capacitance values from the simulations correspond to that expected for the capacitance of an oxidized metallic surface. The use of the capacitance in the equivalent circuit, to model the response of the native oxide layer of the substrate, sheds some light on the discussion regarding to the reliability of the estimated values of the thickness of the oxide layer.

Nevertheless, the experimental data were also simulated by the same equivalent circuits but using constant phase element, CPE, to fit the capacitances. The quality of the fitting notably improves leading to Chi-square values about 10^{-3} (values included in Table 4).

The capacitance is related to film thickness according to [41] as:

$$C = \frac{\varepsilon\varepsilon_0}{d} \quad (1)$$

where C is the capacitance in F/cm^2, ε is the dielectric constant of the surface and ε_0 is the vacuum permittivity, and d the thickness. The thickness of the native oxide film formed on the surface has been estimated assuming the value $\varepsilon = 33$ for an amorphous TiO_2 oxide [42].

Using the values of the fitted parameters for C_{dl}, in Table 3, the thickness of the native oxide layer of the non-anodized sample showed a coarsening with immersion time, from ~0.69 nm to ~2.14 nm, after 672 h, Table 3.

However when a CPE is used to model the double layer capacitance due to the non-ideal interface conditions of the surface, attributed to roughness, non-uniform distribution of the current density on the surface, and/or a distribution of dielectric relaxation times [43,44], the conversion to capacitance from the CPE parameters – the magnitude (Q) and the exponent (α) – is not so straightforward. In order to estimate the values of the capacitance from CPE, different approaches have been done. Hirschorn et al. published a complete study about the applicability of capacitance–CPE relations depending on the appropriate time-constant distribution function. These authors distinguished between surface and normal time-constant distributions [41].

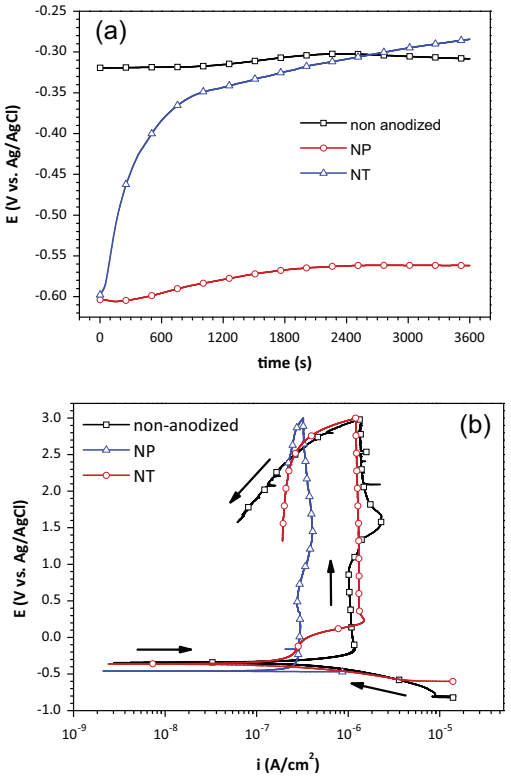

Fig. 5. (a) Evolution of the open circuit potential and (b) potentiodynamic polarization curves for the non-anodized specimen, NP and NT layers in PBS solution at 37 °C.

For a surface time-constant distribution (2-D distribution), the effective capacitance, C_{eff}, associated with the CPE can be expressed as followed:

$$C_{eff} = Q^{1/\alpha}[R_e^{-1} + R_t^{-1}]^{\alpha-1/\alpha} \quad (2)$$

when the impedance of the CPE is expressed using $Z_{CPE} = \frac{1}{Q(jw)^{\alpha}}$. where Q is the magnitude of the CPE, α is exponent of the CPE, R_e is the electrolyte resistance, and R_t is the polarization resistance. This expression is equivalent to that defined by Brug et al. [45] for a surface distribution with a different definition of the Z_{CPE} parameters, $Z_{CPE} = Q/(jw)^{1-\alpha}$.

In the limit that R_{ct} becomes infinitely large, for a blocking electrode, Eq. (2) becomes:

$$C_{eff} = Q^{1/\alpha}R_e^{1-\alpha/\alpha} \quad (3)$$

Table 4 shows the thickness of the native oxide layer, d_{eff}, of the non-anodized specimens using Eq. (2) and the C_{eff} calculated from the CPE using Eq. (3) – 2-D distribution – or (4) – blocking electrode. Although the values also showed the same increasing trend, than that estimated from the C_{dl}, the thickness values calculated from C_{eff} are slightly higher and are of the same order than those reported in literature for titanium and titanium alloys [46]. Moreover, the initial values for the thickness of the native oxide are more consistent than that described using the C_{dl} parameter, which value appears to be too low, 0.69 nm.

On the contrary, NP and NT specimens exhibit more complex impedance responses. The NP specimens – Fig. 6b – show two time-constants placed at high-medium frequencies ($\sim 10^5$–10^2 Hz) related to the response of the barrier layer at the bottom of the nanopores and at low-frequencies ($\sim 10^1$–10^{-2} Hz) due to the contribution of a diffusion process across the layer. Both time constants remain steady until the end of the test. This system can be modelled by a CPE_i in parallel with a resistance R_i, which is in series with a diffusional element, W. The diffusional element, W, is modelled by a CPE_w. In this NP layer, the CPE_i and R_i correspond to the electrical properties of the barrier layer.

The EIS spectra of the NT specimens – Fig. 6c – also show two time constants as the NP specimens but, they are placed in different frequency ranges suggesting that different mechanisms are occurring. An important contribution is observed at low-frequency range ($\sim 10^0$–10^{-2} Hz) at early immersion times that evolves with time. The low-frequency response becomes more relevant and dominates over the time constant recorded at medium-frequency ($\sim 10^3$–10^0 Hz). Both contributions correspond to the response of the substrate, which is covered by a native oxide, placed at the bottom of the inter-tubular space, Fig. 3f. As the PBS solution penetrates through the inter-tubular space and reaches the alloy,

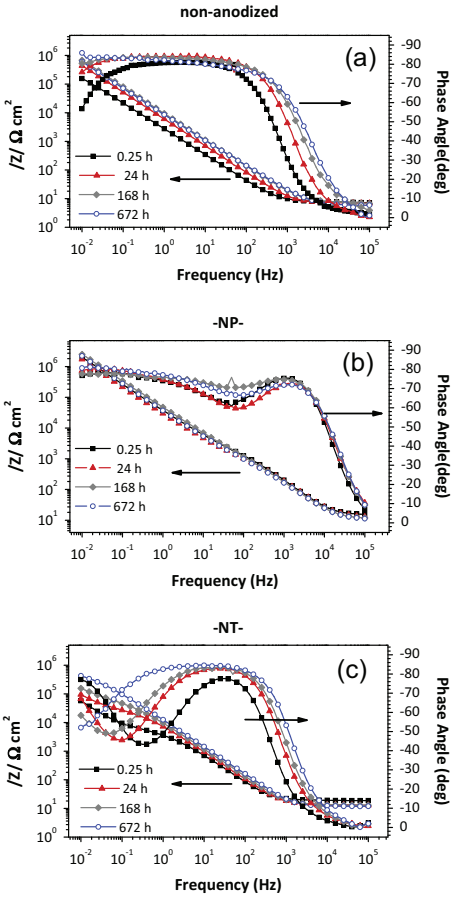

Fig. 6. EIS Bode diagrams corresponding to the non-anodized specimen (a), NP (b) and NT (c) layers at different immersion times.

Table 3
Electrical parameters values of the non-anodized specimen, including the electrical equivalent circuit used to fit the spectra.

Ti13Nb13Zr (non-anodized specimen)				
Circuit parameter	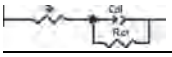			
Time (h)	0.25	24	168	672
R_e (Ω cm^2)	8.97	7.31	7.76	6.93
C_{dl} (μF/cm^2)	42.58	23.85	14.99	13.68
R_{ct} (MΩ cm^2)	0.37[a]	1.27[b]	–	–
Chi-sqr (10^{-3})	370	390	5870	10,640
d (nm)	0.69	1.23	1.95	2.14

[a] Estimated error for R_{ct}: 11%.
[b] Estimated error for R_{ct}: 17%.

Table 4
Electrical parameters values of the non-anodized specimen, including the electrical equivalent circuit with CPE used to fit the spectra. Thickness values of the oxide film formed on the non-anodized specimen estimated from different effective capacitances, C_{eff}.

	Ti13Nb13Zr (non-anodized specimen)				
	Circuit parameter				
	Time (h)	0.25	24	168	672
	R_e (Ω cm^2)	8.79	7.10	7.24	6.33
	CPE_{dl} (μSs^n/cm^2)	54.68	29.82	19.42	20.13
	α	0.92	0.93	0.92	0.90
	R_{ct} (MΩ cm^2)	0.69	3.21	–	–
	Chi-sqr (10^{-3})	3.97	0.94	3.73	5.20
2-D distribution	C_{eff} (μF/cm^2)	28.11	15.77	–	–
	$d_{2\text{-}D}$ (nm)	1.03	1.85	–	–
Blocking electrode	C_{eff} (μF/cm^2)	–	–	8.98	7.43
	$d_{B\text{-}e}$ (nm)	–	–	3.25	3.93

Table 5
Electrical parameters values of the NP and NT layers and electrical equivalent circuit used for simulation.

Circuit parameter	NP				NT			
	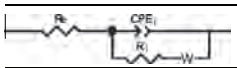							
Time (h)	0.25	24	168	672	0.25	24	168	672
R_e (Ω cm^2)	16.19	13.29	11.84	14.54	18.79	13.24	13.20	11.76
[a]CPE_i (μSs^n/cm^2)	1.37	1.08	1.28	1.54	30.55	21.70	16.81	13.62
α	0.94	0.97	0.95	0.93	0.93	0.95	0.95	0.95
[a]R_i (kΩ cm^2)	1.16	0.76	1.06	1.09	5.59	25.11	46.24	145.47
W								
CPE_w (μSs^n/cm^2)	12.94	15.19	6.96	9.11	178.51	88.62	39.52	6.21
α	0.66	0.63	0.68	0.67	0.86	0.79	0.67	0.42
Chi-sqr (10^{-3})	0.85	1.19	1.00	0.71	3.45			

[a] For the NP layers i means barrier layer (barrier); for the NT layers i means double layer (dl) for the CPE and charge-transfer for the resistance.

Fig. 3h, the current flows through the lower resistance path, and therefore the contribution of the substrate dominates the impedance response of the NT. The time constant at medium-frequency relates to the capacitance of the substrate covered by a native oxide film exposed at the bottom of the inter-tubular space while the low-frequency response corresponds to the diffusive behavior. The low-frequency contribution reveals that the diffusive response is more relevant at longer immersion times, since the native oxide layer at the bottom of the inter-tubular space thickens blocking the cathodic reaction.

The impedance spectra of the NT layers were modelled with the same equivalent circuit than NP, although the electrical parameters have different physical meaning. The CPE_i R_i corresponds to the capacitance associated with the native oxide film and the charge-transfer resistance respectively.

More recently, Cordoba-Torres et al. [38] suggest that an alternative impedance representation data using the effective CPE exponent parameter allow a more accurate analysis of the TiO_2 nanotube porous layers, pointing out that a third time constant can be identified for a TiO_2 double layered interface. Nevertheless,

Table 6
Thickness calculation of the oxide film of the NP and NT layers using a 2-D or 3-D time constant distributions to estimate the effective capacitance, C_{eff}.

		NP				NT			
	Time (h)	0.25	24	168	672	0.25	24	168	672
2-D distribution	C_{eff} (μF/cm^2)	0.68	0.73	0.75	0.72	17.39	14.13	10.80	8.60
	$d_{2\text{-}D}$ (nm)	42.98	40.06	38.85	40.50	1.68	2.07	2.71	3.40
3-D distribution	C_{eff} (μF/cm^2)	0.90	0.98	0.93	0.98	26.7	21.02	16.59	14.12
	$d_{3\text{-}D}$ (nm)	32.53	33.37	31.28	29.85	1.09	1.39	1.76	2.07

in the work, the authors consider that further studies are still required for a in-depth characterization.

Table 5 gathers the electrical equivalent circuits used and the electrochemical parameters obtained in the simulations for the NP and NT layers.

Additionally to the capacitance–CPE relations previously mentioned -2D distribution and blocking electrode-, Hirschorn et al.[41] also described that for a normal time-constant distribution (3-D distribution), the effective capacitance associated with CPE can be expressed as:

$$C_{eff} = Q^{(1/\alpha)} R_f^{(1-\alpha/\alpha)} \quad (4)$$

where R_f is the film resistance. This equation is equivalent to that proposed by Hsu and Mansfeld [47] in terms of w_{max}:

$$C_{eff} = Q w_{max}^{(\alpha-1)} \quad (5)$$

It draws attention that Eqs. 2–4 have the same form, but the resistance used for the calculation of the C_{eff} is different in the three cases, being, respectively, the parallel combination of R_t and R_e for Eq. (2), R_e for Eq. (3) and R_f for Eq. (4).

The effective capacitance (C_{eff}) calculated using Eq. (2) – 2-D distribution – and (4) – 3-D distribution – and the thickness of the oxide layers (d_{eff}) are presented in Table 6.

The determination of the oxide thickness, d_{eff}, from Eq. (1) has been estimated assuming that the dielectric constant of the oxide film are independent of position and $\varepsilon = 33$ corresponding to the dielectric constant of TiO_2 amorphous has been used despite the composition of the anodic oxide is more complex, as it was obtained by RBS.

The d_{eff} of the NT and NP layers calculated using a 2-D distribution is higher than those found with a 3-D distribution, see Table 6.

For all immersion times, the thickness of the barrier layer of the NP specimens using the C_{eff} calculated from the 3-D distribution equation is about 32 nm and about 40 nm from the 2-D distribution equation. The latter is in agreement to that measured by SEM.

The NT layers showed thickness values of the oxide layers in the range of a few nanometers, from 1.68 to 3.40 nm using a 2-D distribution equation to estimate the C_{eff}, Table 6. Thus it is consistent with the evolution of the native oxide layer of the titanium alloy surface in the bottom of the inter-tubular space and not with the thickness of the barrier layer of the nanotube measured by TEM, about 40 nm.

A time-constant distribution on TiO_2 nanotubes has been also explored by Tsui et al. [48]. These authors have used a transmission line model to represent the electrochemical interface of TiO_2 nanotubes grown in low water content organic electrolytes. These authors evaluate the dependence of the electronic transport properties with the presence of deep level defect states.

The EIS results suggest that the assumption of a surface time-constant distribution (2-D distribution) provides satisfactory values for the thickness of the barrier layer for the NP, but also for the coarsening of the native oxide film onto the non-anodized specimens and onto the substrate placed at the bottom of the inter-tubular space in NT anodic films. This work shows that a careful analysis of the impedance response supplies relevant information about the nanostructure of the anodic films.

4. Conclusions

Anodizing of Ti13Nb13Zr alloy in H_2SO_4/HF electrolyte, at controlled voltage, proceeds with formation of nanostructured TiO_2 oxide either on α-phase and β-phase. The grown efficiency of the F-doped nanotubular oxide films in Ti13Nb13Zr is about 56%, much higher efficiency than in organic electrolytes.

The composition of the nanostructured anodic layers (NP and NT) can be expressed as a oxide, $(TiNbZrO)_x$ with ($x < 1$) and a mixture of fluoride compounds, TiF_4, NbF_5, ZrF_4.

Nanoporous anodic layers – NP – grown for 5 min show higher corrosion resistance than nanotubular layers, NT fabricated for 60 min, with superior barrier properties and long term electrochemical stability. The higher compactness of the NP layer – small pore size and the absence of interpores spaces – compared to NT layer appear to be the responsible for the better protective properties.

The impedance results show either the native oxide films or the anodic films present a two dimensional time–constant distribution. The careful analysis of the CPE supplies relevant information of the nanostructural parameters of the oxide layers, such as the barrier thickness and the presence of inter-tubular spaces through the layer that jeopardizes the protective properties.

The control of the nanostructure of the anodic layers fabricated on Ti13Nb13Zr is the key factor to fabricate oxide layers with better performance. Both the nanoporous morphology and the complex composition of the oxide, enhances the corrosion resistance.

Acknowledgements

This work was supported by Spanish Ministry of Science and Innovation under Consolider-Ingenio 2010-CSD-2008-0023-FUNCOAT Project and under the MAT2013-48224-C2-1-R-MUNSUTI Project. Hernández-López J.M. is receptor of the JAE-predoc grant funded by the CSIC.

References

[1] S. Bauer, P. Schmuki, K. von der Mark, J. Park, Engineering biocompatible implant surfaces: Part I: Materials and surfaces, Prog. Mater Sci. 58 (2013) 261–326.
[2] M. Peters, J. Hemptenmacher, J. Kumpfert, C. Leyens, Structure and properties of titanium and titanium alloys, in: Titanium and Titanium Alloys, Wiley-VCH, 2005, pp. 1–36.
[3] A. Bigi, N. Nicoli-Aldini, B. Bracci, B. Zavan, E. Boanini, F. Sbaiz, S. Panzavolta, G. Zorzato, R. Giardino, A. Facchini, G. Abatangelo, R. Cortivo, In vitro culture of mesenchymal cells onto nanocrystalline hydroxyapatite-coated Ti13Nb13Zr alloy, J. Biomed. Mater. Res., Part A 82A (2007) 213–221.
[4] G. Terlinde, G. Fischer, Beta titanium alloys, in: Titanium and Titanium Alloys. Fundamentals and Applications, Wiley-VCH Verlag GmbH & Co. KGaA, 2005, pp. 37–57.
[5] M.T. Mohammed, Z.A. Khan, A.N. Siddiquee, Beta titanium alloys: the lowest elastic modulus for biomedical applications: a review, Int. J. Chem., Nucl., Metall. Mater. Eng. 8 (2014) 1123–1127.

[6] M. Geetha, A.K. Singh, R. Asokamani, A.K. Gogia, Ti based biomaterials, the ultimate choice for orthopaedic implants – a review, Prog. Mater Sci. 54 (2009) 397–425.

[7] I. Cvijović-Alagić, Z. Cvijović, J. Bajat, M. Rakin, Composition and processing effects on the electrochemical characteristics of biomedical titanium alloys, Corros. Sci. 83 (2014) 245–254.

[8] S. Minagar, C.C. Berndt, J. Wang, E. Ivanova, C. Wen, A review of the application of anodization for the fabrication of nanotubes on metal implant surfaces, Acta Biomater. 8 (2012) 2875–2888.

[9] M. Arenas, A. Conde, J. de Damborenea, E. Matikyna, J. Esteban, E. Gómez-Barrena, C. Pérez-Jorge, R. Pérez Tanoira, Materiales de titanio anodizado con fluor, PATENT, PCT/ES2011/070342, Spain, 2010.

[10] E. Matykina, J.M. Hernandez-López, A. Conde, C. Domingo, J.J. de Damborenea, M.A. Arenas, Morphologies of nanostructured TiO_2 doped with F on Ti–6Al–4V alloy, Electrochim. Acta 56 (2011) 2221–2229.

[11] C. Pérez-Jorge, A. Conde, M.A. Arenas, R. Pérez-Tanoira, E. Matykina, J.J. de Damborenea, E. Gómez-Barrena, J. Esteban, In vitro assessment of Staphylococcus epidermidis and Staphylococcus aureus adhesion on TiO_2 nanotubes on Ti–6Al–4V alloy, J. Biomed. Mater. Res., Part A 100A (2012) 1696–1705.

[12] M. Quirynen, M. De Soete, D. Van Steenberghe, Infectious risks for oral implants: a review of the literature, Clin. Oral Implant Res. 13 (2002) 1–19.

[13] Z. Wang, Y. Shen, M. Haapasalo, Dental materials with antibiofilm properties, Dent. Mater. 30 (2014) e1–e16.

[14] M. Aziz-Kerrzo, K.G. Conroy, A.M. Fenelon, S.T. Farrell, C.B. Breslin, Electrochemical studies on the stability and corrosion resistance of titanium-based implant materials, Biomaterials 22 (2001) 1531–1539.

[15] V. Raman, S. Nagarajan, N. Rajendran, Electrochemical impedance spectroscopic characterisation of passive film formed over β Ti–29Nb–13Ta–4.6Zr alloy, Electrochem. Commun. 8 (2006) 1309–1314.

[16] E.A. Ferreira, R.C. Rocha-Filho, S.R. Biaggio, N. Bocchi, Corrosion resistance of the Ti–50Zr at.% alloy after anodization in different acidic electrolytes, Corros. Sci. 52 (2010) 4058–4063.

[17] C. Vasilescu, S.I. Drob, E.I. Neacsu, J.C. Mirza Rosca, Surface analysis and corrosion resistance of a new titanium base alloy in simulated body fluids, Corros. Sci. 65 (2012) 431–440.

[18] A.K. Shukla, R. Balasubramaniam, Effect of surface treatment on electrochemical behavior of CP Ti, Ti–6Al–4V and Ti–13Nb–13Zr alloys in simulated human body fluid, Corros. Sci. 48 (2006) 1696–1720.

[19] S. Ningshen, U. Kamachi Mudali, P. Mukherjee, A. Sarkar, P. Barat, N. Padhy, B. Raj, Influence of oxygen ion irradiation on the corrosion aspects of Ti–5%Ta–2%Nb alloy and oxide coated titanium, Corros. Sci. 50 (2008) 2124–2134.

[20] J.M. Calderon Moreno, E. Vasilescu, P. Drob, P. Osiceanu, C. Vasilescu, S.I. Drob, M. Popa, Surface and electrochemical characterization of a new ternary titanium based alloy behaviour in electrolytes of varying pH, Corros. Sci. 77 (2013) 52–63.

[21] L.T. Duarte, S.R. Biaggio, R.C. Rocha-Filho, N. Bocchi, Surface characterization of oxides grown on the Ti–13Nb–13Zr alloy and their corrosion protection, Corros. Sci. 72 (2013) 35–40.

[22] M. Peters, J. Hemptenmacher, J. Kumpfert, C. Leyens, Structure and properties of titanium and titanium alloys, in: Titanium and Titanium Alloys. Fundamentals and Applications, Wiley-VCH Verlag GmbH & Co. KGaA, 2005, p. 20.

[23] ASTM F1713-08(2013), Standard Specification for Wrought Titanium–13Niobium–13Zirconium Alloy for Surgical Implant Applications (UNS R58130), ASTM International, West Conshohocken, 2013.

[24] M. Geetha, A.K. Singh, K. Muraleedharan, A.K. Gogia, R. Asokamani, Effect of thermomechanical processing on microstructure of a Ti–13Nb–13Zr alloy, J. Alloy. Compd. 329 (2001) 264–271.

[25] Y. Okazaki, Y. Ito, A. Ito, T. Tateishi, Effect of alloying elements on mechanical properties of titanium alloys for medical implants, Mater. Trans., JIM 34 (1993) 1217–1222.

[26] S. Bai, D. Ding, C. Ning, R. Qin, L. Huang, M. Li, D. Mao, Anodic growth of uniform nanotube arrays on biphase Ti35Nb5Zr alloy, Electrochem. Commun. 12 (2010) 152–155.

[27] H. Tsuchiya, T. Akaki, J. Nakata, D. Terada, N. Tsuji, Y. Koizumi, Y. Minamino, P. Schmuki, S. Fujimoto, Anodic oxide nanotube layers on Ti–Ta alloys: substrate composition, microstructure and self-organization on two-size scales, Corros. Sci. 51 (2009) 1528–1533.

[28] V. Saji, H. Choe, W. Brantley, Nanotubular oxide layer formation on Ti–13Nb–13Zr alloy as a function of applied potential, J. Mater. Sci. 44 (2009) 3975–3982.

[29] A. Valota, D.J. LeClere, P. Skeldon, M. Curioni, T. Hashimoto, S. Berger, J. Kunze, P. Schmuki, G.E. Thompson, Influence of water content on nanotubular anodic titania formed in fluoride/glycerol electrolytes, Electrochim. Acta 54 (2009) 4321–4327.

[30] D. Regonini, C.R. Bowen, A. Jaroenworaluck, R. Stevens, A review of growth mechanism, structure and crystallinity of anodized TiO_2 nanotubes, Mater. Sci. Eng.: R: Rep. 74 (2013) 377–406.

[31] P. Roy, S. Berger, P. Schmuki, TiO_2 nanotubes: synthesis and applications, Angew. Chem. 50 (2011) 2904–2939.

[32] C.A. Grimes, G.K. Mor, TiO_2 Nanotube Arrays: Synthesis, Properties, and Applications, Springer, 2009, p. 358.

[33] S. Minagar, C.C. Berndt, T. Gengenbach, C. Wen, Fabrication and characterization of TiO_2–ZrO_2–$ZrTiO_4$ nanotubes on TiZr alloy manufactured via anodization, J. Mater. Chem. B 2 (2014) 71–83.

[34] J. Fornell, N.T.C. Oliveira, E. Pellicer, N. Van Steenberge, M.D. Baró, C. Bolfarini, J. Sort, Anodic formation of self-organized Ti(Nb, Sn) oxide nanotube arrays with tuneable aspect ratio and size distribution, Electrochem. Commun. 33 (2013) 84–87.

[35] E. Matykina, A. Conde, J. de Damborenea, D.M.y. Marero, M.A. Arenas, Growth of TiO_2-based nanotubes on Ti–6Al–4V alloy, Electrochim. Acta 56 (2011) 9209–9218.

[36] M.A. Arenas, C. Pérez-Jorge, A. Conde, E. Matykina, J.M. Hernández-López, R. Pérez-Tanoira, J.J. de Damborenea, E. Gómez-Barrena, J. Esteba, Doped TiO_2 anodic layers of enhanced antibacterial properties, Colloids Surf., B 105 (2013) 106–112.

[37] A. Valota, D.J. Leclere, T. Hashimoto, P. Skeldon, G.E. Thompson, S. Berger, J. Kunze, P. Schmuki, The efficiency of nanotube formation on titanium anodized under voltage and current control in fluoride/glycerol electrolyte, Nanotechnology 19 (2008) 355701.

[38] P. Córdoba-Torres, N.T.C. Oliveira, C. Bolfarini, V. Roche, R.P. Nogueira, Electrochemical impedance analysis of TiO_2 nanotube porous layers based on an alternative representation of impedance data, J. Electroanal. Chem. (2014). http://dx.doi.org/10.1016/j.elechem.2014.06.034.

[39] M.A. Baker, S.L. Assis, O.Z. Higa, I. Costa, Nanocomposite hydroxyapatite formation on a Ti–13Nb–13Zr alloy exposed in a MEM cell culture medium and the effect of H_2O_2 addition, Acta Biomater. 5 (2009) 63–75.

[40] M. Pourbaix, Atlas of Electrochemical Equilibrium in Aqueous Solutions, NACE, USA, 1974.

[41] B. Hirschorn, M.E. Orazem, B. Tribollet, V. Vivier, I. Frateur, M. Musiani, Determination of effective capacitance and film thickness from constant-phase-element parameters, Electrochim. Acta 55 (2010) 6218–6227.

[42] T. Busani, R.A.B. Devine, Dielectric and infrared properties of TiO_2 films containing anatase and rutile, Semicond. Sci. Technol. 20 (2005) 870.

[43] J.-B. Jorcin, M.E. Orazem, N. Pébère, B. Tribollet, CPE analysis by local electrochemical impedance spectroscopy, Electrochim. Acta 51 (2006) 1473–1479.

[44] B. Hirschorn, M.E. Orazem, B. Tribollet, V. Vivier, I. Frateur, M. Musiani, Constant-phase-element behavior caused by resistivity distributions in films: I. Theory, J. Electrochem. Soc. 157 (2010) C452–C457.

[45] G.J. Brug, A.L.G. van den Eeden, M. Sluyters-Rehbach, J.H. Sluyters, The analysis of electrode impedances complicated by the presence of a constant phase element, J. Electroanal. Chem. Interfacial Electrochem. 176 (1984) 275–295.

[46] C.E.B. Marino, E.M.d. Oliveira, R.C. Rocha-Filho, S.R. Biaggio, On the stability of thin-anodic-oxide films of titanium in acid phosphoric media, Corros. Sci. 43 (2001) 1465–1476.

[47] C. Hsu, F. Mansfeld, Technical note: concerning the conversion of the constant phase element parameter Y_0 into a capacitance, Corrosion 57 (2001) 747–748.

[48] L.-K. Tsui, G. Zangari, Water content in the anodization electrolyte affects the electrochemical and electronic transport properties of TiO_2 nanotubes: a study by electrochemical impedance spectroscopy, Electrochim. Acta 121 (2014) 203–209.

Universidad Autónoma de Madrid
Centro Nacional de Investigaciones Metalúrgicas (CENIM-CSIC)